Studies on Off-Nominal Rotor Aerodynamics for eVTOL Aircraft

Thesis by
Ellande Tang

In Partial Fulfillment of the Requirements for the
Degree of
Doctor of Philosophy in Mechanical Engineering

Caltech

CALIFORNIA INSTITUTE OF TECHNOLOGY
Pasadena, California

2023
Defended December 15th, 2022

Ellande Tang
ORCID: 0000-0001-5933-4716

ACKNOWLEDGEMENTS

I have a great many people to thank for helping me complete this work. First and foremost, I would like to thank my advisor, Dr. Soon-Jo Chung, for his guidance for the past 5 years over the course of my time at the institute. He has continuously guided me, motivated me, and has provided inspiration and direction for the projects described herein. I also would like to thank the members of my committee: Joel Burdick, John Dabiri, and Phil Tokumaru. Each has provided thoughtful feedback to my work over my time here. A special thanks also goes out to Tim Colonius, Mory Gharib, and Tony Leonard, faculty who took the time to let me run ideas by them and provided feedback of my work.

My colleagues within my research group have also proven invaluable during my time. I want to give a particular thanks to Matt Anderson without whom I don't believe I could have succeeded. He provided encouragement when needed, backed by his substantial wit. I also want to thank Sorina Lupu, who has always been a perpetual supporting presence. Thanks should also be given to Xichen Shi, Patrick Spieler, and Becca Foust for their help and mentorship. I want to thank Mike O'Connell, Kai Matsuka, Ben Riviere, Jimmy Ragan, and the other members of my lab. I would like to thank the people I have met and had the pleasure of knowing at Caltech and in Los Angeles, such as Niyati Desai, Aidan Fenwick, and Andrew Taylor.

I would like to thank my family, particularly my parents Marie Durquet and Yen-Len Tang for their continual support and love from afar. I would also like to thank my grandparents, Moon-shong and Ya-ing Tang, and Marcel and Thérèse Durquet.

Finally, I would like to thank my wife, Mohar Chatterjee. I want to thank you for believing in me and waiting patiently when I struggled, and pushing me forward when I could not do so myself. You, above all else, made Caltech worthwhile.

ABSTRACT

As electric Vertical Takeoff and Landing (eVTOL) aircraft become increasingly common, improved understanding of rotor aerodynamics in off-nominal conditions becomes ever more important. A better fundamental understanding of these effects can help inform vehicle design, leading to lower power consumption and improved performance. This thesis will cover a selection of topics to gain a better understanding of the expected rotor aerodynamics associated with use in this class of vehicle, as well as the development of tools to aid in the studies and an analysis of the impact of the effects.

To consider special effects on a rotor in hover on such a vehicle, Chapter 2 is the study of obstructions in the upstream of a propeller, representing the effects of a wing or fuselage blocking a propeller's inlet. The next is the effect of forward flight on the forces produced by a rotor. Lifting rotors are often used in eVTOL aircraft as the craft transitions to forward flight, so a study of their performance in forward flight as well as a model are presented in Chapter 3. Having examined rotor-wing interactions in hover and isolated rotor performance in forward flight, the next step is to examine rotor-wing interactions in forward flight. Chapter 6 shows the design of an integrated test stand for studying the aerodynamic interactions between lifting propellers and a wing in low-speed, transitional forward flight, as well as the subsequent results.

This thesis also describes the development and implementation of two tools to aid in the work herein. The first (Chapter 4) is a rapid, low-cost method of extracting the geometry of a propeller using photogrammetry which is subsequently used in simulations. The second (Chapter 5) is low-cost and accessible multi-axis force sensor used in the integrated test stand for propeller-wing interaction studies.

To assess the impact of the findings, the experimental results and models developed are then taken into consideration by applying them to models of existing eVTOL aircraft in Chapter 7. The change in modeling of hover and transition performance is studied with and without the additional modeling.

PUBLISHED CONTENT AND CONTRIBUTIONS

[1] **Tang, Ellande** and Soon-Jo Chung. "Experimental Studies of Propeller-Wing Interactions in Transition from Hover to Forward Flight." en. In: *AIAA SCITECH 2022 Forum*. San Diego, CA & Virtual: American Institute of Aeronautics and Astronautics, Jan. 2022. ISBN: 978-1-62410-631-6. DOI: 10.2514/6.2022-0018.
E.T. participated in the conception of the project, constructed the experimental setup, conducted the experiments, analyzed the data, and wrote the manuscript. Used as source material for Chapter 6, and reprinted by permission of the American Institute of Aeronautics and Astronautics, Inc.

[2] **Tang, Ellande** and Soon-Jo Chung. "Rapid Extraction of Propeller Geometry using Photogrammetry." en. In: *International Journal of Micro Air Vehicles* 14 (Oct. 2022), pp. 1–22. ISSN: 1756-8293, 1756-8307. DOI: 10.1177/17568293221132044.
E.T. participated in the conception of the project, constructed the experimental setup, conducted the experiments, analyzed the data, and wrote the manuscript. Used as source material for Chapter 4.

[3] **Ellande Tang** and Soon-Jo Chung. "Experimental Model of Effects of Large Upstream Obstructions on Drone Scale Propellers." In: *AIAA Scitech 2021 Forum* (Jan. 2021). DOI: 10.2514/6.2021-1648.
E.T. participated in the conception of the project, constructed the experimental setup, conducted the experiments, analyzed the data, and wrote the manuscript. Used as source material for Chapter 2, and reprinted by permission of the American Institute of Aeronautics and Astronautics, Inc.

[4] **Tang, Ellande** and Soon-Jo Chung. "Rapid Extraction of Propeller Geometry Using Photogrammetry." In: *Bulletin of the American Physical Society* 66 (Nov. 2021).
E.T. participated in the conception of the project, constructed the experimental setup, conducted the experiments, analyzed the data, and wrote the manuscript. Used as source material for Chapter 4.

[5] **Tang, Ellande**, Patrick Spieler, Matthew Anderson, and Soon-Jo Chung. "Design of the Next-Generation Autonomous Flying Ambulance." In: *AIAA Scitech 2021 Forum*. Reston, Virginia, Jan. 2021, pp. 1–14. ISBN: 978-1-62410-609-5. DOI: 10.2514/6.2021-1514.
E.T. participated in the conception of the project, contributed to the determination of the vehicle layout, contributed the exterior vehicle surface modeling, and ran simulations to evaluate fuselage designs.

[6] Xichen Shi, Patrick Spieler, **Tang, Ellande**, Elena-Sorina Lupu, Phillip Tokumaru, and Soon-Jo Chung. "Adaptive Nonlinear Control of Fixed-Wing VTOL with Airflow Vector Sensing." In: *ICRA* (Mar. 2020). arXiv: 2003.07558.

DOI: 10.1109/ICRA40945.2020.9197344.
E.T. created the rotor drag formulation used in the vehicle dynamics modeling, participated in running experiments, and assisted in writing the manuscript.

[7] **Tang, Ellande** and Soon-Jo Chung. "Experiments and Modeling of the Ceiling Effect with Drone Scale Propellers." In: *AIAA Journal (under review)* (x).
E.T. participated in the conception of the project, constructed the experimental setup, conducted the experiments, analyzed the data, and wrote the manuscript. Used as source material for Chapter 2, and reprinted by permission of the American Institute of Aeronautics and Astronautics, Inc.

TABLE OF CONTENTS

LIST OF ILLUSTRATIONS

LIST OF TABLES

NOMENCLATURE

Drone. A vehicle without any human pilot, crew, or passengers on board. Conventional usage today typically refers to small-scale consumer vehicles, though also used for some military vehicles. In this work, it will be used interchangeably with the term “multirotor.”

eVTOL. electric Vertical Take-Off and Landing. Aircraft with VTOL capabilities that use electricity for power. Although the consumer drone technically qualifies as an eVTOL, the term generally refers to vehicles with both hovering and fixed-wing capabilities.

Fixed-Wing Aircraft. An aircraft that achieves flight using lift generated by wings that are fixed relative to the aircraft body.

Helicopter. A rotorcraft that supplies lift and thrust through the use of horizontally spinning rotors. An example of a aircraft with VTOL capability.

Multirotor. A vehicle that achieves flight through the use of more than 2 spinning propellers. Conventional usage today typically refers to small-scale consumer vehicles. In this work, it will be used interchangeably with the term “drone.”

Propeller. A device that uses rotation to create a force along said axis of rotation. Historically used on fixed-wing aircraft for forward flight, but the term will be used interchangeably with “rotor.”

Rotor. A device that uses rotation to create a force along said axis of rotation. Historically used to generate lift for hover, but the term will be used interchangeably with “propeller.”

Rotorcraft. Heavier-than-air aircraft with rotary wings or rotor blades.

UAV. Unmanned, Uninhabited, or Uncrewed Aerial Vehicles.

VTOL. Vertical Take-Off and Landing. Aircraft with this capability are generally able to operate without a runway. Examples of craft in this category include helicopters, tiltrotors, and jump-jet aircraft.

INSPIRATIONAL QUOTES

Finish your PhD. – Matt Anderson

Chapter 1

INTRODUCTION

Recent advances in electric energy storage technology and computing power have changed the direction of aircraft development as electric aircraft are now rapidly entering viability. A particular domain that has greatly benefited from electrification is the class of Vertical Takeoff and Landing (VTOL) aircraft. Traditional aircraft have a classical limitation–they need to reach a minimum speed before being able to sustain flight, which necessitating a runway for takeoff and landing in most cases. The helicopter provides an alternative to the fixed-wing aircraft in this regard. Helicopters are the most common example of inhabited VTOL aircraft, but they come with their own set of drawbacks, including higher energy consumption as measured by most metrics. they possess the operational advantage of being able to take of and land without a runway and hold a position for lengths of time, greatly expanding their utility in both military and civilian domains.

The invention of cost effective Lithium-ion and Lithium Polymer (LiPo) batteries has helped make electric air vehicles practical. However the specific energy of electrical energy storage technology is still not on par with fossil fuels, even after accounting for the lower efficiencies of combustion processes. The incentive for developing electric aircraft remains, since electrification confers a number of design benefits. Gas powered engines typically function optimally at a particular rotational speed, and are not conducive to the rapid changes in rotational speed. The typical solution to this is to have a variable pitch propeller to effect the change in thrust required for control, but this solution results in additional mechanical complexity and weight–a problem in traditional rotorcraft such as helicopters.

Traditional rotorcraft feature a complicated set of mechanisms to transfer power into articulated rotors. Electrical motors with fixed pitch propellers in a multirotor vehicle architecture can achieve the same level of versatility by distributing the thrust requirements over multiple smaller propellers instead of articulating a single rotor. Advances in computing power make this form of control not only possible, but practical at a small scale. With these advancements, on many vehicles, the only moving parts on many multirotor aircraft are now just the rotors themselves. Improved aircraft control simply via rotor manipulation has greatly simplified drone designs, allowing a larger population to access this flight platform than ever before. Today, by far the most well-known example of electric VTOL aircraft in the consumer space is the drone.

Unmanned, Uninhabited, or Uncrewed Aerial Vehicles (UAVs) or "Drones" are almost as old as (if not older than) their inhabited counterparts. Typically operated either remotely or featuring some form of autonomous control, these vehicles were not constrained by the additional weight and safety requirements of carrying a human. UAVs have a long history of use in military applications such as cruise missiles and reconnaissance.

Today UAVs are the most common example of the multirotor. The modern UAV is electric, has VTOL capabilities, and fully capitalizes on the aforementioned improvements in technology to deliver capabilities that were not accessible or even possible before. Small, nimble, and relatively cheap, these vehicles have found roles in everything from photography, to exploration, to platforms for conducting scientific studies. While the consumer scale drone is likely the most common eVTOL platform, the advent of electrification has heralded the rise of the electric Urban Air Mobility (UAM) or Advanced Air Mobility (AAM) vehicle. UAMs have the potential to replace the helicopter as a short-range aerial transport of choice and overcome existing technological, noise, and cost limitations to open up new markets in both military and civil sectors.

While electrification has mostly allowed the creation of new platforms at the small scale, there are a great number of potential benefits to using an array of propellers, even outside VTOL craft. The NASA X-57 Maxwell takes advantage of a propeller array along the span of the wing to reduce the takeoff speed of the aircraft. The usage of multiple sources of propulsion also has obvious positive implications on system redundancy, allowing for the system to continue operating even if several motors fail. This has provided an incentive to bringing electrification for inhabited aircraft.

This dissertation draws upon research issues in developing Caltech's Autonomous Flying Ambulance (AFA), a concept vehicle that seeks to quickly transport injured people to hospitals while bypassing traffic or obstructed disaster areas. The medical air transport application is one which could potentially see strong benefits from usage of eVTOL aircraft. Helicopters have a long history of use in the medical setting, dating back to the Second World War where casualties were evacuated from combat zones. Even today, helicopters are used extensively for medical transport, with an estimated 400,000 missions being flown each year in the US alone [1]. Despite helicopters often being the best possible option in this context, they still face a number of serious drawbacks. They are often unable to land next to the patient due to a combination of the terrain and the rotor size. In fact, helicopters often simply dangle a stretcher [2], which is used to transport the patient to an ambulance on the ground. Helicopters and their pilots also represent a significant financial burden [3], costing $1M per year per vehicle to maintain, making their value in urban settings with alternative infrastructure questionable.

Shifting medical services to the air may also help reduce the injuries associated with EMS efforts in the future. During the 1980s, it is estimated that there were as many as 12,000 Emergency Medical Services (EMS) vehicle crashes in the US every year, and transportation-related fatalities among EMS workers is significantly higher than any other emergency service workers [4]. In addition to the recorded crashes, each crash in this period tended to cause approximately four "wake effect" collisions involving other vehicles.

The AFA is a concept designed to bring air medical transport into the modern day with a more versatile and application focused design. The use of an eVTOL platform was also intended to pair synergistically with advances in autonomous systems that could improve performance or even remove pilots completely. The AFA has been a long-running project, and the author has contributed to multiple VTOL designs over the course of this work.

The AFA Version 2 (V2) is seen in Figure 1.1 and was the first version with an aerodynamic shell made of foam. It also featured wings that could fold backwards to reduce the vehicle's footprint while landing. The vehicle suffered from a high energy consumption and stability issues that restricted its practicality for an actual transition flight. The AFA V3 Was an iteration on the same basic design as the V2 and is seen in Figure 1.2. THe structure was replaced by an laser cut structure with a balsa skin to improve the internal volume, an upgraded wing, and larger rotors. It also featured a horizontal tail to help remedy the stability concerns. The vehicle was ultimately not able to transition in a physical flight test.

To remedy the design issues, the AFA V4 was redesigned from the ground up more fixed-wing focused design. The prototype can be seen in Figure 1.3. It has been designed to take into consideration from the beginning energy and stability requirements. The design has also shifted to a boom-on-wing design for mounting the rotors, and a composite shell for the aerodynamic skin and structure.

The main line of AFA vehicles are not the only eVTOL aircraft the author has worked on. Several other aircraft were inspired by or were conceptual offshoots from the AFA project. The aircraft seen in Figure 1.4, was designated the AV VTOL. The craft was a platform for work implementing a novel control algorithm described in [5]. Although a minimalist design for a VTOL platform, the vehicle was fairly robust and featured a 3-dimensional angle-of-attack sensor that used the air airflow vector in its control formulation.

Another vehicle, seen in Figure 1.5 was a proof of concept for VTOL transition during the development of the AFA. The vehicle successfully demonstrated a vertical takeoff, transition and 5-mile forward flight, and vertical landing. The test done internally validated the transition scheme as well as the basic multirotor-plane hybrid design for future vehicles.

Lastly, a vehicle was converted from an existing Skywalker X8 airframe to a quad-plane. The vehicle is seen in Figure 1.6. Extensions were installed to the airframe to attach booms containing the lifting hardware to the vehicle. The vehicle was intended as a controls testbed for the AFA V4 in order to validate any novel transition schemes or control algorithms for testing without risking the AFA V4 airframe. The Skywalker was able to successfully take off vertically and transition to forward flight, but was lost during a back-transition into a vertical landing. While the precise cause of the failure was not conclusively determined, the most likely reason was the entering of an unsteady pitch-roll cycle caused by insufficient thrust overhead at the conclusion of the flight operation.

Figure 1.1: AFA Version 2.

Figure 1.2: AFA Version 3.

Figure 1.3: AFA Version 4.

The AFA belongs to a new class of hybrid style vehicles which mix elements from both multirotor and fixed wing aircraft, and, as a new type of vehicle, there are several unknowns in the design. One is the interaction between the lifting rotors mounted on the side of the vehicle and the two deployable wings mounted at the top of the vehicle. Considering this open question leads to the natural inquiry of the more general case. How does the placement of a rotor affect a lifting surface in flight?

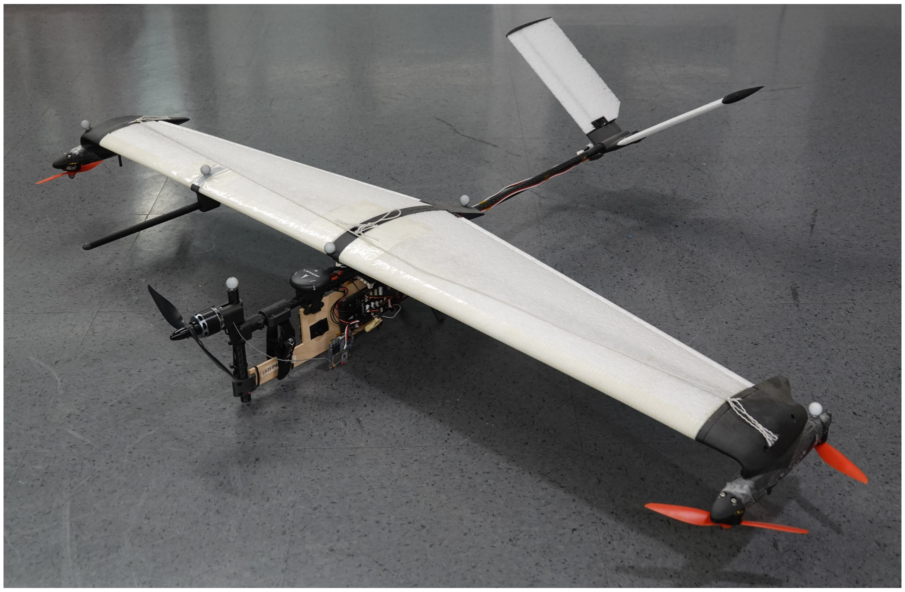

Figure 1.4: AV VTOL.

Figure 1.5: Desert flight VTOL.

This question becomes increasingly important as the popularity of this class of hybrid vehicles as an investment and research target skyrockets. Numerous UAM concepts, also marketed as “flying cars,” aimed at transporting individual humans short distances are being developed by major aerospace and transportation companies such as Airbus [6, 7], Boeing [8], and Uber [9]. Additionally, a number of these types of vehicles are emerging in the drone space as well. All these vehicles pursue the ideal of practical VTOL flight. Despite the additional system complexity, VTOL aircraft remain a desirable goal because of the substantial operational convenience they provide. Without the explicit need for a runway, VTOL aircraft can, in principle, deliver payload, cargo, or passengers directly to destination faster

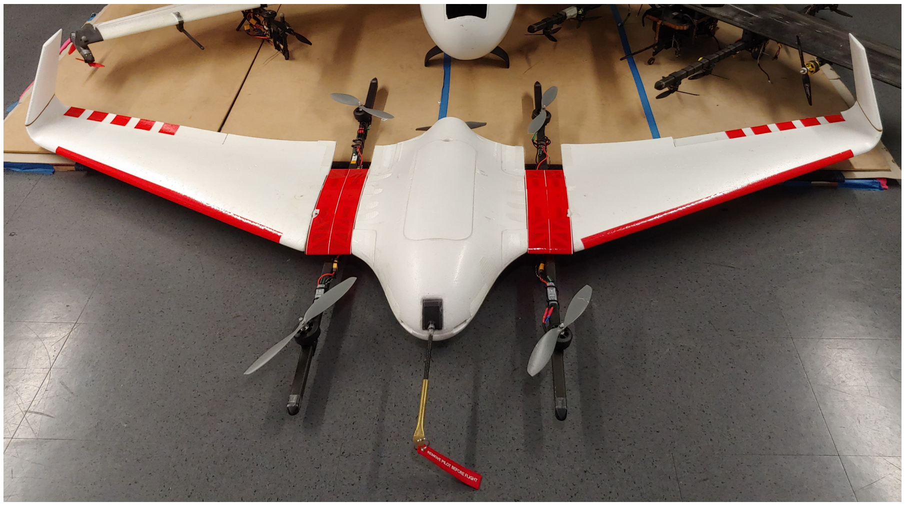

Figure 1.6: Skywalker VTOL conversion.

and more conveniently than any other means of transportation. A VTOL aircraft should be able to incorporate the benefits of both its constituent ideals and the ability to fly further and faster than a typical helicopter by way of using more efficient lifting surfaces. Indeed, many companies are taking airframes that resemble typical aircraft designs and incorporating lifting rotors to add the VTOL capability.

The potential utility of VTOL aircraft, multirotors, and even fixed wing aircraft combined with the increasing popularity of electric motors as their chosen propulsion means that understanding the fundamentals of using electric propulsion with lifting surfaces presents great benefit for scientific, military, and consumer enterprise. The increasing prevalence of such aircraft in civilian life also means that it is critical for these designs to be well understood to prevent potentially life-threating problems and design failures. Personal air vehicles, which will be flying relatively low over populated areas or the AFA, which would be transporting an injured passenger sensitive to aircraft motion, are safety critical systems where a failure could be catastrophic for both the occupants and for their surroundings.

As a flying vehicle, safety is a top consideration. Guaranteeing that a vehicle will not crash is a tremendous priority in aviation not only because of the lives of the passengers, but because, as a highly energetic form of travel, an aircraft has the capacity to do substantial damage to its surroundings. Understanding the dynamics of a class of vehicle to the fullest extent possible is a key component to establishing safety. If the vehicle's dynamics are unknown during certain regions of its flight envelope, there is no way to guarantee that it will not fail. Furthermore, accurate vehicle dynamics are an important part of developing intelligent control algorithms. Without accurate vehicle dynamics, there is no way to guarantee safety in control, and the vehicle is vulnerable to unseen instabilities in the interaction between the control law on the craft and its dynamics.

1.1 Prior Work

Extensive research exists on helicopters, but a key difference is that UAM concepts and hybrid VTOL drones feature rotors that are much smaller scale than those found in helicopters. The result is that the Reynolds number of the phenomena are much smaller.

Of particular interest at the drone scale are several experimental studies which indicate the possibility of beneficial effects of having a wing positioned in the slipstream of a propeller. Recent experiments indicate for Reynolds Numbers from 50,000–300,000, placing a propeller in front of a wing led to a nearly 70% increase in the lift to drag ratio of the wing [10]. This builds off a previous study that found similar results, finding an optimal aspect ratio wing to reap the benefits of having the system in the slipstream [11]. The authors of these studies note that the efficiency of the wing in the propeller slipstream is actually higher than in the clean configuration. The authors also note in other publications that there is a dearth of research for aerodynamic surfaces in the low Reynolds number region that MAVs typically operate, and seek to fill this [12, 13, 14, 15].

One project relevant to this proposal is the NASA X-57 Maxwell. The X-57 is an ongoing project that seeks to push the state of the art for electric aircraft [16]. Among its goals include a five-fold reduction in energy use at high-speed cruise compared to traditional propulsion while having zero in-flight carbon emissions. Preliminary testing for evaluating the feasibility of the design has been promising, and the administration is working to modify an Italian Tecnam P2006T with wings incorporating the fan array. A computational study done by members of the development team also shows promising results [17]. The computational study reports that the wing immersed in the propeller slipstream is able to increase the lift coefficient by a factor of 1.7 as compared to the unblown wing. Additionally, the cruise propulsors mounted at the wingtips reduce the induced drag by 7.5 percent by rotating counter to the wingtip vortices, suggesting an additional avenue for potential study.

With the existence of modern VTOL aircraft, a substantial quantity of research has been carried out on helicopter and tiltrotor aerodynamics. Recently, Computational Fluid Dynamics (CFD) has been used to study rotorcraft in a variety of scenarios [18, 19, 20]. Being a more recent invention, the modern multirotor has less aerodynamics research devoted to it. Some older CFD has been used to model MAV blades with some success, though the values for the figure of merit of the propeller were overestimated [21]. Some studies do also attempt to study the interaction between propellers and lifting surfaces with CFD, mainly by modeling the propeller with a actuator disk or line [22, 23, 24].

Besides CFD where the entire fluid domain is discretized, a large number of studies also try to model the properties of rotors using either panel methods, Blade Element Theory, or Free-Vortex Wake model [25, 26, 27]. One study actually used a vortex panel solver in conjunction with a Navier-Stokes solver to examine a wind-turbine blade [28, 29, 30]. There are also numerous empirical studies of the flow downstream of a propeller against which to compare models [13, 31, 32, 33].

One interesting body of work is that of researchers at TU Delft [34, 35, 36], who have done extensive work on propeller-wing interactions. In Leo Veldhuis's doctoral thesis in particular, he uses a conjunction of CFD, Panel Methods, and experiments to study the effects of a tractor propeller on a wing and optimize the wings geometry to best take advantage of the wing's slipstream. One important result is that the Vortex Lattice Method used was found to accurately predict the effects of the propeller with certain criteria applied. This encourages the notion that a panel method may be used for relatively quick iteration of design and to gain an at least cursory analysis of a given configuration. The other work by researchers at TU Delft attempt to optimize propulsion in relation to the wingtip vortices, an avenue for efficiency gain postulated above. It would appear that there remain worthwhile topics to explore, even within the domain of tractor propellers.

The text "Aerodynamics of V/STOL Flight" [37] has a section dedicated to the behavior of a wing in a propeller slipstream. In the text of both the 1967 and the 1999 editions, the author states that "Several approaches to the problem of a wing in a propeller slipstream can be found in the literature. None of these is quite satisfactory. Either the physical model is too simplified and restricted in its range of application or more exact solutions are too complicated for practical application." The information presented here indicates that there exists a substantial body of research into the aerodynamics of rotors and the interactions of rotors in the tractor and pusher configurations with lifting surfaces. Less research can be found explicitly dealing with the interaction of lifting rotors with lifting surfaces. Some research does exist, often concerned with rotor download [38, 39, 40]. Research into lifting propeller wing interactions in forward flight is substantially scarcer, and likewise with multi-propeller interactions. With the advent of new personal VTOL aircraft, interest in general frameworks for evaluating these designs is increasing. One example is the development of a Vortex Particle Method for this purpose [41]. Despite the overlap with multiple areas of aerodynamics and aircraft design, this subject appears to be ripe for study and innovation.

1.2 Research Vision and Objective

The objective of this dissertation is to identify how to place propellers on an eVTOL aircraft. As eVTOL craft possess propellers that are often being used outside the nominal conditions of their design, focus will be directed to their use in off-nominal situations such as their interactions with external bodies. By conducting experiments and analysis, models can be constructed that either lend insight into the physical phenomenon or provide design guidelines for future craft. While the interactions between rotors and lifting surfaces or other bodies are too complex to model definitively, by focusing on select topics relevant to the field, progress can be made. This work will expand knowledge on effects that are relevant to the design of eVTOL aircraft and develop broad "rules of thumb" that will inform the design of future vehicles.

1.3 Thesis Contributions

- A comprehensive study to describe the interaction between a propeller and a large upstream obstruction is presented. The study combines experimental data, simulation, and physics based theory in describing the effect and the interaction. It is shown that a non-dimensionalization method presented is able to successfully collapse the net force of an arrangement to a single curve. Subsequent CFD simulations of the phenomena show that the Transition SST turbulence model in ANSYS agrees well with both overall force and pressure measurements taken on the surface of the upstream obstruction. The flow separation near the axis of rotation of the propeller is identified and found to an inherent feature of the flow, and the locations of the separation points are found. It is shown that the prediction of the separation location using Thwaites' Criterion [42] agrees well with the simulation results.

- Implementation of the Morillo flowfield model [43] for axial, steady state conditions. Discrepancies with the CFD simulation results are noted and discussed, and a correction is derived. In particular, phenomena that are not captured by the analytical model are highlighted. The Morillo flowfield model is then applied with the method of images to simulate a wall boundary. The accuracy is compared to the CFD and experimental results and good agreement is found.

- A study quantifying and modeling the drag of a rotor in forward flight is presented. Experimental data is used to develop a non-dimensional model that represents the data well. The coefficients for the model are similar across the majority of propellers studied. Vortex Particle Method (VPM) simulations are compared to the experimental results and are demonstrated to consistently underpredict the rotor drag.

- A complete, end-to-end workflow to extract the geometry of an off-the-shelf propeller efficiently, quickly, and with easily accessible equipment has been developed. The workflow consists of a set of systematic guidelines is presented for photo collection to reliably produce a dense and accurate pointcloud of a propeller using photogrammetry as well as an algorithm for alignment, scaling and feature extraction of the pointcloud that requires minimal human input was also developed.

- Hardware design and accuracy evaluation of a 6 degree of freedom force sensor for aerodynamic measurement applications. The sensor is built using inexpensive, easily accessible, or easy to manufacture components. The sensor is also robust to individual sensor failures and overloading, being compatible to repair and part replacement.

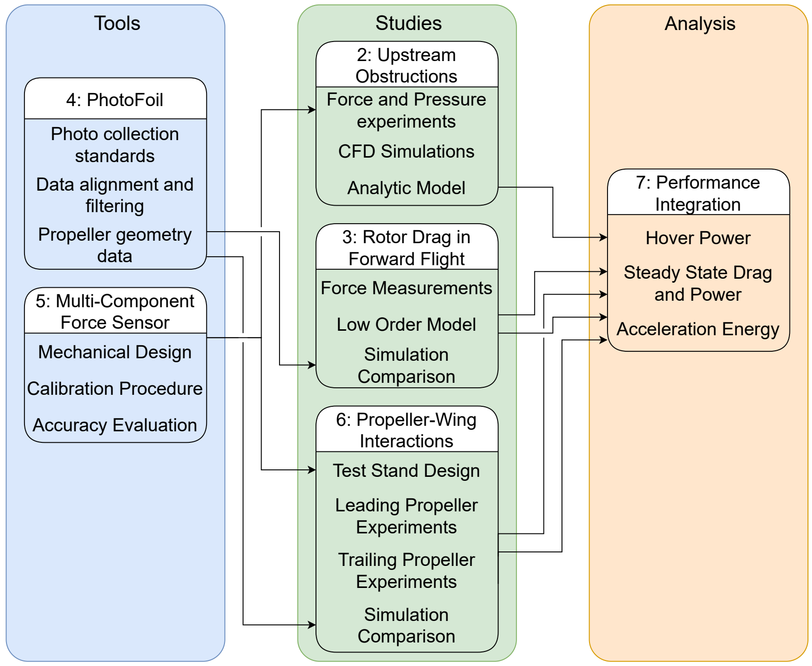

Figure 1.7: Illustration of the relations between chapters.

- The design of a test assembly integrating multiple sensor elements and automated positioning for study of the aerodynamic interaction between a propeller and a wing. Force data for the interactions between a lifting propeller and a wing in both a leading and trailing configuration. An empirical fit to describe the change in aerodynamic coefficients from propeller-wing interactions

- Integration of rotor drag and propeller wing interaction into models of existing eVTOL aircraft to showcase the change in energy and drag prediction that results from the inclusion of the models.

1.4 Thesis Structure

This thesis will examine various topics pertaining to the aerodynamics of eVTOL aircraft over the course of 6 chapters, alongside an introduction and a conclusion. Each chapter concerns a different topic, tool, or analysis and seeks to be a relatively self contained entry on its respective subject. Each chapter thus has its respective context and associated literature survey, theory, methodology, and results. A diagram illustrating the interconnections between the chapters is shown in Figure 1.7.

Each chapter of the thesis addresses a different topic relevant to the operational envelope of an eVTOL aircraft. As the craft takeoff and land vertically, some portion of the flight regime will be in hover. This raises the question of how the placement of lifting hardware on the aircraft affects their performance. Chapter 2 outlines the effect of having a large obstruction in the vicinity of a propeller in hover. This topic examines the canonical case to better inform the placement of a propeller relative to portions of the aircraft such as wings or the fuselage.

As the craft transitions to forward flight, the vehicle begins picking up horizontal velocity, reducing dependence on the rotors as the wing provides more lift. The rotors, normally used for hover conditions, are subjected to forward motion and the resulting aerodynamic effects. Chapter 3 details studies of lifting drone propellers in forward flight. The use of lifting propellers in forward flight has been found to have a substantial drag penalty, and this section outlines experiments, modeling, and analysis of this effect.

To conduct some of the analysis detailed in this work, simulation was used. Because published geometry for particular propellers is scarcely available, it was necessary to develop a method of extracting the geometry of off the shelf propellers. Chapter 4 describes the development and use of a novel software tool used to achieve this. The developed workflow and software, PhotoFoil, uses photogrammetry to scan the geometry in a rapid and contactless manner that requires no specialized equipment and leverages existing photogrammetry software. In addition to describing techniques to improve the resolution of the geometric data produced, the chapter also outlines the steps used to interpret the data into a convenient format, as well as the data's accuracy.

As the vehicle accelerates, the lifting rotors are not necessarily operating in isolation. Their close proximity to the lifting surfaces of the vehicle can result in aerodynamic interaction. With a rotor in hover and an isolated rotor in forward flight examined, the next area of study is the aerodynamic interaction between a rotor and a finite wing. Studying this requires additional measurement hardware to measure the forces on the finite wing independently of the propeller. Chapter 5 outlines the development and evaluation of a 6-degree of freedom force sensor for this purpose. Chapter 6 then describes the remainder of the experimental assembly as well as the experimental studies conducted examining the propeller wing interaction and the conclusions drawn.

Finally, Chapter 7 implements the findings on three models of existing eVTOL aircraft. Integration of the findings into each vehicle's model highlights the change in vehicle characteristics and performance provided by the additional detail.

References

[1] AAMS. *AAMS Fact Sheet and FAQs*. 2020. URL: https://aams.org/member-services/fact-sheet-faqs/ (visited on 06/03/2020).

[2] Christopher Brito. *Dramatic Video Shows Helicopter Rescue of Injured Woman Spinning Wildly Out of Control*. June 2019. URL: https://www.cbsnews.com/news/helicopter-rescue-spinning-phoenix-arizona-piestewa-peak-stretcher/ (visited on 06/03/2020).

[3] Bryan Bledsoe. *EMS Myth #6: Air Medical Helicopters Save Lives and are Cost-Effective*. 2003. URL: https://www.emsworld.com/article/10325077/ems-myth-6-air-medical-helicopters-save-lives-and-are-cost-effective (visited on 06/03/2020).

[4] Douglas F. Kupas. *Lights and Siren Use by Emergency Medical Services (EMS): Above All Do No Harm*. Tech. rep. U.S. Department of Transportation: National Highway Traffic Safey Administration Office of Emergency Medical Services (EMS), 2017.

[5] Xichen Shi, Patrick Spieler, **Tang, Ellande**, Elena-Sorina Lupu, Phillip Tokumaru, and Soon-Jo Chung. "Adaptive Nonlinear Control of Fixed-Wing VTOL with Airflow Vector Sensing." In: *ICRA* (Mar. 2020). arXiv: 2003.07558. DOI: 10.1109/ICRA40945.2020.9197344.

[6] Airbus. *Vahana*. https://www.airbus-sv.com/projects/1. Accessed: May 1st, 2019. (Visited on 05/01/2019).

[7] Airbus. *CityAirbus - Urban Air Mobility - Airbus*. https://www.airbus.com/innovation/zero-emission/urban-air-mobility/cityairbus.html. 2020.

[8] Aurora. *Urban Air Mobility*. en-US. (Visited on 12/01/2022).

[9] Uber. *Uber Elevate*. https://www.uber.com/us/en/elevate/. (Visited on 11/30/2022).

[10] Gavin K. Ananda, Michael S. Selig, and Robert W. Deters. "Experiments of Propeller-Induced Flow Effects on a Low-Reynolds-Number Wing." In: *AIAA Journal* 56.8 (Aug. 2018), pp. 3279–3294. ISSN: 0001-1452. DOI: 10.2514/1.J056667.

[11] Gavin Kumar Ananda Krishnan, Robert W. Deters, and Michael S. Selig. "Propeller-Induced Flow Effects on Wings of Varying Aspect Ratio at Low Reynolds Numbers." In: *32nd AIAA Applied Aerodynamics Conference*. June. Reston, Virginia: American Institute of Aeronautics and Astronautics, June 2014, pp. 1–20. ISBN: 978-1-62410-288-2. DOI: 10.2514/6.2014-2152.

[12] Gavin K. Ananda, Pritam P. Sukumar, and Michael S. Selig. "Measured Aerodynamic Characteristics of Wings at Low Reynolds Numbers." In: *Aerospace Science and Technology* 42 (Apr. 2015), pp. 392–406. ISSN: 12709638. DOI: 10.1016/j.ast.2014.11.016.

[13] Robert W. Deters, Gavin K. Ananda, and Michael S. Selig. "Slipstream Measurements of Small-Scale Propellers at Low Reynolds Numbers." In: *33rd AIAA Applied Aerodynamics Conference*. June. Reston, Virginia: American Institute of Aeronautics and Astronautics, June 2015, pp. 1–25. ISBN: 978-1-62410-363-6. DOI: 10.2514/6.2015-2265.

[14] John Brandt and Michael Selig. "Propeller Performance Data at Low Reynolds Numbers." In: *49th AIAA Aerospace Sciences Meeting including the New Horizons Forum and Aerospace Exposition*. January. Reston, Virigina: American Institute of Aeronautics and Astronautics, Jan. 2011, AIAA 2011–1255. ISBN: 978-1-60086-950-1. DOI: 10.2514/6.2011-1255.

[15] Robert W. Deters, Or D. Dantsker, Stefan Kleinke, Narcrisha Norman, and Michael Selig. "Static Performance Results of Propellers Used on Nano, Micro, and Mini Quadrotors." In: *2018 Applied Aerodynamics Conference*. Issue: July. Reston, Virginia: American Institute of Aeronautics and Astronautics, June 2018, pp. 1–15. ISBN: 978-1-62410-559-3. DOI: 10.2514/6.2018-4122.

[16] Yvonne Gibbs. *NASA Armstrong Fact Sheet: NASA X-57 Maxwell*. https://www.nasa.gov/centers/armstrong/news/FactSheets/FS-109.html. Accessed: April 28th, 2019. 2018. (Visited on 04/28/2019).

[17] Karen A. Deere, Jeffrey K. Viken, Sally Viken, Melissa B. Carter, Michael Wiese, and Norma Farr. "Computational Analysis of a Wing Designed for the X-57 Distributed Electric Propulsion Aircraft." In: *35th AIAA Applied Aerodynamics Conference*. Reston, Virginia: American Institute of Aeronautics and Astronautics, June 2017. ISBN: 978-1-62410-501-2. DOI: 10.2514/6.2017-3923.

[18] Massimo Biava, Walid Khier, and Luigi Vigevano. "CFD Prediction of Air Flow Past a Full Helicopter Configuration." In: *Aerospace Science and Technology* 19.1 (June 2012), pp. 3–18. ISSN: 12709638. DOI: 10.1016/j.ast.2011.08.007.

[19] Ilker Oruc, Joseph F Horn, and Jeremy Shipman. "Coupled Flight Dynamics and CFD Simulations of Rotorcraft/Terrain Interactions." In: *AIAA Modeling and Simulation Technologies Conference*. January. Reston, Virginia: American Institute of Aeronautics and Astronautics, Jan. 2016. ISBN: 978-1-62410-387-2. DOI: 10.2514/6.2016-2136.

[20] Ilker Oruc, Jeremy Shipman, and Joseph F. Horn. "Towards Real-Time Fully Coupled Flight Dynamics and CFD Simulations of the Helicopter / Ship

Dynamic Interface Rajiv Shenoy.” In: *AHS International 71st Annual Forum*. May. Virginia Beach, 2015, pp. 1–10.

[21] Felipe Bohorquez, Falcon Rankins, James Baeder, and Daryll Pines. “Hover Performance of Rotor Blades at Low Reynolds Numbers for Rotary Wing Micro Air Vehicles. An Experimental and CFD Study.” In: *21st AIAA Applied Aerodynamics Conference*. Reston, Virigina: American Institute of Aeronautics and Astronautics, June 2003. ISBN: 978-1-62410-092-5. DOI: 10.2514/6.2003-3930.

[22] Sven Schmitz and Pankaj K. Jha. “Modeling the Wakes of Wind Turbines and Rotorcraft Using the Actuator-Line Method in an OpenFOAM -LES Solver Modeling the Wakes of Wind Turbines and Rotorcraft Using the Actuator-Line Method in an OpenFOAM - LES Solver.” In: *AHS 69th Annual Forum*. May. Phoenix, 2013.

[23] Kwanchai Chinwicharnam, Edgard David Gomez Ariza, Jean-Marc Moschetta, and Chinnapat Thipyopas. “A Computation Study on the Aerodynamic Influence of Interaction Wing-Propeller for a Tilt-Body MAV.” en. In: *Aircraft Engineering and Aerospace Technology* 87.6 (Oct. 2015). Ed. by Prof Renuganth Varatharajoo, pp. 521–529. ISSN: 0002-2667. DOI: 10.1108/AEAT-06-2014-0087.

[24] Sparsh A. Chadha, Brent W. Pomeroy, and Michael S. Selig. “Computational Study of a Lifting Surface in Propeller Slipstreams.” In: *34th AIAA Applied Aerodynamics Conference*. June. Reston, Virginia: American Institute of Aeronautics and Astronautics, June 2016, pp. 1–19. ISBN: 978-1-62410-437-4. DOI: 10.2514/6.2016-3132.

[25] Sandeep Gupta and John Leishman. “Comparison Of Momentum And Vortex Methods For The Aerodynamic Analysis Of Wind Turbines.” In: *43rd AIAA Aerospace Sciences Meeting and Exhibit*. January. Reston, Virigina: American Institute of Aeronautics and Astronautics, Jan. 2005. ISBN: 978-1-62410-064-2. DOI: 10.2514/6.2005-594.

[26] Sandeep Gupta and J. Gordon Leishman. “Accuracy of the Induced Velocity from Helicoidal Wake Vortices Using Straight-Line Segmentation.” In: *AIAA Journal* 43.1 (Jan. 2005), pp. 29–40. ISSN: 0001-1452. DOI: 10.2514/1.1213.

[27] Shreyas Ananthan, J. Gordon Leishman, and Manikandan Ramasamy. “The Role Of Filament Stretching In The Free-vortex Modeling Of Rotor Wakes.” In: *58th Annual Forum and Technology Display of the American Helicopter Society International*. Vol. 3. 2. Montreal, 2002, pp. 635–641.

[28] Sven Schmitz and Jean-Jacques Chattot. “A Coupled Navier–Stokes/Vortex–Panel Solver for the Numerical Analysis of Wind Turbines.” In: *Computers & Fluids* 35.7 (Aug. 2006). Ed. by Alexander Kuzmin. Publisher: Springer Berlin Hei-

delberg Place: Berlin, Heidelberg ISBN: 978-3-642-17883-2, pp. 742–745. ISSN: 00457930. DOI: 10.1016/j.compfluid.2006.01.006.

[29] Sven Schmitz and Jean-Jacques Chattot. "Influence of the Vortical Wake Behind Wind Turbines using a Coupled Navier-Stokes/Vortex-Panel Methodology." In: *Third MIT Conference on Computational Fluid and Solid Mechanics* (2005), pp. 832–836.

[30] Sven Schmitz, Mahendra Bhagwat, and Francis Caradonna. "A Generalized Potential Method for Modeling Rotor Wake Flows." In: *27th AIAA Applied Aerodynamics Conference*. June. Reston, Virigina: American Institute of Aeronautics and Astronautics, June 2009, pp. 1–15. ISBN: 978-1-62410-130-4. DOI: 10.2514/6.2009-3856.

[31] Preston B. Martin and J. Gordon Leishman. "Trailing Vortex Measurements in the Wake of a Hovering Rotor Blade With Various Tip Shapes." In: *58th Annual Forum of the AHS International*. Montreal, 2002, pp. 2058–2080.

[32] K. W. McAlister, C. A. Schuler, L. Branum, and J. C. Wu. *3-D Wake Measurements Near a Hovering Rotor for Determining Profile and Induced Drag*. Tech. rep. NASA-TP-3577. 1995.

[33] Manikandan Ramasamy, J. Gordon Leishman, and Timothy E. Lee. "Flowfield of a Rotating-Wing Micro Air Vehicle." In: *Journal of Aircraft* 44.4 (July 2007), pp. 1236–1244. ISSN: 0021-8669. DOI: 10.2514/1.26415.

[34] Leo Veldhuis. *Propeller Wing Aerodynamic Interference*. Delft, 2005.

[35] Bas Nootebos. "Aerodynamic Analysis and Optimisation of Wingtip-Mounted Pusher Propellers." MS. Delft University of Technology, 2018.

[36] Thijs Bouquet. "Modelling the Propeller Slipstream Effect on the Longitudinal Stability and Control." M.S. Delft University of Technology, 2016, p. 76.

[37] Barnes W. McCormick. *Aerodynamics of V/STOL Flight*. Academic Pr, 1967. ISBN: 0124823505.

[38] Michael R. Derby and Larry A. Young. *Rotor/Wing Interactions in Hover*. Tech. rep. TM-2002-211392. NASA, 2002.

[39] Daniel A. Wachspress, Todd R. Quackenbush, and Alexander H. Boschitsch. "First-Principles Free-Vortex Wake Analysis for Helicopters and Tiltrotors." In: *AHS 59th Forum* (2003), p. 1.

[40] Vinit Gupta and James D. Baeder. "Quad Tiltrotor Aerodynamics in Ground Effect." In: *58th Annual Forum, American Helicopter Society*. 2002.

[41] Eduardo J. Alvarez and Andrew Ning. "Development of a Vortex Particle Code for the Modeling of Wake Interaction in Distributed Propulsion." In: *2018 Applied Aerodynamics Conference*. Reston, Virginia: American Institute of Aeronautics and Astronautics, June 2018. ISBN: 978-1-62410-559-3. DOI: 10.2514/6.2018-3646.

[42] Tuncer Cebeci, G. J. Mosinskis, and A. M. O. Smith. "Calculation of Separation Points in Incompressible Turbulent Flows." In: *Journal of Aircraft* 9 (9 Sept. 1972), pp. 618–624. ISSN: 0021-8669. DOI: 10.2514/3.59049.

[43] Jorge A. Morillo and David A. Peters. "Velocity Field Above a Rotor Disk by a New Dynamic Inflow Model." en. In: *Journal of Aircraft* 39.5 (Sept. 2002), pp. 731–738. ISSN: 0021-8669, 1533-3868. DOI: 10.2514/2.3019.

Chapter 2

INTERACTION BETWEEN A PROPELLER AND A LARGE UPSTREAM OBSTRUCTION

2.1 Introduction

Breakthroughs in computing power and small scale electronics in the recent decades have led to Uninhabited Aerial Vehicles (UAVs) becoming increasingly ubiquitous. Recently, there has been a push to marry the design components of electric multirotors and fixed-wing aircraft for various applications, resulting in the designation of electric Vertical Takeoff and Landing (eVTOL) aircraft. Many different companies are producing a variety of designs to meet these mission criteria [1]. The recent improvements in electric propulsion have made the use of multiple smaller sources of propulsion economical, but have resulted in unknown aerodynamic interactions between the propulsion components and other aspects of the system. Such an arrangement can be seen in Figure 2.1a, where the wings of the aircraft are located directly above some of the aircraft's propellers. This obstruction is also seen in Figure 2.1b, and was an important design consideration in the placement of the tip mounted propellers on the vehicle [2].

Choosing how to place a propeller in relation to a wing or a fuselage on an aircraft is expected to be a common design consideration for future eVTOL aircraft. Developing a model to predict the effects of this interaction would allow rotors to be more intelligently placed in the design phase of these future vehicles. To achieve this, this paper collects empirical data, runs simulations, and examines the physics to develop a model predicting the force interaction between a propeller and a large obstructing surface in its upstream.

Prior Work

The effect of large upstream propeller obstructions, also called the ceiling effect, is relatively unstudied. Although there is known synergy between propulsors and wakes of bodies in forward flight [6, 7, 8], fixed wing aircraft rarely hover in any capacity, so large obstructions near propellers in static conditions would not be of interest. Rotorcraft, on the other hand, often have a main rotor disk area that is larger than the rest of the body. The lifting rotor is also typically above the aircraft body for reasons of practicality. The vehicle thus would have little reason or even

(a) The 4th version of the Caltech Autonomous Flying Ambulance scale model [3, 4, 5]

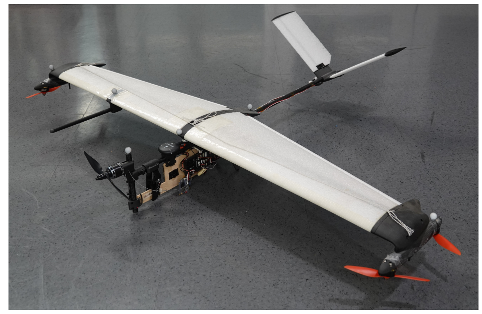

(b) Caltech VTOL test platform [2]

Figure 2.1: eVTOL aircraft from Caltech.

the possibility of operating with an obstruction upstream of the rotor and rarely, if ever, operate near an external obstruction large enough to occlude the propeller from above.

In contrast, the opposite configuration, the ground effect, is quite well studied. Obstructions downstream of a propeller are known to be beneficial to performance if external to the vehicle such as a ground plane. They can also be detrimental if a part of the vehicle. For instance, a significant portion of a rotorcraft's thrust is lost as a result of the fuselage being in the rotor's wake, and the effect of the wing in the rotor downwash was an area of study during the development of the V-22 Osprey and related tiltrotors [9, 10, 11, 12].

One of the few older treatments of the problem is seen in Rossow [13] where the interaction of a single rotor in the ground and ceiling effect is addressed in the context of mitigation the influence of the boundaries during wind tunnel testing. Rossow also develops a theory using the method of images with cylindrical vortex sheets to attempt to model the ceiling and ground effects using the theory of Knight and Hefner [14, 15]. This theory depends on the shed vorticity from a rotor disk rather than the representing the rotor as a disk actuator. Beyond this, the closest classical research identified by the authors was that concerning the performance of pusher configuration helicopter tail rotors in relation to the tail fin [16], which reaches similar conclusions to those in this paper albeit with less rigor.

Multirotors do have the possibility of obstructions in the propeller upstream. Propellers are mounted below the craft in some designs, and the vehicles are often used indoors. It is well known in the hobby community that flying a multirotor near a ceiling is a dangerous maneuver, as the craft can be sucked onto the surface, striking the rotors and crashing. These applications combined with the rise in popularity of multirotors has meant that the ceiling effect has recently become a subject of interest.

One of the first modern works identified that examined the ceiling effect was work by Conyers [17]. A multirotor and an individual rotor are examined empirically in this work and the results related to a classical ground effect model by Cheeseman [18]. Another that was identified which sought to study this effect was Nohara [19]. The authors measured the change in thrust and developed a vehicle to capitalize upon the effect. However, they did not examine the force on the surface with which they interacted, so this work is insufficient for providing guidelines for determining the effect of components of the craft upon the rotor.

Work by Carter [20] and Gao [21] has also studied the ceiling effect, albeit from the perspective of influence on a multirotor. These works utilized some flow visualization and provided empirically fitted models to match the force results. A commonality between the multirotor studies is that they typically examine the forces on the multirotor only, not examining the force on the ceiling. The force on the obstruction may not be relevant for drone navigation in interior environments, but it is potentially important for VTOL aircraft design. Work by Karnatowski [22] is a recent work more relevant to this study. In this work, the problem of package transportation above a drone is considered, thus requiring data on both the propellers and the surface. However, the aerodynamic treatment is brief and empirical, with little modeling.

Work by Cai [23, 24, 25] on the ceiling effect is relevant. Cai examines the effect of various shapes and sizes of obstruction on the propeller are paired with pressure measurements. Tuft measurements also identified a “stagnation zone” within a certain radius on the obstruction surface. This region is likely the same as the separated flow region identified and described later in this work. The work by Cai is often more focused on looking at the change in power consumption, and how the shape of the obstruction affects the response.

Many of the aforementioned works utilize ground effect models in their attempts to develop an analytical theory. In particular the work of Cheeseman [18] who references Betz [26] is used. These works treat the rotor as a singular source or sink and estimate the change in performance based on the change in velocity at the source using the method of images. However, this highly simplistic model is insufficient to compute the flow field around the propeller. It also fails to consider the physically important phenomenon of the shed vortex sheet from the rotor. Generally, as the ceiling effect was initially studied because of physical considerations for mitigation or avoidance, existing work is typically application focused with little effort dedicated to developing a theory or providing an understanding of the underlying phenomenon.

Contributions

In contrast to previous work which broadly examines the influence of different shapes of upstream obstruction and the change in performance of particular propellers, the work presented in this paper examines in depth the canonical case of a theoretically infinite obstruction and its interaction with a propeller. To do so, the problem is studied with a variety of tools from experimental force and pressure measurements to Computational Fluid Dynamics (CFD) simulations and an analytic, physics based model. It is believed that focus on the mechanism of the phenomena and its cause will help inform future VTOL aircraft design, and will better describe multirotor behavior in the proximity of obstructions, allowing for a better description of the physics of navigating in indoor environments. The contributions of this work are the following:

1. Force data for both the propeller and the obstructing surface are collected and represented using non-dimensional coefficients. These results quantify and illustrate the change in a selection of propellers' performance relative to one another as they are brought near the upstream obstruction. The non-dimensionalization method presented here is able to successfully collapse the net force of an arrangement to a single curve. Portions of this paper were previously presented in our prior conference paper [27].

2. Pressure measurements on the surface of the upstream obstruction. To help describe the phenomena, the pressure is surveyed along the upstream obstruction for various separation distances and rotor rotation speeds. This data is used to help describe the flow field at the surface. A linear relation is dimensionally derived and shown to be a good predictor of the relationship between the disc loading and the measured pressure.

3. CFD simulations of the upstream obstruction phenomena including velocity vector fields, pressure contours, and force measurements. The phenomena is studied using a uniform disk actuator model using the commercial soft-

ware package ANSYS Fluent [28]. Pressure and force measurements are corroborated with data from the experiments and good agreement is found. Various simulation models are also compared to determine the best model for accuracy.

4. Identification and explanation of the flow separation near the axis of rotation of the propeller. This phenomenon is identified as an inherent feature of the flow, and the locations of the separation points are found. These locations are then compared to locations predicted by a separation criterion using the results of inviscid simulation.

5. Implementation of the Morillo flowfield model [29] for axial, steady state conditions. Discrepancies with the CFD simulation results are noted and discussed, and a correction is applied. In particular, phenomena that are not captured by the analytical model are highlighted. The Morillo flowfield model is then applied with the method of images to simulate a surface boundary. The accuracy is compared to the CFD and experimental results and good agreement is found.

6. A correction is provided to resolve numerical floating point errors while calculating the values of large complex inputs to Legendre functions of the second kind.

Organization

This chapter is broadly organized in three parts. Section 2.2 details experiments conducted to measure and understand the physical effect of the obstruction on a propeller alongside pressure measurements at the surface of the obstruction. Section 2.3 then examines the aerodynamic effects of interest from the previous section using ANSYS Fluent, comparing the CFD simulations with the experimental results and producing explanations for some of the observed effects. The third part of the work in Section 2.4 seeks to find a solution to describe the problem using theory derived from physics. The section reviews the assumptions and the derivation of the rotorcraft model used. The results of the model are then compared to the CFD results for accuracy, and corrections are applied.

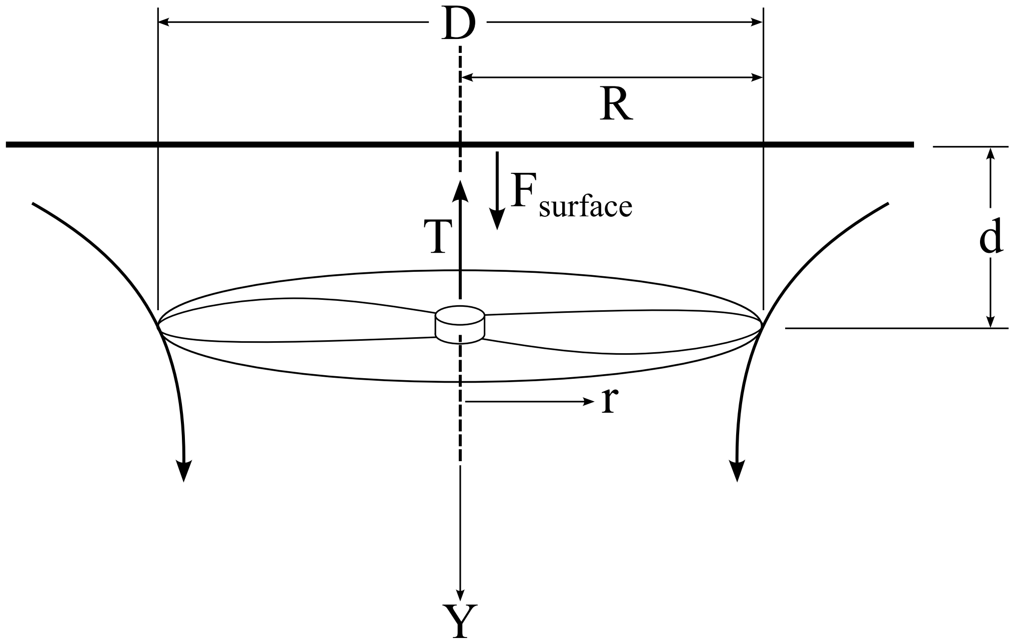

Figure 2.2: Coordinate system using axisymmetric notation.

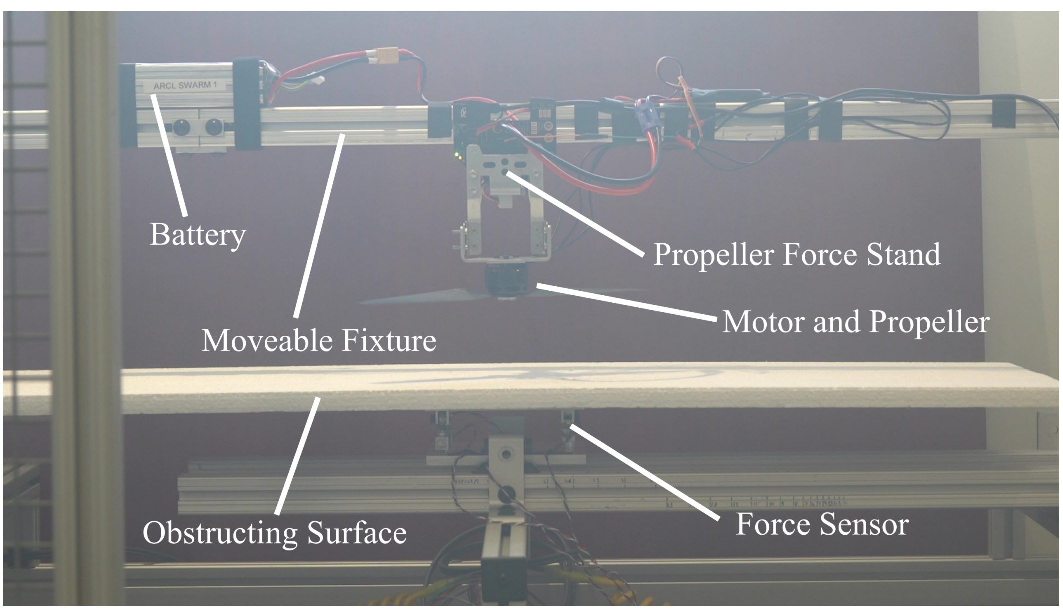

Figure 2.3: Propeller test stand with a foam obstruction and the force sensor seen beneath it.

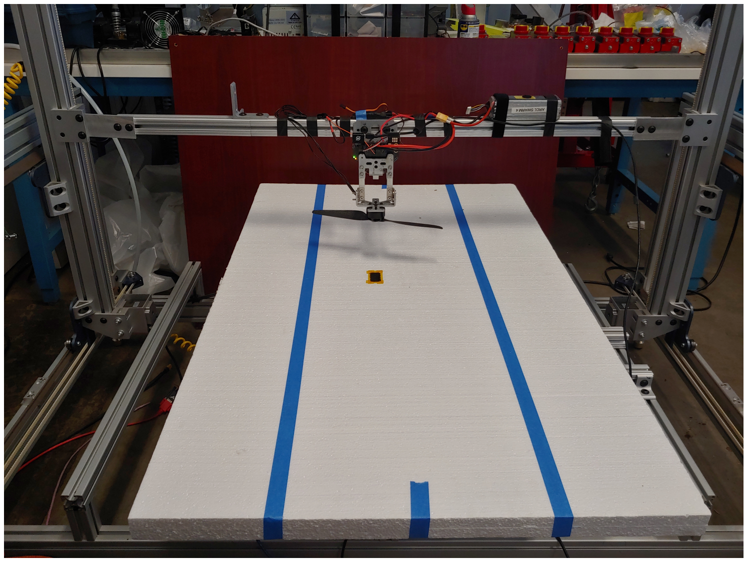

Figure 2.4: Alternate view of experimental setup. Obstruction with pressure sensors is installed.

Horizontal travel (in)	30
Vertical Travel (in)	38
Space Width (in)	48
Extrusion pitch (in)	1.5

Table 2.1: Specifications for the CNC Test Stand.

2.2 Experimental Studies

Experimental Setup

The notation and coordinate system used in this work can be seen in Figure 2.2. Non-dimensionalization using the rotor radius R and the rotor diameter D will be done frequently throughout this work, as will the use of the radial coordinate r, and the propeller-obstruction separation distance d and its parallel, the axial coordinate Y. Where applicable, the origin is taken to be at the intersection of the propeller rotation axis and the wall surface. Experiments on a selection of propellers were conducted to study the ceiling effect. The propellers were typically different in diameter and, for one diameter, several different pitches. As the force and torque readings of the propeller were what was directly measured, different motors appropriate for each propeller were used in the tests. Each propeller-motor combination was mounted to an RCbenchmark 1585 Thrust Stand [30] capable of measuring thrust and torque as well as electrical voltage and current. The occluding surface was mounted to a custom-built force stand composed of 4-cantilever beam load cells. The hardware arrangement made the force stand unreliable for forces that included large moments due to the mechanical coupling, but was quite accurate in static conditions for forces in a consistent location (less than 0.5 % error). The stand was mounted such that its center was aligned with the propeller's axis during experiments.

The two force stands were mounted onto a rigid frame assembled from 8020 extrusion. The position of the propeller thrust stand was adjusted by manually uninstalling and reinstalling the stand in a new position. There was some difficulty in measuring the distance from the propeller to the obstruction. In disk actuator theory, also called momentum theory, a propeller is idealized as an infinitely thin disk, but a physical propeller has thickness, and the blades have twist and camber. The center of the propeller hub was chosen as the reference point for the propeller disk, and was measured to the surface of the obstruction. The occluding surface was selected to be at least two propeller diameters in any direction and was the largest that the frame could accommodate. The environmental temperature, pressure, and humidity were collected from instruments included in a handheld anemometer at the beginning of each test run to calculate the air density.

After the initial run of data, a second structure was used to collect additional data for this study in a more convenient manner, as shown in Figures 2.3 and 2.4. The propeller test stand was mounted on a 2-axis CNC to computerize and precisely control the propeller's position relative to the obstruction. The force stand attached to the obstruction was also improved to consist of 3-cantilever beam load cells attached to one surface with ball joints. Once again, moment measurements were inaccurate, but linear forces could now be accurately measured independent of application location. Error during calibration was found to be less than 1% with weight anywhere on the obstructing surface. The 2 degrees of motion in the stand was useful for the subsequent pressure measurement tests as well as for potential experiments involving non-infinite upstream obstructions. The improvement in the obstruction force sensor also meant that the force could be accurately measured as the propeller was moved spatially during the pressure measurement tests.

RCbenchmark Thrust Stand Calibration

While the RCbenchmark 1585 Thrust Stand has calibration instructions integrated into the software for the stand, it was desired to evaluate the accuracy of the stand in some form. The standard calibration procedure is done as described in the datasheet, by loading the calibration weight in the thrust direction by placing a weight on the stand directly, and in the weight and torque directions using the calibration torque arm. The stand uses cantilever load cells with a Wheatstone bridge arrangement of strain gauges. This arrangement is expected to result in a linear relationship between the output voltage of the bridge and the applied load on the load cell. This relationship was evaluated by doing the recommended calibration procedure with additional calibrated weights to compare the signal to the measured load. For each applied load, roughly 100 samples were collected and the mean and standard deviation of the signals were collected. The averaged data were referenced to samples taken with no load as a tare condition.

The sensor response during the thrust calibration can be seen in Figure 2.5. From the figure, it can be seen that the signal for the thrust load cell appears to vary linearly with the applied load. The datapoints are shown with 95% confidence intervals computed from 2 standard deviations of the sampled data. In static conditions, the standard deviation of the sampled data is quite small, and the confidence intervals reflect the consistency of the measured data. This 95% confidence interval was found to correspond to between 1 and 0.1% of the signal value, with larger loadings having a smaller interval. This suggests that,under static conditions, measurements from the stand will have an error of less than 1%. The drawn lines are linear fits to the data, and low deviation between the measurements and the linear fit can be seen in the plot. The responses of the left and right load cells, which should not have a response during the thrust calibration are also shown. The data show that the sensors have a minimal response while the thrust component is being loaded.

Similar plots are seen for the weight and torque calibration steps. Figure 2.6 shows the weight calibration step, where the left and right load cells are symmetrically loaded. A linear relationship is again seen for the left and right load cells with the applied load, while the thrust load cell signal is near zero. The torque calibration step produces a similar plot in Figure 2.7.

The data show that the response of the sensor is indeed highly linear in the applied range of forces. In addition to the sensor readings having a relatively low standard deviation in static conditions, the linear fits applied to the tared data all had adjusted R^2 values of greater than 0.9999, indicating very good agreement with a linear model. The results indicate that it is appropriate to use a linear calibration matrix to compute forces and torque from the measures signals of the sensor.

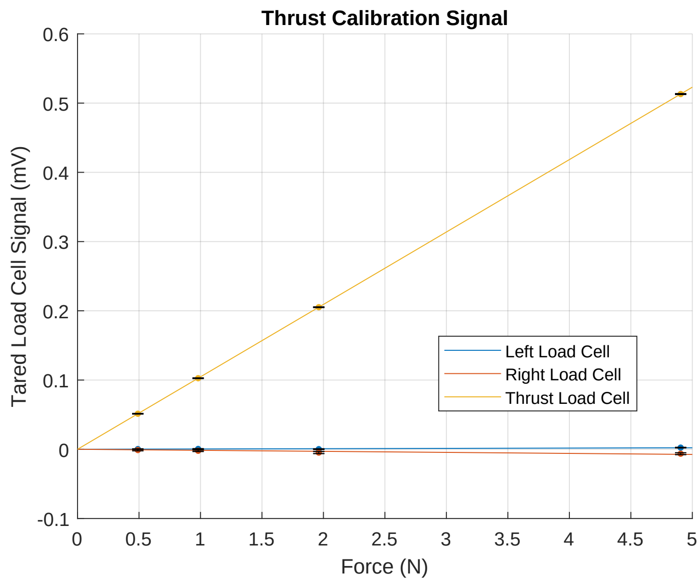

Figure 2.5: Sensor signals during thrust calibration with 95% confidence intervals and linear fits.

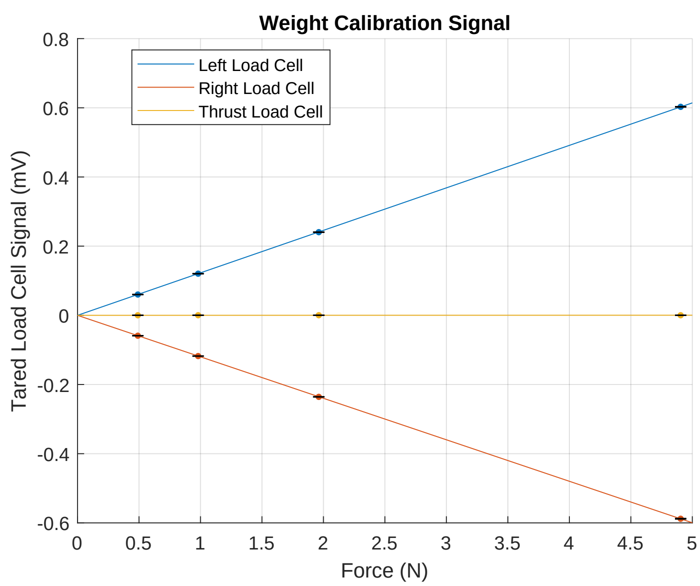

Figure 2.6: Sensor signals during weight calibration with 95% confidence intervals and linear fits.

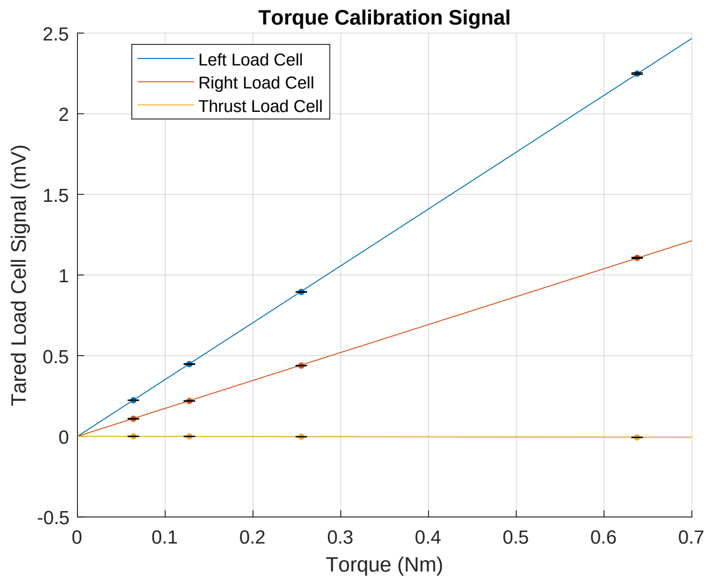

Figure 2.7: Sensor signals during weight calibration with 95% confidence intervals and linear fits.

Force Data and Analysis

As the data were collected, the results were compiled and analyzed. In order to relate the selection of propellers studied, the results were non-dimensionalized using relevant variables.

Notation and Non-dimensionalization

This work uses the non-dimensionalization typical in propeller studies [31, 32] and assumes steady state conditions. The thrust T and torque Q produced by the propeller are non-dimensionalized using the air density ρ, propeller rotation speed ω, and propeller diameter D. Note that this work uses ω in radians per second, rather than n in revolutions per second as in some other works. By matching the units of the quantities, we can arrive at the expressions

$$T = C_T \rho \omega^2 D^4 \tag{2.1}$$

$$Q = C_Q \rho \omega^2 D^5 \tag{2.2}$$

where C_T is a dimensionless thrust coefficient that is characteristic of the propeller and C_Q is the dimensionless torque coefficient. A useful metric of the efficiency of a propeller is the thrust produced per unit of torque. This can be found using the previous non-dimensionalizations as

$$\frac{T}{Q} = \frac{C_T}{C_Q} \frac{1}{D}. \tag{2.3}$$

This is a similar metric to the hover figure of merit which, with the stated definitions is

$$M = \frac{P_{\text{ideal}}}{P_{\text{measured}}} = \frac{TV_i}{Q\omega} = \frac{C_T^{3/2}}{C_Q}\sqrt{\frac{2}{\pi}} \tag{2.4}$$

where V_i is the velocity induced by the propeller at the disk from disk actuator theory, which can also be related to propellers disk loading $\Delta P = T/A$

$$V_i = \sqrt{\frac{T}{2\rho A}} = \sqrt{\frac{\Delta P}{2\rho}} \tag{2.5}$$

In addition to the thrust, we also have the measured force on the surface F_{surface}, and the combined force on both the surface and the propeller F_{net}. Each of these measured forces also have associated coefficients C_{surface} and C_{net} non-dimensionalized with the same independent variables as before.

$$F_{\text{net}} = T + F_{\text{surface}} \tag{2.6}$$

$$F_{\text{surface}} = C_{\text{surface}}\rho\omega^2 D^4 \tag{2.7}$$

$$F_{\text{net}} = C_{\text{net}}\rho\omega^2 D^4 \tag{2.8}$$

While the coefficients would typically be considered constants when characterizing a propeller, it was observed that the thrust produced by a propeller for a given rotational speed changed as the proximity to the obstruction changed. The results will thus be presented in relation to baseline thrust and torque coefficients for that propeller, C_{T_0} and C_{Q_0}, respectively, which were fit to data taken with the propeller without the presence of the large upstream obstruction.

Experimental Force Results

Example data for one propeller are shown in Figure 2.8. The propeller stand software automatically steps the throttle of the brushless DC motor to set values, effectively holding it at a fixed rpm, then collects data and averages 20 samples at a time. The surface stand has data collected for the duration of the test, and is post-processed to extract force values at the appropriate times. Once values have been aligned, the data is non-dimensionalized and fit to produce a thrust coefficient for the propeller. The thrust coefficient is then plotted for each propeller against the distance of separation from the occluding surface non-dimensionalized with the propellers diameter. Various results are seen in Figure 2.9. The fitted non-dimensional coefficients are plotted alongside 95% confidence intervals. Subsequent plots showing fitted coefficients will also show 95% confidence intervals for each value.

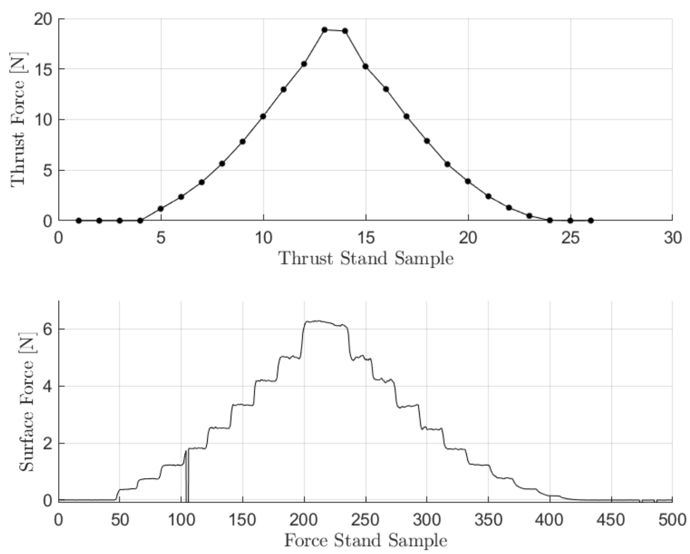

Figure 2.8: Sample raw data of a T-Motor 12"×4" (305 mm × 102 mm) propeller at roughly 2" from the surface.

For all propeller pitches and diameters, there is a clear trend in the effect of the upstream obstruction on the force produced. As the distance between the two entities decreases, the propeller's thrust coefficient increases, nearly doubling in some cases, and the torque required to drive it appears to decrease, visible in Figures 2.10 and 2.11. However, the force on the surface also increases, resulting in nearly zero net force at close separations. This effect is nearly negligible compared to the measured baseline once the separation exceeds one-half diameter. Though this

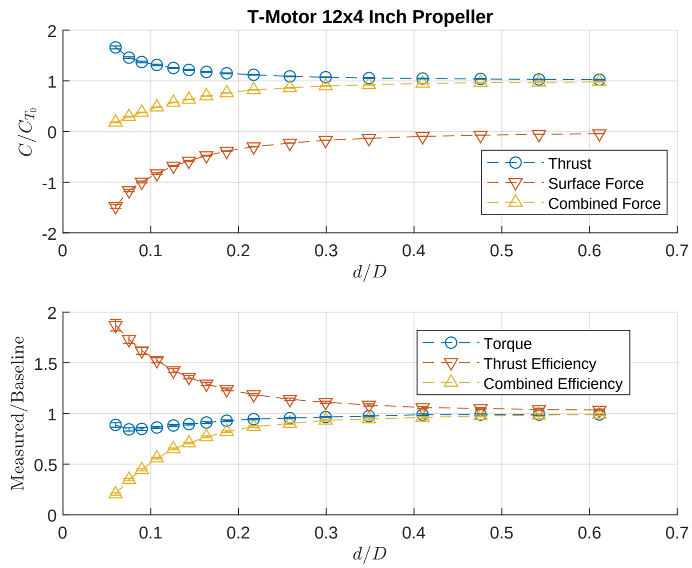

Figure 2.9: Non-dimensionalized data for a T-Motor 12"×4" (305 mm × 102 mm) propeller with 95% fit confidence intervals.

trend is consistent across all the propellers tested, the degree to which the propeller thrust changes does not seem to have a clear trend based on propeller diameter or pitch. Part of this may be due to the large variability in propeller designs between different manufacturers. The same trend is visible in Figure 2.12, which plots the aforementioned efficiency metric. The thrust efficiency generally increases as separation decreases due to both the increase in thrust and reduction in required torque.

Figure 2.13 demonstrates that, in addition to the prior observations, the non-dimensionalized net force curves are all remarkably similar, regardless of diameter and pitch. Data at smaller distances was difficult to collect, both because the blade thickness would lead to interference, and because of vibration. Though not directly measured here, close proximity was observed to also induce larger than typical vibrations. Though the propeller was mounted with clearance, these vibrations may induce striking with the surface in certain extreme circumstances or if the propeller blade flexes under load.

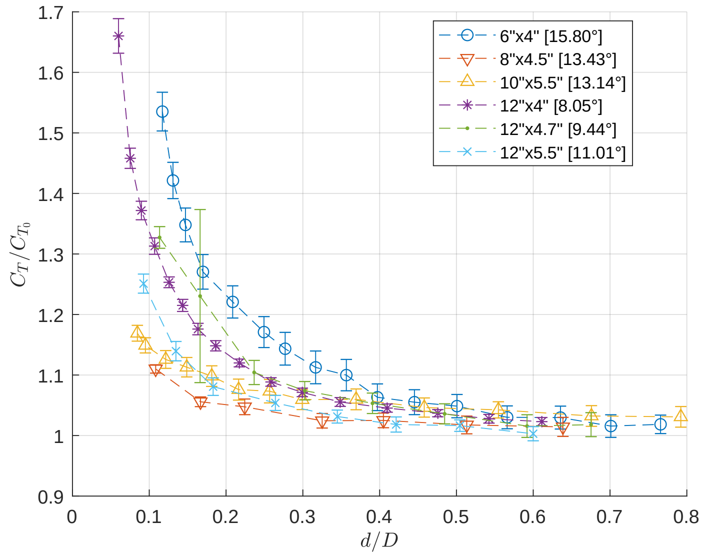

Figure 2.10: Change in normalized thrust coefficient with respect to obstruction distance.

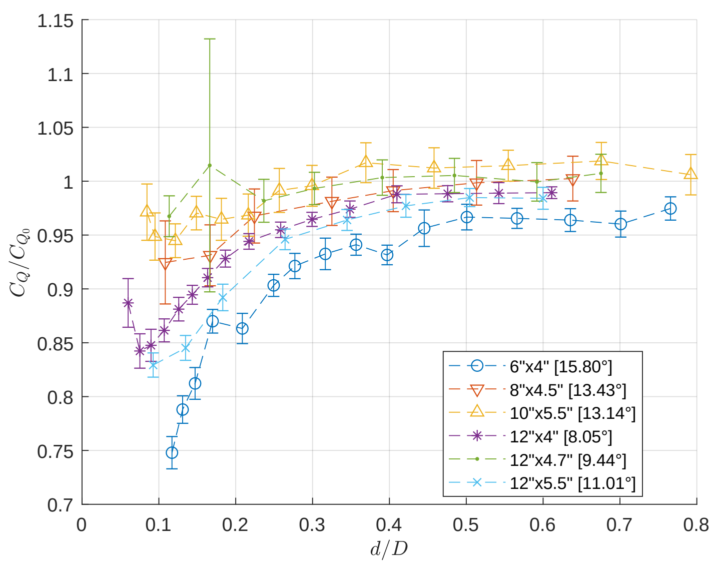

Figure 2.11: Change in normalized torque coefficient with respect to obstruction distance.

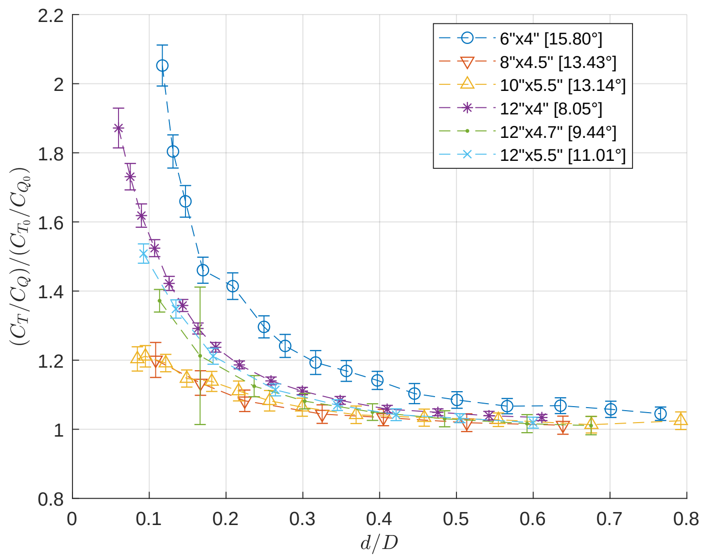

Figure 2.12: Change in thrust efficiency with respect to obstruction distance.

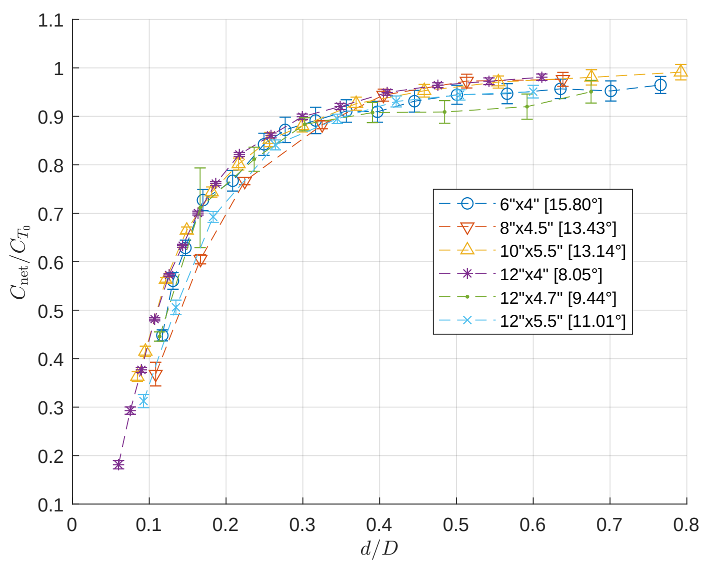

Figure 2.13: Change in normalized net force with respect to obstruction distance.

Given that the non-dimensionalized effect on performance was found to be so similar regardless of the propeller tested, it was desired to conduct a wider study of the effect of the geometric placement relative to the obstruction with a smaller selection of the propellers. One such study was examining the change in the net force as the propeller was only partially obstructed by bringing it into proximity of the edge of an obstruction. A diagram and coordinates for this are shown in Figure 2.14. The X coordinate used is the distance between the obstruction edge and the axis of rotation. At each position of occlusion, data were collected for various separation distances until the force response on the propeller and the obstructing surface returned to baseline. To produce an empirical fit, qualitative constraints include that the behavior should approach baseline as one moves the propeller along the positive Y and negative X axes and that motion in the positive X direction should converge to something. The data for the study are shown in Figure 2.15, alongside the empirically fit surface. The fitted equation for the T-Motor 12×4 propeller is seen in Eq. (2.9).

$$\frac{C_{\text{net}}}{C_{T_0}} = 1 - C_1 \left[(y + C_2)^{C_3} \right] \frac{1 + \tanh\left[C_4 \left(x - C_5 \right) \right]}{2} \tag{2.9}$$

The model used for this fit does not take into account the slight benefit apparently gained at close to zero coverage. For the T-Motor 12×4 propeller the results of the fit are the coefficients shown in Table 2.2.

C_1	C_2	C_3	C_4	C_5
0.09887	0.5806	-4.746	3.448	0.0008

Table 2.2: Fit coefficients for partial obstruction of T-Motor 12×4 propeller.

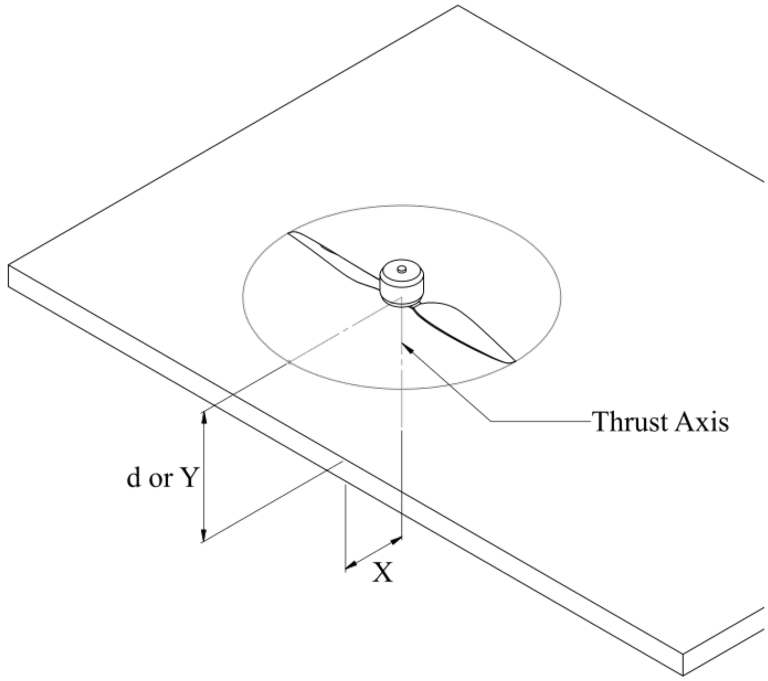

Figure 2.14: Coordinate system used for partial obstruction testing.

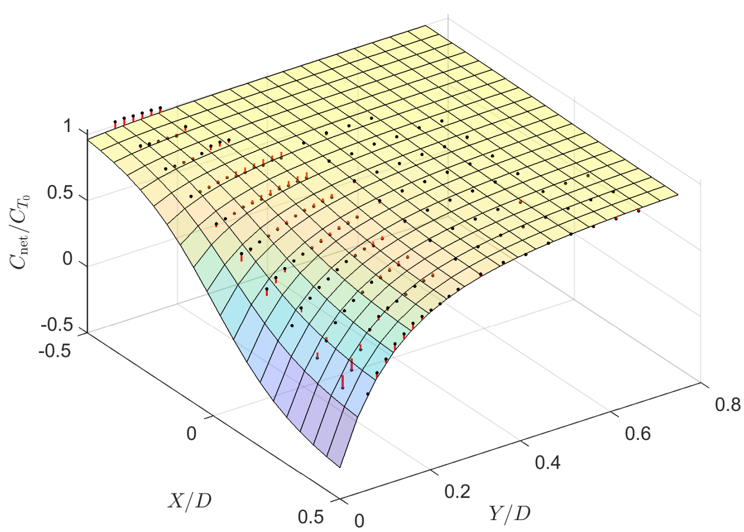

Figure 2.15: Change in normalized net force coefficient of a T-Motor 12"×4" propeller based on position with points indicating data and the surface being a curve fit.

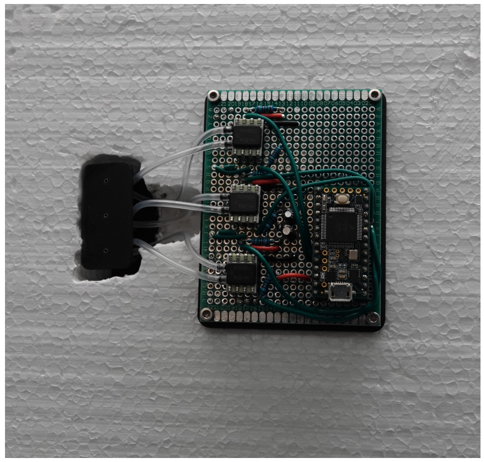

Figure 2.16: Pressure sensor board attached to the obstruction body.

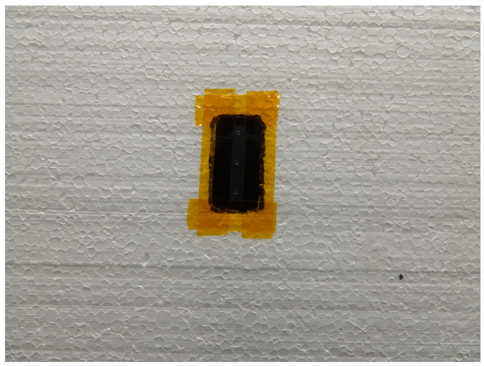

Figure 2.17: Pressure sensor tap layout on obstructing surface.

Pressure Sensing

To gain physical insight into the effect of the obstruction in the upstream, we take pressure measurements at the surface of the large obstruction. This is done by embedding differential pressure sensors into the surface. The pressure sensors used were three Honeywell RSCDRRI002NDSE3 differential pressure sensors [33], which have a stated accuracy of ±0.1%. The stated error is small enough that error bars will not be drawn on individual pressure measurements. Each individual pressure sensor measures the pressure differential from either side of the obstruction. The pressure tap locations were arranged in a line each spaced 0.5" apart. Figure 2.16 shows the sensors alongside their electronics mounted to the circuit board with the data collection microcontroller. It also shows the sensor connected using tubing to the pressure taps. Figure 2.17 shows the pressure taps on the surface of the obstruction. The taps and their mount are installed to be as flush as possible on the surface so as to be as unobtrusive to the aerodynamics as possible.

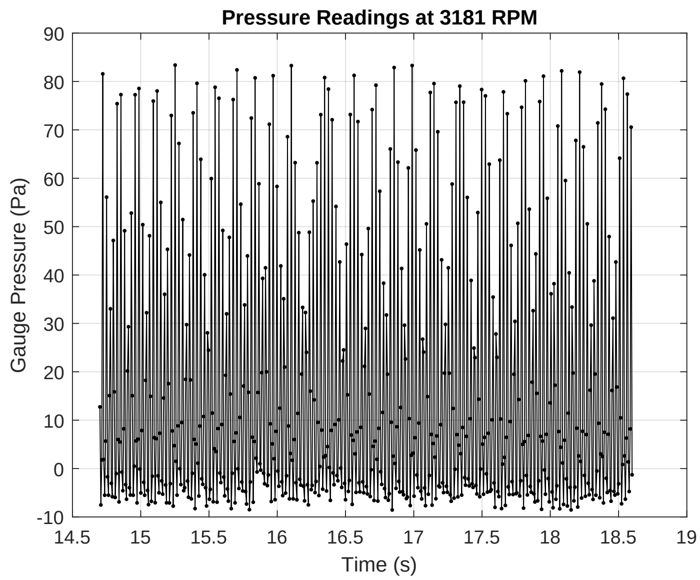

Figure 2.18: Time Series of Pressure Data.

An example of the raw pressure data can be seen in Figure 2.18. Here we see a clear periodicity of the pressure read by the pressure sensor, consistent with the fact that a rotating propeller blade is passing nearby at a constant frequency. Interestingly, a frequency domain analysis of the shown in Figure 2.19, shows that, while there are various peaks in terms of the dominant frequencies, the expected propeller frequency is not the dominant one. One potential cause of this is that, while the sample rate is higher than the Nyquist frequency of the propeller rotation, the sensors themselves have a poor frequency response at higher frequencies. Fortunately, we are interested in steady state conditions, so collecting pressure data and computing the time average produces the desired experimental value. While the time resolution of the sensor is not high enough to resolve the pressure profile, the time average pressure is taken over many revolutions to produce a quality steady state value. At the tested RPMs, the pressure sensor is expected to see between 300 and 500 cycles of the periodic effect, producing a value that should be representative of the steady state pressure average.

Pressure field data is collected by keeping the sensors fixed and translating the propeller to various locations, measuring the pressure at various relative positions to the propeller. In order to relate the thrust from the propeller to the pressure readings at the surface of the obstruction, we consider their dimensionality and the physical relationships between the variables.

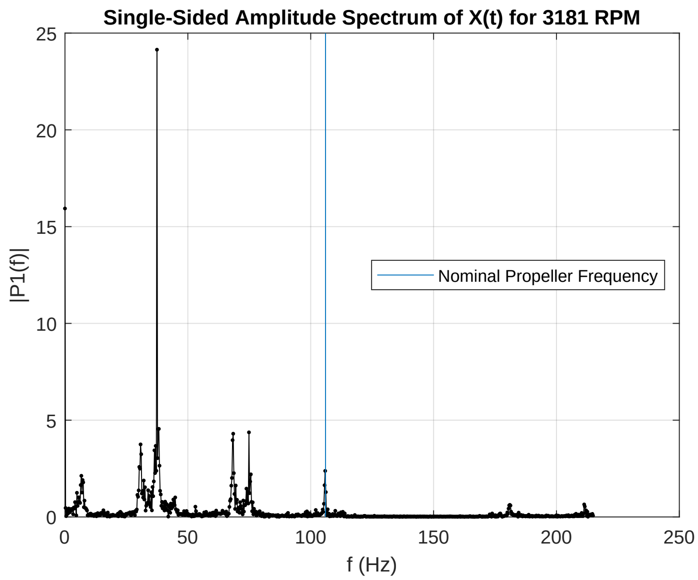

Figure 2.19: Frequency Analysis of Pressure Data.

In Eq. (2.5), the velocity induced by the propeller at the disk was related to its disk loading. Based on Bernoulli's principle, we have that generally there is a quadratic correlation between the pressure divided by the fluid density and the flow velocity. Combining the two, we expect that the pressure will be directly proportional to the disk loading. We also expect that at zero thrust the pressure p will also be zero as there will be no airflow motion. The result is that a simple relation of the form

$$p \propto \frac{T}{A} \tag{2.10}$$

is expected. Indeed, when we compare the surface pressure measurements at various locations with the disk loading, we see a linear relationship, as seen in Figure 2.20. The coefficient relating the disk loading to the pressure changes with location, but this means that these coefficients can be compiled to describe the non-dimensional pressure contour produced at the surface as seen in Figure 2.21. The pressure contours are shown with 95% confidence intervals from the linear fit. These coefficients are used in Section 2.3 for comparison with the CFD results. The scalability of the pressure in the solution with respect to the disk loading is further studied in simulation in Section 2.3.

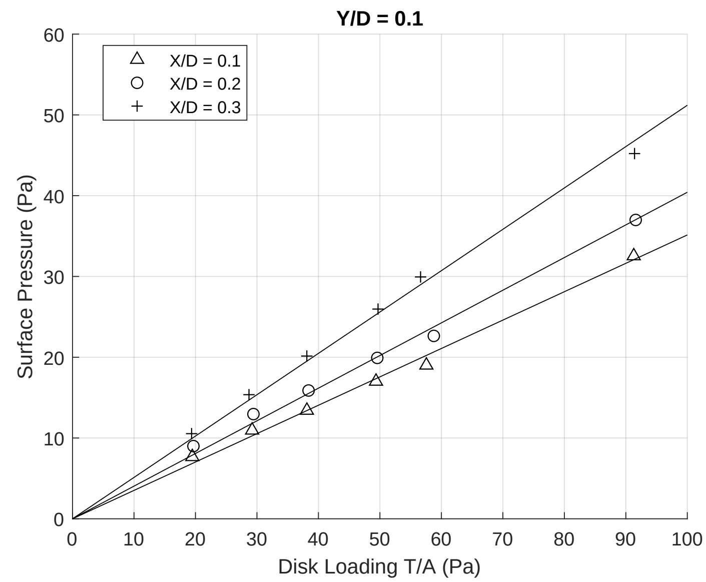

Figure 2.20: Time averaged pressure versus disk loading (T/A).

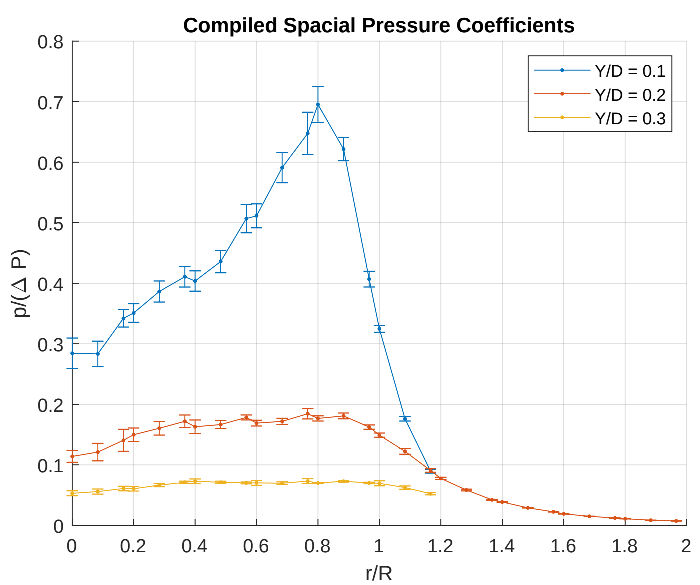

Figure 2.21: Compiled pressure coefficients in space with 95% confidence intervals.

2.3 CFD Analysis for the Ceiling Effect

The results of the previous section showed the existence of several interesting effects. In order to corroborate the experimental results and derive additional insight into the phenomena, the problem was simulated in ANSYS Fluent. To maximize the variety of cases that could be run, the simulations were limited to only 2D axisymmetric cases with the propeller represented by a disk actuator. This greatly reduced the required number of elements in the simulation and therefore the simulation time. It was found that the mesh resolution required for good solution convergence in the axisymmetric case is well within the capabilities of a modern desktop computer, but more advanced cases such as those requiring 3-dimensional simulations might either require a high performance computing setup, considerable amounts of time per case, or both.

One disadvantage in representing the propeller as an actuator disk is that the propeller's rotation is abstracted away in favor of representing it solely by its disk loading. This removes the rotation speed as a predictive variable in favor of looking at the problem from a more fundamental perspective. As shown in Section 2.2, the response of a propeller to an upstream obstruction with respect to its rotation speed is highly variable between the various propellers. Given this variability, it was elected to study the fundamental representation of the problem captured by the disk loading rather than attempting to predict the performance of a specific propeller.

As a model and a simulation, the fidelity of the CFD is always in question. The accuracy and physicality of the results is verified by comparing computed forces and pressures are compared to the analogous experimental results, with particular focus on how the choice of simulation method within ANSYS affects the accuracy of the results. Once a model is chosen, simulations are run to examine general features in the flow and focus on phenomena of interest and how they compare to physical experiment. Then, various subtopics derived from the CFD analyses are then examined, such as the wake properties, small pressure jumps, and prediction of the flow separation.

Simulation Set-up and Boundary Conditions

The rotor is abstracted as a disk actuator in Fluent using a fan boundary condition with a constant pressure jump across its surface. This is how a propeller is represented in classical disk actuator theory. In a real propeller, the time average effect does mean that it can be represented by a pressure jump, but with slight differences.

The pressure jump at the axis of rotation must decay to zero, as the translational velocity of the propeller is zero at that location and generally does not generate lift. Likewise, the lift at the propeller tip should decay to zero as the propeller chord tapers off. In reality, the propeller must also be mounted to some form of shaft or motor that provides the torque input and fixture to rotate it, but simulation allows for the propeller to be represented as a free floating disk.

As an abstraction, a disk with a constant pressure jump across the entire surface is appropriate as it represents the most basic form of a propeller, and only has 2 parameters to describe it: the magnitude of the pressure jump and the disk diameter. This is in keeping with the desire to study the observed effect in as fundamental of a manner as possible.

Domain Mesh and Grid Sensitivity

> If you have to make a mesh, make a bad mesh. If you make a good mesh, you become the guy that's good at meshing.
>
> Anonymous

Key to running an accurate simulation is the subdivision of the domain into finite elements to create a mesh. In this series of studies, a mesh produced using adaptive refinement was used. With the simplicity of the problem, the domain was first meshed into a rectilinear grid of square cells with a side length of 0.05 D. The mesh was then refined by subdividing targeted cells every 50 iterations. Cells were targeted by identifying regions in the top 80 % of velocity curvature scaled by zone average. Doing this produced good cell resolution in regions with large changes in velocity, enhancing the simulation resolution of the wake, near the actuator, and at the surface.

To study the sensitivity of the problem to the grid used the solution was sampled over the course of the simulation prior to each mesh adaption for a test case. The case in question was a Transition SST simulation with $d/D = .2$ and $\Delta P = 250$ Pa. The simulation was allowed to run for 1000 total iterations with the aforementioned strategy of mesh refinement every 50 iterations. The final Surface Force output of this simulation was 2.3427249 N. Figure 2.22 shows the force output sampled at the end of each set of 50 iterations normalized by the final output of the simulation versus

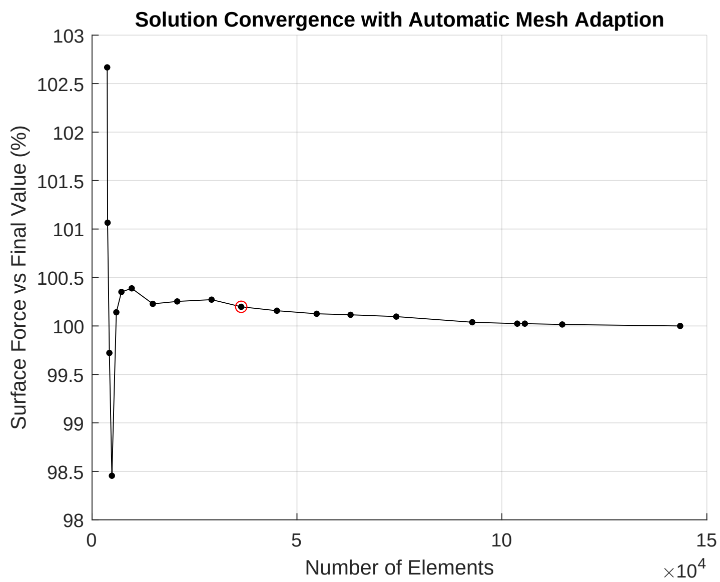

Figure 2.22: Convergence of simulation with adaptive mesh refinement. Typical stopping point of simulations of 549 iterations with 10 refinements is circled in red.

the number of elements for the simulation. Even after relatively few refinements, the force value is very close to the final computed value. At 10 refinements plus 49 iterations, the typical stopping point for the subsequent simulations described in this work, the force solution is within half of a percent of the final value.

For comparison, a sensitivity study of the grid based on setting the elements throughout the entire grid to the same size was conducted and is shown in Figure 2.23. The results are normalized by the final solution from the adaptive mesh simulation. There is more error, but even simulations with an element size of .001 m or .5% of the diameter D are within 5% of the final surface force output. However, because globally setting the mesh element size put elements in regions of little interest, the simulation quickly became impractically large. Because of the reduced computational cost and better solution convergence, the automatic mesh adaption strategy was used for all subsequent simulations in this work.

Analysis of Domain Size

As a larger domain means a larger number of computational elements, it is advantageous to minimize the domain size while still producing accurate results. Doing so will reduce the computation time of the overall study. In order to determine the minimum requisite size of the domain, we first run a simulation with a much larger domain than we expect is required for the problem. As the propeller thrust is

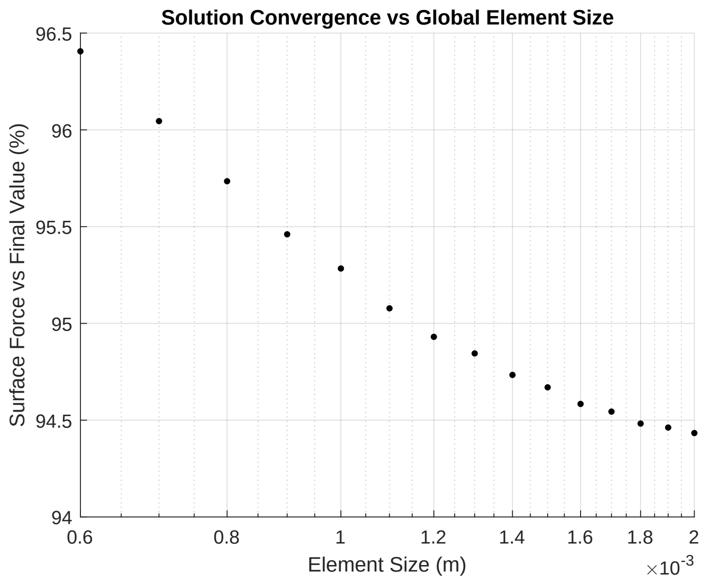

Figure 2.23: Simulation output relative to the 2.3427249 N value from the adaptive mesh refinement simulation with mesh element size globally set.

prescribed, the relevant metric for determining accuracy is the surface force. The total surface force is given in this axisymmetric problem by

$$F_{\text{surface}} = \int_{r=0}^{\infty} p 2\pi r dr \tag{2.11}$$

where p is the pressure measured at the surface. As the computational domain must be finite, we can not integrate to infinity, but we can examine at what point along the surface the pressure becomes so small that its contribution to the force is inconsequential. Choosing a domain to encompass this cutoff should result in the error between the computed surface force and the true value being acceptable small. To do this we first run a simulation on a domain size of 5 disk diameters in diameter, and 3.5 diameters downstream. Taking the computed total force on the surface, we can evaluate at what radius the force is an acceptable deviation from the total. As an arbitrary choice, we choose to look at the radius at which the integrated force is 99% of the total. As seen in Figure 2.25, this threshold is reached between 3.5 and 4 radii. A cutoff of 3.5 radii was chosen as it was decided that this gave sufficient accuracy, having only 1.5% error.

Subsequent simulation data shows that the extent of the pressure influence of the rotor changes as the rotor separation distance changes. Relative to the largest magnitude pressure that is observed for a given case, the effect of the pressure is felt over a

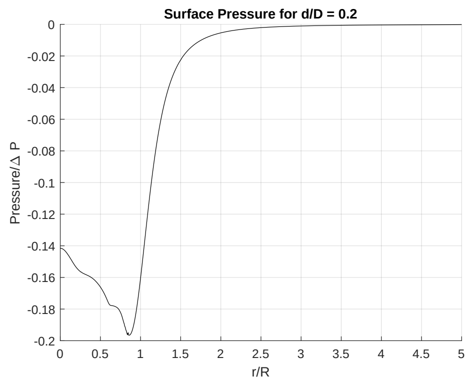

Figure 2.24: Surface pressure for extended domain.

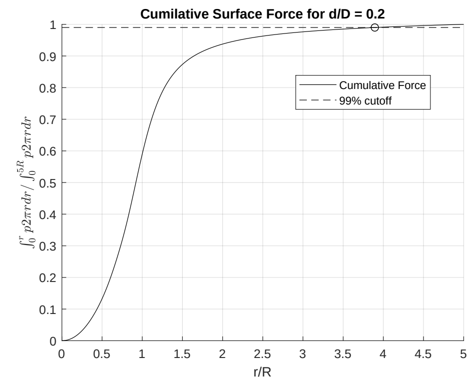

Figure 2.25: Cumulative surface force for extended domain.

larger radius the further the separation distance. Nevertheless the domain bound of 3.5 diameters was maintained, as the total surface force experienced in these cases is substantially smaller than the disk force, meaning that the error associated is less significant.

Comparison of Simulation Method with Experimental Results

In order to validate the CFD, the results of various solvers were compared against the pressure data collected. The results are seen in Figures 2.26a, 2.26b, and 2.26c. From these results, we see that there is good agreement with some of the chosen methods of computation. For the $d/D = 0.2$ case, we generally see good agreement with many of the turbulent models such as K-ω, Spalart-Allmaras, Transition SST. The K-ϵ model substantially under-predicts the pressure near the axis. The Laminar model has similar characteristics up until the pressure peak, but has markedly different characteristics within the disc radius relative to the experimental data. Lastly, the inviscid method is qualitatively distinct from the other results, exhibiting full pressure recovery towards the axis of symmetry.

One feature that is more evident in these plots is the irregularity of the pressure data. In each off the plots, it can be seen that the fitted pressure values have a visible "jaggedness" in the contour that is particularly noticeable near the peak of the pressure. As all the sensors read 0 pressure in still conditions during each test, sensor tare was not the cause of the error. The most likely explanation for this is related to the pressure sensing hardware. Because the pressure data was collected spatially using three different pressure sensors, every third point on the pressure contours corresponds to data from the same sensor. The irregularity in the pressure contours appears every third data point, suggesting that it is more likely that there

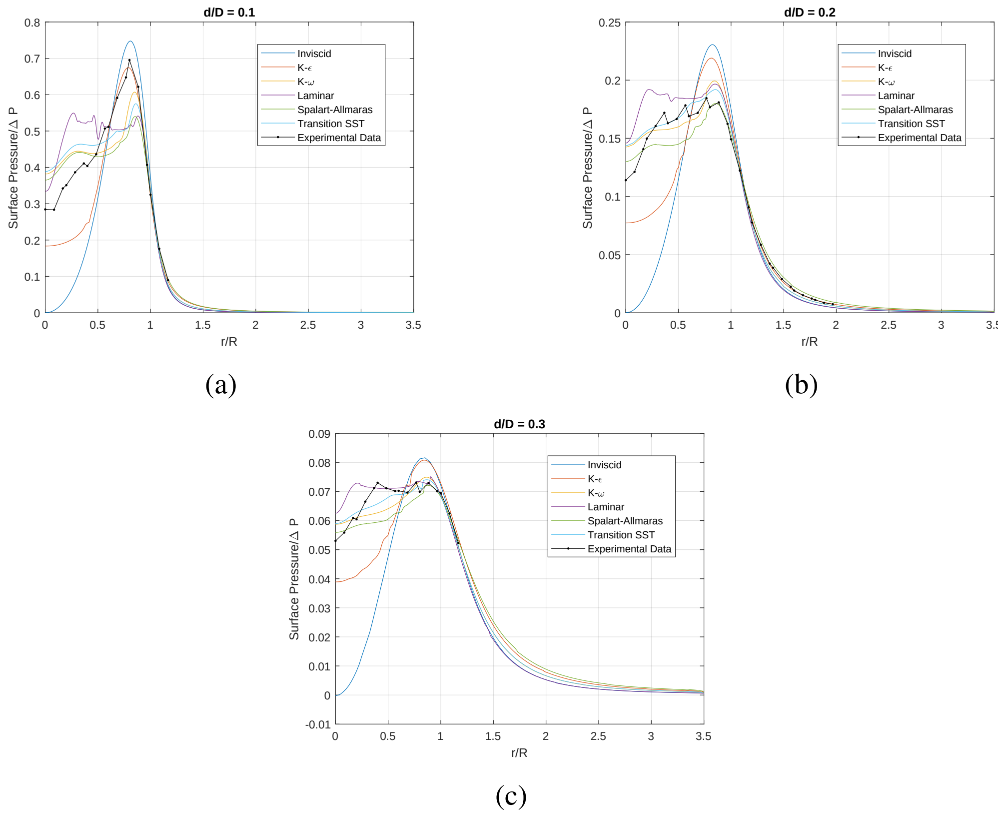

Figure 2.26: Simulation methods vs pressure data at various d/D.

is a sensor bias for the particular sensor rather than the true pressure contour being irregular. While the manufacturer stated sensor accuracy is so small that plotting error bars associated with it would not be useful, it is clear that there exists a systematic error in the sensor. Unfortunately, as the means to sufficiently verify or calibrate the sensor were not available at the time of the experiment, the sensor data is presented here without correction.

While the various models evaluated match the experimental results to varying degrees, the Transition SST model was elected to be used for subsequent turbulent simulation in this work. This model has been used previously in the literature for vertical and horizontal wind turbine simulations [34, 35]. The Transition SST model in conjunction with an actuator disk representation in ANSYS Fluent has also been used previously to successfully represent the interaction of a propeller with a body [36]. In addition to matching the experimental pressure contours reasonable well, this model also qualitatively exhibits wake spreading in the downstream. The inviscid model is also further studied because of its ties to potential flow theory and provides guidance for an analytical solution to the problem.

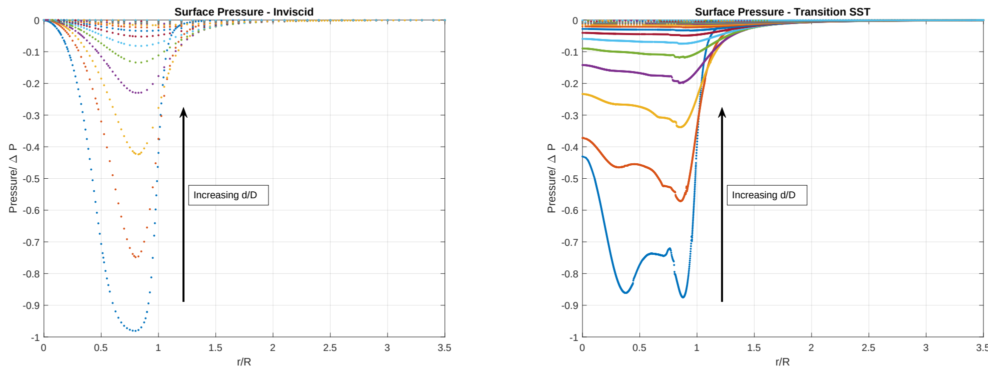

(a) Inviscid simulation

(b) Transition SST simulation

Figure 2.27: Surface pressure contours at various separation distances. Separation distance d/D starts at 0.05 and increments by 0.05 up to 1.

Surface Pressure Curves

> The quality of the simulation is commensurate to the number of colors used in the resultant plots.
>
> — Anonymous

The pressure output from the CFD allows us to compute the force of the obstruction, but also provides qualitative flow information. With the comparison of methods in the previous section we can do a finer resolution study using the methods of interest. We extract pressure curves for the inviscid method in Figure 2.27a and for the Transition SST in Figure 2.27b.

Symmetry boundary condition vs wall boundary condition

The results of the Transition SST and other viscous simulations shown were produced using a no-slip wall boundary condition to simulate a physical boundary of the surface. A potential alternative is the Symmetric boundary condition. The ANSYS theory guide [37] specifies that the symmetric boundary condition is applied as a no-penetration condition, meaning that velocity at the "wall" is allowed in this case. This bears similarities to the Inviscid simulation, where the theory manual specifies that any wall boundary condition is solely a non-penetration condition, as the no slip condition is not physically present. The comparison of these results can be seen in Figure 2.28. As expected, the symmetry and wall boundary conditions are identical in the case of the Inviscid simulation. In this case, the Laminar and Transition SST simulation methods are nearly identical to the Inviscid results. The results suggest that the presence of wall friction is highly significant in the qualitative results of simulation. Specifically, the separated region near the axis does not appear to form without it, even in simulations involving viscosity.

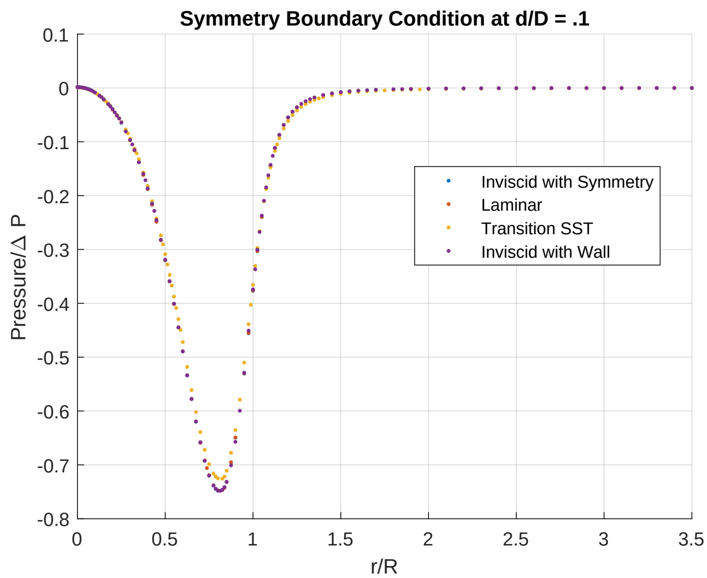

Figure 2.28: Comparison of normalized surface pressure with the symmetric boundary condition.

Flow Properties

There are a number of features of note in the flow field computed by the CFD simulation. In Figure 2.29b, we see the velocity magnitude for an SST simulation. As expected from an actuator disk, there is an induced flow and a wake shed into the downstream. In the case of the actuator disk, we also see that there is a mixing layer between the wake and the quiescent fluid which grows in a linear fashion. Upstream of the actuator disk, the flow accelerates to a maximum near the disk radius. However, there appears to a separated region of flow near after this point, closer to the axis. This is consistent with the pressure curves seen in Section 2.3, and is elaborated on in Section 2.3.

In Figure 2.29a, we see a velocity magnitude contour plot for an inviscid simulation. This version exhibits some key differences with the Transition SST simulation. Rather than a mixing layer between the wake and surrounding fluid, the downstream wake from the actuator disk appears to be a constant diameter cylindrical stream tube, separated from the surrounding flow by a cylindrical vortex sheet. Furthermore, the

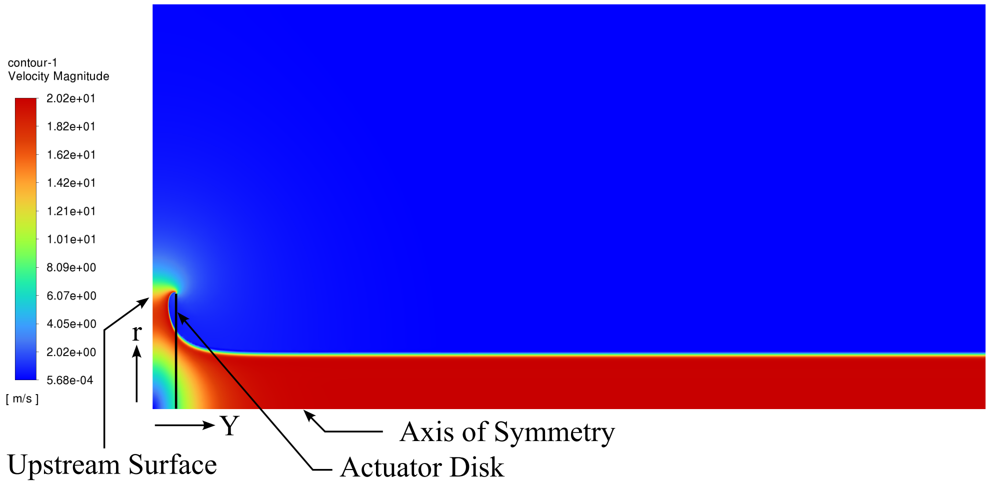

(a) Inviscid simulation

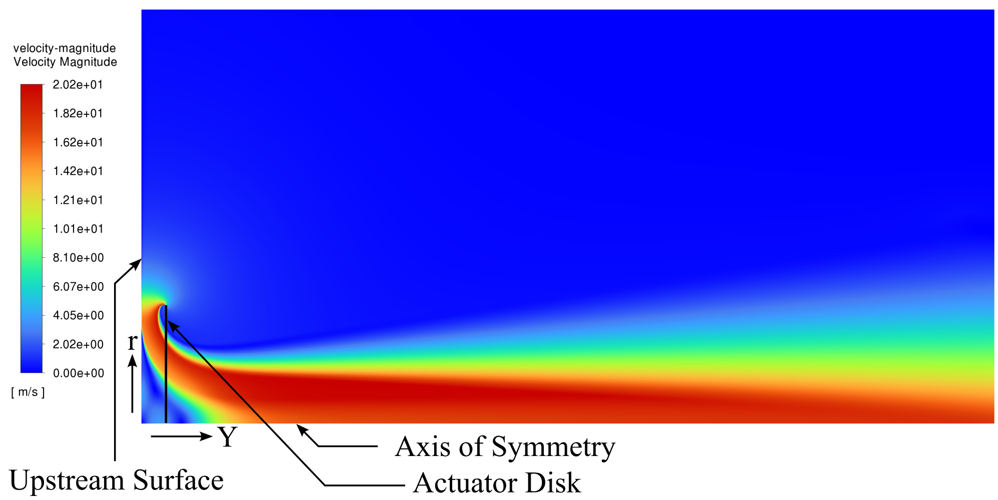

(b) Transition SST simulation

Figure 2.29: Velocity magnitude contours. The axis of symmetry is at the lower edge, and the upstream obstruction is the left edge.

Inciscid simulation does not have a separated region near the axis, a fact supported by the pressure measurement at the surface in the simulation.

The aforementioned properties can be observed in better detail in Figure 2.30. Here it is shown that there is a distinct flow reversal and recirculation in the separated region. Figure 2.31 is a similar plot with a focus on the disk tip, providing more detail of the tip effects and the induced flow there. Figure 2.32 shows the velocity vectors for an inviscid simulation. In this we observe how, though there is a similar vortex sheet created by the actuator disk, there is no flow separation at the surface boundary.

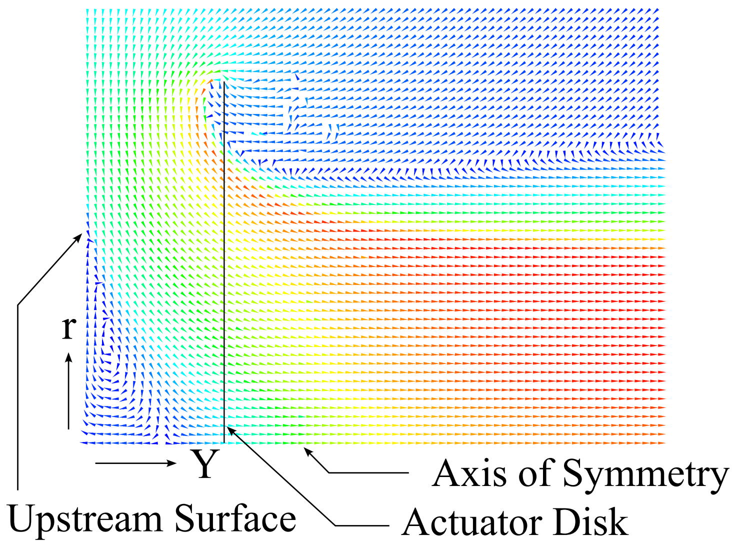

Figure 2.30: Normalized velocity vectors for a Transition SST simulation. The axis of symmetry is on the bottom, the upstream obstruction is at the left edge, and the actuator disk is drawn in black.

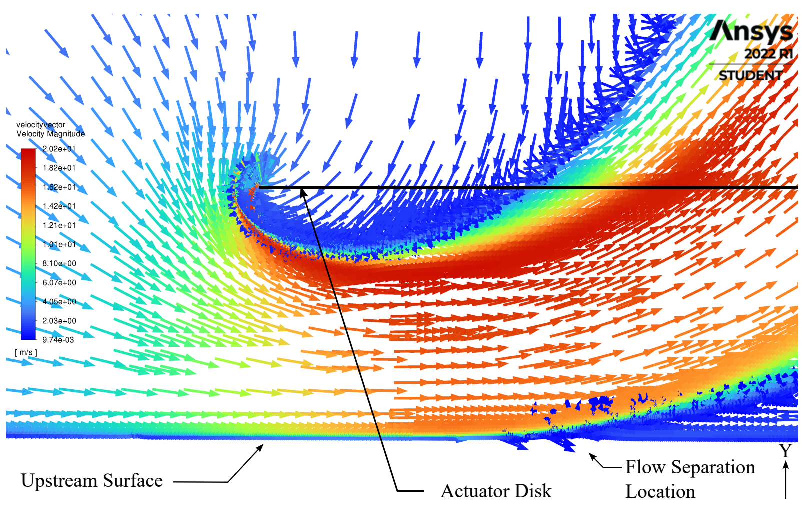

Figure 2.31: Normalized Velocity Vectors for a Transition SST Simulation with focus on the edge of the actuator disk. The axis of symmetry is on the right and the upstream obstruction is at the bottom edge.

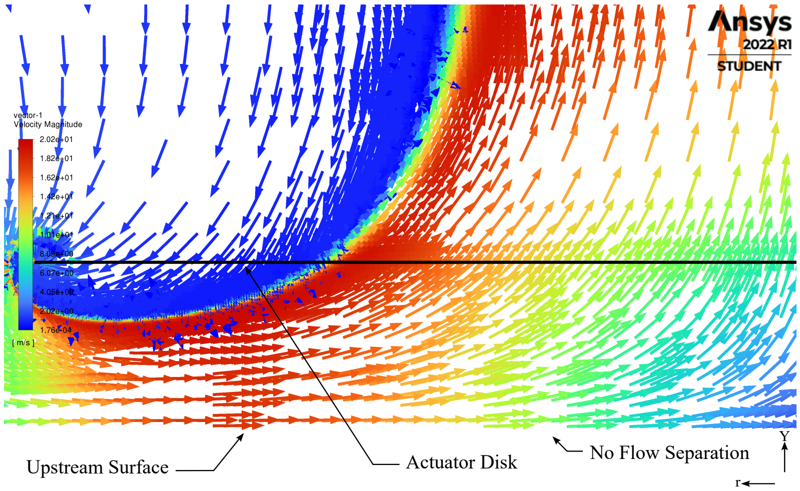

Figure 2.32: Normalized Velocity Vectors for an Inviscid Simulation. The axis of symmetry is on the right and the upstream obstruction is at the bottom edge.

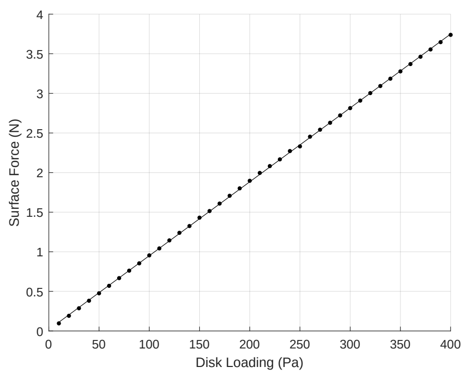

Figure 2.33: Simulation surface force values for different disk loadings with a linear fit drawn.

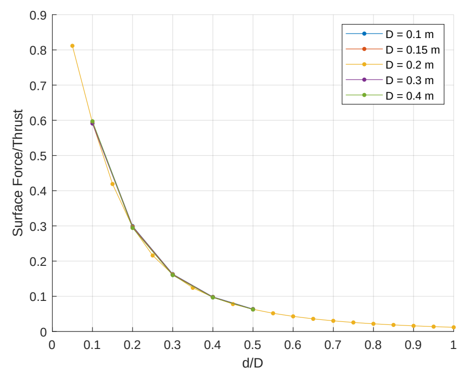

Figure 2.34: Transition SST simulation surface force of various disk diameters.

Problem Scalability

While conducting analysis of the problem in CFD it was desired to examine how the pressure jump imposed across the disk would affect the surface force. While the dimensional analysis and pressure measurements above indicate that this is a correct assumption, further verification in CFD was desired. The analysis conducted with the 0.2 m diameter disk at a fixed distance of $\frac{d}{D} = 0.2$ with various disk loadings is shown in Figure 2.33. The simulation was run with an adaptive refinement mesh for a Transition SST simulation.

The results indicate that, for the disk diameter and separation distance chosen, that the surface force scales linearly with the pressure jump imposed across the disk. The strong linear correlation suggests that the relationship implied by the non-dimensional analysis holds and that the pressure field scales linearly with respect to the pressure jump.

To push the limits of the self similarity, it was desired to examine the problem at very low Reynolds numbers, ideally in the sub 1 range. While the linear analysis kept the disk loading in ranges expected in small rotorcraft, for this analysis the pressure jump was lowered several orders of magnitude and the effects studied. Disk loadings below 1e-6 caused errors in the simulation. The output data indicate that this is because the pressure magnitude was small enough that the inlet and outlet boundary conditions began to experience numerical errors that were similar in magnitude to the flow induced by the disk actuator. The results are seen in Section 2.35.

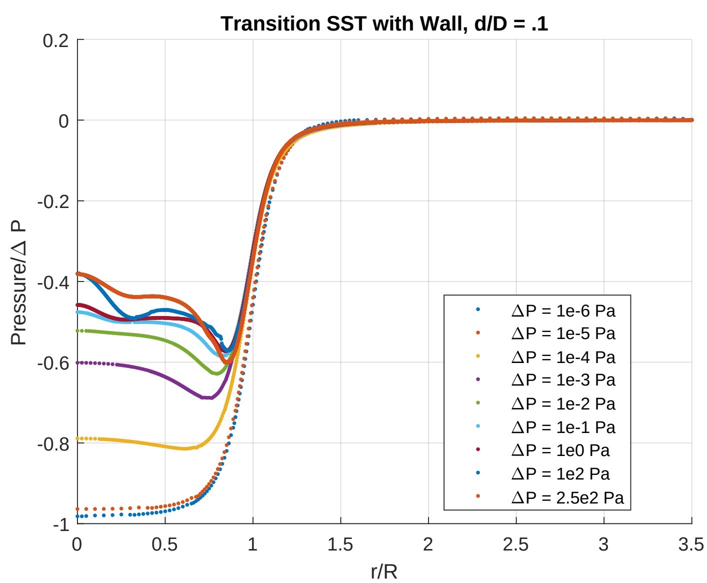

Figure 2.35: Normalized surface pressure for cases with small pressure jumps.

There are several interesting observations to be made regarding the effect of Reynolds number on the problem. The solution appears to converge from one type to another based on the pressure jump. The very low Reynolds number case featured the same exponential decay of pressure at the surface beyond the disk radius as other cases. However, when the pressure reaches is maximum magnitude, is does not return to trend back towards zero but rather stays level near its maximum. It is unclear however if this is a true phenomena, or the result of small number errors affecting the simulation. Nevertheless, as the pressure jump increases, the previously observed trend returning to 0 is seen, along with the purported separation. As the disk loading increases back into the range experienced by rotorcraft, we see the pressure contour take on its familiar shape once again. Given the previous analysis involving the effect of the pressure jump and the observed effect here with extreme cases of low Reynolds numbers, it is believed that the effect of Reynolds number is small in the relevant cases studied that are intended to be representative of rotorcraft loadings.

From the experimental results, we also observed that the force on the surface, when normalized by the expected disk force, is roughly independent of the propeller diameter or pitch. It was desired to see if this would remain true for the simulations run using CFD. The results of the normalized surface force for different simulation diameters can be seen in Figure 2.34. From these results, we see that the normalized surface force is virtually identical between the studied diameters as a function of the non-dimensional separation distance.

A comparison of the effect of diameter on the solution can be seen in Figure 2.36. Examination of the pressure curves at the surface show that the solution for various non-dimensional separation distances are very similar between the various diameters. For radii outside the pressure magnitude maximum, the curves are virtually identical across all the diameters. Within the disk radius however, there appears to be flow separation as before, and the shape of the pressure curve varies with diameter. As evidenced by the force results though, the differences in the curves do not appear to be significant enough to change the overall normalized surface force. The affected area is relatively small in the context of the total integral for the surface force, which is likely a contributor to the similarity in overall surface force values.

These simulation results indicate that the solution to the problem can be described by a particular choice of pressure jump and normalized separation distance. As the pressure field normalized by the pressure jump appears to be constant across different cases for a given normalized separation distance, the solution should be scalable to different diameter rotors and thrusts.

Flow Separation

A key quality of the observed flow is the separated region near the axis of symmetry. This separated region is the main discrepancy between the inviscid simulation and viscous model results. Simulations using a symmetry boundary condition rather than a surface show that the viscous pressure would be the same as the inviscid solution without surface friction. Given this the separated region is also likely the

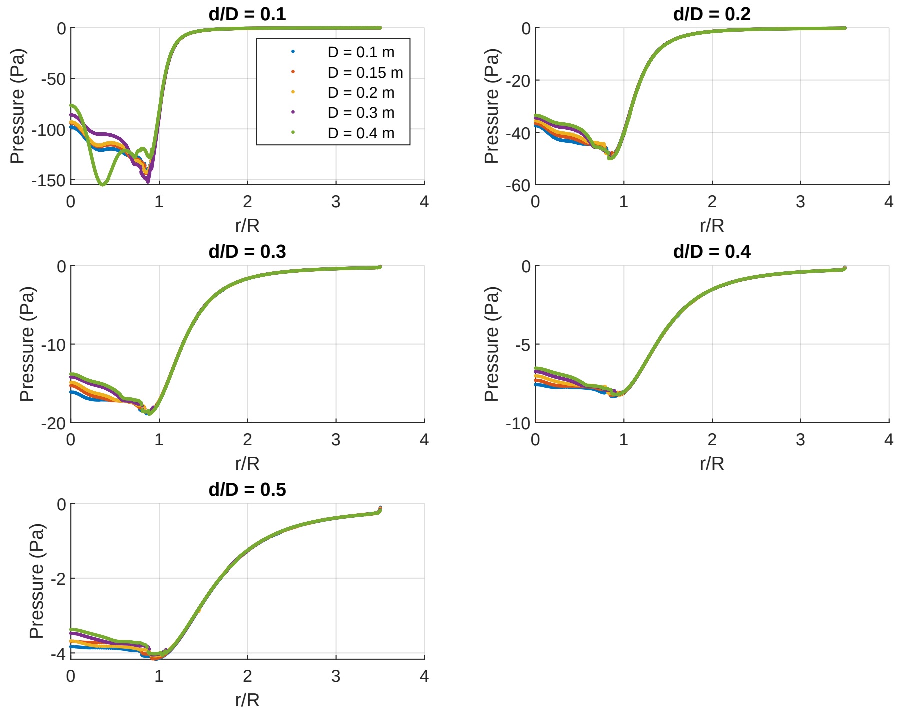

Figure 2.36: Transition SST surface pressure contours for $\Delta P = 250Pa$ at various Disk Diameters.

cause of the difference in maximum pressure magnitude between the models as well. Accurate prediction of the separation location in concert with an inviscid solution would provide a model to qualitatively predict the flow similar to Roshko's Cylinder. In addition to the qualitative markers of flow separation seen in the various velocity plots simulation affords the simple option of reading the surface shear stress. With the shear stress data at the surface for the Transition SST case we can then find the zero crossing to identify the separation location. We can then compare this with a separation model applied to the inviscid results to evaluate the accuracy. In this example, we use Thwaites separation criterion [38], which predicts separation when

$$C_p^{1/2}\left(x\frac{dC_p}{dx}\right) = 0.102. \tag{2.12}$$

An example of this is seen in Figure 2.38. While Thwaites is not explicitly applicable to axisymmetric cases, the results show decent agreement between the simulation separation locations and the predicted separation location.

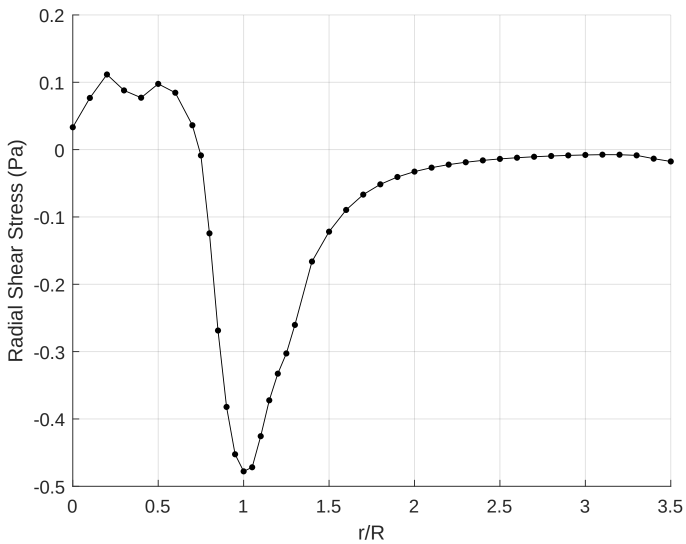

Figure 2.37: Sample of the simulated radial shear stress at the surface.

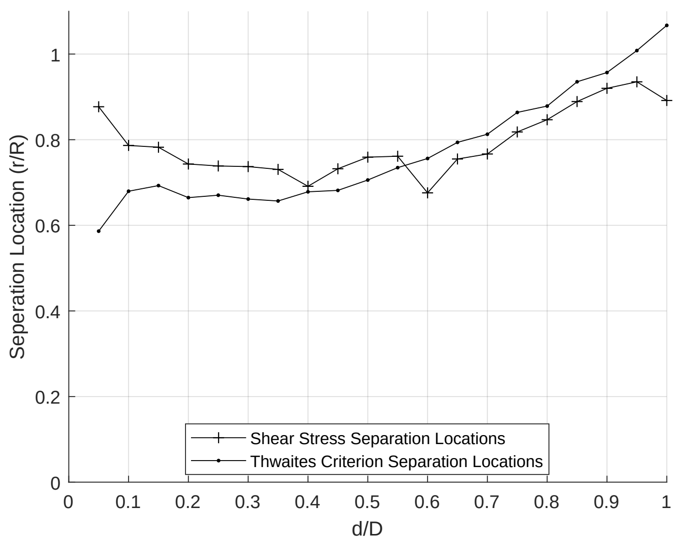

Figure 2.38: Separation locations from shear stress criteria vs Thwaites.

Inviscid Simulation Modeling

While the inviscid results were qualitatively quite different from the Transition SST results, the overall force computed was very similar, as shown in Figure 2.42. Although the inviscid simulation fails to capture some key physical phenomena such as flow separation and wake spreading, the discrepancy in the overall force is quite small. The relative error of the force prediction of the inviscid simulation to the Transition SST simulation is quite small, below 3% for most separation distances as seen in Figure 2.43a.

One feature of interest is the wake produced in the inviscid simulation as seen in Figure 2.29a. Being of constant diameter and not having any mixing, the wake is easy to characterize. Sampling the simulation results show that the axial velocity is nearly constant within and outside the wake boundary. Basic attempts to model the boundary show that the Vatistas vortex model as well as a generic hyperbolic tangent function are both good options for the transition shape.

To study how the wake changes based on the upstream obstruction, the wake was sampled for various values of d. The radius of the wake was calculated by computing the axial velocity within and outside the wake and identifying the radius at which the axial velocity crosses the midpoint between these values. Figure 2.40 shows how this computed radius changes with d. The plot shown in Figure 2.41 provides physical intuition for the change in wake area. As seen, there is a strong linear relationship between the normalized net force and the normalized wake area calculated from the measured wake radius. The relationship implies a physical meaning behind the wake area and the net thrust. We can apply basic momentum theory by recognizing that the actuator disk is pulling from still air and accelerating it, therefore the change in momentum should be captured by the wake. Assuming a uniform flow velocity v_{wake} within the wake, and a wake cross sectional area A_{wake}, the force associated with this is $F_{\text{wake}} = v_{\text{wake}}^2 \rho A_{\text{wake}}$. Given the axisymmetric nature of the problem, the wake is expected to be circular, and thus $A_{\text{wake}} = \pi R_{\text{wake}}^2$. If this is normalized by thrust and its relation to the induced velocity from disk actuator theory, the values used to plot the graph are recovered.

$$\frac{F_{\text{wake}}}{T} = \frac{v_{\text{wake}}^2 \rho A_{\text{wake}}}{V_i^2 2\rho A} \tag{2.13}$$

The results of the simulation indicate that the wake velocity remained virtually constant while the wake radius changed. This is used in the above equation by allowing v_{wake} to act as a constant with d/D. Being constant, it should be equal to the wake velocity in unobstructed conditions. Disk actuator theory also says that, in hover, the wake velocity is equal to twice the induced velocity at the disk (see Appendix C). Substituting this relation in simplifies Eq. (2.13) to

$$\frac{F_{\text{wake}}}{T} = \frac{2A_{\text{wake}}}{A}. \tag{2.14}$$

Because the actuator disk and the obstructing surface are the only surfaces in the scenario, the force associated with the fluid momentum of the wake should be equivalent to the net force F_{net}. Therefore, the wake area is changing to match the

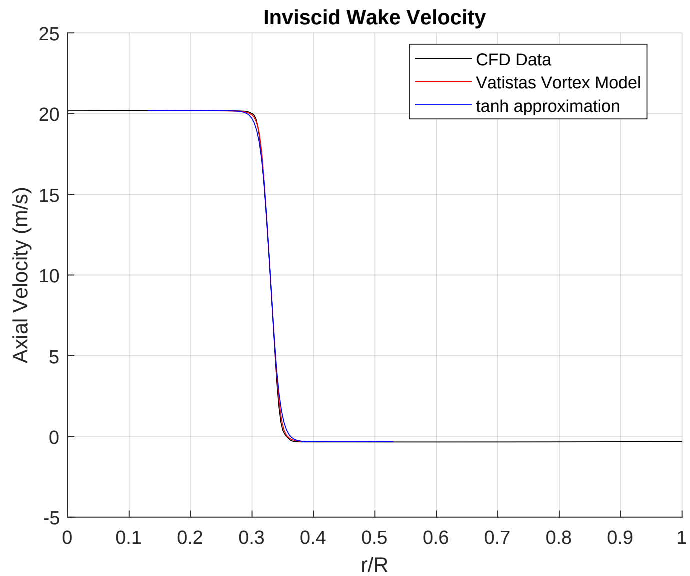

Figure 2.39: Radial Sample of the axial flow velocity showing the wake interface.

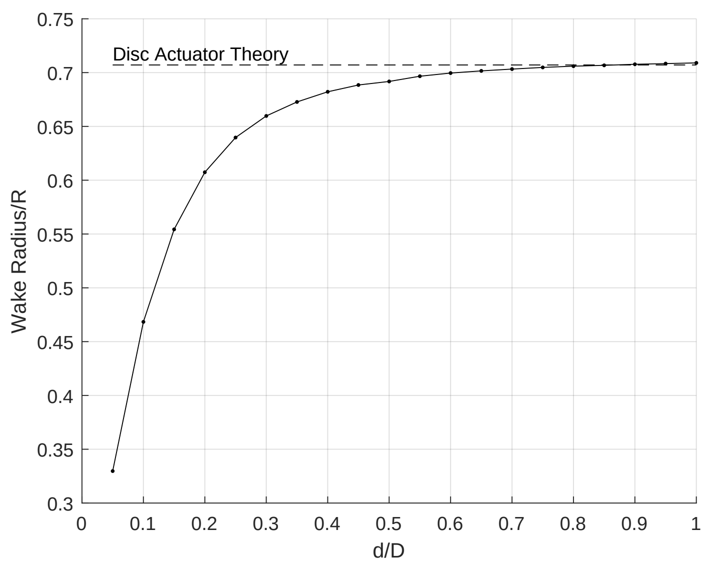

Figure 2.40: Variation of the simulated wake radius with separation distance.

momentum associated with the net force generated by the arrangement, as shown in Figure 2.41. In fact, as disk actuator theory states that the wake area is half of the disk area A, this means that the ratio of wake areas is equivalent to the ratio of the net force and thrust. One consequence of this is that analytic models that factor the shed vortex cylinder into the calculation of the flowfield must either know a priori the net force to properly compute the shed wake, or must iterate until convergence.

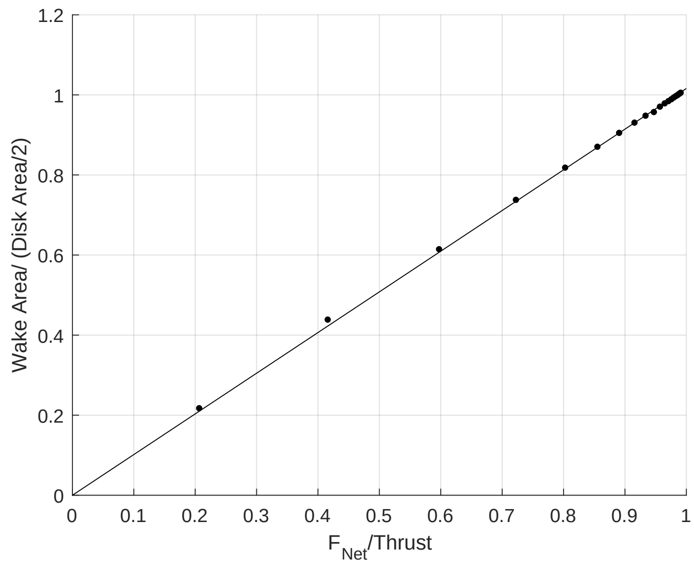

Figure 2.41: Variation in nondimensional wake area with nondimensional net force with a linear fit drawn.

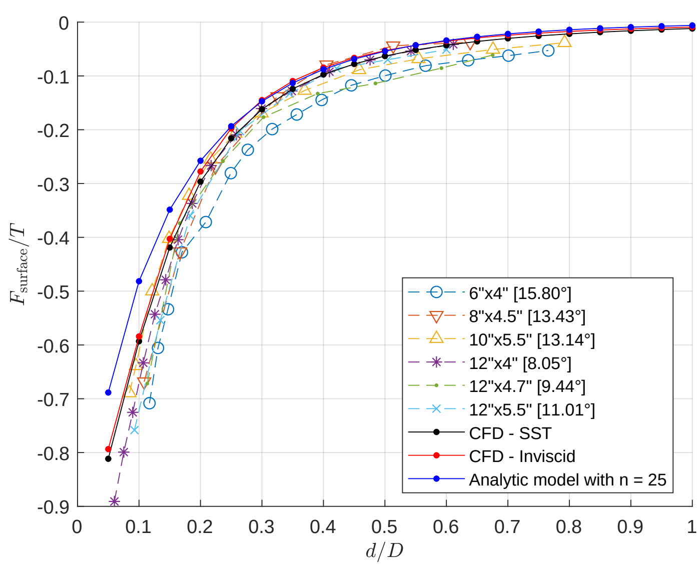

Figure 2.42: A comparison of the normalized surface force for all the experimental, simulation, and analytic results.

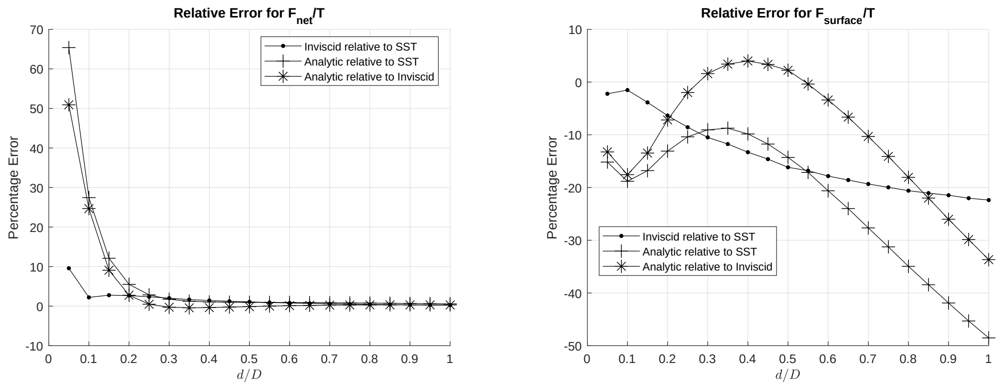

(a) Normalized net force (b) Normalized surface force

Figure 2.43: Force Errors Metrics.

2.4 Analytical Solution of the Ceiling Effect

While the CFD results of Section 2.3 lend insight into the flowfield of the problem, it is still desired to gain a physics based understanding of the problem. By developing a better understanding of the rotor's interaction with other bodies, accuracy of representations of the problem can be improved. An analytic model, even one with assumptions, can be incorporated into lower order simulations such as codes that use the panel method. These models are highly useful for preliminary design, where a fully representative simulation of a propeller would be computationally expensive and impractical while determining high level design parameters.

Given that the inviscid flow simulation seen in the CFD simulations from ANSYS Fluent were accurate in terms of the total force on the surface as shown in Section 2.3, it is proposed that a sufficient approximation to represent the interaction would be to develop a potential flow solution utilizing the same physics. This is done by first applying the chosen assumptions to the Morillo flowfield model, then comparing the results with the CFD simulations from Section 2.3, the experimental data of Section 2.2, and specific verification cases from the CFD.

Assumptions and Theory

One method of modeling the rotor disk from an analytic perspective can be found from rotorcraft modeling. The work of Morillo and Peters [39, 29] in particular is expected to be applicable here. While the underlying physics described by numerous authors is fundamentally the same, the notation used specifically by Morillo is used here. Normally a dynamic model to describe the flowfield above a rotor Morillo and Peters is an extension from previous work, namely Peters and He [40]. The

Peters and He inflow model is a dynamic model used to compute the inflow on the idealized disk region of a helicopter rotor in forward flight. The Peters and He model is a progression from the Pitt and Peters model [41] and is also based on work by Mangler and Squire [42], as well Joglekar and Loewy [43]. Both of these works are also derived by work from Kinner [44].

To apply and simplify the Morillo model, some assumptions about the flow are made:

- Flow is steady, axisymmetric with no swirl, and inviscid in the region of interest.
- There is no freestream velocity, equivalent to hover conditions.
- If possible, a uniform pressure jump across the disk will be imposed.
- No external body forces on the fluid such as gravity.

The relevant equations that govern the fluid motion in this application are conservation of mass (continuity equation) and conservation of momentum (Navier-Stokes equations) [45].

$$\frac{\partial \rho}{\partial t} + \boldsymbol{\nabla} \cdot (\rho \vec{v}_t) = 0 \tag{2.15}$$

$$\rho \frac{\partial \vec{v}_t}{\partial t} + \rho(\vec{v}_t \cdot \boldsymbol{\nabla})\vec{v}_t = -\boldsymbol{\nabla} p + \boldsymbol{\nabla}(\lambda \boldsymbol{\nabla} \cdot \vec{v}_t) + \mu[\boldsymbol{\nabla}(\boldsymbol{\nabla} \cdot \vec{v}_t) + (\boldsymbol{\nabla} \cdot \boldsymbol{\nabla})\vec{v}_t] + \rho \vec{f} \tag{2.16}$$

Here, ρ is the fluid density, $\vec{v}_t$ is the vector velocity, p is the pressure, λ and μ are the second and dynamic viscosity coefficients, respectively, and $\vec{f}$ represents external body forces. We can then apply some of our assumptions to the problem, specifically those of an inviscid, incompressible fluid with no external body forces. The equations of motion then reduce to the following

$$\boldsymbol{\nabla} \cdot \vec{v}_t = 0 \tag{2.17}$$

$$\frac{\partial \vec{v}_t}{\partial t} + (\vec{v}_t \cdot \boldsymbol{\nabla})\vec{v}_t = \frac{-\boldsymbol{\nabla} p}{\rho}. \tag{2.18}$$

In Morillo as well as previous works, the reduced momentum equation is typically normalized by the freestream velocity V_∞. This is not physically meaningful however for the case of hover, where the freestream velocity is defined as equal to 0. Peters and Morillo both assert that the models are valid in hover, and an alternative non-dimensionalization is used. Rather than the freestream velocity, the induced velocity due to the rotor at the rotor disk V_i can be considered the dominant velocity. Here, the derivation is first done assuming a non-zero freestream velocity.

Consider the total velocity to be composed of a constant, uniform freestream velocity V_∞ in an arbitrary direction $\vec{\xi}$ constrained to the x-z plane plus a relatively small perturbation velocity $\delta\vec{v}_t = (\delta v_x, \delta v_y, \delta v_z)$

$$\vec{v}_t = V_\infty\vec{\xi} + (\delta v_x, \delta v_y, \delta v_z) \tag{2.19}$$

$$\delta v_x, \delta v_y, \delta v_z \ll V_\infty. \tag{2.20}$$

With the freestream being constant in space and time, the mass equation reduces to just the perturbation velocity:

$$\boldsymbol{\nabla} \cdot \delta\vec{v}_t = 0. \tag{2.21}$$

Similarly, the time derivative in the momentum equation also reduces to just the perturbation velocity

$$\frac{\partial\vec{v}_t}{\partial t} = \frac{\partial\delta\vec{v}_t}{\partial t}. \tag{2.22}$$

Before continuing, the rest of the inertial forces in the momentum equation must be linearized

$$(\vec{v}_t \cdot \boldsymbol{\nabla})\vec{v}_t = ((V_\infty\vec{\xi} + \delta\vec{v}_t) \cdot \boldsymbol{\nabla})(V_\infty\vec{\xi} + \delta\vec{v}_t). \tag{2.23}$$

Due to the relative sizes of the freestream and perturbation velocities, the momentum equation thus reduces to

$$\frac{\partial\delta\vec{v}_t}{\partial t} - V_\infty\frac{\partial\delta\vec{v}_t}{\partial\xi} = \frac{-\boldsymbol{\nabla}p}{\rho}. \tag{2.24}$$

The values are then non-dimensionalized using V_∞ for velocity, rotor radius R for length and air density ρ for its contribution to mass. The entire equation is thus multiplied by $\frac{R}{V_\infty^2}$, canceling the dimensionality of each term With this non-dimensionalization, the continuity and momentum equations then become

$$\boldsymbol{\nabla} \cdot \vec{v} = 0 \tag{2.25}$$

$$\frac{\partial\vec{v}}{\partial\tau} - \frac{\partial\vec{v}}{\partial\xi} = -\boldsymbol{\nabla}P \tag{2.26}$$

where τ is the non-dimensional time , $\vec{v}$ is the non-dimensional velocity vector field, P is the non-dimensional pressure field, and ξ is the nondimensional coordinate along the freestream line, positive upstream.

Rather than using the freestream velocity for the non-dimensionalization, an alternative per Peters [46] is to use the velocity

$$V = \frac{\mu^2 + (\lambda + V_i)(\lambda + 2V_i)}{\sqrt{\mu^2 + (\lambda + V_i)^2}} \tag{2.27}$$

where μ is the edgewise component of the free stream velocity on the disk, λ is the component of the freestream normal to the disk, and V_i is the induced velocity at the disk predicted by disk actuator theory as in Eq. (2.5). As there is no freestream velocity in hover, this velocity reduces to

$$V = 2V_i \tag{2.28}$$

which is also the downstream wake velocity predicted by disk actuator theory. This non-dimensionalization has a convenient property. Expressing the velocity and pressure using Morillo's notation

$$\vec{v} = \frac{\vec{v}_t}{2V_i},\ P = \frac{p}{\rho(2V_i)^2} \tag{2.29}$$

$$(2V_i)^2 = 4V_i^2 = 4\frac{\Delta P}{2\rho} = \frac{\Delta P}{\frac{1}{2}\rho} \tag{2.30}$$

$$|\vec{v}|^2 = \frac{|\vec{v}_t|^2}{4V_i^2} = \frac{\frac{1}{2}\rho|\vec{v}_t|^2}{\Delta P} \tag{2.31}$$

$$P = \frac{p}{2\Delta P} \tag{2.32}$$

where $\vec{v}_t$ is the dimensional velocity vector field and p is the dimensional pressure field. We see from the right hand side of Eq. (2.31) that taking the square of the non-dimensional velocity is equivalent to computing the dynamic pressure normalized by the disk loading.

If the non-dimensional velocity is represented by the gradient of a function Ψ as in

$$\vec{v} = \boldsymbol{\nabla}\Psi. \tag{2.33}$$

then this can be substituted into the continuity equation, and it is found that the function Ψ satisfies the Laplace equation

$$\boldsymbol{\nabla} \cdot \boldsymbol{\nabla}\Psi = \boldsymbol{\nabla}^2\Psi = \Delta\Psi = 0. \tag{2.34}$$

Additionally, substituting the velocity potential function into Eq. (2.26) and pre-multiplying both sides with a divergence results in

$$\left(\frac{\partial \nabla \cdot \nabla \Psi}{\partial \tau} - \frac{\partial \nabla \cdot \nabla \Psi}{\partial \xi}\right) = -\nabla \cdot \nabla P. \tag{2.35}$$

Because $\nabla \cdot \nabla \Psi = 0$, the left hand side is equal to 0, and the pressure field must also satisfy the Laplace Equation.

$$\Delta P = 0 \tag{2.36}$$

Morillo's solution to the flow relies on solving the Laplace equation represented in an ellipsoidal coordinate system described in Appendix A. Valid solutions to the Laplace equation are the set of functions

$$\Phi_n^{mc}(\nu, \eta, \overline{\psi}) = \overline{P}_n^m(\nu)\overline{Q}_n^m(\eta)\cos\left(m\overline{\psi}\right) \tag{2.37}$$

$$\Phi_n^{ms}(\nu, \eta, \overline{\psi}) = \overline{P}_n^m(\nu)\overline{Q}_n^m(\eta)\sin\left(m\overline{\psi}\right) \tag{2.38}$$

where $\overline{P}_n^m(\nu)$ and $\overline{Q}_n^m(\eta)$ are normalized Legendre functions of the first and second kind, respectively, defined in Appendix B. The pressure expansion is thus represented with a linear combination of the basis functions as in the following equation

$$P = -\sum_{m=0}^{\infty}\sum_{n=m+1}^{\infty}[\tau_n^{mc}\Phi_n^{mc} + \tau_n^{ms}\Phi_n^{ms}] \tag{2.39}$$

where τ_n^{mc} and τ_n^{ms} are the associated cosine and sine coefficients, respectively, (distinct from the non-dimensional time τ). This can be related this to the pressure rise across the disk, the thrust other words. At the disk, $\eta = 0$ so $Q_n^m(i\eta) = 1$. Furthermore, P_n^m is an odd function when $n+m$ is odd, and even when $n+m$ is even. If we are subtracting the pressure on the lower face from the pressure on the upper face, then all terms where $n+m$ is even will cancel out, and only the odd terms will remain. The pressure jump across the disk at any point on its surface is therefore represented by the following equation

$$\frac{\Delta p}{\rho V^2} = [P_{\text{lower}} - P_{\text{upper}}]_{\eta=0} = 2\sum_{m=0}^{\infty}\sum_{n=m+1,m+3,\ldots}^{\infty}\overline{P}_n^m(\nu)\tau_n^{mc}\cos\left(m\overline{\psi}\right) + \overline{P}_n^m(\nu)\tau_n^{ms}\sin\left(m\overline{\psi}\right). \tag{2.40}$$

The velocity $\vec{v}$ is represented by the summation of the gradient of velocity potentials Φ. The velocity potential basis functions are connected to the pressure basis functions by

$$\begin{gathered}\Psi_n^{mc} = \int_{\xi}^{\infty}\Phi_n^{mc}d\xi, \qquad \Psi_n^{ms} = \int_{\xi}^{\infty}\Phi_n^{ms}d\xi \\ m = 0, 1, 2, \ldots, \infty, \quad n = m, m+1, m+2, \ldots, \infty\end{gathered} \tag{2.41}$$

and the velocity becomes

$$\vec{v} = \sum_{m=0}^{\infty}\sum_{n=m}^{\infty}(\hat{a}_n^m(\tau)\nabla\Psi_n^{mc} + \hat{b}_n^m(\tau)\nabla\Psi_n^{ms}). \tag{2.42}$$

Here $\hat{a}_n^m(\tau)$ and $\hat{b}_n^m(\tau)$ are coefficients to define the velocity field. The subsequent steps of the formulation apply a Galerkin approach to reduce the equations to a set of ordinary differential equations for the velocity coefficients in toms of the pressure coefficients.

Morillo Model

The relation between the pressure and velocity coefficients can be summarized by the system of equations

$$[\tilde{L}^c]\{\overset{*}{\hat{a}}{}_n^m\} + [D^c]\{\hat{a}_n^m\} = [D^c]\{\tau_n^{mc}\} \tag{2.43}$$

$$[\tilde{L}^s]\{\overset{*}{\hat{b}}{}_n^m\} + [D^s]\{\hat{b}_n^m\} = [D^s]\{\tau_n^{ms}\}. \tag{2.44}$$

To express the velocity potential Ψ in terms of the basis functions Φ without requiring numerical integration, a change of variable is introduced

$$\{\hat{a}_n^m\}^T\{\Psi_n^{mc}\} = \{a_n^m\}^T\{\sigma_n^m\Phi_{n+1}^{mc} + \varsigma_n^m\Phi_{n-1}^{mc}\} \tag{2.45}$$

$$\sigma_n^m = \frac{1}{K_n^m\sqrt{(2n+1)(2n+3)((n+1)^2-m^2)}} \tag{2.46}$$

$$\varsigma_n^m = \frac{1}{K_n^m\sqrt{(4n^2-1)(n^2-m^2)}},\ n \neq m. \tag{2.47}$$

Reduced Model

With the given assumptions, we can simplify the Morillo model considerably. The axisymmetric condition means that there can be no azimuthal variation in the pressure and velocity, significantly constraining the values of the pressure coefficients. Examination of the Pressure basis functions Φ reveals that any non-zero value m will lead to an azimuthal variation in pressure. Therefore $m = 0$ for this analysis. This has the effect of completely removing the sin terms from consideration, as $\sin\left(0\,\overline{\psi}\right) = 0$. With the sin component of the pressure $\Phi_n^{0s} = 0$, the pressure coefficients τ_n^{0s} should have no influence on the subsequent flow field and can thus be disregarded.

Another assumption is that only the steady state condition is considered. This removes the time dependence from the equation. Because of this, the derivative of the velocity coefficients will therefore be equal to 0, and the velocity coefficients will be equal to the pressure coefficients

$$\{\hat{a}_n^m\} = \{\tau_n^{mc}\}. \tag{2.48}$$

With these simplifications, the expression for the non-dimensional velocity in terms of the pressure coefficients and basis functions becomes the following

$$\vec{v} = \sum_{m=0}^{\infty} \sum_{n=m+1}^{\infty} \tau_n^{mc} (\sigma_n^m \nabla \Phi_{n+1}^{mc} + \varsigma_n^m \nabla \Phi_{n-1}^{mc}) \tag{2.49}$$

where the gradients of the basis functions can be computed using the relations for cartesian derivatives in an ellipsoidal coordinate system and the derivatives for the Legendre functions of the first and second kinds.

Modeling Finite Pressure Jump

To properly replicate the simulation conducted in ANSYS Fluent, it was required to similarly model the input conditions. One of these was a constant, finite pressure jump across the surface. To do so, the appropriate coefficients for the pressure basis functions were identified. This was done in two ways. One could either use an inner product integral to find coefficents analytically or numerically, or use a numerical least squares to numerically identify coefficients. As the fitting is done at the disk surface, the inner product used was the same as used to normalize the Legendre function of the first kind. For two arbitrary functions $f(x)$ and $g(x)$

$$\langle f(x), g(x) \rangle = \int_0^1 f(x) g(x) dx. \tag{2.50}$$

Coefficients can then be found using an orthogonal decomposition process. Legendre polynomials are complete on the interval $[-1, 1]$, but not necessarily on the interval $[0, 1]$. Furthermore, restricting the case to no mass injection as an input condition means that only the odd harmonic Legendre polynomials are used to model the pressure jump, meaning that the full space of polynomials are not useable to model functions in general. The level of fidelity is dependent on the number of basis functions used. More harmonics will lead to a flatter pressure distribution, albeit with a Gibbs phenomenon at the edge of the disk, as seen in Figure 2.44. For comparison with the freestream curves, harmonics up to a maximum n of 25 were used.

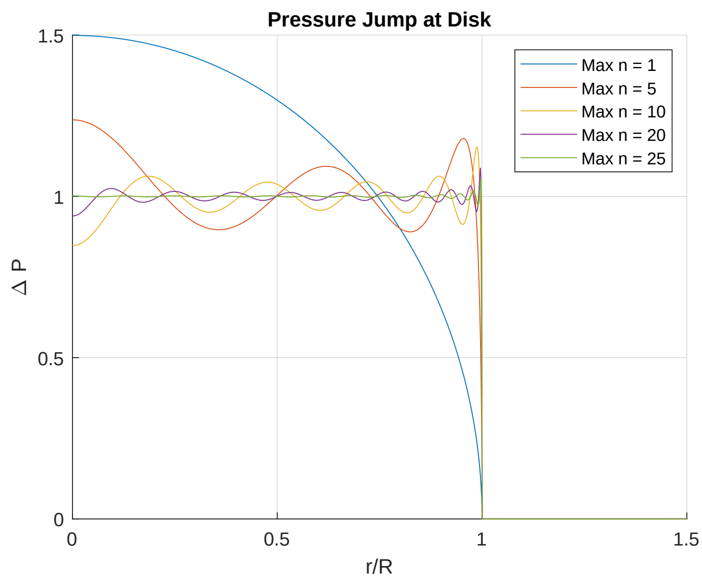

Figure 2.44: Pressure jump across the actuator disk versus radius for a uniform pressure jump with different maximum numbers of harmonics.

Agreement with Freestream Curves

To determine the agreement of the Morillo model with the ANSYS simulation, the velocity contours above the rotor disk were compared between the analytical solution and the simulation results. Figures 2.45 and 2.46 show the axial and radial velocities computed from a freestream disk in CFD and compare them to the analytical results. The velocities are sampled at various planes upstream and parallel to the rotor disk. Some interesting qualitative features in the flow are seen in the plots, particularly at the disk. While the axial velocity at the disk is roughly constant for the majority of its diameter, there are two significant tip effects observed. The first is an abrupt and significant decrease in the axial flow velocity in the streamwise direction near the tip. This change corresponds to the location of where the vortex sheet created by the pressure jump crosses the plane of the disk. The second is an apparently asymptotic behavior of the velocity in the vicinity of the disk radius, with a profile similar to that of a vortex ring.

The analytic curves presented have a sizeable discrepancy with the CFD results. The solutions were thus modified with a correction factor

$$r_{\text{corrected}} = 0.85r \tag{2.51}$$

$$\vec{v}_{\text{corrected}} = \vec{v}\left(1.25 - 0.5\frac{d}{D}\right) \tag{2.52}$$

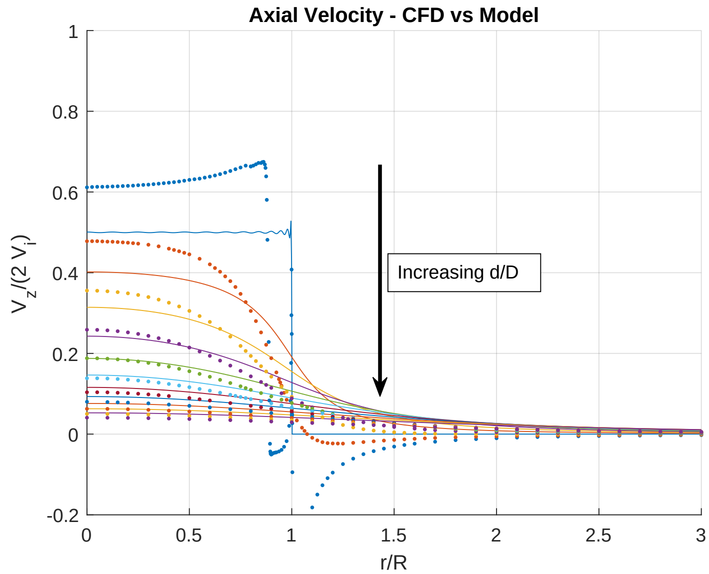

Figure 2.45: Normalized unobstructed axial velocity at various stations. Solid lines are predictions from the Morillo flow field. Sample distance d/D starts at 0 and increments by 0.1 up to 1.

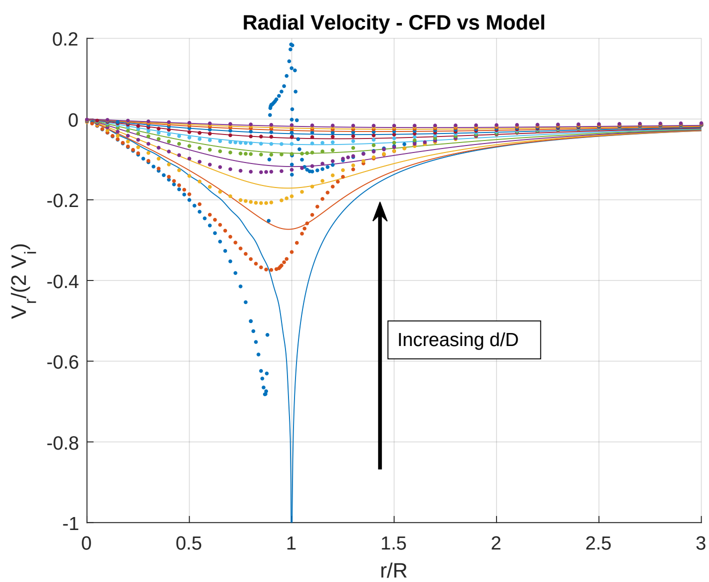

Figure 2.46: Normalized unobstructed radial velocity at various stations. Solid lines are predictions from the Morillo flow field. Sample distance d/D starts at 0 and increments by 0.1 up to 1.

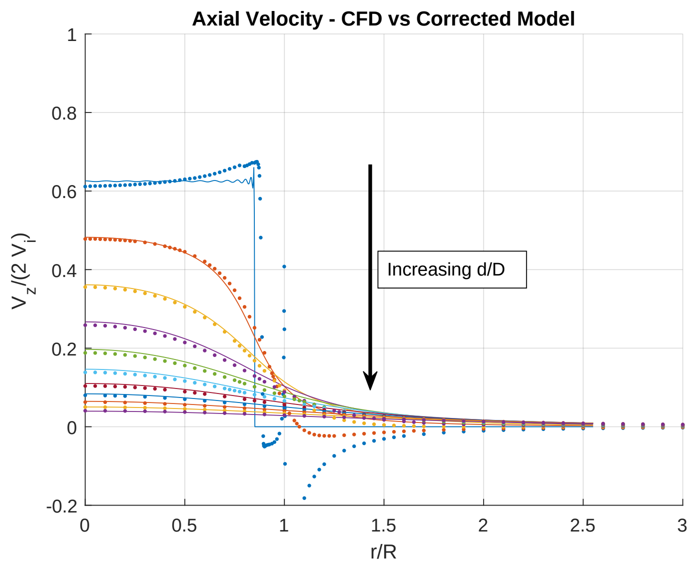

Figure 2.47: Normalized unobstructed axial velocity at various stations. Solid lines are corrected predictions from the Morillo flow field. Sample distance d/D starts at 0 and increments by 0.1 up to 1.

to match the curves produced by CFD. There is a radial coordinate correction as well as a velocity magnitude correction. Plotting the corrected values against the CFD results as in Figures 2.47 and 2.48 shows good agreement for both the axial and radial components of velocity, respectively.

Although the input conditions were constrained to attempt to replicate the conditions used in the CFD, it appears that even the corrected Morillo model does not capture some of the effects computed in FEM CFD of a pure disk actuator. For instance the vortex ring that appears to be centered at the disk boundary does not seem to be captured, nor does the effect of the vortex sheet on the outboard velocity.

The original Morillo model assumes a skewed cylindrical wake shed from the rotor disk. With the assumptions imposed, it also asserts that the axial velocity profile at the disk should be equal to the pressure jump profile imposed across the disk surface. As the simulation results show, this does not appear to be the case when the problem is examined with a more general solver. The Morillo model appears to be unable to predict the flow associated with the portion of the vortex sheet that is in the upstream of the rotor disk, and the accuracy of the velocity profiles suffer as a result. The provided correction for the models appears to match the velocity profiles well in the range of sample locations studied.

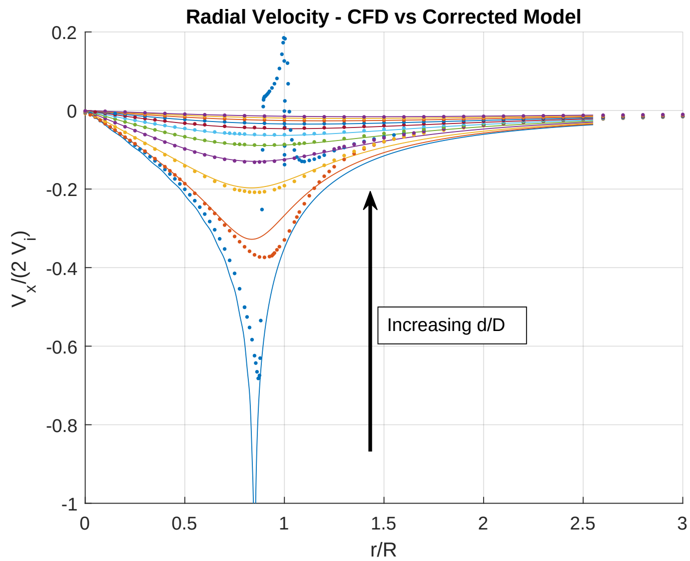

Figure 2.48: Normalized unobstructed radial velocity at various stations. Solid lines are corrected predictions from the Morillo flow field. Sample distance d/D starts at 0 and increments by 0.1 up to 1.

Application with the method of images

In order to evaluate the interaction between the actuator disk and an infinite boundary, the method of images is used. The method of images achieves this taking a phenomena and mirroring it about an arbitrary boundary. Due to symmetry, there can be no flow through this boundary, effectively modeling a surface with the no-penetration condition. From a practical standpoint, this means that the velocity at the surface of symmetry and therefore the virtual surface can be calculated by simply doubling the x component of velocity at the distance for the freestream case. In practice there is a discrepancy between double the freestream velocity at a location, and the velocity at the surface boundary computed using CFD, as seen in Figure 2.49. It is unclear precisely why that is. This suggests that, even if the Morillo model successfully predicts the velocity upstream of a disk actuator, that a correction is still required to model the pressure at a large upstream obstruction in a manner analogous to the solution of the CFD.

Comparison of the peaks of the respective curves helps to highlight the discrepancy. This is seen in Figure 2.50. The peaks of the radial velocity curves have a slight discrepancy in the radial location in the first couple entries but are generally consistent for most distances. This is also true for the peak magnitude, though the method of images value is roughly 6% undervalued. This can be mitigated with a small correction factor if desired.

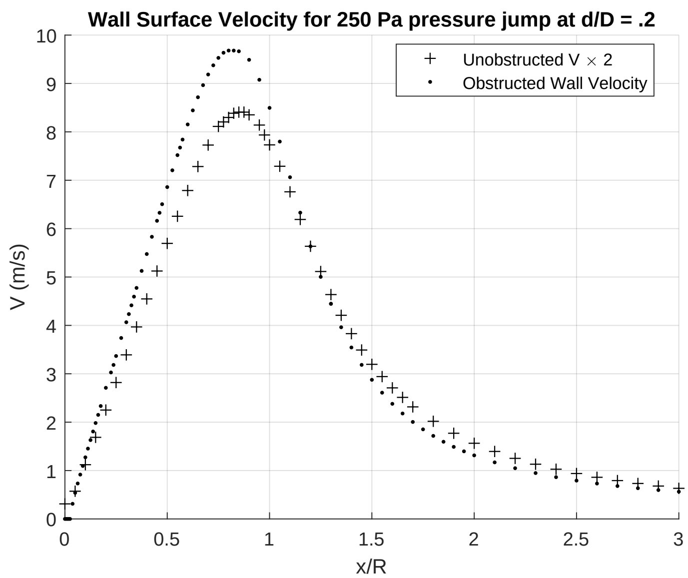

Figure 2.49: Comparison of the velocity profiles from an inviscid simulation from a freestream and and obstructed case.

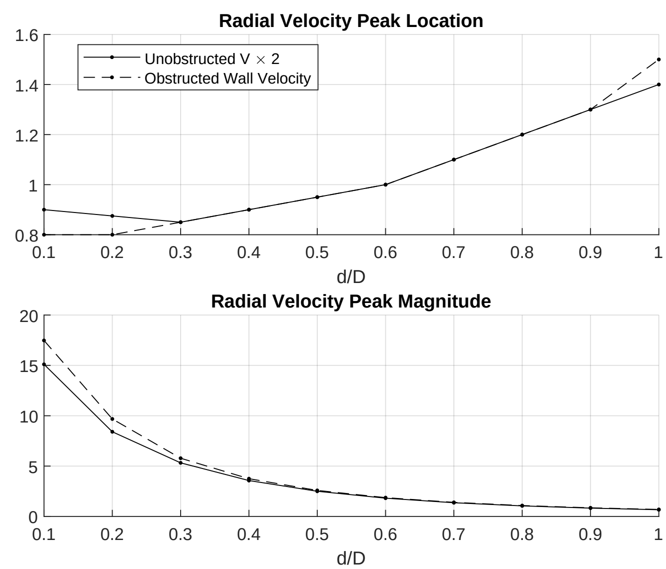

Figure 2.50: Comparison of measured velocity peaks between the doubled freestream radial velocity and the obstructed inviscid surface velocity.

Based upon the equations describing the fluid motion, it is expected that superposition is a valid assumption. The velocity potential is intended to satisfy the Laplace equation, which is a linear operator. This means that two or more velocity potential functions that independently satisfy the Laplace equation can be combined to form a velocity potential that also satisfies the equation. It is also expect that the superposition of two different fields will not interfere with the pressure jump of either. This is because the pressure jump is imposed using a discontinuity in the coordinate system near the origin. Beyond the discontinuity, the velocity field is continuous. Therefore, the superposition of an additional actuator disk into the flow should not change the pressure jump across any point of the disc's surface.

Surface Force

Application of the Morillo model to the problem using the method of images is straightforward. As the region of interest is the surface forming the plane of symmetry in the method of images, the no penetration condition inherent in its formulation means that the axial velocity need not be considered. The radial velocity is then calculated by doubling the velocity associated with the freestream case, as it is the sum of the original actuator disk and its mirror image, both of which are the same distance from the boundary. The pressure is then found by applying the Bernoulli principle, based upon the assumption that the flow is inviscid in the region of interest. This means that, provided an accurate velocity profile is computed, an accurate pressure profile should also result relative to the inviscid simulation. The pressure can then be numerically integrated to produce the surface force. The results of applying the method of images can be seen in Figure 2.42. There is relatively good agreement between the analytic computation and the various CFD methods as well as the experimental data.

The relative error between the Transition SST simulation, inviscid Simulation, and Analytical Solution can be seen in Figures 2.43a and 2.43b. There is a slight distinction in how the results are presented. Figure 2.43b shows the error of the surface force, which decays to 0 as the separation increases. Meanwhile Figure 2.43a shows the net force, which goes to 1 as the separation increases. The two normalized forces are related by

$$\frac{F_{\text{net}}}{T} = \frac{F_{\text{surface}} + T}{T} = \frac{F_{\text{surface}}}{T} + 1. \tag{2.53}$$

Depending on which force is more relevant however, the percentage error changes substantially, so both are presented. Error between the various models is up to 10 to 20 %, depending on what range of separation distances are examined. For most of the range of separation distances studied however, the deviation is quite small, less than 5 %.

Closed Form Solution of the Ceiling Effect

Maybe it's all part of a great big ineffable plan.

The Nice and Accurate Prophecies of Agnes Nutter

While the results shown in Figures 2.47, 2.48, and 2.42 were computed numerically with various programmatic steps, we can compile the identified expressions and assumptions into a closed form. This allows for the surface pressure associated with a uniform pressure jump to be computed for a particular separation distance.

$$\frac{p(\frac{r}{R},\frac{d}{D})}{\Delta P} = -\left(2\left(1.25 - 0.5\frac{d}{D}\right)\sum_{n=1}^{\infty}\tau_n\left[\sigma_n^0\frac{\partial}{\partial r}\Phi_{n+1}(\nu',\eta') + \varsigma_n^0\frac{\partial}{\partial r}\Phi_{n-1}(\nu',\eta')\right]\right)^2 \tag{2.54}$$

where σ_n^0 and ς_n^0 are defined by

$$\sigma_n^0 = \frac{1}{K_n^0\sqrt{(2n+1)(2n+3)(n+1)^2}} \tag{2.55}$$

$$\varsigma_n^0 = \frac{1}{K_n^0\sqrt{(4n^2-1)(n^2)}},\ n \neq 0. \tag{2.56}$$

The definition of K_n^0 can be found in Section B.

The corrected ellipsoidal coordinates ν' and η' are computed from the cartesian coordinates using the coordinate system relations. Note that, in the original coordinate system $R = 1$, so d/D is equivalent to $z/(2R)$. The correct input into the coordinate conversions is thus $2d/D$.

$$\nu' = \frac{1}{\sqrt{2}}\sqrt{1 - \overline{S}' + \sqrt{(\overline{S}'-1)^2 + 4\left(2\frac{d}{D}\right)^2}} \tag{2.57}$$

$$\eta' = \frac{1}{\sqrt{2}}\sqrt{\overline{S}' - 1 + \sqrt{(\overline{S}'-1)^2 + 4\left(2\frac{d}{D}\right)^2}} \tag{2.58}$$

$$\overline{S}' = \left(\frac{r}{R}\frac{1}{.85}\right)^2 + \left(2\frac{d}{D}\right)^2 \tag{2.59}$$

For the uniform pressure jump, the pressure coefficients are calculated as

$$\tau_n = \frac{1}{2}\frac{\int_0^1 \overline{P}_n(\nu)d\nu}{\int_0^1 (\overline{P}_n(\nu))^2 d\nu} \tag{2.60}$$

to an arbitrary degree n.

From this we can calculate the normalized surface force F_{surface}/T for which we need the the area $A = \pi R^2 = \pi$

$$\frac{F_{\text{surface}}}{T} = \int_0^\infty \frac{p}{\Delta P}\frac{1}{A}2\pi r dr = \int_0^\infty \frac{p}{\Delta P}2\pi r dr \frac{1}{\pi R^2} \tag{2.61}$$

which can be further transformed into the non-dimensional radial coordinates

$$\frac{F_{\text{surface}}}{T} = \int_0^\infty \frac{p}{\Delta P}2\pi \frac{r}{R} d\left(\frac{r}{R}\right) R^2 \frac{1}{\pi R^2} = \int_0^\infty \frac{p}{\Delta P} 2 \frac{r}{R} d\left(\frac{r}{R}\right). \tag{2.62}$$

Due to the complexity of the ellipsoidal coordinate system, evaluating this integral analytically is difficult. However, it can be easily evaluated to the desired level of precision numerically. Furthermore, due to the scalability of the problem, the domain of cases that need to be evaluated is relatively small. A single solution to the pressure field can be scaled to apply to a range of disk diameters and disk loadings that should comfortably include expected values in multirotor operations.

The associated analytic expression can be quite verbose. For example, the expression for only n = 1 is

$$\frac{p\left(\frac{r}{R}, \frac{d}{D}\right)}{\Delta P} = -\left(\left(\frac{d}{D}\right) - \frac{5}{2}\right)^2 \left(\frac{15\frac{r}{R}\sqrt{-289 + f_1}}{\sqrt{2}(289 + f_1)} - \frac{15}{34}\frac{r}{R}\tan^{-1}\left(\frac{\sqrt{2}}{f_2}\right)\right)^2 \tag{2.63}$$

where

$$f_1 = 1156\left(\frac{d}{D}\right)^2 + 400\left(\frac{r}{R}\right)^2 + \sqrt{1336336\left(\frac{d}{D}\right)^4 + 2312\left(\frac{d}{D}\right)^2\left(400\left(\frac{r}{R}\right)^2 + 289\right) + \left(289 - 400\left(\frac{r}{R}\right)^2\right)^2}. \tag{2.64}$$

$$f_2 = \sqrt{\sqrt{\left(4\left(\frac{d}{D}\right)^2 + \frac{400\left(\frac{r}{R}\right)^2}{289} - 1\right)^2 + 16\left(\frac{d}{D}\right)^2} + 4\left(\frac{d}{D}\right)^2 + \frac{400\left(\frac{r}{R}\right)^2}{289} - 1} \tag{2.65}$$

The result of the force prediction with only the first harmonic can be seen in Figure 2.51. The single term prediction with the correction has excellent agreement with the CFD results, generally less than 5% error relative over the range of separation distances.

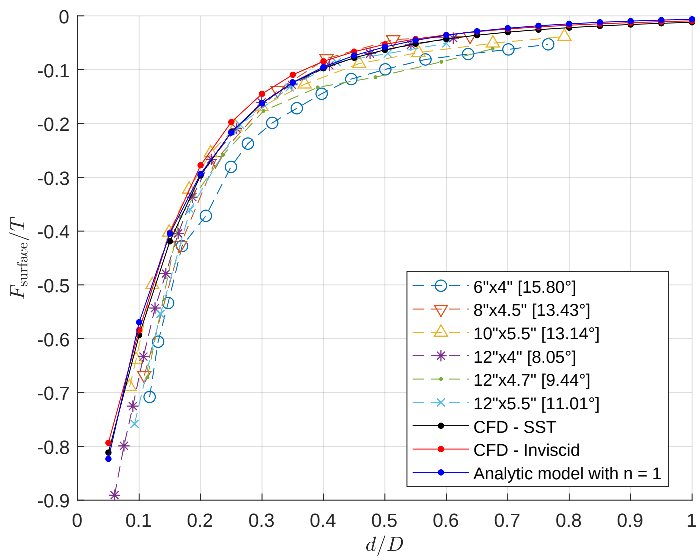

Figure 2.51: A comparison of the normalized surface force for all the experimental, simulation, and analytic results with only the first harmonic.

Discussion

The mismatch of the Morillo model with the CFD results highlights qualitative features that are not captured even in freestream conditions. In particular, the formation of the vortex sheet and apparent vortex ring at the disk edge are not represented. The result of the Morillo model is that steady state hover conditions should produce axial flow in a profile that is equivalent to the input pressure jump profile, but this is in contradiction to the CFD results because of the observed vortical structures. Attempts to reconcile the model without the correction via the introduction of a vortex ring were unsuccessful. It was found that adjusting the strength of the vortex ring in an attempt to match the computed velocity contours required different strengths to match the profile at different distances above the rotor disk. The required strengths also did not correlate in a predictable manner with the distances.

The better agreement with the single harmonic pressure jump over the modeling of the finite pressure suggests that the disk loading profile represented by the first term is a better representation of the loading than the uniform pressure jump. This is only reflected in the aggregate value of the total surface force experienced. Because the Morillo flowfield is used to replicate the inviscid simulation case, it does not capture physically observed effects such as the flow separation. This separation location can be estimated using the Thwaites separation criterion though as described in

Section 2.3. The single harmonic pressure jump is simple enough that the velocity profile it produces could be implemented as a simple model for applications such as panel methods that require simplistic representations of actuator disks.

2.5 Future Work

The work presented here suggests multiple potential avenues for further exploration in the subject. Resolving the discrepancy in the velocity profile at the disc computed in ANSYS and the profile produced using the theory of Morillo would significantly improve understanding of the flowfield around an actuator disk. A choice of a more physically accurate pressure distribution may also be worth studying, such as a distribution where the pressure profile drops to 0 at the center and edge of the disk, reflecting the lack of lift as the propeller blades end and at the center where the rotor translational velocity is zero. Similarly, incorporating swirl velocity could be a physically relevant feature to include. The Morillo model could even be used to dynamically model a specific propeller to more specifically predict its performance.

There are still discrepancies between the theory and the simulation, thus requiring the correction. Identification of the precise cause of these discrepancies would be ideal. As the Morillo model requires that the pressure jump drop to zero at the edge of the disk, it is possible that a study of a more physical pressure profile would help resolve some of these discrepancies.

The Morillo flowfield described here is a versatile model, and is used in only a very restricted case. The qualities of the model are conducive to a number of further uses. Though this work highlights and emphasizes the relevance of the simplified representation to the phenomenon, the Morillo model could be used to dynamically model a specific propeller to more specifically predict its performance. Morillo also mentions that the model also has an exact solution provided via convolution integral. Given the simplicity of the particular case studied in this work, it may be worthwhile to study the problem using the exact solution.

An additional potential application of the analytical model has to do with flow control. As the Morillo model provides a relationship between the velocity field and the pressure distribution, the model could also be used to determine the requisite pressure profile to produce a desired velocity field. The pressure field solution can the be used to inform a rotor design or collective and swashplate control inputs depending on the level of control available.

Though the Morillo model provides the flow field above the rotor, there have been more recent advances in the work to provide the flowfield throughout the entire domain. In particular Fei [47] computed the flowfield in the region below the rotor disk and Huang [48, 49] blended the solution to form a complete flowfield solution. It is possible that incorporating advances in the flowfield physics could improve the quality of the model. Improvements would be beneficial for applying this method to obstructions beyond only an infinite plane. While the CFD model is cheap to evaluate for the case outlined in this work, anything outside an axisymmetric situation will increase the computational cost tremendously. Combining this model with a panel method to simulate bodies or other obstructions would provide a low cost means of simulating these configurations.

Lastly, while this work chose to focus on examining only a single rotor in detail, multiple rotors in close proximity to one another is the typical use case. Applying the studies here to multiple propellers would be of some interest. One example would be identifying if the non-dimensional scaling is still applicable to a collection of propellers based upon their total area and average disc loading.

2.6 Conclusion

Upstream obstructions have a significant effect on the thrust performance of the propeller. When measured independently, some propellers experienced a nearly two-fold increase in thrust with a reduction in required torque. A positive application would be that drones could feasibly double their flight time if an external flat surface is taken advantage of. However, if the force on the surface is included, the net force drops to nearly zero. The force interaction between the two nearly disappears once the separation exceeds half a propeller diameter. To the authors knowledge, this is the first work identifying that the non-dimensionalized sum of the propeller and surface forces from propellers of different diameters and pitches collapse to a single curve. This commonality suggests that the one-half diameter maxim presented can be taken as a general design rule.

The pressure measurements taken at the surface with the obstruction were corroborated with CFD simulations in ANSYS Fluent and good agreement between the two is shown. Subsequent simulations also help demonstrate that the results found are scalable to different rotor diameters and pressure jumps. This scalability means that solutions can be generalized and applied to a variety of cases without requiring in-depth analysis of an individual propeller. The simulations provide insight into the separated flow region near the axis of the propeller and finds that the Thwaites method for separation prediction is a satisfactory predictor for the separation location.

Lastly, an analytic model based on the Morillo flowfield was implemented. This model can provide a framework for improving future simulations, panel-codes, or low order models and is compared to the CFD results. Some qualitative discrepancies between the Morillo model and the simulation are found and discussed. Despite the differences, with a correction applied to the model informed by the simulation results, the model agrees well with the simulation and experiment. The corrected version is simple enough to potentially be implemented in reduced order models or to provide a starting point for future theoretical analyses.

References

[1] Alessandro Bacchini and Enrico Cestino. “Electric VTOL Configurations Comparison.” In: *Aerospace* 6.3 (Feb. 2019), p. 26. DOI: 10.3390/aerospace6030026.

[2] Xichen Shi, Patrick Spieler, **Tang, Ellande**, Elena-Sorina Lupu, Phillip Tokumaru, and Soon-Jo Chung. “Adaptive Nonlinear Control of Fixed-Wing VTOL with Airflow Vector Sensing.” In: *ICRA* (Mar. 2020). arXiv: 2003.07558. DOI: 10.1109/ICRA40945.2020.9197344.

[3] Xichen Shi, Kyunam Kim, Salar Rahili, and Soon Jo Chung. “Nonlinear Control of Autonomous Flying Cars with Wings and Distributed Electric Propulsion.” In: *Proceedings of the IEEE Conference on Decision and Control* 2018-December.Cdc (2019), pp. 5326–5333. ISSN: 07431546. DOI: 10.1109/CDC.2018.8619578.

[4] Kyunam Kim, Salar Rahili, Xichen Shi, Soon-Jo Chung, and Morteza Gharib. “Controllability and Design of Unmanned Multirotor Aircraft Robust to Rotor Failure.” In: *AIAA Scitech 2019 Forum*. 2019, p. 1787.

[5] **Tang, Ellande**, Patrick Spieler, Matthew Anderson, and Soon-Jo Chung. “Design of the Next-Generation Autonomous Flying Ambulance.” In: *AIAA Scitech 2021 Forum*. Reston, Virginia, Jan. 2021, pp. 1–14. ISBN: 978-1-62410-609-5. DOI: 10.2514/6.2021-1514.

[6] Daniel P. Raymer. *Aircraft Design: A Conceptual Approach*. Third. Reston, Virginia: American Institute of Aeronautics and Astronautics, Inc, 1999. ISBN: 1-56347-281-3.

[7] Leroy H. Smith. “Wake Ingestion Propulsion Benefit.” en. In: *Journal of Propulsion and Power* 9.1 (Jan. 1993), pp. 74–82. ISSN: 0748-4658, 1533-3876. DOI: 10.2514/3.11487.

[8] Paul Bevilaqua and Christopher Yam. “Propulsive Efficiency of Wake Ingestion.” In: *Journal of Propulsion and Power* 36.4 (July 2020), pp. 517–526. ISSN: 1533-3876. DOI: 10.2514/1.B37695.

[9] Michael R. Derby and Larry A. Young. *Rotor/Wing Interactions in Hover*. Tech. rep. TM-2002-211392. NASA, 2002.

[10] Daniel A. Wachspress, Todd R. Quackenbush, and Alexander H. Boschitsch. “First-Principles Free-Vortex Wake Analysis for Helicopters and Tiltrotors.” In: *AHS 59th Forum* (2003), p. 1.

[11] Anand Radhakrishnan and Fredric Schmitz. “Quad Tilt Rotor Aerodynamics in Ground Effect.” In: *23rd AIAA Applied Aerodynamics Conference*. June. Reston, Virigina: American Institute of Aeronautics and Astronautics, June 2005. ISBN: 978-1-62410-058-1. DOI: 10.2514/6.2005-5218.

[12] Vinit Gupta and James D. Baeder. “Quad Tiltrotor Aerodynamics in Ground Effect.” In: *58th Annual Forum, American Helicopter Society*. 2002.

[13] Vernon J. Rossow. *Effect of Ground and/or Ceiling Planes on Thrust of Rotors in Hover*. Tech. rep. TM-86754. NASA, 1985.

[14] Montgomery Knight and Ralph A. Hefner. *Static Thrust Analysis of the Lifting Airscrew*. Tech. rep. TN-626. NACA, 1937.

[15] Montgomery Knight and Ralph A. Hefner. *Analysis of Ground Effect on the Lifting Airscrew*. Tech. rep. TN-835. NACA, 1941.

[16] R. R. Lynn, F. D. Robinson, N. N. Batra, and J. M. Duhon. “Tail Rotor Design Part I: Aerodynamics.” In: *Journal of the American Helicopter Society* 15.4 (Oct. 1970), pp. 2–15. ISSN: 2161-6027. DOI: 10.4050/JAHS.15.4.2.

[17] Stephen A. Conyers, Matthew J. Rutherford, and Kimon P. Valavanis. “An Empirical Evaluation of Ceiling Effect for Small-Scale Rotorcraft.” In: Institute of Electrical and Electronics Engineers Inc., Aug. 2018, pp. 243–249. ISBN: 9781538613535. DOI: 10.1109/ICUAS.2018.8453469.

[18] I. C. Cheeseman and W. E. Bennett. “The Effect of the Ground on a Helicopter Rotor in Forward Flight.” In: *Aeronautical Research Council Reports and Memoranda* 3021.3021 (1955), p. 12.

[19] Kodai Nohara, Jae Hoon Lee, and Shingo Okamoto. “Experimental Evaluation of Adhesion Plate and Development of Novel Drone Capable of Adhering to Ceiling and Wall.” In: *Proceedings - 2019 3rd International Conference on Control, Artificial Intelligence, Robotics and Optimization, ICCAIRO 2019* (2019), pp. 13–18. DOI: 10.1109/ICCAIRO47923.2019.00011.

[20] Darius J. Carter, Lauren Bouchard, and Daniel B. Quinn. “Influence of the Ground, Ceiling, and Sidewall on Micro-Quadrotors.” In: *AIAA Journal* 59 (4 Apr. 2021), pp. 1398–1405. ISSN: 0001-1452. DOI: 10.2514/1.J059787.

[21] Shijie Gao, Carmelo Di Franco, Darius Carter, Daniel Quinn, and Nicola Bezzo. "Exploiting Ground and Ceiling Effects on Autonomous UAV Motion Planning." In: IEEE, June 2019, pp. 768–777. ISBN: 978-1-7281-0333-4. DOI: 10.1109/ICUAS.2019.8798091.

[22] Przemyslaw M. Kornatowski, Mir Feroskhan, William J. Stewart, and Dario Floreano. "Downside Up:Rethinking Parcel Position for Aerial Delivery." In: *IEEE Robotics and Automation Letters* 5 (3 2020), pp. 4297–4304. ISSN: 23773766. DOI: 10.1109/LRA.2020.2993768.

[23] Jielong Cai, Sidaard Gunasekaran, Anwar Ahmed, and Michael V. Ol. "Changes In Propeller Performance Due to Ground Proximity." en. In: *AIAA Scitech 2019 Forum*. San Diego, California: American Institute of Aeronautics and Astronautics, Jan. 2019. ISBN: 978-1-62410-578-4. DOI: 10.2514/6.2019-1097.

[24] Jielong Cai. "Changes In Propeller Performance Due to Ground and Partial Ground Proximity." MA thesis. University of Dayton, 2020.

[25] Jielong Cai, Sidaard Gunasekaran, and Michael V. Ol. "Propeller Partial Ground and Ceiling Effect Prediction." In: American Institute of Aeronautics and Astronautics, Jan. 2021. ISBN: 978-1-62410-609-5. DOI: 10.2514/6.2021-0614.

[26] A. Betz. *The Ground Effect On Lifting Propellers*. Tech. rep. TM-836. NACA, 1937.

[27] **Ellande Tang** and Soon-Jo Chung. "Experimental Model of Effects of Large Upstream Obstructions on Drone Scale Propellers." In: *AIAA Scitech 2021 Forum* (Jan. 2021). DOI: 10.2514/6.2021-1648.

[28] *Ansys® Academic Research Fluent, Release 22.1*. 2022.

[29] Jorge A. Morillo and David A. Peters. "Velocity Field Above a Rotor Disk by a New Dynamic Inflow Model." en. In: *Journal of Aircraft* 39.5 (Sept. 2002), pp. 731–738. ISSN: 0021-8669, 1533-3868. DOI: 10.2514/2.3019.

[30] *Series 1585 Test Stand Datasheet*. Jan. 2022. URL: https://cdn.rcbenchmark.com/landing_pages/Manuals/Series%201585%20Datasheet.pdf (visited on 10/05/2022).

[31] W. H. Gray. *Wind-Tunnel Tests of Single and Dual-Rotating Tractor Propellers at Low Blade Angles and of Two-and Three-blade Tractor Propellers at Blade Angles up to 65 Degrees*. Tech. rep. Issue: February. 1943.

[32] John Brandt and Michael Selig. "Propeller Performance Data at Low Reynolds Numbers." In: *49th AIAA Aerospace Sciences Meeting including the New Horizons Forum and Aerospace Exposition*. January. Reston, Virigina: American Institute of Aeronautics and Astronautics, Jan. 2011, AIAA 2011–1255. ISBN: 978-1-60086-950-1. DOI: 10.2514/6.2011-1255.

[33] Honeywell. *TruStability™ Board Mount Pressure Sensors*. 2022.

[34] Rosario Lanzafame, Stefano Mauro, and Michele Messina. "2D CFD Modeling of H-Darrieus Wind Turbines Using a Transition Turbulence Model." en. In: *Energy Procedia* 45 (2014), pp. 131–140. ISSN: 18766102. DOI: 10.1016/j.egypro.2014.01.015.

[35] R. Lanzafame, S. Mauro, and M. Messina. "Wind Turbine CFD Modeling using a Correlation-Based Transitional Model." en. In: *Renewable Energy* 52 (Apr. 2013), pp. 31–39. ISSN: 09601481. DOI: 10.1016/j.renene.2012.10.007.

[36] Garrett R. McHugh. "Propulsive Effects and Design Parameters of a Wake Ingesting Propeller." PhD thesis. University of Akron, Dec. 2021.

[37] *Ansys® Fluent Theory Guide, Release 16.0, ANSYS, Inc.* 2016.

[38] Tuncer Cebeci, G. J. Mosinskis, and A. M. O. Smith. "Calculation of Separation Points in Incompressible Turbulent Flows." In: *Journal of Aircraft* 9 (9 Sept. 1972), pp. 618–624. ISSN: 0021-8669. DOI: 10.2514/3.59049.

[39] Jorge A. Morillo. "A Fully Three-Dimensional Unsteady Rotor Inflow Model From a Galerkin Approach." PhD thesis. Washington University in St. Louis, 2001.

[40] David A. Peters and Cheng Jian He. "Correlation of Measured Induced Velocities with a Finite-State Wake Model." In: *Journal of the American Helicopter Society* 36 (3 July 1991), pp. 59–70. ISSN: 2161-6027. DOI: 10.4050/JAHS.36.59.

[41] Dale M. Pitt and David A. Peters. "Theoretical Prediction of Dynamic-Inflow Derivatives." In: *Vertica* 5 (1981), pp. 21–34.

[42] K. W. Mangler and H. B. Squire. *The Induced Velocity Field of a Rotor*. Tech. rep. Volume: 2642. 1950.

[43] M. Joglekar and R. Loewy. *An Actuator-Disc Analysis of Helicopter Wake Geometry and the Corresponding Blade Response*. Tech. rep. USAAVLABS-TR-69-66. 1970.

[44] Wilhelm Kinner. "Theory of the Circular Wing." In: *Ingenieur Archiv.* 7 (1937), p. 47.

[45] Iain G. Currie. *Fundamental Mechanics of Fluids*. 4th ed. Boca Raton, FL: Taylor & Francis, 2013. ISBN: 978-1-4398-7460-8.

[46] David A. Peters and Ninh HaQuang. "Technical Note: Dynamic Inflow for Practical Applications." In: *Journal of the American Helicopter Society* 33 (4 Oct. 1988), pp. 64–68. ISSN: 2161-6027. DOI: 10.4050/JAHS.33.64.

[47] Zhongyang Fei. "A Rigorous Solution for Finite-State Inflow throughout the Flowfield." PhD thesis. Washington University in St. Louis, 2013.

[48] Jianzhe Huang, David A. Peters, and J. V. R. Prasad. "Converged Velocity Field for Rotors by a Blended Potential Flow Method." In: *GSTF Journal on Aviation Technology* 1.2 (Mar. 2015). ISSN: 23825758, 2382591X. DOI: 10.5176/2382-5758_1.2.8.

[49] Jianzhe Huang. "Potential-flow Inflow Model Including Wake Distortion and Potential-flow Inflow Model Including Wake Distortion and Contraction." PhD thesis. Washington University in St. Louis, 2015.

Chapter 3

FORCES ON A DRONE PROPELLER IN FORWARD FLIGHT

3.1 Introduction

Many urban aerial mobility concept vehicles and prototypes feature a configuration wherein lifting rotors provide the vehicles lift until it is able to produce enough forward speed to generate lift with only the wings. In this configuration, early experimental results suggested that there is a component of force that is often ignored that significantly affects the efficiency of the craft. Specifically, generation of lift by a rotor in forward flight is accompanied by a drag component large enough to be significant in the context of the craft's energy consumption. A diagram of the forces can be seen in Figure 3.1, with the force in question being the rotor drag H.

Aircraft that are in a "quadplane" configuration typically have several different flight regimes. These craft typically need to go from some form of hover state to their fixed wing flight condition. The intermediate between these two states is a transition region where the aircraft is using lifting rotors to provide partial lift while increasing forward flight speed. Although less common, some eVTOL concepts also choose not to transition fully to forward flight and instead only use a lifting wing to contribute to the lift [1]. There is also the possibility that the vehicle will choose to travel in multirotor mode for short distances rather transitioning fully to forward flight. A vehicle that is trying to hover in place might also have to counter disturbances such as wind, and the additional drag from rotors could potentially factor into the vehicle dynamics. Foremost however is that energy expenditure is always a relevant concern with aerial vehicles, given the limits of current energy storage technologies. Range and flight time is a significant limitation for many VTOL concepts at present. As Urban Air Mobility concepts gain popularity, even small improvements to the energy efficiency can be significant for increasing the viability of the designs.

Prior Work

Several models appear for rotors in forwards flight [2]. The most basic of these, momentum models that are extensions of disk actuator theory, do not account for the rotor drag. This is because these models assume the forces a priori and solve for other parameters based on that condition. Momentum models are thus not very effective for determining the rotor drag. Nevertheless, the rotor drag has been

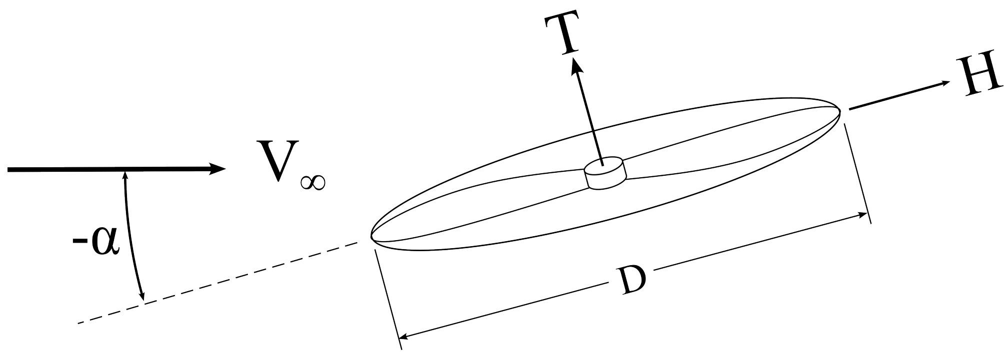

Figure 3.1: Diagram of forces on a propeller in forward flight.

previously considered in other rotorcraft models. A typical means of estimating the forces on a rotor is to compute its performance using Blade Element Theory (BET). This theory calculates the forces by abstracting the rotor blade as a series of aerodynamic sections, and computing their forces based on local flow conditions. The results are then integrated along the blade to produce the aggregate forces by the rotor. An example from Johnson [3] of an expression to calculate the rotor drag is

$$\frac{C_H}{\sigma a} = \int_0^1 \left\{ \sin(\psi) \left[\frac{1}{2}(u_P u_T \theta - u_P^2) + \frac{c_d}{2a} u_T^2 \right] - \beta \cos(\psi) \left[\frac{1}{2}(u_T^2 \theta - u_P u_T) \right] \right\} dr \tag{3.1}$$

where

$$u_T = r + \mu \sin \psi \tag{3.2}$$

$$u_P = \lambda + r\dot{\beta} + \beta \mu cos\psi \tag{3.3}$$

$$\beta = \beta_0 + \beta_{1c} \cos \psi + \beta_{1s} \cos \psi + \beta_{2c} \cos 2\psi + \beta_{2s} \cos 2\psi + \dots \tag{3.4}$$

$$\theta = \theta_0 + \theta_{tw} r + \theta_{1c} cos\psi + \theta_{1s} sin\psi \tag{3.5}$$

where σ is blade solidity, β is the angle associated with blade flapping, μ in plane advance ratio, λ is inflow advance ratio. This model assumes linear twist, constant chord, small angle approximations, and uniform inflow. The assumptions do not apply well to propellers at the drone scale, meaning that much of the theory geared towards helicopter aerodynamics may not be strictly applicable.

The assumption of a uniform inflow is also a large simplifying assumption. Multiple inflow models exist in the literature and the choice is a significant factor in accurate rotorcraft modeling. The choice of inflow model also creates a coupled problem, where the forces from the rotor affect the aerodynamics and a closed form solution is not guaranteed, requiring numerical iteration. A more modern inflow model is the Peters and He inflow model [4], which is a dynamic inflow model that uses a pressure jump profile to compute the induced flow at the rotor disk. Implementing this model analytically is impractical, and it is typically implemented numerically. Additionally, an accurate model requires the blade geometry be known. In the past, this has not been always been available or convenient to acquire, but Chapter 4 of this work details an accessible technique to produce this. BET requires a high amount of detail for work in multirotors. While it may be practical in rotorcraft where the specifics of the main rotor are likely well known and quantified, it is less practical for work with multirotors where propellers typically come off the shelf with few technical details. Furthermore, the integrated expression is not necessarily succinct or in a format conducive to robotics controls work.

A numerical implementation of BET might still not be sufficient. As will be shown in Section 3.5, a Vortex Particle Method (VPM) simulation, which is effectively a BET solution using the Vortex Particle Method to propagate the wake and compute the inflow velocity, does not accurately predict the rotor drag force. Furthermore, in terms of developing a control algorithm, a likely process might be to tabulate numerical results computed from such a method and fit a function that is more compatible with control theory. This means that a BET model would not be directly used in a controls or dynamics model, instead being pre-computed.

Several previous works have examined and quantified this force while evaluating rotors, or recognized this force as a component in the overall forces a rotor experiences. One work [5] provide raw quantification for a Graupner E-prop 9×5 propeller in the full 0 to 180 degrees of inflow angle. It is a good collection of raw data, but there is little insight presented in the propeller. There are several older works that recognize the existence of the force as well. NACA and NASA also collected data on the side force while investigating and developing early tiltrotor concepts. Reports by Ribner [6, 7] are geared towards propellers in axial forward flight. The reports note that the side force on the propeller causes it to act like a fin in the context of the vehicle dynamics. Drape and Kuhn [8, 9] examine a propeller wing combination and even identify the propeller drag specifically as the "propeller normal force." However, they spend little time discussing the force and are mostly concerned with the pitching moment associated with the propeller. Yaggy [10] quantifying and compiles the force, but is still mostly a data compilation work. Because of the scale, the Reynolds numbers involved are also much larger than those associated with small multirotors, putting its scalability into question. One work runs simulations and experiments for rotors in off-nominal conditions but do not explicitly focus on the impact of the force, focusing on the change in thrust and power consumption inf forward flight [11]. Another recognizes the existence of rotor drag in a coaxial arrangement, but does not provide a clear model and is more concerned with rotor failure [12]. Work that has sought to specifically identify or quantify this force at the multirotor scale includes work by D'Andrea [13], which combines BET and Blade Element Momentum Theory (BEMT). The work reduces the required parameters to just a few parameters which are fit experimentally.

While the above demonstrates that there does exist a body of work describing rotor drag, it is not necessarily in a format that is convenient. Experimental data is typically specific to a particular propeller with little generalization. Work that does describe the force from a theoretical perspective does so using some form of BET, so the expressions are typically unwieldy. As an alternative, this work seeks to use a variation of the model shown in [14]. This model is dimensionally derived, and simple enough to be suitable for use to develop a control law for a VTOL aircraft.

Contributions

This work seeks to further develop a low-order model that describes the rotor drag and evaluate its efficacy on a variety of propellers. The contributions of this work are the following:

- Experimental data quantifying the rotor drag for a selection of propellers. An experimental setup is used to collect data from a selection of propellers. The propeller thrust, drag, and torque are measured for various propeller Rpm, freestream Velocities, and angles of attack.
- A dimensionally derived fit to the experimental data. By examining trends in the experimental data and utilizing dimensional analysis, a model is derived. This model is then applied to the experimental data and the coefficients associated with the model are compared between the various propellers. The results show that the power and angle of attack coefficients associated with the various propellers tested are similar to one another. The side force coefficient however is far more variable between the various propellers, being more akin to a drag coefficient that describes the relative efficacy of various bodies.

- Vortex Particle Method simulations for comparison. As simulation is an important tool in modern engineering, a mid-fidelity analysis tool called DUST is used to simulate experimental cases. The simulation uses a VPM representation to propagate the wake as well as a surface panel representation of the propeller blades to compute the forces. The simulation results are compared directly to the experimental results for a limited number of cases, as well as to the remaining experimental data by fitting the low order model to the simulation data and comparing the coefficients. The results show that while simulation predicts the propeller thrust and torque quite well, it significantly underpredicts the rotor drag.

Organization

This work is organized into four parts. Section 3.2 first outlines the lower order model used to model the force. Section 3.3 then describes the setup used to collect experimental data as well as the derivation for the model that will be used to fit the data. It also describes steps taken experimentally to ensure data was solely for the associated propeller. Section 3.4 then compiles the experimental results and applies the fit to the data. The results are compared for the propellers and discussed. Section 3.5 covers the implementation and results of applying DUST to the problem. The section shows the convergence of the simulation with various simulation parameters to verify that the implementation is done correctly. It then compares the results by evaluating the model and comparing the results. Because of the discrepancies between the simulation and the experimental data, potential sources of error are discussed.

3.2 Theory: Non-Dimensional Analysis

One approach to describing the side force in forward flight is to examine the problem with Non-Dimensional analysis. To do this, we examine the relevant variables of the problem, consider the assumptions, and attempt to match the dimensionality of the variables in a physically intuitive manner.

variable	dimensions	description
ρ	M L^{-3}	fluid density
D	L	Rotor diameter
ω	T^{-1}	rotor rotation speed
V_∞	L T^{-1}	forward flight speed
α	none	angle of attack
H	M L T^{-2}	rotor drag

It is known that there will be some dependence on the angle of attack α and it will factor into our expression, but as it is dimensionless it will not be considered in the dimensional analysis. There are thus 5 relevant dimensional variables and 3 dimensions to consider, resulting in 2 dimensional groups. The first quantity is one that is typical in rotorcraft, the advance ratio. This is composed of the ratio between the freestream and rotor tip velocities

$$\mu = \frac{V_\infty}{\omega D/2}. \tag{3.6}$$

The second non dimensional expression must involve the remaining variables, so we see that this can be formed using

$$\frac{H}{\rho\omega^2 D^4} \tag{3.7}$$

which is a typical method of non-dimensionalizing the force in rotorcraft theory. Note that, as represented by the advance ratio, ωD and V are able to be interchanged dimensionally in expressions. Doing so for the second value results in a drag non dimensionalization analogous to that used in aircraft, with a V^2 and area style term. If the additional force associated specifically with the propeller rotating rather than simply its static drag is being considered, the force is expected to disappear at $V = 0$ and $\omega = 0$. There is also expected to be some dependence on the angle of attack α. We can represent the expected expression relating the quantities with generic functions f and g as

$$\frac{H}{\rho\omega^2 D^4} = C_H f\left(\frac{V_\infty}{\omega D/2}\right) g(\alpha) \tag{3.8}$$

with a nondimensional rotor drag parameter C_H. Further insight for determining what form the dependence on advance ratio and angle of attack takes is studied by collecting experimental data.

3.3 Experimental Setup

In order to develop the model, experimental data on a selection of propellers were collected and analyzed. To collect the data, various propellers were placed in front of the Center for Autonomous Systems and Technologies (CAST) Fan-Array Wind tunnel on a force measurement test stand. The Fan Array Wind Tunnel was first characterized to quantify the velocity it produced. The propeller force stand was then calibrated, and steps were taken to isolate the force solely associated with the propeller by quantifying extraneous sources of drag.

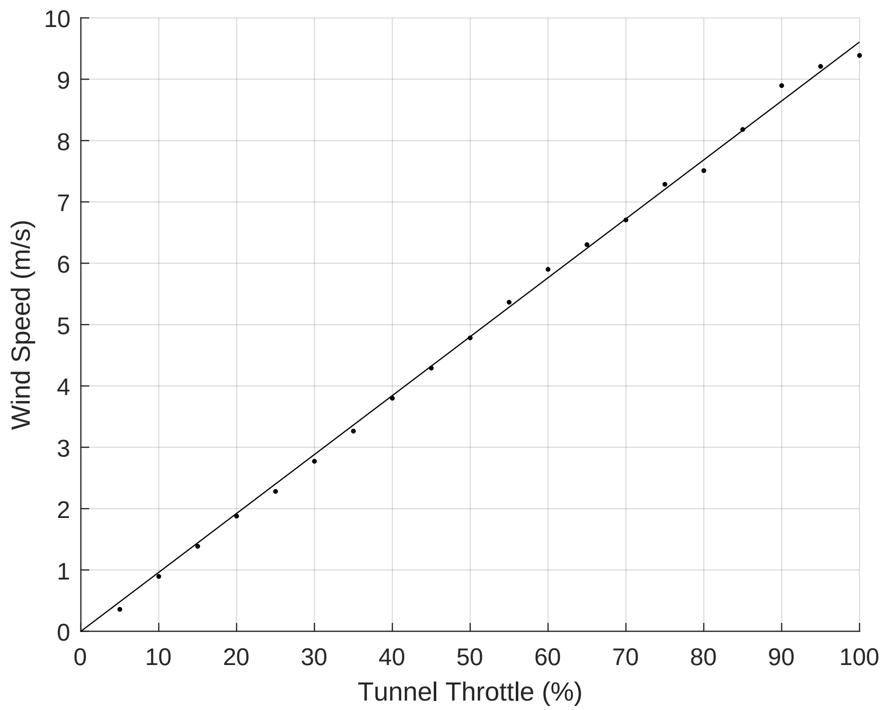

Figure 3.2: Measured flow speed versus tunnel throttle for a 13-by-13 array of fans.

Wind Tunnel Characterization

Testing was conducted in front of the CAST fan array wind tunnel. As the Fan Array has the capacity to selectively control which fans are operating, it was decided to conduct the bulk of the experiments using less than the full array of fans. Doing so would reduce the power consumption of the array as well as the acoustic noise. It was desired to quantify how little of the fan array could be used to produce viable results. To do so, data were collected with different array sizes, both drag data of a test article and wind speed data from a handheld anemometer. Array arrangements were squares of various sizes, with the same throttle signal sent to all fans within the square. Example data for one array size can be seen in Figure 3.2. From the data, we see that measured wind speed is quite linear with the input throttle to the tunnel. The linear fit applied to the data is also shown. The fit in question is based on the assumption that the wind speed has a linear relationship with the tunnel throttle, and that the y-intercept of the line is 0. That is, the wind speed is 0 when the throttle is 0. By collecting data of the flow speed versus the tunnel throttle and performing a linear fit for each of them, we can compile and compare the calculated slopes of each curve. The result is shown in Figure 3.3.

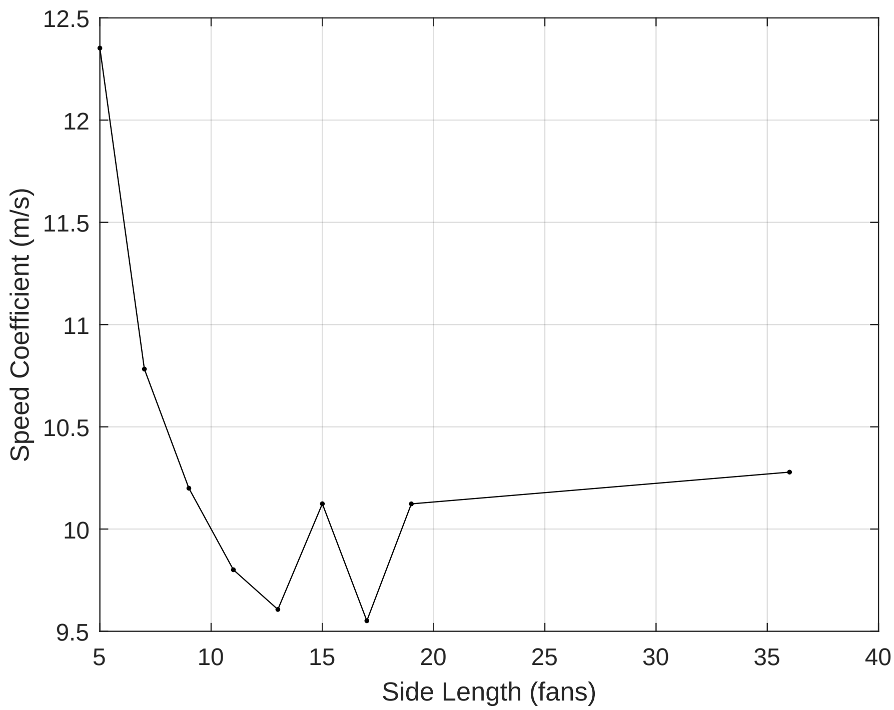

Figure 3.3: Calculated curve slopes for various array sizes.

We see that there is a significant variation in the speed of the flow produced by the tunnel as the size of the array changes. At a size 13 array and below, the tunnel appears to form a continuous curve, however the measurements for the size 15 and 19 arrays appear to deviate significantly from the expected curve. A measurement of the full array, taken for comparison, also appears to deviate from this curve. This variability is likely related to the position of the sub-array square within the greater Fan Array, and is likely related to environmental factors such as proximity of the square to the ground, nearby walls, or to the edge of the fan array.

Array size was measured assuming that the article in question was centered around a single fan. With the exception of the tests run using the entirety of the array, the array pattern used was a square centered on the measured position of the test article. The results can be shown in Figure 3.4. Here we see that the measured drag on the object, the T-motor U3 motor with a T-motor 12×4 inch propeller in this case, changes substantially based upon the area of the fan array used. Note that, because of the branding, propellers will typically be referred by the name of the supplier followed by the diameter and pitch in inches. For instance, the T-motor 12×4 propeller is made by T-motor with a 12-inch diameter and 4-inch pitch. For smaller array areas, we see that there is a dramatic dropoff in the measured drag, most

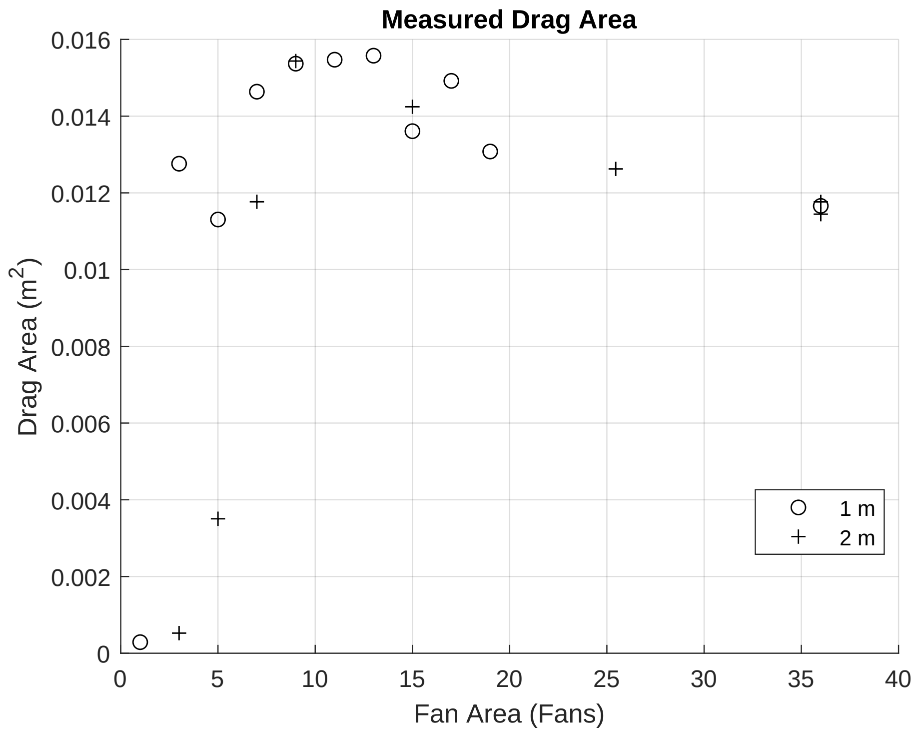

Figure 3.4: Comparison of Measured Drag Coefficients of a test object at different distances from the Fan Array.

likely because the envelope of the flow is not large enough to fully encompass the propeller and motor in a uniform flow region. For fan areas above the region where the flow envelope is too small, we see a significant change in the measured drag. Furthermore, the measurements at a distance or 2 meters from the array indicate that the drag drops off at a smaller array size than when measurements were taken at 1 meter. For the subsequent experiments, we chose to use the 13-by-13 array with the test article positioned 1 meter from the array. These conditions provided a flow region that were sizeable enough to produce meaningful drag data while only using roughly 13% of the fan array.

Propeller Test Stand

Forces were measured on an RCbenchmark 1585 test stand [15]. The stand measures the propeller thrust and torque through the use of 3 load cells, one for thrust, and 2 spaced apart for torque. The propeller test stand includes a user friendly software package that streams data from the various sensors on the test stand and is able to run scripts stepping the installed motor to various throttles while logging and writing the data to csv format files. The software also has a calibration procedure that walks

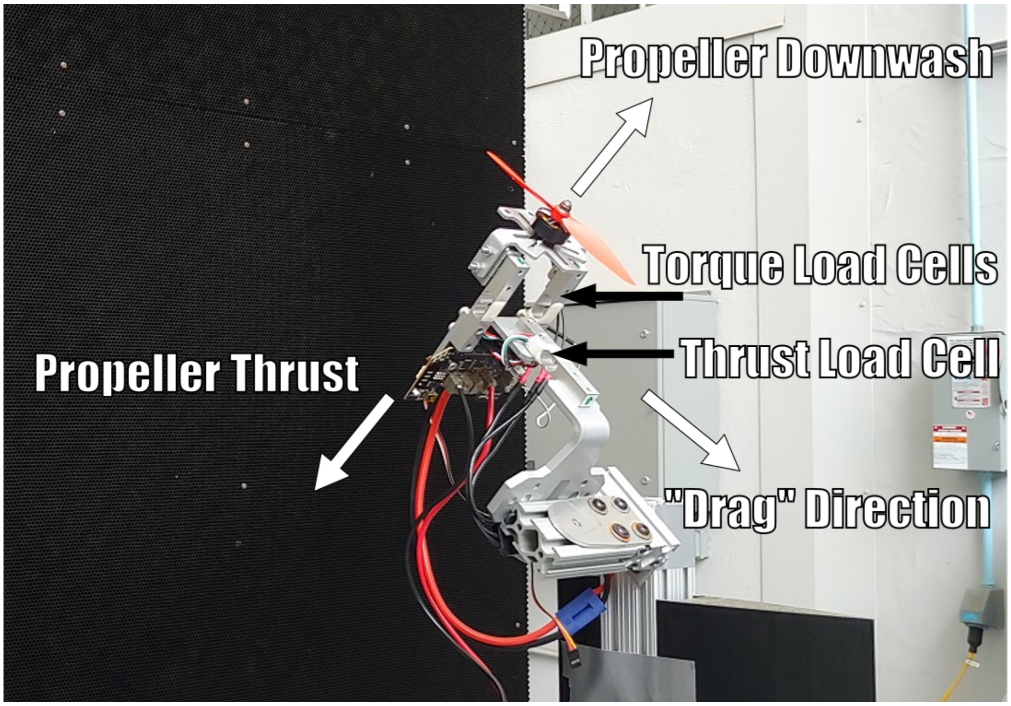

Figure 3.5: Picture of the experimental setup in front of the CAST Fan Array Wind Tunnel.

the user through applying the included calibration weight at various positions to produce a calibration matrix for the sensor and translate the load cell measurements into force and torque values. While the packaged software does not output rotor drag, the user is able to measure this value by reading the exported load cell values and applying their own calibration.

An annotated picture of the experimental setup can be seen in Figure 3.3. A diagram of the forces was shown in Figure 3.1. Here we see the thrust T and the rotor drag designated as H per Johnson which are aligned with the rotors frame of reference. The angle of attack convention used in this work is a multirotor-centric definition, where pure edgewise flow is defined as 0 angle of attack and a negative angle of attack would correspond to the thrust vector being inclined forward into the freestream.

Motor Drag Measurements

In order to analyze the effect of the the rotation of the rotor on it's measured force, measurements were taken of the relevant motors by themselves in various wind conditions. Furthermore, when force data of the propellers were collected while the propeller was not rotating, it was done at the position with the propeller in line with the freestream flow to minimize the experienced drag and provide a good tare condition. As the static position of the propeller was subject to the resting positions of the magnetic poles of the motors, some positional inaccuracy was present.

In order to quantify the effect that solely the rotation of the propeller has on the measured component of force, we subtract any additional sources of drag such as that of the motor. To do so, we measure the drag of the motor at the same test conditions and subtract it out from subsequent measurements. As the data are collected at different times, there needs to be compensation for the change in atmospheric conditions. The side force associated from propeller motion is thus

$$H = F_{\text{measured}} - F_{\text{motor}} \frac{\rho_{\text{measured}}}{\rho_{\text{motor}}} \tag{3.9}$$

3.4 Propeller Drag Results

The experimental data collected provided sufficient information to further refine the low order model described in Section 3.2. Trends or commonalities observed in the propellers can then be noted and discussed.

Initial data and development of an expression

Initial studies on the problem looked extensively at the forces produced by a King Kong 6X4P 2-bladed propeller mounted to a T-Motor F-80 Pro Brushless DC motor in forward flight to derive some understanding of what the modeling would look like and understand how the non-dimensional quantities interacted with the side force. One propeller was studied extensively, with a large sample of angles of attack, freestream velocities and rotation speeds. What was found when the effect was studied using the non-dimensional terms described in Section 3.2, was that at fixed angles of attack there appeared to be a power relationship between the advance ratio and the non-dimensionalized side force. This can be observed in Figure 3.6, where we see a slight, nonlinear relationship between the two. We note that, based on the shown selection, there is a dependence on angle of attack as well.

While the two non-dimensional quantities described in Section 3.2 do function as valid variables for plotting and analysis, slight variations were made based on practical considerations with the data. In testing, the velocity was held at a small set of fixed values in contrast to the angular velocity which varied considerably throughout the tests, even at the same throttle as the battery used ran down. As a result, there were several datapoints in the experimental data with values of ω that were relatively small, creating near singularities and excessively large values of the advance ratio. To combat this, one can either filter out datapoints with lower values of angular velocity, or use the reciprocal of the advance ratio. For fitting the results, the latter option was used. Placing the rotation speed in the numerator allows for data values to approach 0 continuously with the variety of rotation speeds measured in experiments. The reciprocal of the advance ratio is also called the Tip Speed Ratio in Wind Turbine literature and is sometimes represented by the symbol λ. A similar concern arises for the non-dimensionalization of the rotor drag, so V is used in place of ωR. As values of V were highly discrete values in these experiments, it was simple to remove datapoints that would be problematic in analysis, in particular ones where $V = 0$ and the rotor drag has an expected value of 0. A sample of this can be seen in Figure 3.6. In addition to showing how that data collapse to the same curve using the chosen parametrization, it also highlights that the curve changes based on the angle of attack of the propeller. The angle of attack is dimensionless, so it did not factor into the dimensional analysis of the problem, but there is clearly a dependence. This is further shown in Figure 3.7.

To model this dependence, we consider some assumptions. By symmetry, it is expected that there will be no rotor drag at ± 90 degrees angle of attack. The data shown in Figure 3.7 also show a slight asymmetry, such that the maximum of the force does not occur at 0 degrees. To model these features, the relation with angle of attack was modeled with the minimum power polynomial possible: cubic with roots at $\pm\frac{\pi}{2}$ radians. With these changes, the expected model used for fitting is thus represented by the following equation

$$\frac{H}{\rho V^2 D^2} = C_H \left(\frac{\omega D/2}{V}\right)^{C_n} \left(\left(\frac{\pi}{2}\right)^2 - \alpha^2\right)(\alpha - C_a) \tag{3.10}$$

This equation can be converted back into the previous form seen in Eq. 3.8 by rearranging variables slightly. The coefficients will change slightly as a result.

Comparison of results across propellers

Figures 3.8, 3.9, 3.10, 3.11, 3.12, and 3.13 show the experimental data and fits for a selection of propellers. Though the magnitude varies, the shape of the data is similar across different propellers. We also see fitted surface in the plots to illustrate the fit of the model to the experimental data. The fit coefficients are compared in Figures 3.14, 3.15, and 3.16 along with 95% confidence intervals for each of the parameters. We see that, across the majority of the propellers tested with the exception of the APC 10×4.7, the fitted constants C_a and C_n are very similar. This suggests that these constants might be tied more to the physical nature of the

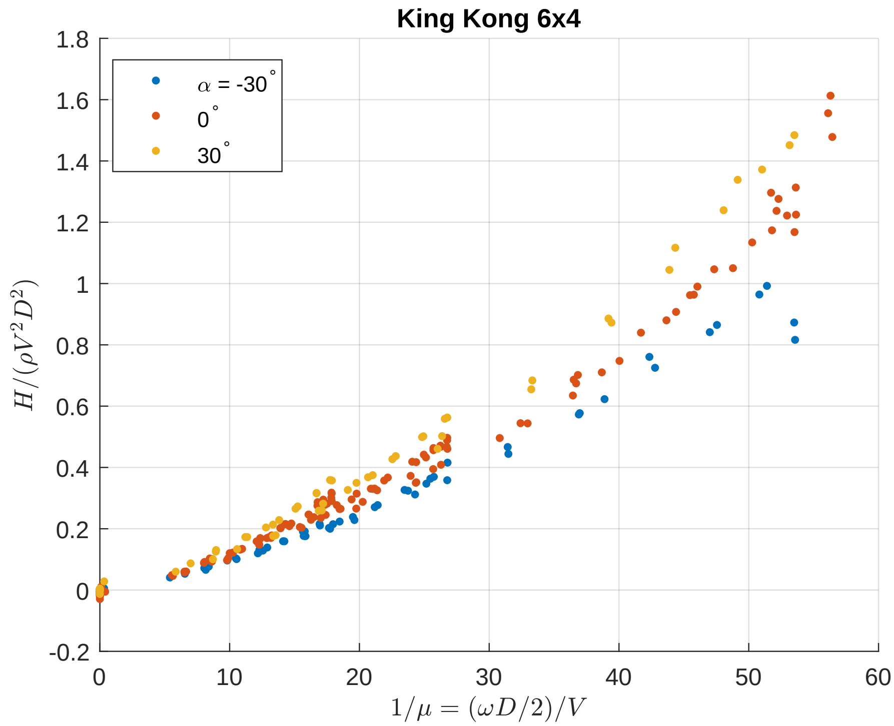

Figure 3.6: Sample data showing relationship between non-dimensional quantities and change based on angle of attack.

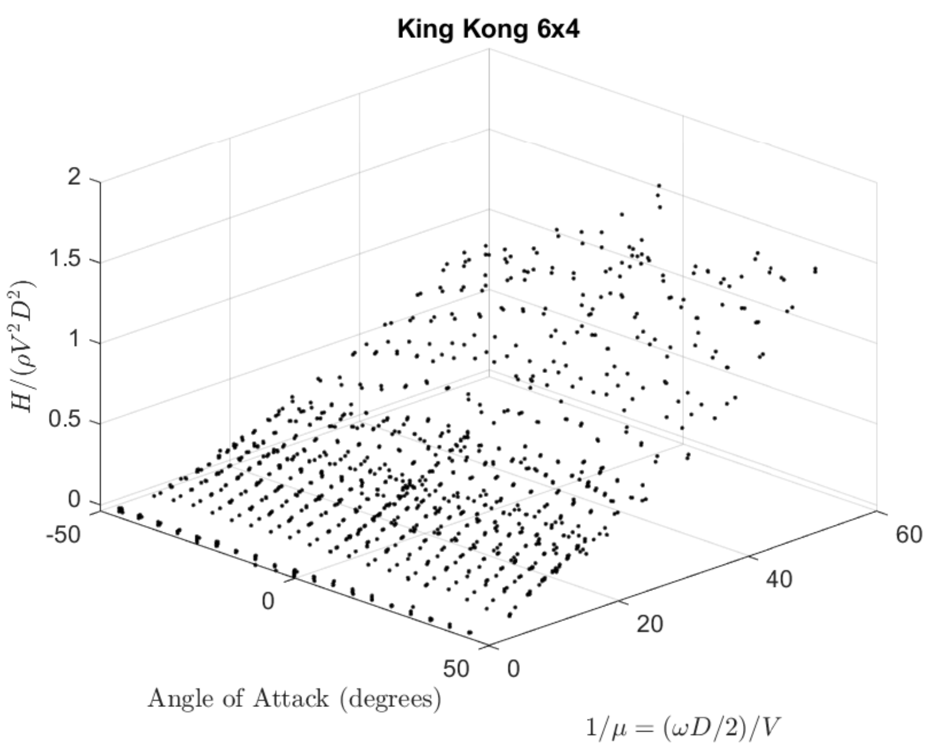

Figure 3.7: Data for a propeller showing the change in Rotor Drag based on angle of attack and advance ratio.

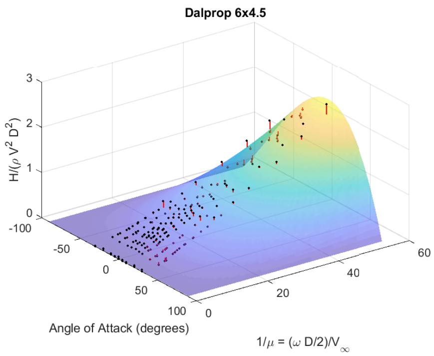

Figure 3.8: Data and fit for rotor drag of a Dalprop 6x4.5 propeller.

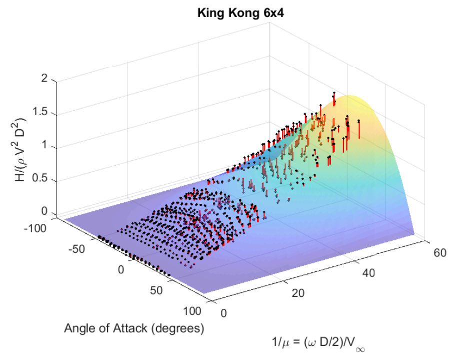

Figure 3.9: Data and fit for rotor drag of a King-Kong 6x4 propeller.

phenomenon rather than the specific design of the propeller. In contrast, the constant C_H varies significantly by propeller. This suggests that C_H is more representative of the quality of the propeller design for this performance metric, analogous to the drag coefficient for aerodynamic bodies. The confidence intervals also lend some insight into the parameters. The intervals for the power parameter C_n for instance are very small relative to the value. The other parameters have intervals that vary in size with propeller. The APC 10 inch propeller has a fairly large interval for its angle of attack parameter, which is substantially larger in value than those of the other propellers. Figure 3.17 shows the result of the adjusted R^2 value for each of the fits. The fit is quite good, being above 98% for all the propellers studied. The Adjusted R^2 value of the fit is computed as

$$\mathrm{Adj}R^2 = 1 - (1 - R^2)\frac{n-1}{n-p} \tag{3.11}$$

where n is the sample size, p is the number of variables in the model, and R^2 is the coefficient of determination computed by

$$R^2 = 1 - \frac{\sum_i (y_i - f_i)^2}{\sum_i (y_i - \overline{y})^2} \tag{3.12}$$

where y_i is the ith sample data point, f_i is the predicted value, and $\overline{y}$ is the mean of the sample points.

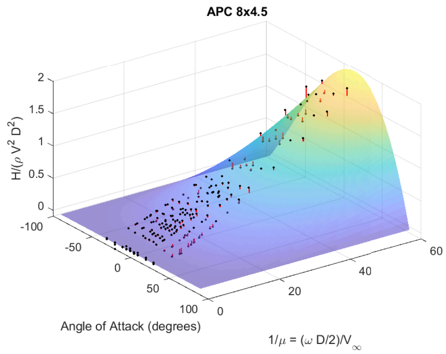

Figure 3.10: Data and fit for rotor drag of an APC 8x4.5 propeller.

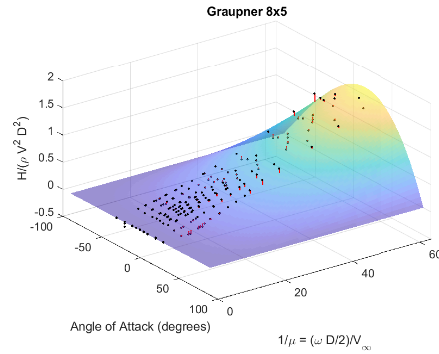

Figure 3.11: Data and fit for rotor drag of a Graupner 8x5 propeller.

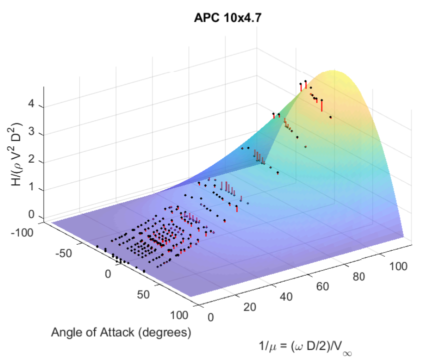

Figure 3.12: Data and fit for rotor drag of an APC 10×4.7 propeller.

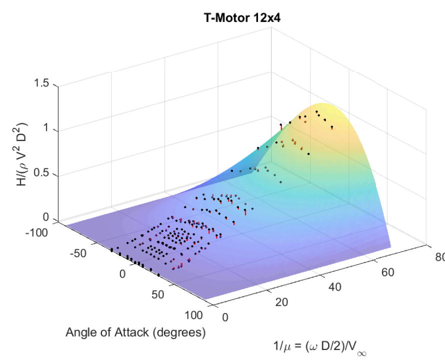

Figure 3.13: Data and fit for rotor drag of a T-Motor 12×4 propeller.

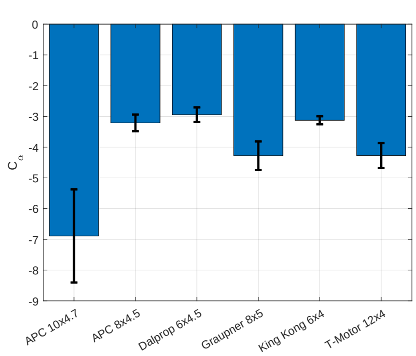

Figure 3.14: Angle of attack parameter with 95% confidence intervals.

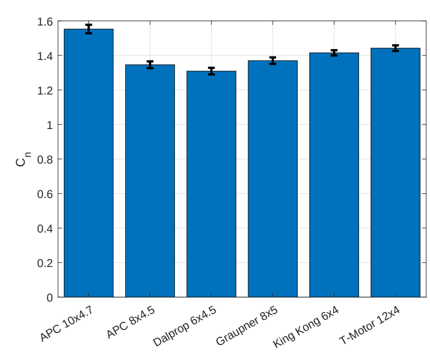

Figure 3.15: Advance ratio power parameter with 95% confidence intervals.

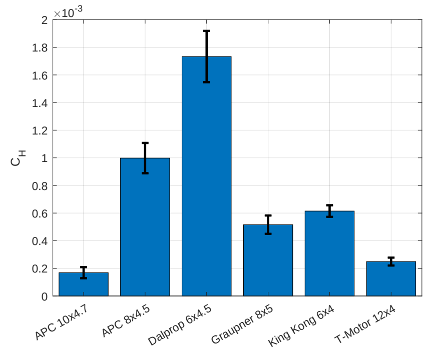

Figure 3.16: Rotor drag parameter with 95% confidence intervals.

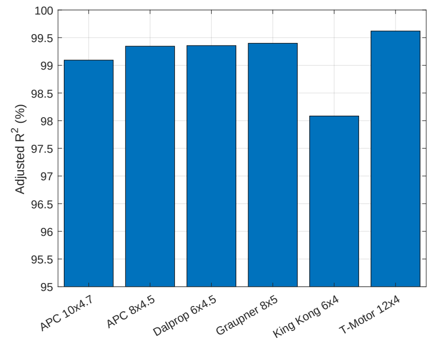

Figure 3.17: Adjusted R^2 values of fits for each propeller.

Lift-to-drag

Relevant for the design of aircraft is the comparison of the rotor-drag produced to the thrust generated. In forward flight, this is analogous to the Lift-to-Drag ratio. Using the models developed, this ratio can be computed analytically. Assuming level flight with 0 aoa, we examine the ratio for a single propeller, with the expectation that this result can be extrapolated to the rest of a vehicle.

$$\frac{T}{H} = \frac{C_T \rho \omega^2 D^4}{C_H(\rho V_\infty^2 D^2)\left(\frac{\omega D/2}{V_\infty}\right)^{C_n}(\pi/2)^2(-C_a)} \tag{3.13}$$

$$= \frac{C_T}{C_H} 4 \left(\frac{V_\infty}{\omega D/2}\right)^{C_n - 2} \frac{1}{(\pi/2)^2(-C_a)} \tag{3.14}$$

with the value of n generally in the vicinity of 1.3 in experiments, the ratio has a power law relationship with the advance ratio. This equation can be seen applied to fits from the various propellers studied in Figure 3.18. While not tremendous, at typical drone conditions, it can be significant. Full size rotorcraft like helicopters typically operate below an advance ratio of 0.7 where compressibility and sonic effects become a concern. To estimate a typical advance ratio range for the drone scale, we use the rule-of-thumb and assume the propeller is operating at its maximum safe rotation speed. The tip speed will then be

$$\frac{100000 \text{ rpm/in}}{(D/.0254) \text{ in}} \frac{1}{60 \text{ min}} 2\pi \frac{D \text{ m}}{2} \approx 133 \text{ m/s}. \tag{3.15}$$

Flight speeds from 0 to 30 m/s would correspond to advance ratios of 0 to .226. At this maximum advance ratio, the thrust-over-drag ratio could be as high as 15, but could also be as low as 2 from the propellers studied. This would highly limit the maximum effective lift-over-drag of the vehicle in either case, as the ratio for

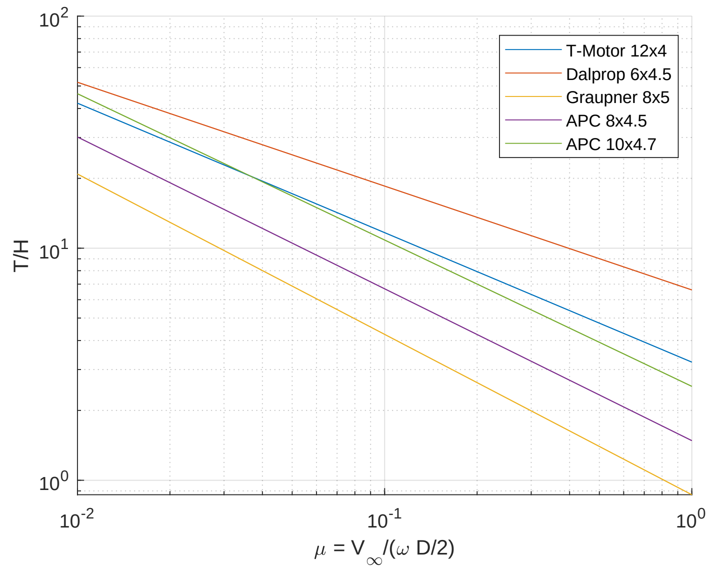

Figure 3.18: Model derived thrust over drag ratio vs advance ratio.

the vehicle could not exceed the thrust-over-drag ratio if all the lift is derived from the propeller, and would likely be lower in that case as the vehicle body would also contribute to the drag.

3.5 Simulation

Much modern vehicle design is done using simulation. In order to evaluate whether this effect is well captured by current simulations, the experimental effects are compared to results from a mid-fidelity Vortex Particle Method called DUST [16]. DUST is able to simulate aerodynamic bodies either through a lifting line representation, vortex lattice elements for lifting surfaces, or surface panels for solid bodies. The simulations shown in this work use surface panels to represent the bodies studied. As all the relevant bodies are lifting surfaces though, a lifting line representation should also be valid. Surface panels are modeled using a piecewise uniform distribution of doublets and sources [17]. Because the shed vortex particles make the velocity field not irrotational, forces on the surface panels are calculated using the solution of a Poisson's problem per [18] rather than Bernoulli principles. DUST has been evaluated against existing experimental and CFD data for the XV-15 tiltrotor as a representative case for propeller wing interactions, and good agreement is found in [19, 20] relative to [21]. Observations in [20] note that the representation of the propeller accurately predict the thrust (<5% error), but underpredict the torque by about 6-8%, while surface panel representation of the wing has good prediction of the lift (<10 % error), but a significant underprediction of drag, near 30% for the wing in isolation. There are several potential explanations for the underprediction that may be relevant to subsequent investigations. It is noted in the theory section of DUST that the panel method uses doublets and sources to formulate the velocity potential. This implies that the solution for an arbitrary body would not include viscous effects, and that calculated drag would be produced primarily from the induced drag experienced by a body and would neglect viscous drag as well as be unable to compute separation effects. This could be circumvented by using the correct airfoil polar for the airfoil sections representing the propeller blades or wing, but it is not guaranteed that experimental data exists. The simulations run using the panel method to represent the geometry as a point of reference, as it does not rely on airfoil polars, instead being handled entirely internally by the simulation. While this will introduce error in the simulated results, particularly with regards to drag, it removes the uncertainty of airfoil section modeling from consideration. This was also considered to be representative of a standard workflow to simulate a propeller, and a worthwhile comparison to evaluate the simulation accuracy. To present the results of the simulation, Section 3.5 first discusses the relevant Reynolds number and how it might affect the simulation results. Section 3.5 then covers the steps taken to ensure that the simulation was run at sufficient resolution to be valid. The presentation and discussion of the simulation results then follows.

Blade Reynolds Number

One distinction of propellers at the scale used in most commercial multirotors is that they are often operating at relatively low Reynolds number. The Reynolds number is defined as the ratio of inertial to viscous forces, and is typically computed as

$$\mathrm{Re} = \frac{\rho l V}{\mu} \tag{3.16}$$

where ρ is the air density, l is a representative length, V is a representative fluid velocity, and mu is the dynamic viscosity. For this, we use the kinematic viscosity $\nu = \frac{\mu}{\rho}$, which at 1 atmosphere and 20 degrees Celsius is approximately 1.5e-5 m^2/s. To estimate the Reynolds number for the propellers studied, we use the local tangential velocity $V = \omega r$, and the local chord c. The maximum expected RPM of a propeller varies by design, but generally scales inversely by diameter. From experience, the author's rule for maximum RPM while running experiments is $\mathrm{RPM}_{\mathrm{max}} = 100000/D$. Plotting the expected Reynolds number at this maximum rotation speed can be seen in Figure 3.19. From the plot we see that the maximum

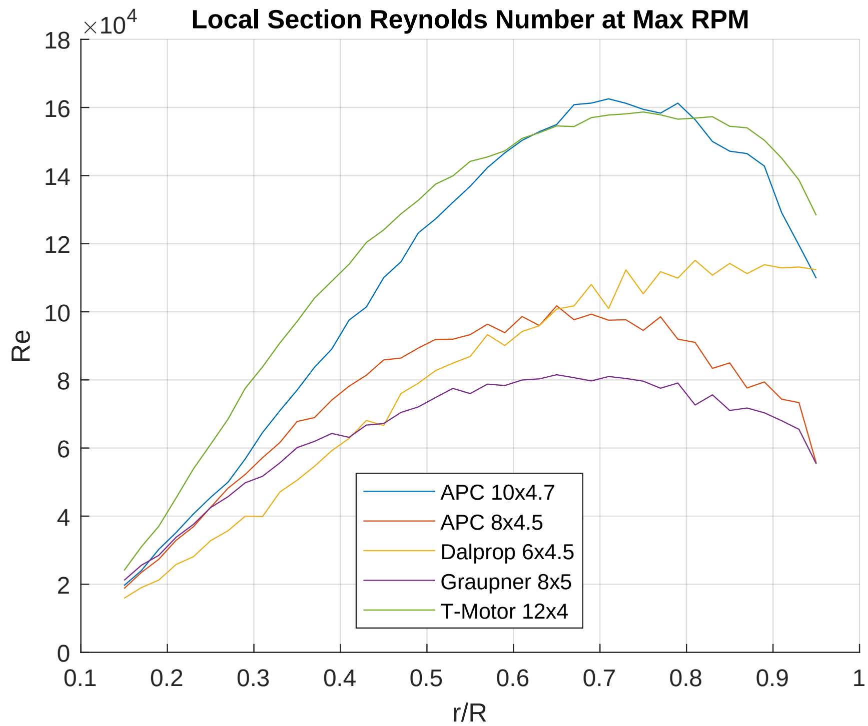

Figure 3.19: Estimate of Reynolds number on various propellers in hover conditions at the maximum propeller RPM.

expected Reynolds number across the tested propellers is less than 2×10^5, and that several of the propellers have values that are near or below 1×10^5. Because this is the maximum, much of the experimental data of the propellers will be collected when the the Reynolds number across the blades is even lower. One issue with this is that the performance of airfoils can change significantly below a Reynolds number of 8×10^4 [22]. Airfoils that normally perform well above this Reynolds number can perform very poorly and vice versa. This is a potential source of error in modeling and simulation. Much of the airfoil data that is easily available [23] is for Reynolds numbers greater than 1×10^6. Data for a wide variety of airfoils at the lower Reynolds numbers expected at the drone scale is less centralized and rarely guaranteed to exist. Variability of performance with Reynolds number also means that existing data might change significantly with circumstance or even exhibit dynamic responses that are poorly captured by steady state lift drag polars but would come into play in the periodic nature of propeller flows. The results of typical airfoil analysis programs such as XFOIL also become less accurate at Reynolds numbers these low, meaning simulation results for airfoil section are not necessarily accurate.

Simulation Verification

As a factor in using simulations, the accuracy is evaluated with respect to various simulation parameters. While a significant factor in the Vortex Particle Method is normally the number of particles, this will not be explicitly studied because of how DUST steps the simulation. The relevant simulation parameters studied with respect to modeling a rotor are the length of time of the simulation or, equivalently, the number of revolutions, the angular change of the rotor between time steps, and the number of elements representing the geometry of the blade.

DUST operates by shedding a particle from a lifting surface at each time step from the trailing edge of each section of the simulated bodies. This means that the number of particles by the end of the simulation is directly related to the number of time steps and is controlled by the aforementioned parameters. The length of time that a simulation is run expected to affect the solution because it is directly related to the calculation of a fully developed wake. Similarly, the time step resolution is relevant because it affects whether the wake is captured in sufficient detail, as well as the changing forces on the rotor blade over the course of a revolution. Because simulations are run at a variety of different rotation speeds, the number of steps per rotation was chosen over the length of time step as the preferred parameter. This translates well between different cases and leads to the number of propeller revolutions being the relevant simulation time metric while examining convergence.

In the surface panel representation chosen for this work, the propeller is defined by a choice of the number of chordwise panels, and the number of spanwise sections. These each improve the represent the geometric representation of the propeller in their respective directions. The spanwise resolution has the additional effect of increasing the number of particles in the simulation, as particles are shed from the trailing wake of each section at each time step. This directly increases the resolution of the simulation as well as the wall clock time required as more particles increases the solution time to proceed to the next step.

Verification cases were run on the T-motor 12×4 propeller. Where appropriate, the propeller was run with the maximum number of 41 spanwise sections from the geometry data provided by PhotoFoil, as well as the smallest step angle studied of 5 degrees. A moderate case of 6000 RPM was selected based on the RPM range of this propeller, as well as a forward flight speed of 5 m/s at 0 angle of attack for most verification cases.

Time convergence

Studying the forces experienced by the rotor blade shows the convergence of the forces over time. Figure 3.20 shows how the six components of force and moment converge over time. As there is a freestream velocity component, the forces do not converge to continuous values. The data show that the forces do converge to some form of periodic solution in as little as three or four revolutions. The time averaged values of the forces, averaged over 1 rotation, can be seen in Figure 3.21. Here is it evident that the forces converge to a steady result in three to four rotations as observed. To properly evaluate the convergence, the revolution averaged forces and moments are normalized by the rotation averaged value at the final time step, as shown in Figure 3.22. These results show that the fores converge to acceptable levels of error relative to the revolution 10 value by four rotations, but that an arbitrary error threshold of 5% requires closer to six or seven rotations.

One observation from subsequent simulations regarding the time for convergence is that it generally occurs more quickly with a higher freestream velocity or, more specifically, higher advance ratios μ. The reason for this is that the freestream convects the particles away more quickly, allowing the system to reach its steady state more quickly. In hover, for instance, the simulation needs to be run until the shed vortex particles are numerous and strong enough to create a steady wake and convect newly shed particles away in an expedient manner. DUST has a feature to assist with this called the Hover Convergence Augmentation System (HCAS) which applies a temporary velocity field to help convect away the initially shed particles as the wake develops.

Time step Resolution

The choice of step size has direct impact on the computational cost, as increasing the step size reduces the number of time steps to reach a certain number of rotations as well as reduces the number particles in the computational domain. Simulating the test case for various step sizes produces the thrust values seen in Figure 3.23. The step size has a surprisingly small influence on the calculated Thrust value. While there was not a clear pattern of convergence, a step size of 10 degrees was chosen for subsequent simulations, having comparable accuracy to the 5 degree simulations while being half as computationally intensive.

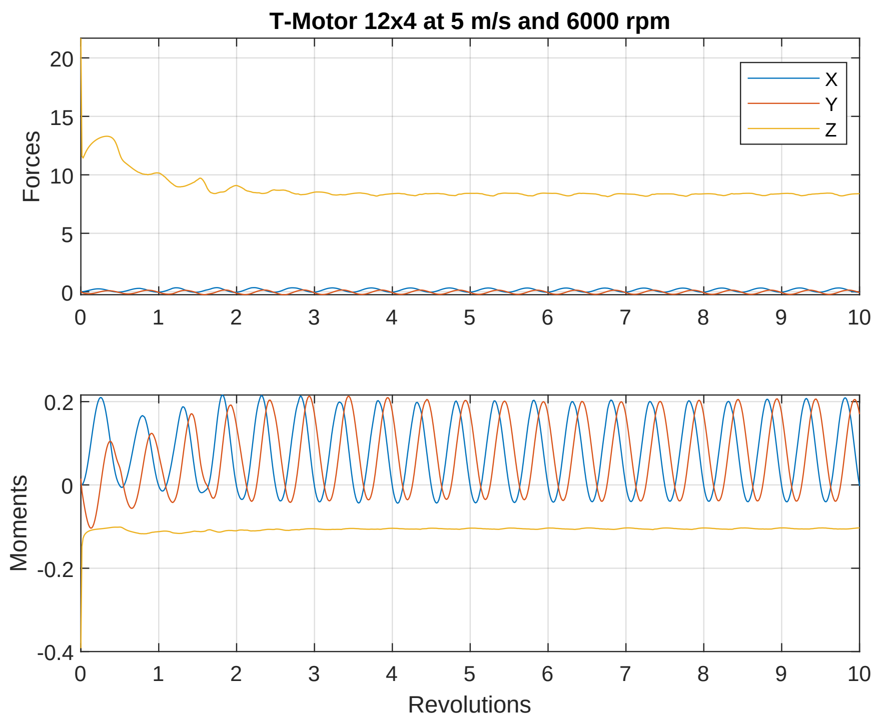

Figure 3.20: Forces and moments experienced by propeller over time.

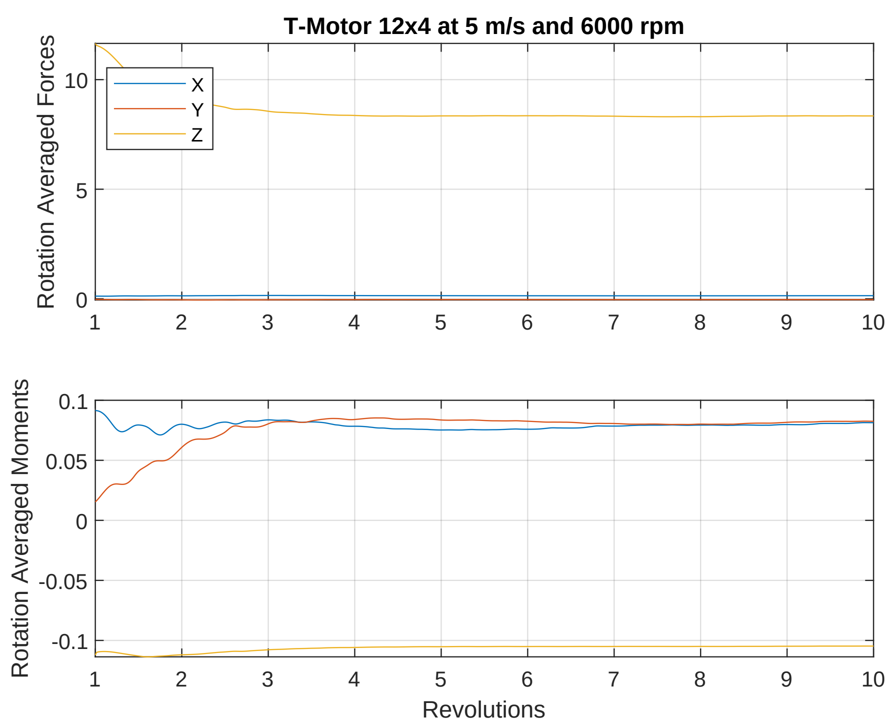

Figure 3.21: Forces and moments averaged over one rotation.

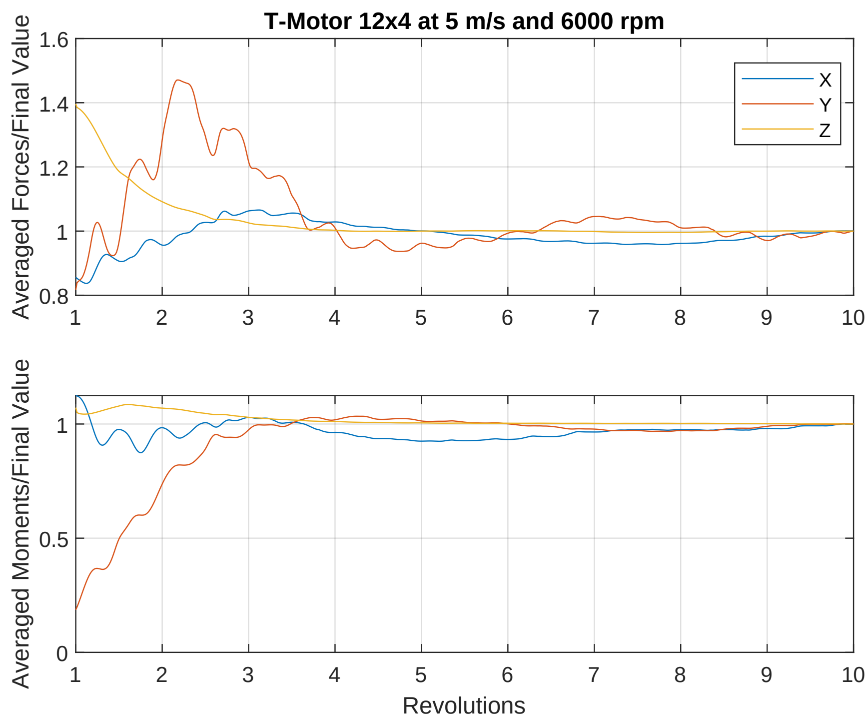

Figure 3.22: Forces and moments averaged over one rotation normalized by final value.

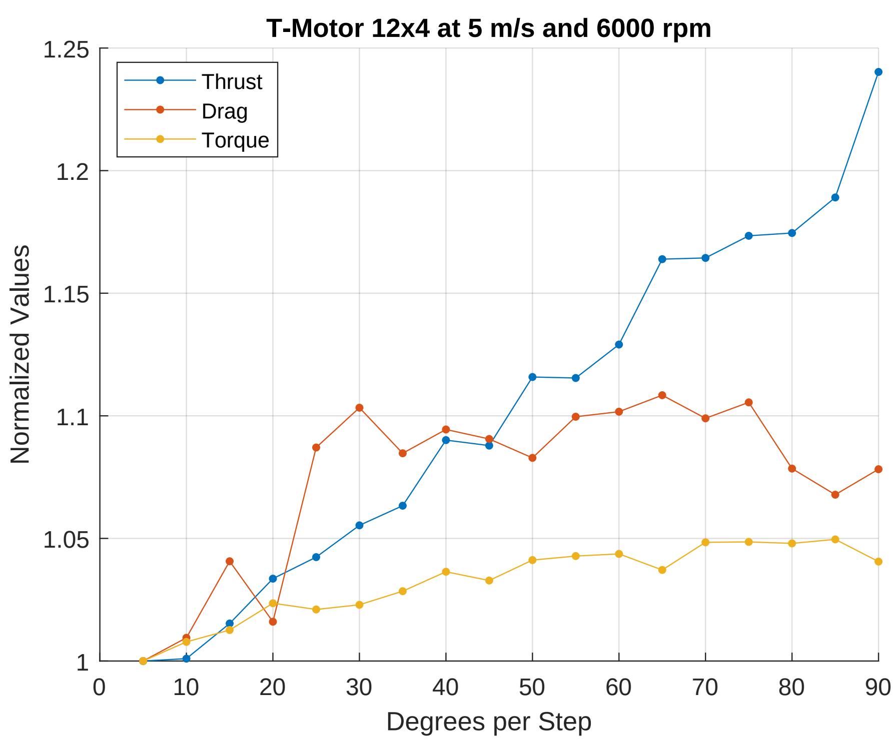

Figure 3.23: Thrust value produced by rotor based on angular step size.

Blade Resolution

The chordwise resolution of the blade is expected to have an influence on the results. More elements along the chord should improve the representation of the airfoil as well as the force calculation over its surface. The effect of chord resolution on the force results were noted in [19] as having an effect on the simulation resolution relative to the CFD results. The results shown in Figure 3.24 show that the number of chordwise elements do not have a huge effect on the results. The forces are normalized by the highest resolution simulation at 100 chordwise elements. The forces calculated relative to this solution have an error of only 10% even in the simulation with the smallest number of panels. The number of chordwise elements chosen for simulations was 50.

A similar study was done with the number of spanwise sections representing the blade, as shown in Figure 3.25. There is not a clear and consistent convergence behavior visible, but the error associated with using only a small number of spanwise elements is relatively small. The thrust and torque are observed to approach the final value in a fairly continuous manner, but the rotor drag is substantially more chaotic in its approach, varying considerably but still with a reasonably error. Simulations were typically run with 25 spanwise elements for the propeller as a compromise on quality and computation time.

Results

Simulations were run using the geometry of several propellers extracted using the PhotoFoil process described in Chapter 4. A comparison between simulation and experiment for the T-Motor 12×4 inch propeller can be seen in Figure 3.26. There is good agreement between the experimental and simulated thrust. The simulated torque is close to the experimental value, but is under-predicted. Fitting non-dimensional coefficients C_T and C_Q to the experimental and simulation data, the values are compared in Figures 3.27 and 3.28. The results show that the prediction of thrust is good across all of the propellers studies, with the exception of the APC 10×4.7, but that torque is under-predicted across all the studied propellers. While conclusively determining the cause for the under-prediction was not feasible without extensive force measurement or flow visualization, drag prediction of bodies in simulation is often poor or inaccurate. It is not unprecedented that this would extend to under-prediction of the drag of certain sections, and that the torque would be underestimated as a result.

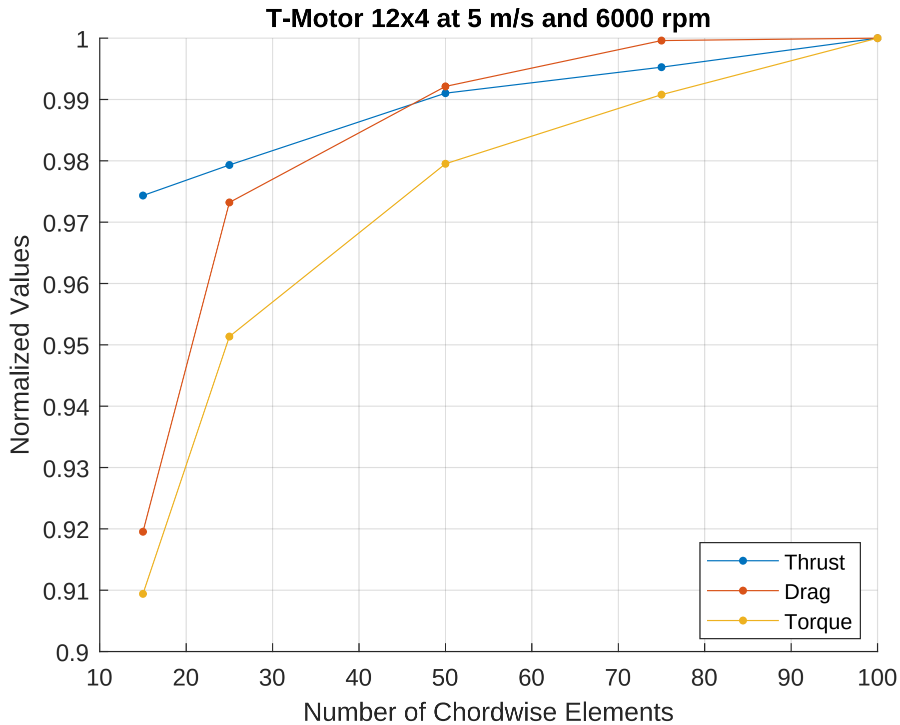

Figure 3.24: Thrust value produced by rotor based on number of chord sections.

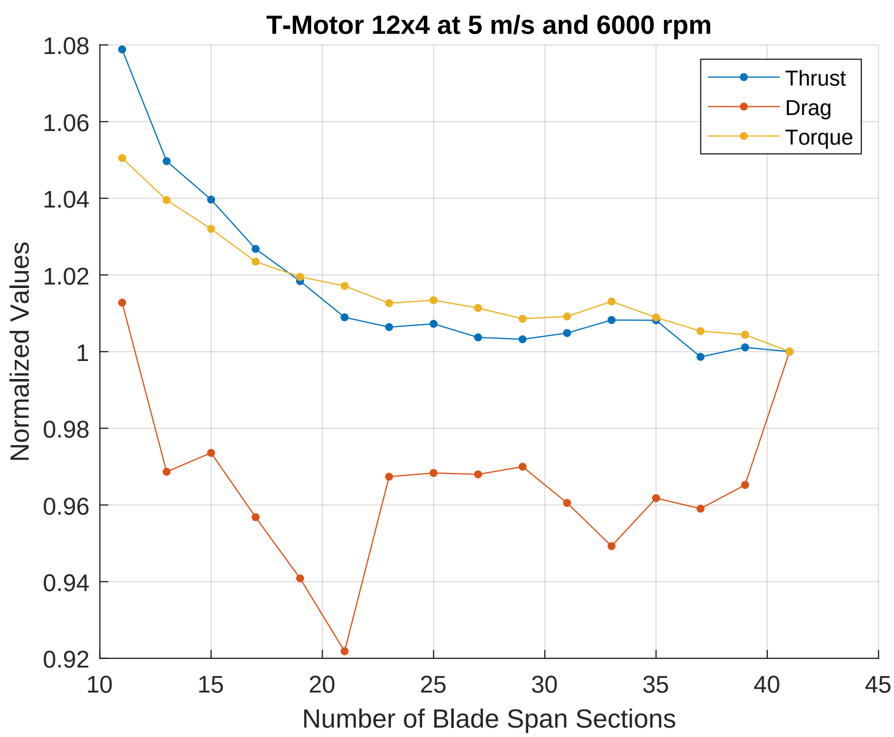

Figure 3.25: Thrust value produced by rotor based on blade span section.

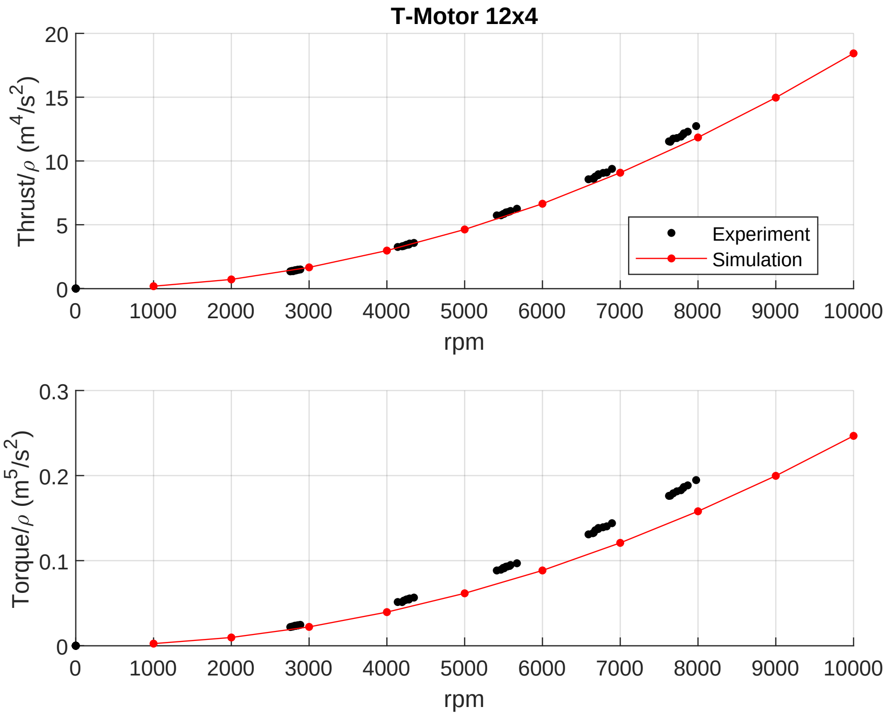

Figure 3.26: Example of experimental and simulation results for the T-Motor 12×4 propeller.

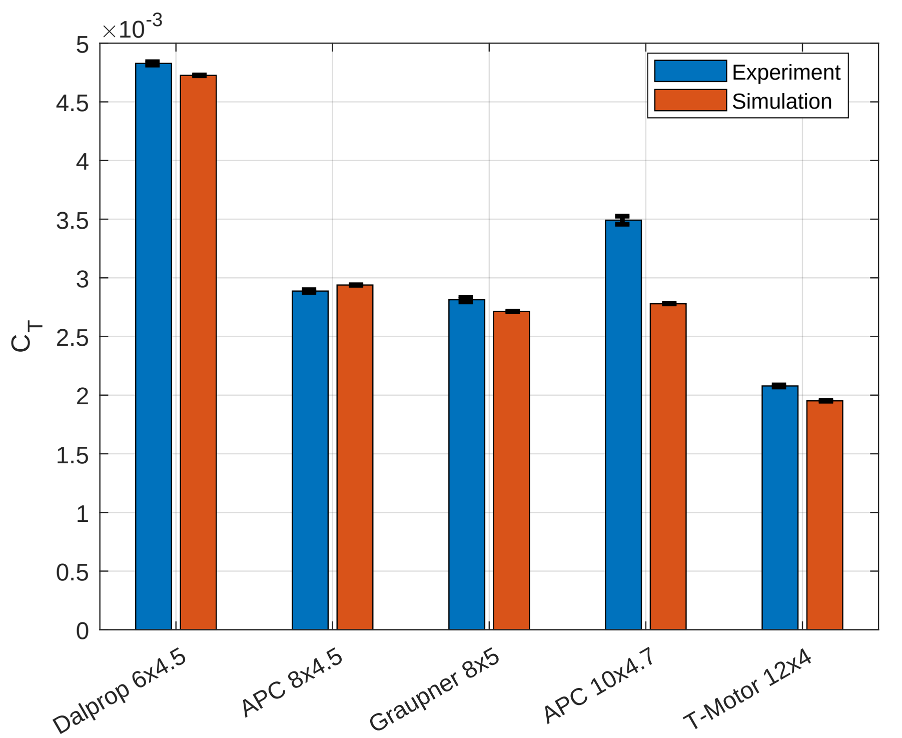

Figure 3.27: Comparison of fitted experimental and simulation thrust coefficients with 95% confidence interval error bars.

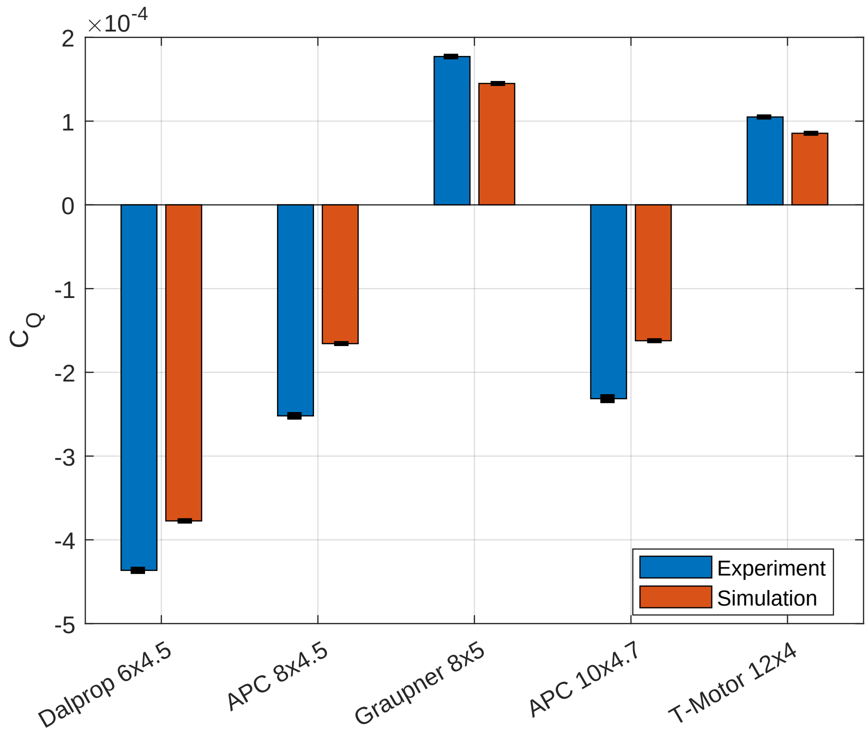

Figure 3.28: Comparison of fitted experimental and simulation torque coefficients with 95% confidence interval error bars.

Though there is not an exact match in the UIUC propeller data base, the static coefficients of similar propellers can be compared to the experimental and simulation values. To do so, propellers with the same diameter but pitches that contain the pitch value of the propeller studied here are selected. The static coefficients computed from the data are seen in Table 3.1. We see that the experimental and simulation values for the two APC propellers are similar to the results here. The values of C_Q for both propellers are near or within the values of the propellers with their respective diameters. The value of C_T for the 8-inch propeller is near the upper bound of the UIUC data, while the value for the 10-inch propeller is slightly larger. APC also has simulation data for their propellers [24]. The published coefficient of the 10-inch propeller is approximately 0.003741, while that of the 8 inch propeller is .00323, within about 10 percent of the experimental values.

Continuing to evaluating the simulation performance in forward flight, we can see a typical example in Figure 3.29 for the T-motor 12×4 propeller at 0 angle of attack. From the data available, the thrust prediction in forward flight appears accurate, as in the static case. Likewise, the torque is consistently underpredicted. In contrast to the other two metrics, the rotor drag appears to be significantly underpredicted. The

Propeller	C_T	C_Q
APCe 10x5	0.00242	0.000150
APCe 10x7	0.00268	0.000214
APCe 8x4	0.00238	0.000160
APCe 8x6	0.00285	0.000301

Table 3.1: Values for similar propellers from the UIUC Propeller Database [25].

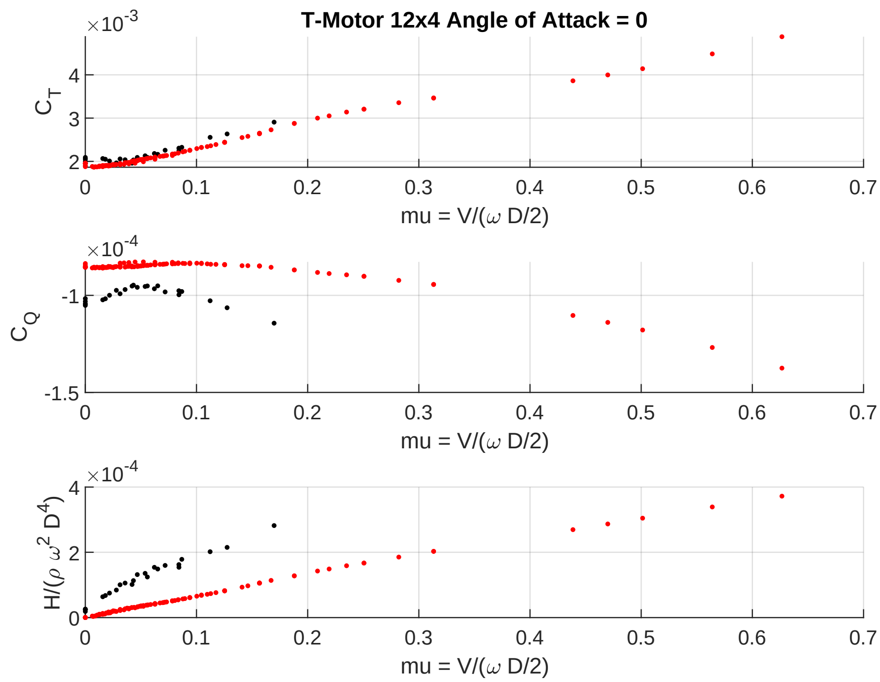

Figure 3.29: Thrust, torque, rotor drag plots for a T-motor 12×4 propeller at 0 angle of attack.

experimental data suggest a power relationship with advance ratio, but the simulation results appear nearly linear and substantially underpredicted. This difference is further highlighted in Figure 3.30. The same underprediction is visible across all angles of attack for the T-Motor 12×4 propeller.

This deficiency in prediction is not unique to just one propeller, and appears to be a characteristic of the simulation. The fitting process for the low-order model is applied to the simulation data as the experimental data and the resulting coefficients are compared in Figures 3.31, 3.32, and 3.33, alongside the adjusted R^2 of the fit in Figure 3.34. The observations made regarding the T-Motor 12×4 propeller generally hold true across the propellers studied. The C_H coefficient from the simulation data is substantially smaller than the experimental values, with the exception of the APC

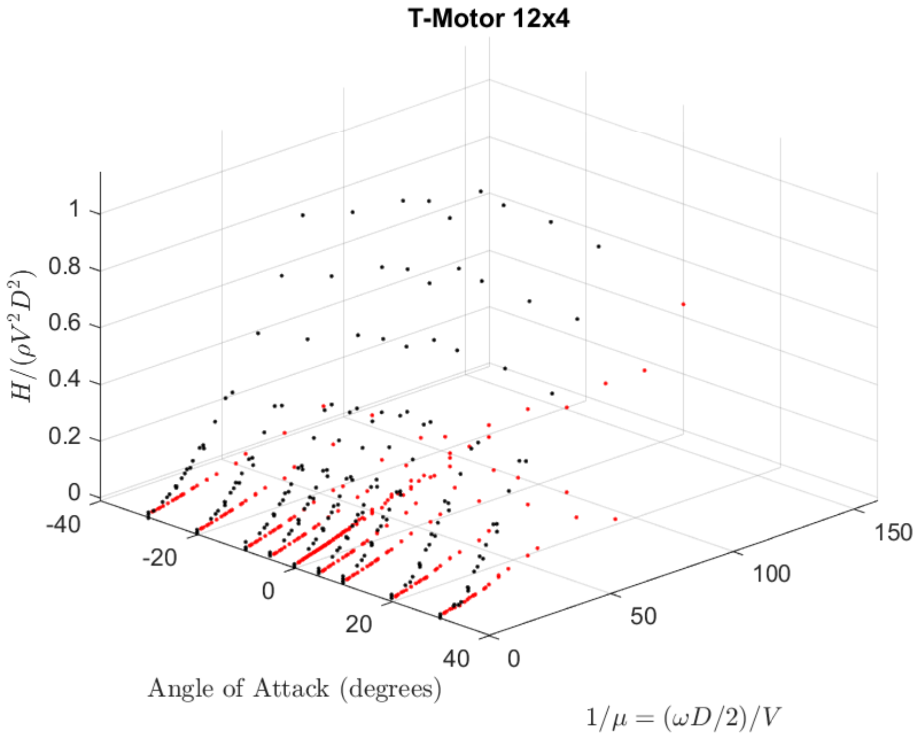

Figure 3.30: 3D representation of the experimental rotor drag of a T-motor 12×4 in black with analogous simulation results in red.

10×4.7 propeller. The power constant n is also slightly smaller than experimental values, being closer to 1 across the various propellers. The angle of attack constant is substantially larger for the simulation results, suggesting a differently located function peak in simulation compared to experiment. Lastly, the adjusted R^2 for the simulation results is slightly better than for the experiments. This is expected, given that the simulation should theoretically lack much of the noise or sources of error present in experimental studies.

Change in Thrust Coefficient

The data were also examined to determine what, if any, the effect of forward flight was upon the thrust produced by the propeller. A sample of such data is seen in Figure 3.35. What can be seen here is the that the thrust coefficient remains virtually flat across the studied advance ratios and angles of attack. While Glauert momentum theory does predict a change in the thrust production of the propeller as the forward flight velocity increases, the range of flight speeds here, combined with the propeller being in primarily edgewise flow lead to a minimal change in thrust observed. The exception to this is at near zero reciprocal advance ratios, where the

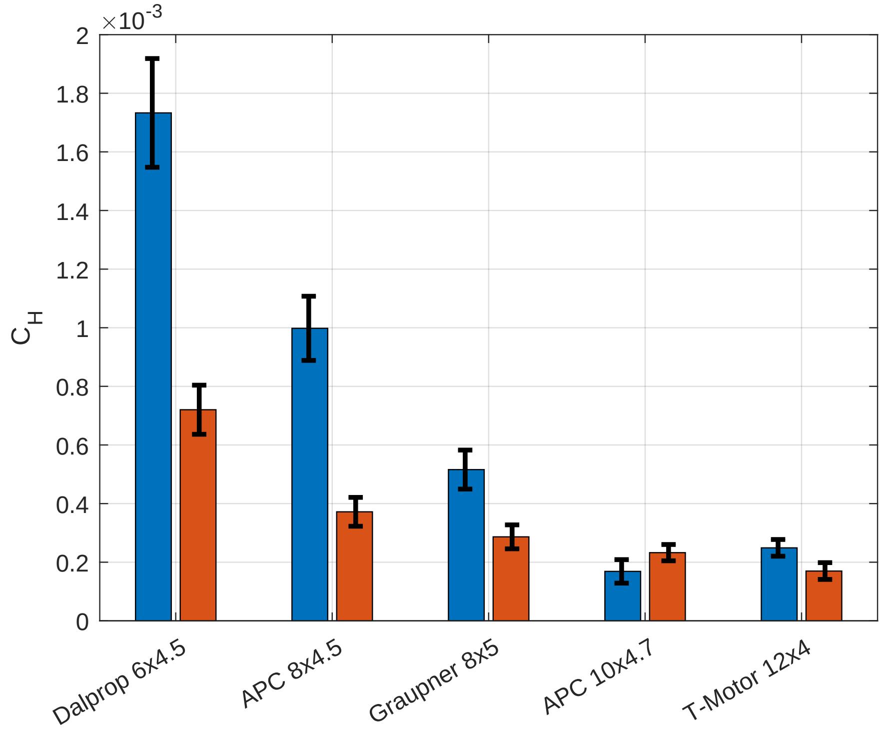

Figure 3.31: Comparison of fitted C_H parameter for selected propellers.

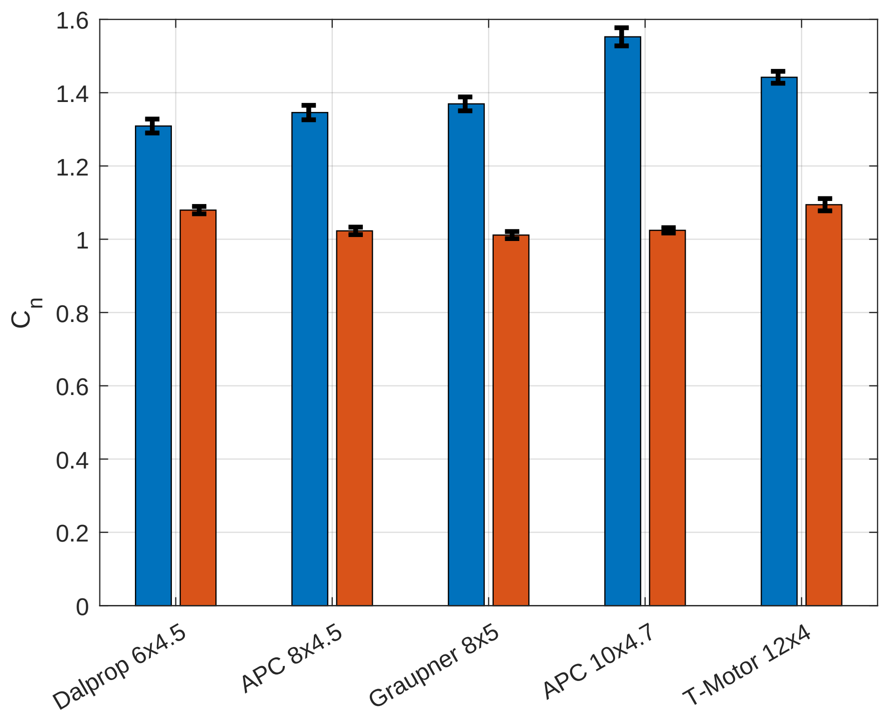

Figure 3.32: Comparison of fitted C_n parameter for selected propellers.

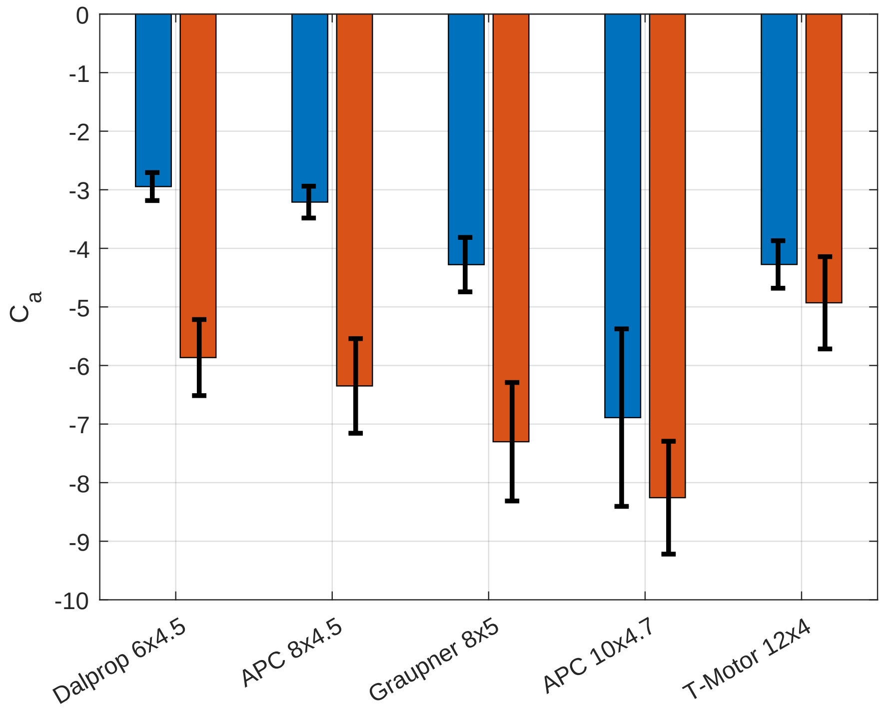

Figure 3.33: Comparison of fitted C_a parameter for selected propellers.

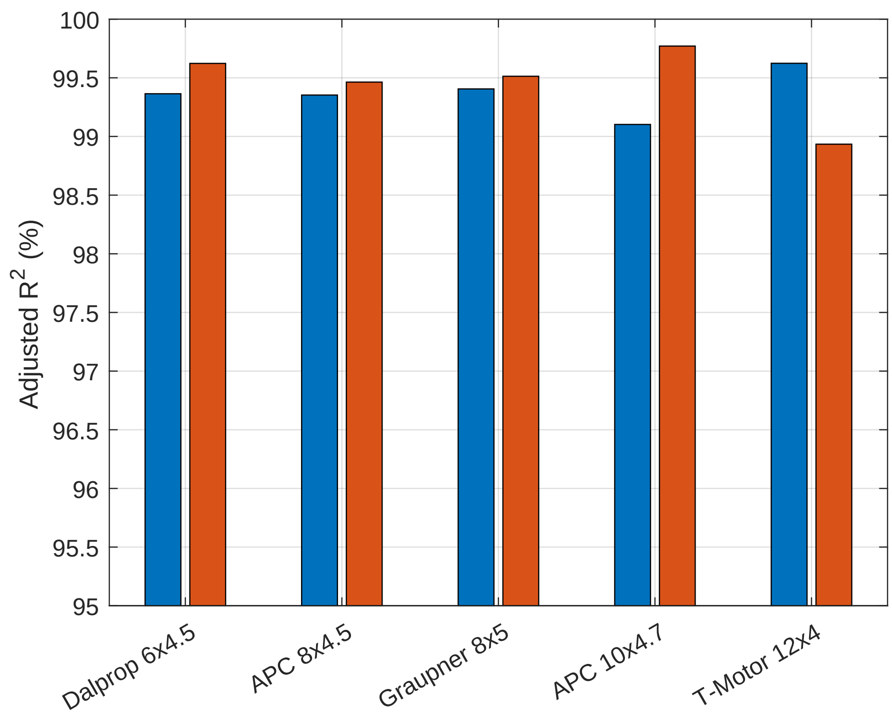

Figure 3.34: Adjusted R^2 of the fit for each propeller.

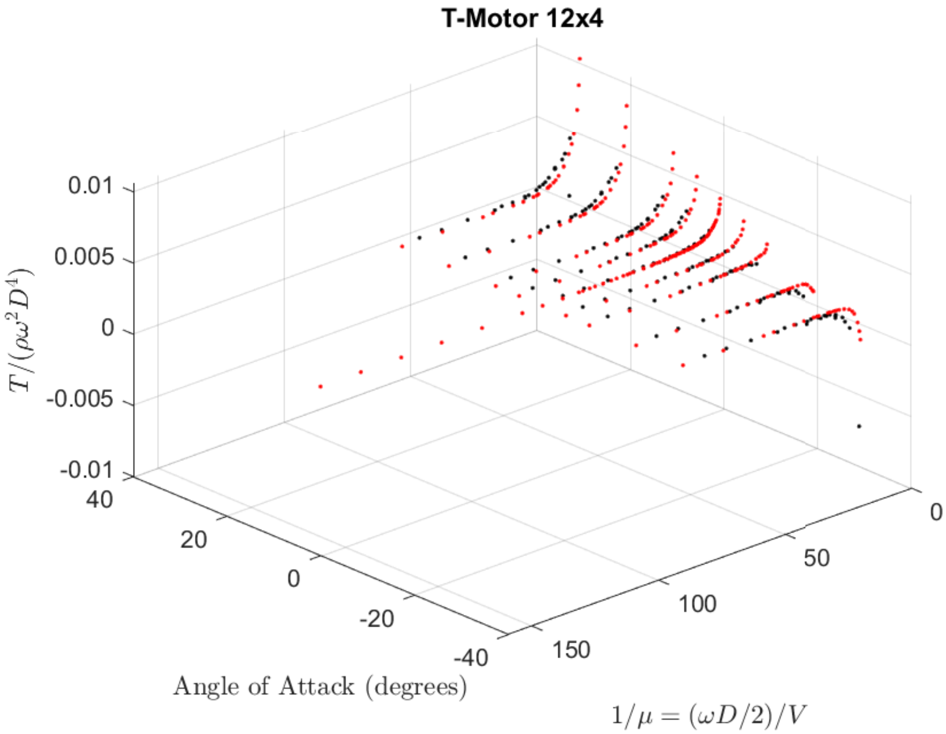

Figure 3.35: Thrust coefficient vs angle of attack and inverse advance ratio. Experimental data is black and simulation data is red.

rotational speed is low, but the freestream velocity is relatively high. There is a high dependence of the thrust here on the angle of attack. One potential explanation for the observed effect is that the thrust force produced is less associated with the rotation of the propeller, and more with the propeller as a body that produces lift and drag. As thrust is measured as the force along the axis of rotation, and the direction changes with the angle of attack, the force in the traditional drag direction along the freestream, would contribute significantly to the thrust. The thrust coefficient is also computed with the rotational speed in the denominator, so small rotational speeds would make the thrust coefficient increase in a singular fashion as ω approached 0.

Lifting Line Representation

To try and understand the discrepancy between the surface panel simulation and the experimental results, simulations were run with a lifting line representation of the propeller and were compared to the experimental data and panel method. To represent the rotor blade using the lifting line method, polars are provided to DUST in the c81 format. The version of the format that DUST uses also accepts polar tables for multiple Reynolds numbers.

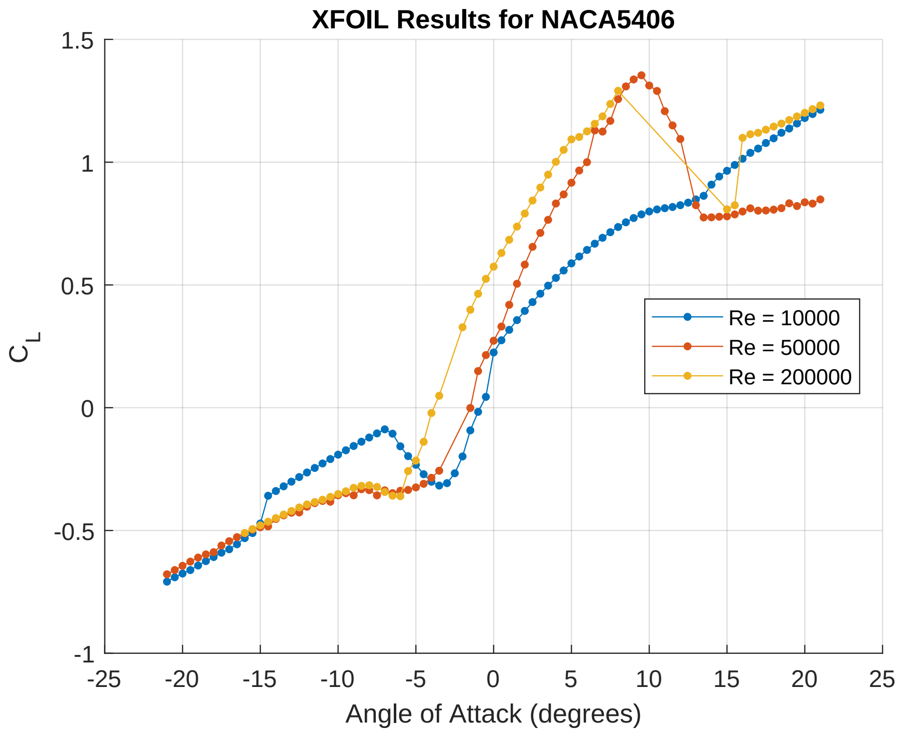

Figure 3.36: Selection of lift polars for a NACA 5406 at various Reynolds numbers.

To produce the airfoil polars at the expected Reynolds numbers for the airfoil, the properties are simulated in XFOIL [26]. As noted previously, the results of simulation can be unreliable at the Reynolds numbers experienced by propellers. In Figure 3.36, the lift coefficient for a NACA5406 airfoil, the airfoil fit to the geometry of the T-Motor 12×4 propeller, is shown. The results of the simulation are shown for a selection of Reynolds numbers, and demonstrate how the simulation results change considerably with Reynolds number. The slope and shape change, the y-intercept is different, and there are numerous unconverged points and sudden jumps in the solution, even at the Re = 200,000 case.

Because a propeller blade typically experiences some region of reversed flow, it is necessary to have a polar with data for the full angular domain from -180 to 180 degrees. To do this, the lift, drag, and moment polars from XFOIL are merged with a continuous function as detailed in [20]. Samples of the full lift polars can be seen in Figure 3.37.

Comparing the rotor performance in forward flight at 0 angle-of-attack to the experimental and surface panel simulation data as before, we see the results in Figure 3.38. The results are not substantially different between the lifting line representation and

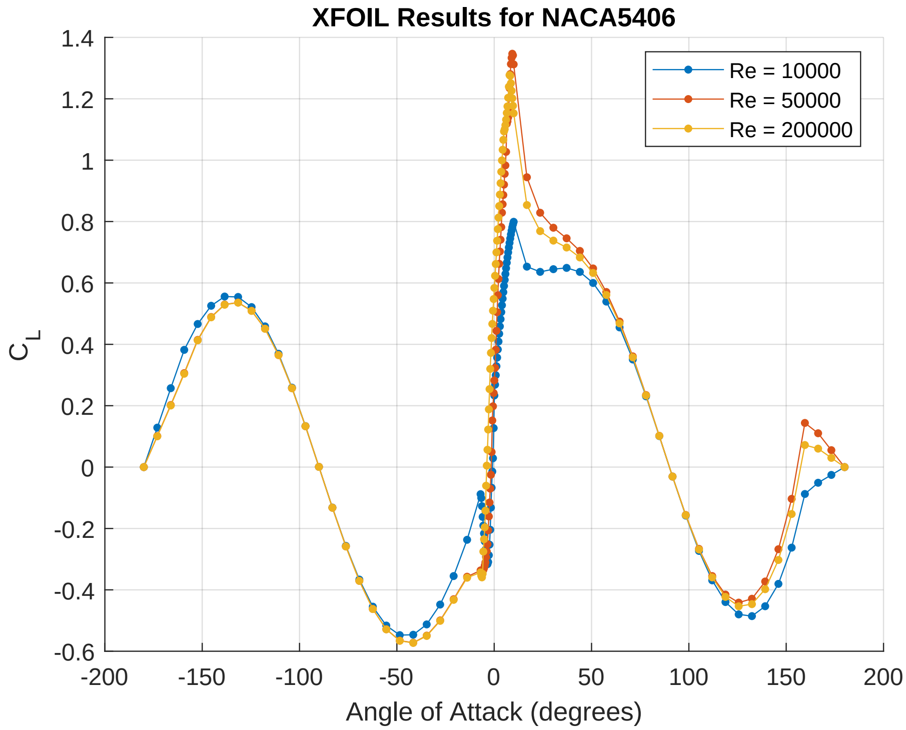

Figure 3.37: Lift polars with the merged function at various Reynolds numbers

the surface panel representation. The thrust prediction is poorer in forward flight, but the torque prediction is slihtly improved. The rotor drag prediction is nearly identical between the lifting line and surface panel methods however.

Implementing the lifting line method for the simulation had additional difficulties. Many of the cases at higher RPM failed to converge, and the polars produced by simulation as well as the merged function used to provide data for the full range of angles-of-attack were used with no verification. With little improvement in accuracy but considerably more effort to set up, the lifting line representation seems to be a less preferable option for simulation at these Reynolds numbers. However, if accurate airfoil polar data could be implemented into the simulation, it should reduce computation time and implicitly include some degree of viscous effects into the model, improving its accuracy.

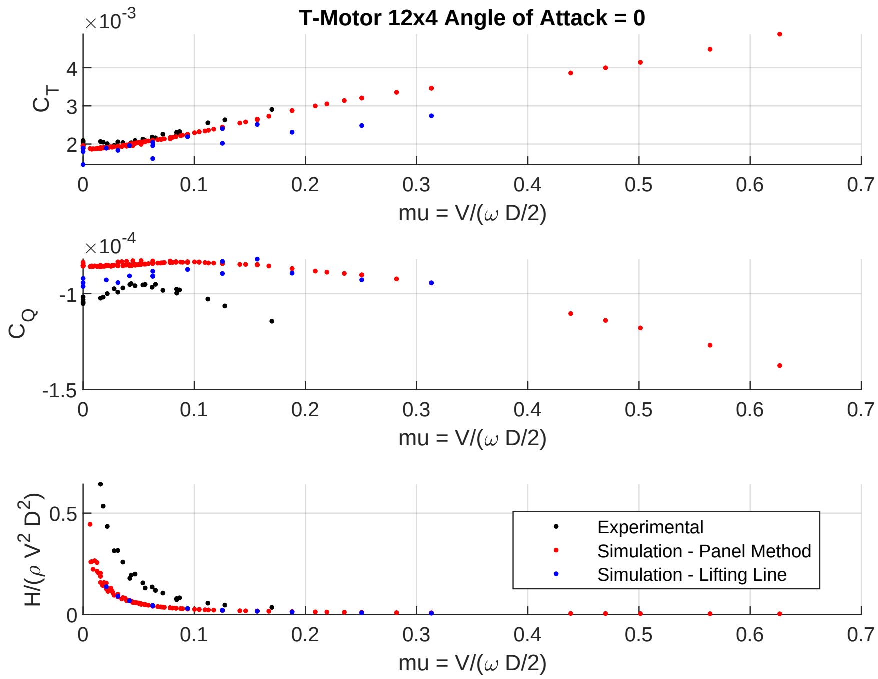

Figure 3.38: Rotor Performance at 0 angle-of-attack with lifting line simulation data

Discussion

While the non-dimensional fit provides a simple, lower order model for the data, the fit is still empirical. Simulation is far more accessible if a wind tunnel and the associated sensing hardware is not available. However, the results show that the simulation significantly underpredicts the rotor drag. As simulation is an important tool in modern engineering, it is important to consider the source of the inaccuracy.

There are a number of explanations for the discrepancy between the simulation and the experiment. The most likely set of explanations have to do with the low Reynolds number of the studied cases. Airfoil performance is known to significantly degrade at low Reynolds numbers [27, 28] or to have a dependency not seen at higher Reynolds numbers [29, 30]. A common reason for this is the formation of the laminar separation bubble. There is also the effect of Reynolds number on the region of reverse flow [31]. All these effects are subtleties that are not necessarily captured by a panel method, particularly with a lack of boundary layer effect.

An alternative perspective on the results is that, because boundary layer and separation effects on the blades are not considered, the panel method simulation is providing the rotor drag associated primarily with the induced drag of the rotor, meaning that the discrepancy would be primarily viscous or pressure drag. If correct, this would provide useful information as to the relative sources of drag in physical experiments.

A potential source of the discrepancy is that there is a systematic experimental error increasing the drag above the simulation value. While the simulation does not incorporate physical features such as the propeller hub, the motor, or the test stand, efforts were made in the experimental sections of the work to remove the influence of these from the final drag measurements by measuring them without propeller rotation.

3.6 Future Work

Future work would consist of turning the results shown into a more concrete design tool as well as resolving the observed discrepancies. One potential avenue of study is in how the coefficients in the propeller design are correlated with aspects of the propeller design. The values of the power constant n as well as the angle-of-attack constant a are both similar for the majority of propellers studied. The experimental data are not enough to determine the origin of the value nor the precise reason for the similarity in values. Conclusively determining whether the values are typical of drone scale propellers would improve the utility of the non-dimensional fit described here by potentially reducing the coefficients that need to be studied to just C_h.

As simulation is and continues to be an important tool in engineering, identifying the source of the observed discrepancy would be useful. While it is useful to be aware of deficiencies, identifying the precise cause can help improve the underlying simulation. Several possibilities for the discrepancy in results regarding the rotor drag have been proposed, but verification requires more in depth analysis. If Reynolds number accurate airfoil data could be acquired for the airfoil sections associated with the propellers, it would eliminate that as a source of error. The lifting line method could then be implemented correctly to better assess the simulation accuracy.

Hardware limitations meant that the studies in this work were done with only a single isolated propeller. Most eVTOL vehicles have multiple propellers that are close enough to be likely to interact with one another aerodynamically. Much as multiple bodies in forward flight can interact with one another and mutually change the respective forces each experiences, it would be expected that the rotor drag would change if multiple propellers are near to each other or to an external body. For instance, one propeller immersed in the wake of fuselage or wing might be expected to experience less rotor drag, as the flow velocity seen by the propeller should be reduced by virtue of the momentum deficit in the wake of the upstream entity. Quantifying or understanding the change in rotor drag with respect to proximal entities would be a strong addition to analysis techniques for this type of craft. Studying the interactions in depth would likely be most easily done in simulation, given the ability to extract data from the entire flowfield.

3.7 Conclusions

The work here demonstrates experimental quantification of the Rotor Drag experienced by a selection of drone scale propellers in forward flight. Experimental data are collected for a set of propellers of different diameters at the drone scale. A novel model derived from both the dimensionality of the problem and informed by the experimental data is created and applied to the data collected. It is found that the model fits well with the experimental data and that there are trends amongst the derived coefficients. The power parameter as well as the angle of attack parameter are both fairly similar across the various propellers. While the rotor drag parameter had more variability between the propellers, the similarity of the power and angle of attack parameters suggests that $C_n = 1.3$ and $C_a = -3$ are useful rough estimates for the parameters for this class of propellers. While it is not certain where these values physically originate from, they held true for the majority of the propellers studied.

Simulations in DUST provide good agreement with thrust and decent agreement with torque, meaning that this level of simulation is sufficient to predict these two in the range of conditions studied. The drag prediction still has a substantial discrepancy between the simulation and the experiment however, and the cause is not conclusively known. It is known that DUST does not model certain aerodynamic effects such as boundary layer effects or flow separation, but an effort to compensate for this using the lifting line model did not produce significantly different results. Regardless, the results indicate that the simulation is still lacking with regards to accurate prediction, but that a rough correction of multiplying the output by two is a basic method to compensate for the error.

References

[1] Bjorn Fehrm. *Bjorn's Corner: Sustainable Air Transport. Part 32. Mixed architectures, Part 2.* en-US. Aug. 2022. URL: https://leehamnews.com/2022/08/12/bjorns-corner-sustainable-air-transport-part-30-mixed-architectures-part-2/ (visited on 10/20/2022).

[2] Barnes W. McCormick. *Aerodynamics of V/STOL Flight*. Academic Pr, 1967. ISBN: 0124823505.

[3] Wayne Johnson. *Helicopter Theory*. Revised. Dover Publications, Dec. 1994. ISBN: 0-486-68230-7.

[4] David A. Peters, David Doug Boyd, and Cheng Jian He. "Finite-State Induced-Flow Model for Rotors in Hover and Forward Flight." In: *Journal of the American Helicopter Society* 34.4 (Oct. 1989). ISBN: 9780470559277, pp. 5–17. ISSN: 2161-6027. DOI: 10.4050/JAHS.34.5.

[5] B. Theys, G. Dimitriadis, T. Andrianne, P. Hendrick, and J. De Schutter. "Wind Tunnel Testing of a VTOL MAV Propeller in Tilted Operating Mode." en. In: *2014 International Conference on Unmanned Aircraft Systems (ICUAS)*. Orlando, FL, USA: IEEE, May 2014, pp. 1064–1072. ISBN: 978-1-4799-2376-2. DOI: 10.1109/ICUAS.2014.6842358.

[6] Herbert S. Ribner. *Formulas for Propellers in Yaw and Charts of the Side-Force Derivative*. Tech. rep. NACA-TR-819. Jan. 1945.

[7] Herbert S. Ribner. *Propellers in Yaw*. Tech. rep. NACA-TR-820. Jan. 1945.

[8] John W. Draper and Richard E. Kuhn. *Investigation of the Aerodynamic Characteristics of a Model Wing-Propeller Combination and of the Wing and Propeller Separately at Angles of Attack up to 90 Degrees*. en. Tech. rep. NACA-TN-3304. Nov. 1954, p. 73.

[9] Richard E. Kuhn and John W. Draper. *Investigation of the Aerodynamic Characteristics of a Model Wing-Propeller Combination and of the Wing and Propeller Separately at Angles of Attack up to 90 Degrees*. Tech. rep. NACA Report 1263. Jan. 1956.

[10] Paul F. Yaggy and Vernon L. Rogallo. *A Wind-Tunnel Investigation of Three Propellers Through an Angle-of-Attack Range from 0 deg to 85 deg*. Tech. rep. NASA-TN-D-318. May 1960.

[11] Michael Cerny and Christian Breitsamter. "Investigation of Small-Scale Propellers under Non-Axial Inflow Conditions." en. In: *Aerospace Science and Technology* 106 (Nov. 2020), p. 106048. ISSN: 12709638. DOI: 10.1016/j.ast.2020.106048.

[12] Katarzyna Pobikrowska and Tomasz Goetzendorf-Grabowski. "Wind Tunnel Tests of Hovering Propellers in the Transition State of Quad-Plane." en. In: *Bulletin of the Polish Academy of Sciences Technical Sciences* 69.6 (2021). Publisher: (:unav). DOI: 10.24425/BPASTS.2021.138821.

[13] Rajan Gill and Raffaello D'Andrea. "Propeller Thrust and Drag in Forward Flight." In: *2017 IEEE Conference on Control Technology and Applications (CCTA)*. ISSN: 0307904X. Mauna Lani Resort, HI, USA: IEEE, Aug. 2017, pp. 73–79. ISBN: 978-1-5090-2182-6. DOI: 10.1109/CCTA.2017.8062443.

[14] Xichen Shi, Patrick Spieler, **Tang, Ellande**, Elena-Sorina Lupu, Phillip Tokumaru, and Soon-Jo Chung. "Adaptive Nonlinear Control of Fixed-Wing VTOL with Airflow Vector Sensing." In: *ICRA* (Mar. 2020). arXiv: 2003.07558. DOI: 10.1109/ICRA40945.2020.9197344.

[15] *Series 1585 Test Stand Datasheet*. Jan. 2022. URL: https://cdn.rcbenchmark.com/landing_pages/Manuals/Series%201585%20Datasheet.pdf (visited on 10/05/2022).

[16] Matteo Tugnoli, Davide Montagnani, Monica Syal, Giovanni Droandi, and Alex Zanotti. "Mid-Fidelity Approach to Aerodynamic Simulations of Unconventional VTOL Aircraft Configurations." en. In: *Aerospace Science and Technology* 115 (Aug. 2021), p. 106804. ISSN: 1270-9638. DOI: 10.1016/j.ast.2021.106804.

[17] Luigi Morino and Ching-Chiang Kuo. "Subsonic Potential Aerodynamics for Complex Configurations : A General Theory." In: *AIAA Journal* 12.2 (Feb. 1974). Publisher: American Institute of Aeronautics and Astronautics, pp. 191–197. ISSN: 0001-1452. DOI: 10.2514/3.49191.

[18] J. S. Uhlman Jr. *An Integral Equation Formulation of the Equations of Motion of an Incompressible Fluid:* en. Tech. rep. 10086. Fort Belvoir, VA: Defense Technical Information Center, July 1992. DOI: 10.21236/ADA416252.

[19] Alex Zanotti, Alberto Savino, Michele Palazzi, Matteo Tugnoli, and Vincenzo Muscarello. "Assessment of a Mid-Fidelity Numerical Approach for the Investigation of Tiltrotor Aerodynamics." en. In: *Applied Sciences* 11.8 (Jan. 2021). Number: 8 Publisher: Multidisciplinary Digital Publishing Institute, p. 3385. ISSN: 2076-3417. DOI: 10.3390/app11083385.

[20] Michele Palazzi. "Mid-Fidelity Approach to Tiltrotor Aerodynamics." MA thesis. Milan, Italy: Politecnico di Milano, 2020.

[21] Joon W. Lim. "Fundamental Investigation of Proprotor and Wing Interactions in Tiltrotor Aircraft." en. In: *75th Annual Vertical Flight Society Forum and Technology Display*. Philadelphia, PA, USA: The Vertical Flight Society, May 2019.

[22] Lance W. Traub and Cory Coffman. "Efficient Low-Reynolds-Number Airfoils." en. In: *Journal of Aircraft* 56.5 (Sept. 2019), pp. 1987–2003. ISSN: 1533-3868. DOI: 10.2514/1.C035515.

[23] Ira H. Abbott and A. E. von Doenhoff. *Theory of Wing Sections: Including a Summary of Airfoil Data*. Dover Publications, 1959. ISBN: 9780486605869.

[24] *APC Propellers Performance Data*. en-US. URL: https://www.apcprop.com/technical-information/performance-data/ (visited on 10/24/2022).

[25] J.B. Brandt, R.W. Deters, G.K. Ananda, O. D. Dantsker, and M.S. Selig. *UIUC Propeller Database, Vols 1-4*. Oct. 2022.

[26] Mark Drela and Harold Youngren. *XFOIL-Subsonic Airfoil Development Sytem*. 2013.

[27] Thomas J. Mueller and Stephen M. Batill. "Experimental Studies of Separation on a Two-Dimensional Airfoil at Low Reynolds Numbers." en. In: *AIAA Journal* 20.4 (Apr. 1982), pp. 457–463. ISSN: 0001-1452, 1533-385X. DOI: 10.2514/3.51095.

[28] Michael Selig, James Guglielmo, Andy Broern, and Philippe Giguere. "Experiments on Airfoils at Low Reynolds Numbers." en. In: *34th Aerospace Sciences Meeting and Exhibit*. Reno,NV,U.S.A.: American Institute of Aeronautics and Astronautics, Jan. 1996. DOI: 10.2514/6.1996-62.

[29] Jan Michna and Krzysztof Rogowski. "Numerical Study of the Effect of the Reynolds Number and the Turbulence Intensity on the Performance of the NACA 0018 Airfoil at the Low Reynolds Number Regime." en. In: *Processes* 10.5 (May 2022), p. 1004. ISSN: 2227-9717. DOI: 10.3390/pr10051004.

[30] Tim Burdett, Jason Gregg, and Kenneth Van Treuren. "An Examination of the Effect of Reynolds Number on Airfoil Performance." en. In: *ASME 2011 5th International Conference on Energy Sustainability, Parts A, B, and C*. Washington, DC, USA: ASMEDC, Jan. 2011, pp. 2203–2213. ISBN: 978-0-7918-5468-6. DOI: 10.1115/ES2011-54720.

[31] Andrew H. Lind, Luke R. Smith, Joseph I. Milluzzo, and Anya R. Jones. "Reynolds Number Effects on Rotor Blade Sections in Reverse Flow." en. In: *Journal of Aircraft* 53.5 (Sept. 2016), pp. 1248–1260. ISSN: 0021-8669, 1533-3868. DOI: 10.2514/1.C033556.

Chapter 4

PROPELLER GEOMETRY EXTRACTION WITH PHOTOFOIL

4.1 Introduction

The increasing popularity of small Uninhabited Aerial Systems (sUAS) in various fields and applications has made them a subject of academic interest. Multirotors or, colloquially, ”drones” are seeing use in aerial photography, scientific surveying, law enforcement, and even delivery. As the name implies, these vehicles fly using multiple propellers to provide the lift required to counteract gravity as well as to maneuver. The ubiquity of drones means that aerodynamic analysis of propellers in these conditions is important to determine the efficiency of a design, and to characterize its dynamics.

Existing simulation methods can accomplish both these tasks to varying degrees of accuracy and complexity. The most basic analysis possible is the classical actuator disc model [1]. The actuator disc model may capture the general effects of a rotor on the surrounding fluid, but does not capture the specifics of a particular propeller. This analysis method provides a basic relation between thrust, and the momentum and energy in the flow, but says little about how that relates to a propeller rotation speed necessary for a controls formulation nor how the airflow may interact with other portions of the drone. Simulation methods that do consider the propeller geometry are Blade Element Theory (BET) or Blade Element Momentum Theory (BEMT) [2]. These predict the propeller performance by considering each section of the blade in a psuedo 2D manner. Another method is the Vortex Particle Method [3], which has the advantage of numerically propagating the vorticity from the propeller, allowing for a prediction of the interaction between the propeller and other structures on the aircraft in a grid free manner. Accurately shedding vortex particles from the propeller blades requires knowledge of the blade geometry to calculate the lift distribution along the blade span. There are also Computational Fluid Dynamics (CFD) approaches involving mesh-based Reynolds-averaged Navier-Stokes (RANS) simulations [4]. While this is the most comprehensive simulation method, it is computationally expensive. Results from one case at a particular rotation speed, freestream speed, etc. are not necessarily transferable to a different case, making studies inconvenient if one desires to study a multitude of cases. One commonality of all the aforementioned methods, except for the disk actuator method, is that the propeller geometry must be known in some form in order to simulate the aerodynamics properly. Furthermore, while mesh-based simulations might be able to accept a diversity of 3D model formats for the propeller, the lower-order methods require a description of the propeller either geometrically or aerodynamically at stations along the blade span.

With the popularity of computational methods for analysis and performance improvement, accurate 3D models of component geometry are more critical than ever. However, most popular manufacturers of propellers for this size of vehicle do not provide detailed geometric specifications for their propellers and instead only provide the diameter and pitch, a simple measure of the blade inclination. Some suppliers publicly provide design information beyond these metrics [5], but many do not. A lack of published geometry necessitates reverse engineering this data. While databases do exist of some of these efforts [6], they do not keep pace with the wide range of available products for drone enthusiasts and researchers today. There is a clear dearth of accurate and accessible propeller geometry data for researchers. While there are existing techniques for the accurate extraction of propeller geometry, they are often expensive, time consuming, destructive, or some combination thereof. This work addresses the inaccessibility of propeller geometry by outlining a non-destructive technique that requires little specialized equipment, is comparatively rapid compared to similar techniques, and requires little human input. This method is shown to produce geometric data that, when simulated, produced thrust values within 10 % of experimental results.

Requirements and Review of Existing Methods

While various 3D scanning technologies exist, there is always a trade-off among speed, cost, and accuracy. To consider available technologies, we first consider what level of accuracy is needed. Ideally, the measured geometry of the airfoil would be at a resolution such that we could correctly distinguish between two airfoils within the same family. Taking the NACA four digit series for reference [7], the last two digits represent the maximum thickness of the airfoil in percentage of the airfoil's chord. Resolving the cross section with sufficient accuracy to differentiate one four digit airfoil from another, requires ordinates of the airfoil of the propellers cross section to be accurate to within one percent of the station's chord. For the propellers examined in the paper with blade chords of roughly 10 mm, this corresponds to a thickness accuracy of less than 0.1 mm.

A classical method of surface extraction is with a Coordinate Measuring Machine (CMM) [8]. A computer-controlled CMM can measure geometry to very high precision (on the order of microns in some cases [9]), but the process is slow. As a contact based method of measurement, the process may also be sensitive to the flexibility of the part. This displacement can be unacceptably large dependant on the material and size of the propeller and may necessitate an application specific CMM [10]. The hardware required for these scans can also be prohibitively expensive. The probe component alone can cost thousands of dollars [11], far more than might be worthwhile for just one step in a larger process of simulation.

Laser scanning is a similar, more mobile technology suited for the problem. By projecting a slender line onto an object and viewing the resulting contour from a camera with known relative position, the observed contour can be interpreted to create a virtual body. A system capable of measuring the geometry to sufficient accuracy is quite costly however, given the specific application [12].

A popular, low cost, technique for small Uninhabited Aerial System (sUAS)-scale propellers is to cast the propeller in resin, cut the propeller into sections and scan the faces on a conventional document scanner [13, 14]. This has the advantage of having high dimensional accuracy and requiring little specialized equipment, but is time consuming and destroys the propeller. This method of extraction is used for comparison later in this work. Additional low cost propeller-specific techniques include matching the section using a piece of solder [15] which is still time consuming, and measuring the properties using a pitch gauge setup [16] which is simple and quick, but requires a specialized tool and does not convey the airfoil section of the propeller.

Photogrammetry is a potential avenue to sidestep the deficiencies of the preceding methods. Photogrammetry can require very little specialized equipment and theoretically has the requisite accuracy; close range photogrammetry has a potential measurement precision of 1:500,000 relative to the largest object dimension [17]. Photogrammetry has been applied in the field of aerodynamic study previously. One work looks at the accuracy of the method and uses it to quantify wing aeroelastic deflection [18]. Another that successfully extracts a surface from a flapping dragonfly inspired wing uses the surface texture [19].

There exists previous work to extract specifically propeller geometry using photogrammetry. One work [20] details a high quality method using the commercial V-STARS system for marine propeller applications. At the time, the system appeared to require specific patterns of markers to be applied to the surface of the object to be measured, a clear inconvenience for something the size of drone scale propellers. A more recent paper [10] compares various scanning technologies, again for a marine propeller. The paper includes photogrammetry in the comparison, and uses a now defunct commercial package, Photomodeler Scanner [21], as well as a no longer extant online service, ARC 3D [22]. This study also mentions previous work [23] as a basis for some of the work done where the authors developed their own photogrammetry process for evaluation of marine propellers and ship hulls. Another work compares the relative deformation of two blades of a propeller using photogrammetry [24]. This work however still uses targets applied to the surface and only uses the data to compare the geometry between blades rather than extract their base geometry. Lastly, a recent paper [14] aims to achieve very similar goal to the work outlined here, but takes a different approach to the physical modeling of the blade. In that work, a T-spline surface is fit to the photogrammetry mesh, and the result deviates significantly from the true blade section collected by slicing the propeller. Sections illustrated in this work show a rounded trailing edge in contract to the sharp edge that one might expect from an airfoil section. Furthermore, a surface description of the propeller might be appropriate for a mesh-based simulation, but would require additional processing before it could be used in a lower order simulation methods such as BET [1].

Summarizing the results of the literature survey in the previous paragraph, existing work often used a commercial photogrammetry systems or software, required the application of specific markers to the propeller surface, or did not reconstruct the propeller in a convenient format. While commercial off the shelf photogrammetry systems are available, they and other 3D scanning systems are costly. There is a lack of a complete, start-to-finish methodology for those wanting to produce accurate propeller geometry using photogrammetry.

Contribution of the Work

The preceding survey of existing methods highlights both the importance of accurate geometry for modern simulation, as well as the inadequacy or inaccessibility of existing technologies to provide this in a convenient manner. The contributions of this work are as follows. First, a set of systematic guidelines is presented for photo collection to reliably produce a dense and accurate pointcloud of a propeller using photogrammetry. Second, an algorithm for alignment, scaling and feature extraction of the pointcloud that requires minimal human input is presented. Third, in contrast with existing work, we present a complete, end-to-end pipeline uniting all the steps which, to the authors' knowledge, has not been done before. Fourth, the objective of this work is to present the technique with sufficient information to function as a tutorial for the community. This methodology is outlined in Figure 4.1.

Furthermore, while this process was conceived and has been optimized for use with propellers, it is also applicable to adjacent problems. The process could be easily applied to a wing on a UAV with virtually no modifications, and other shapes could be analyzed using the same algorithms if one changed the shape parametrization in the Airfoil Extraction step.

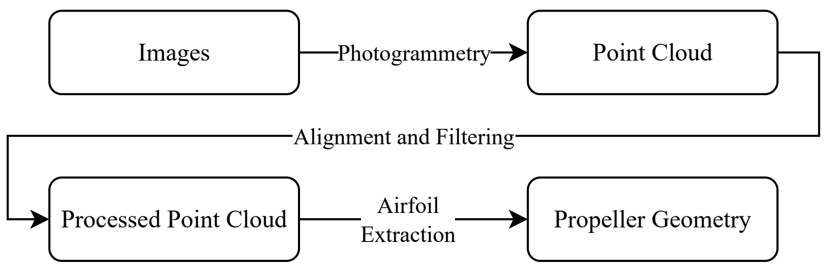

Figure 4.1: Flowchart of propeller property extraction process.

Portions of this work were previously presented at the American Physical Society annual Division of Fluid Dynamics meeting [25]. Progression on this work since then has included improvements in the manual fitting functionality, implementation of the automatic fitting algorithm for coordinate system alignment, and the simulation of the propeller performance as well as its comparison with experimental data. General improvements to the code have also occurred since then to implement these new features and make the process more user-friendly.

Organization

The rest of the paper will follow the ordering shown in Figure 4.1 and is organized as follows. Section 4.2 describes the process by which the point cloud is generated. This includes techniques in the photo collection phase that will improve the quality of the point cloud and a description of the photogrammetry software. Section 4.3 describes the process to align the information to a useful coordinate system, and filter the data. Section 4.4 describes how the propeller properties are extracted from the point cloud. Section 4.5 then takes the results of using the methodology on several propellers and evaluates their accuracy. Section 4.6 takes the computed geometry and simulates their performance, comparing the results against experimental data.

As the techniques described in this work use math from several different fields, nomenclature will be described in specific sections.

4.2 Photogrammetry Setup for Propellers

Generating a quality point cloud is the foundation of this process. The subsequent sections describe techniques relevant to this process that help a user produce quality geometric data for drone propellers.

Available photogrammetry software is now powerful and user friendly enough that a high quality point cloud can be produced with very little knowledge of photogrammetry and with some consideration for the photos taken. The software primarily used in this work to produce the point cloud is COLMAP [26, 27], a general-purpose Structure-from-Motion (SfM) and Multi-View Stereo (MVS) software. While the directions provided in this work reflect the choice of software, many alternative free photogrammetry softwares are available such as Meshroom [28], MicMac [29], Multi-View Environment [30], OpenMVG [31], Regard3D [32], and VisualSFM [33, 34, 35]. As long as the choice of photogrammetry software can produce geometric data that can be edited and manipulated, the user can proceed to use the described techniques to align and filter data. Finally, the described algorithm can be used to fit and extract the relevant the geometric parameters describing the propeller.

Photo Collection

A number of simple considerations, taken into account when photographing the propeller, help the photogrammetry algorithms produce a sufficiently dense point cloud. The techniques described in this section were found to significantly improve the results of the photogrammetry. In this work, image sets were mainly taken with a Sony Rx 10 IV which has a 21 Megapixel sensor. However, it was found that the images from the camera of a modern (at the time of writing) smartphone with a 16 Megapixel sensor could also produce quality results. While higher quality images lead to a better quality point cloud, the required quality of image was not studied in depth. Quantifying image quality can be subjective based on the mechanical limitations of the camera, or image focus and other factors beside pure resolution. Furthermore, the image quality of the camera on a typical smartphone is already sufficient for this application and is generally expected to increase. The setup for how the images are taken, as described in this section, was found to have a much larger influence on the quality of the photogrammetry.

Initially, it was attempted to simply take a video of the propeller and extract still frames for analysis. While this technique had some success, the results had lower resolution than desired. Generally, regardless of if the camera was moved and the object held in place or vice versa, there were issues with focus and motion blur. Any built in video compression would also detract from the still frame quality. Extracting useful frames from the camera, which was supposed to improve the ease of collecting a data set, instead became laborious as frames with minimal blurring were needed to produce a usable point cloud.

It was instead elected to keep the camera at a fixed position with fixed zoom and focus and simply rotate the propeller to extract the point cloud. Though initially a turn-table connected to a servo was constructed to rotate the propeller automatically, placing the propeller on a manually-rotated swivel chair was found to be a better and faster solution. The chair is assumed to remain stationary, however small translations will not impact the results provided the propeller remains in the field of view and acceptable depth of field of the camera.

To help facilitate this, the propeller is placed as near as possible to the axis of rotation of the chair and remains in the same position relative to the camera. By keeping the parameters of the camera such as focal length, zoom, aperture, and ISO constant, there is no need for adjustment between photos as the propeller is rotated, shortening the data collection process. Additionally, fixed camera settings carry the added advantage of simplifying the camera characterization problem, reducing it to just one set of settings for the session rather than a set of unknown characteristics for each image. Although the object would ideally be under consistent lighting conditions throughout image collection, sufficiently diffuse lighting and small enough changes between images still allow features to be recognized effectively in the software.

It was found that roughly 50 images, evenly spaced in a circular pattern around the propeller were sufficient to produce a good quality point cloud. This number was chosen primarily because of the limitations of the photogrammetry process. 50 was the number of images that resulted when photos were taken with a small enough angular displacement for the software to reliably find a solution to the camera positions relative to one another while having photo coverage of the entire propeller. This corresponds to between a 5 to 10 degree angular displacement between shots.

In order to properly extract the propeller surface geometry, there need to be features that can be recognized and correlated between images. Features that are well recognized are typically regions of high color or brightness contrast. Propellers sold for sUAS applications are often a single color and glossy, preventing good feature recognition on their surfaces. To improve feature acquisition, a small variety of patterns were drawn on the propeller surface with a marker of a contrasting color. For example, one of the propellers used in this work was made of a glossy orange plastic, so black marker stood out well and the application of a layer of ink was deemed thin enough such that it would likely not impact the geometry of the propeller or its performance. The patterns drawn on the propeller were a random, medium density speckle pattern as well as a loose grid. The change in quality of the point cloud is clearly visible in different regions of the propeller corresponding to these patterns. The hand-drawn grid was sufficient to produce good results. As seen in Figure 4.2, the effect of the pattern on the point cloud is clear. In region A, the pattern drawn on the hub cylinder wall produces a denser point cloud than that produced at region B, where the lack of pattern has resulted in a gap in the cloud. Likewise, the point cloud density appears adequate around each of the drawn dots in region C, but the sparseness of the dots means that there are still gaps in the surface. In contrast, the grid drawn in region D results in a much higher density point cloud. While a sufficiently dense dot pattern can create a useable point cloud, the authors found the grid pattern to be easier to draw.

Also note that in the point cloud in Figure 4.2b, there are a number of points clustered around the edges of the propeller with the color of the background. A method of addressing these is described in section *Color Based Filtering*.

An alternative to a hand-drawn pattern is a spray painted speckle pattern, similar to what is used in Digital Image Correlation processes. With proper application, the underlying color of the propeller is irrelevant, and the entire surface will have a good quality pattern. It was found that the addition of paint will add roughly 0.025-0.04 mm to a surface. Disadvantages are that the process may impact the propeller's usability on vehicles. Potential effects are unbalancing the propeller and interactions between the surface boundary layer and the paint. Some paints also contain solvents, such as acetone, that could potentially damage the propeller, rendering it structurally unsound.

In addition to applying a pattern to the propeller surface, it was also found important to have a clear, identifiable pattern in the background of the image; a recognizable pattern solely on the object was found to be insufficient. The common features between images provided by the background are used to estimate the position of the camera, which is a critical part of the reconstruction process. A checkerboard pattern, even non-planar and out of focus was found to provide a good reference.

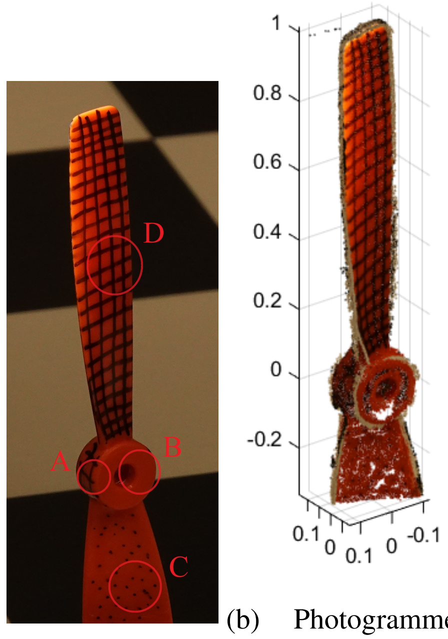

(a) Sample image (b) Photogrammetry point cloud

Figure 4.2: Comparison of point cloud resolution of different regions on the propeller based upon surface pattern.

The challenge, though, is that the background needs to move with the propeller. As the photogrammetry software relies on the assumption of a static scene and a moving camera, having the reverse can cause problems if the region of interest is moved relative to the camera but background elements remain fixed. As the software has no inherent way to identify background elements that are not relevant to the scene, the camera needs to either be set up to exclude these elements, or the images need to be filtered with a mask. As seen in the setup shown in Figure 4.3 this objective is achieved by having the checkerboard pattern rotate with the object. The camera was positioned and the zoom set such that the propeller and checkerboards occupied as much of the field of view as possible, minimizing the effect of the background. This constraint also drove the vertical placement of the camera relative to the propeller. Placing the plain, featureless floor in the background of the shot by facing the camera downwards helped to prevent any features being incorrectly recognized for the camera position calculation.

The application of the described suggestions should reliably produce viable image sets and improve output quality. A summary of these guidelines can be seen in Table 4.1.

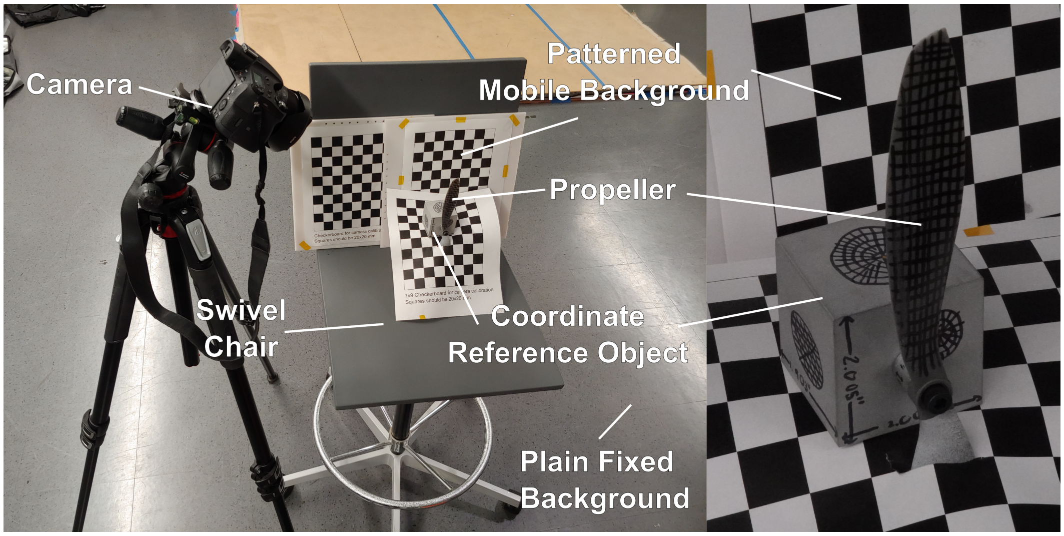

Figure 4.3: Experimental setup used for photo collection.

Guideline	Effect
Propeller on rotating surface, near axis of rotation	Propeller moves rather than camera, allowing for fixed camera settings
Fixed camera settings during collection	Reduces complexity of photogrammetry problem, speeds up collection by removing focusing time
Maximize propeller in field of view	Reduces extraneous points in point cloud, maximizes resolution on the propeller, minimizes stationary background in the frame
High contrast background patterns moving with the propeller	Improves likelihood of correctly calculating camera position, allowing for that image to be used in the reconstruction
Dense, high-contrast pattern on propeller surface	Increases feature recognition on the propeller surface and increases point cloud density
Textured reference object attached to the propeller	Provides coordinate system and scale reference for the point cloud

Table 4.1: Summary of photo collection guidelines.

Point Cloud Generation

In order to reconstruct the 3 dimensional data from the set of captured images, we use a photogrammetry software. COLMAP, the software used in this work, features sparse and dense reconstruction processes. It is expected that a similar procedure can be carried out for any photogrammetry software. The sparse reconstruction process identifies common features within each photo and attempts to extract the camera properties and position for each photo. Using the same camera settings for each shot and taking photos in a sequential manner and selecting the relevant options to take advantage of this improves the success rate of the sparse reconstruction process. A successful reconstruction can be seen in Figure 4.4. The camera positions calculated appear to all lie on the same circle, which is consistent with how the pictures were taken. The view angles are also relatively dense, meaning that all the relevant surfaces of the propeller will get good photo coverage. One of the indicators of a good image set that the authors identified is that the software identifies the relative locations of the camera for all the images in the set without discarding any. This step of the reconstruction takes little time, on the order of minutes, so one can quickly determine if the image set collected is of sufficient quality using this criteria.

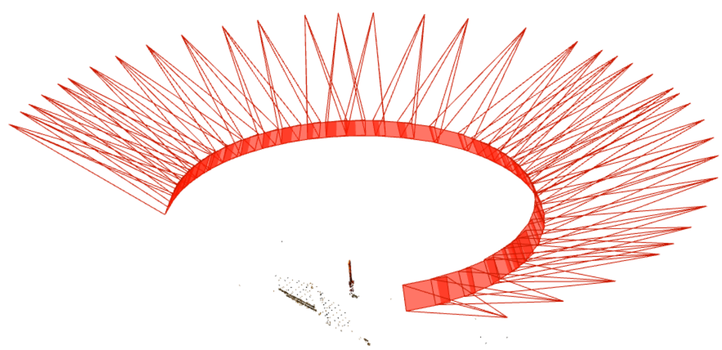

Figure 4.4: Graphical representation of estimated camera positions produced by COLMAP

Once the sparse reconstruction is completed, the dense reconstruction is run on the data. This software requires a computer with a GPU to perform the dense point cloud reconstruction. On a computer with an Nvidia RTX 970 the reconstruction process takes about 1 hour for a set of roughly 50 images. Additional images may improve the resolution, but will also take additional computational time. Given that reconstruction time on the order of an hour produced a point cloud that was considered to be of sufficient density, little study was devoted to comparing size of the image set, reconstruction time, and point cloud quality. Once the dense reconstruction process is complete, the point cloud can be exported for the subsequent manipulations.

4.3 Point Cloud Post-Processing

The raw data produced from photogrammetry needs to be prepped before it can be interpreted. The following sections describe how the data are aligned and cleaned.

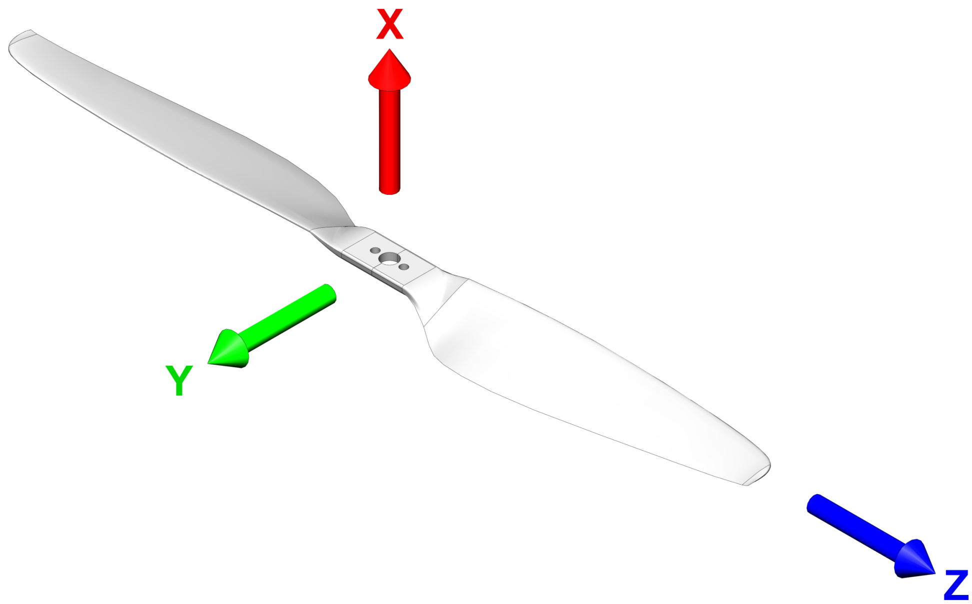

Figure 4.5: Coordinate system for the propeller

Point Cloud Alignment

Initially, the point cloud is described in a coordinate system that is determined by the photogrammetry algorithm, and is functionally random in orientation and scale. To produce useful parameters, we must first orient the data into a more useful coordinate system and scale it accurately. In this work, we choose to place the coordinate system origin at the center of the propeller hub and orient the blade such that the propeller's thrust axis is aligned with the positive X-axis and the blade of interest is aligned with the positive Z-axis. The Y-axis is then chosen to form a right handed coordinate system. An illustration of this is shown in Figure 4.5. The correct scaling is determined using a reference from the scene that is of known length.

Manual Alignment Process

Manual coordinate system alignment is possible, but relies on visually determining whether parts are at the correct angles. To do this, we select two points, one near the blade tip and one near the blade root to use as our first pass at a Z basis vector. The data is then transformed and displayed, and rotation corrections are applied to orient the data as desired.

The specifics of the process are the following: choose two initial points x_a and x_b from the point cloud such that x_a is near the root of the blade and x_b to be near the tip of the blade.

$$\vec{v_1} = \frac{\vec{x_b} - \vec{x_a}}{||\vec{x_b} - \vec{x_a}||} \tag{4.1}$$

$$\vec{v_2} = \vec{v_1} \times \vec{i_x} \tag{4.2}$$

$$\vec{v_3} = \vec{v_1} \times \vec{v_2} \tag{4.3}$$

$\vec{i_x}$ is the unit vector in the global X direction, simply to provide a starting point to produce a vector orthogonal to $\vec{v_1}$. The orthonormal basis describing the propeller coordinate system in the initial point cloud coordinate system is described by the matrix

$$\vec{A} = [\quad \vec{v_2} \qquad \vec{v_3} \qquad \vec{v_1} \quad]\,. \tag{4.4}$$

We then apply rotations using an XYZ rotation sequence to visually correct the misalignment. Finally, the data is scaled to match the physical dimensions of the propeller. The scaling is done by identifying an object with known size within the point cloud, and linearly scaling all the coordinates until the size of the reference object in the point cloud reflects reality. In the data collected, the calibration pattern with a checkerboard of known size was used as a reference for length. Lastly, we shift the point cloud such that the origin is coincident with the center of the propeller hub. The complete transformation from points in the raw point cloud coordinate system X_{raw} to points in our chosen working coordinate system X_{working} is

$$X_{\text{working}} = S_{\text{Length}}\left(R_x R_y R_z(\vec{A} X_{\text{raw}}) - X_0\right) \tag{4.5}$$

$$R_x = \begin{bmatrix} 1 & 0 & 0 \\ 0 & \cos(\theta_X) & -\sin(\theta_X) \\ 0 & \sin(\theta_X) & \cos(\theta_X) \end{bmatrix}$$

$$R_y = \begin{bmatrix} \cos(\theta_Y) & 0 & \sin(\theta_Y) \\ 0 & 1 & 0 \\ -\sin(\theta_Y) & 0 & \cos(\theta_Y) \end{bmatrix}$$

$$R_z = \begin{bmatrix} \cos(\theta_Z) & -\sin(\theta_Z) & 0 \\ \sin(\theta_Z) & \cos(\theta_Z) & 0 \\ 0 & 0 & 1 \end{bmatrix}$$

where S_{Length} is the scaling factor used, calculated as $L_{\text{true}}/L_{\text{raw}}$. L_{raw} is the length of a reference object or distance within the point cloud and L_{true} is the analogous true distance in a chosen unit system. X_0 is the coordinate of the desired origin within the original raw coordinate system.

Automatic Alignment with a Known Reference Object

If available, a more convenient alternative to visual point cloud orientation is to include a reference object of known dimensions and orientation relative to the propeller. In this work, a rectangular prism was machined for this purpose. The prism was then bead blasted to a matte finish so reflections would not interfere with the photogrammetry and patterns were drawn on the faces for improved recognition. A hole was also drilled and tapped to install the propeller at a known position relative to the cube.

Fitting of the point cloud to the known object geometry is conducted through a mix of user inputs and a point-to-plane algorithm. As the photogrammetry process used has no means of establishing an initial orientation or scale, the user first selects seed points on the surface of the cube as represented in the point cloud. Points within a user defined radius of each seed point are then chosen as sample points of each planar face. By having the user identify which faces of the object these points refer to, this provides an initial guess to orient and scale the point cloud. As shown in Figure 4.6, the initial point cloud is in a seemingly random orientation with an indeterminate scale. The highlighted points are then used to orient the point cloud closer to the desired coordinate system.

A point-to-plane algorithm [36] can then be used to match points to their corresponding reference geometry. The algorithm cited was modified to compute the correct scaling. In the work, the rigid transformation is described by a combination of translation and rotation operations described by augmented matrices $\vec{T}$ and $\vec{R}$, respectively.

$$\vec{M} = \vec{T}(t_x, t_y, t_z) \cdot \vec{R}(\alpha, \beta, \gamma) \tag{4.6}$$

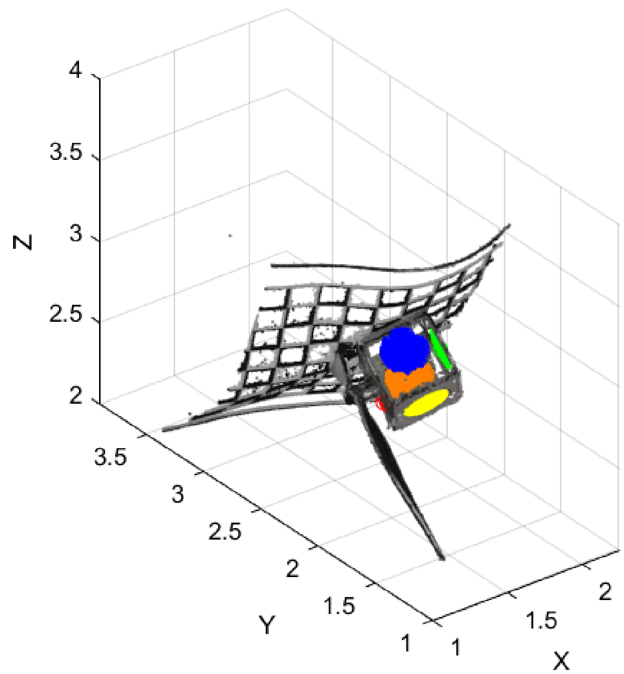

Figure 4.6: Raw point cloud with points on faces used for alignment highlighted.

We add a scaling matrix $\mathbf{S}(L)$ to the transformation to account for the unknown scale of the point cloud initially.

$$\mathbf{S}(L) = \begin{pmatrix} L & 0 & 0 & 0 \\ 0 & L & 0 & 0 \\ 0 & 0 & L & 0 \\ 0 & 0 & 0 & 1 \end{pmatrix} \tag{4.7}$$

Applying the scaling before the other transformations changes the full transformation to

$$\mathbf{M} = \mathbf{T}(t_x, t_y, t_z) \cdot \mathbf{R}(\alpha, \beta, \gamma) \cdot \mathbf{S}(L). \tag{4.8}$$

This propagates well through the subsequent steps in the work, resulting in a slightly altered, but still linear system of equations that can be solved in a similar fashion to the original system.

$$\mathbf{Ax} = \mathbf{b} \tag{4.9}$$

$$\mathbf{a} = \begin{pmatrix} s_1 \times n_1 \\ s_2 \times n_2 \\ \vdots \\ s_N \times n_N \end{pmatrix} \tag{4.10}$$

$$\mathbf{A} = \begin{pmatrix} a_{1x} & a_{1y} & a_{1z} & n_{1x} & n_{1y} & n_{1z} & ns_1 \\ a_{2x} & a_{2y} & a_{2z} & n_{2x} & n_{2y} & n_{2z} & ns_2 \\ \vdots \\ a_{Nx} & a_{Ny} & a_{Nz} & n_{Nx} & n_{Ny} & n_{Nz} & ns_N \end{pmatrix} \tag{4.11}$$

$$ns_i = n_{ix}s_{ix} + n_{iy}s_{iy} + n_{iz}s_{iz} \tag{4.12}$$

$$\mathbf{x} = \begin{pmatrix} \alpha L & \beta L & \gamma L & t_x & t_y & t_z & L \end{pmatrix}^T \tag{4.13}$$

$$\mathbf{b} = \begin{pmatrix} n_{1x}d_{1x} + n_{1y}d_{1y} + n_{1z}d_{1z} \\ n_{2x}d_{2x} + n_{2y}d_{2y} + n_{2z}d_{2z} \\ \vdots \\ n_{Nx}d_{Nx} + n_{Ny}d_{Ny} + n_{Nz}d_{Nz} \end{pmatrix} \tag{4.14}$$

Here $\vec{s}_i = (s_{ix}, s_{iy}, s_{iz}, 1)^T$ is a source point, $\vec{d}_i = (d_{ix}, d_{iy}, d_{iz}, 1)^T$ is the associated destination point, and $\vec{n}_i = (n_{ix}, n_{iy}, n_{iz}, 0)^T$ is the unit normal vector associated with the destination point.

By selecting a minimum of four faces from the reference object, the algorithm is able to align a coordinate system to the object as well as identify a correct scale. Shifting the origin to the desired location on the propeller is then easily done by offsetting the point clouds coordinates using knowledge of the propeller's mounting to the reference object.

Color Based Filtering

Since the initial point cloud produced by the photogrammetry is indiscriminate in what objects it digitizes, there are a large number of extraneous data points. We wish to only examine the point cloud representing the propeller blade. Once the point cloud has been transformed into the desired coordinate system, we select a region of interest in the vicinity of the blade and remove all datapoints outside of it. This removes points associated with background objects, leaving just the points associated with the blade to be examined.

An additional challenge is the "noise" present primarily at the leading and trailing edges of the propeller. These points are generally present because the photogrammetry algorithm has no way to distinguish near and far objects at a sharp edge. One option to remove extraneous data is to use *a priori* knowledge of the propeller color or the background to exclude any points that have an associated color sufficiently close to those of objects we would like to remove. Though relatively simple, the method results in a substantial improvement in the point cloud quality. For this work, a simple euclidean distance was used. If the chosen color to be removed is described by RGB values r_{filter}, g_{filter}, b_{filter}, and the color of the ith point is described by r_i,g_i,b_i, then the criteria to filter certain points out is

$$\text{Remove if } (r_i - r_{\text{filter}})^2 + (g_i - g_{\text{filter}})^2 + (b_i - b_{\text{filter}})^2 < c_{\text{filter}}. \tag{4.15}$$

The cutoff constant c_{filter} requires some tuning to filter the correct points. One method to help identify the cutoff is to plot the distance between the colors on a histogram, such as in Figure 4.7. If one is seeking to remove a large group of points with similar colors, then there should be a spike near the lower end of the scale. Other dominant colors, like those of the propeller and its pattern, should be grouped together, but have a larger value, suggesting an upper limit for c_{filter}.

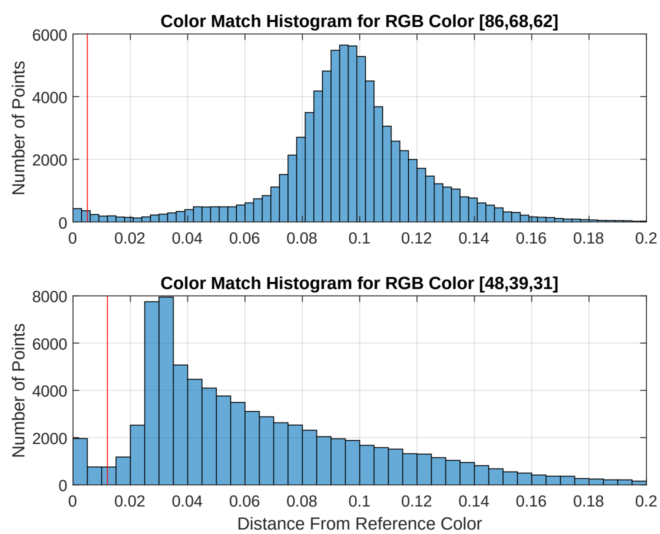

Figure 4.7: Example histogram showing matches to selected colors within the point cloud with cutoff threshold indicated in red.

Figure 4.8 illustrates the points removed using such a filtering method and how removing these data points improves the quality of the individual sections. On some parts on the blade, the filtering does remove portions of the blade surface, so care must be taken to ensure that enough data remains for a usable fit.

4.4 Propeller Property Extraction

Once the point cloud is constructed, there is still the task of converting the raw cloud data into meaningful propeller design parameters. Photogrammetry softwares often have the option to attempt a mesh construction based on the data, but the result is

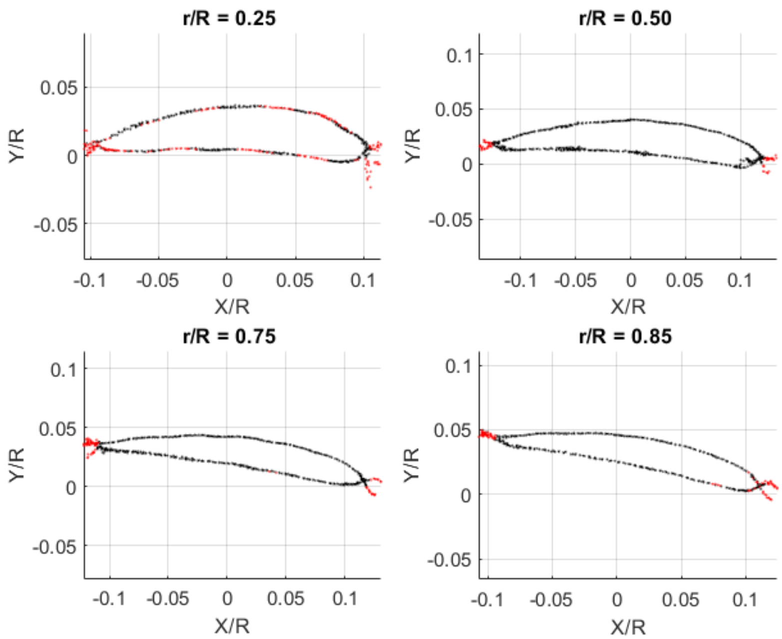

Figure 4.8: Sample of sections along the blade with data filtered out highlighted in red.

not necessarily superior to working with the point cloud. The mesh is potentially useful in CFD, but does not by itself describe the propeller in a useful parametric format. Figure 4.9 shows cross sections of an example of a constructed mesh.

The cross sections show that the generated mesh is not necessarily smooth and that portions of the noise on the leading and trailing edge have been incorporated into the geometry. This absorption removes the points that correctly reflect the position of the leading edge, making identifying it more difficult. We can instead use the knowledge that the blade was likely designed with a series of airfoils to examine 2D slices of data and fit an airfoil to it to produce geometric information that would be useful for a designer reconstructing the blade. With this approach it is more sensible to use the original point cloud data and fit to all available points rather than do a similar action with a generated mesh.

Propeller Design Assumptions

Some basic assumptions are made of how the propeller is designed - the propeller has relatively smooth functions to describe the chord, twist, and other airfoil properties along the radius. It is also assumed that the propeller is designed using a series of 2D airfoils at various radial stations. This provides a convenient starting point for our geometry extraction. Rather than trying to reconstruct a 3D shape from

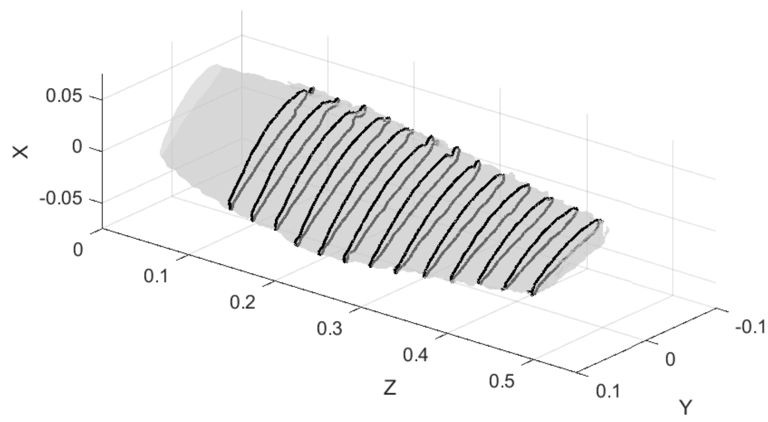

Figure 4.9: An unscaled automatic triangular mesh produced from the point cloud with cross sections highlighted.

a point cloud, we can use nearby data to recreate a number of 2D shapes with initial knowledge of what the shape should look like. To be compatible with BET, the geometry is extracted along planes perpendicular to the spanwise axis of the propeller blade. Though this technique may be applied to any airfoil that can be represented by a series of coordinates, this implementation restricts the airfoils to NACA 4-digit series, reducing the optimization space to simply a camber, thickness, and camber location.

Automatic Fitting Algorithm

In order to minimize required human input, an automatic fitting algorithm was developed to fit 2D contours to the point cloud data. This was done by formulating the problem as an optimization problem to be solved using a coventional optimization software pacakge (e.g., MATLAB's FMINCON function). This function requires a cost function as well as various constraints. A flowchart illustrating the Automatic Fitting Algorithm is shown in Figure 4.10.

Blade Subdivision

To extract the airfoil parameters, a number of radial stations are selected at which to fit the airfoils. At each station, a slice of the point cloud is chosen by defining a plane perpendicular to the Z-axis at this radius and projecting nearby points onto

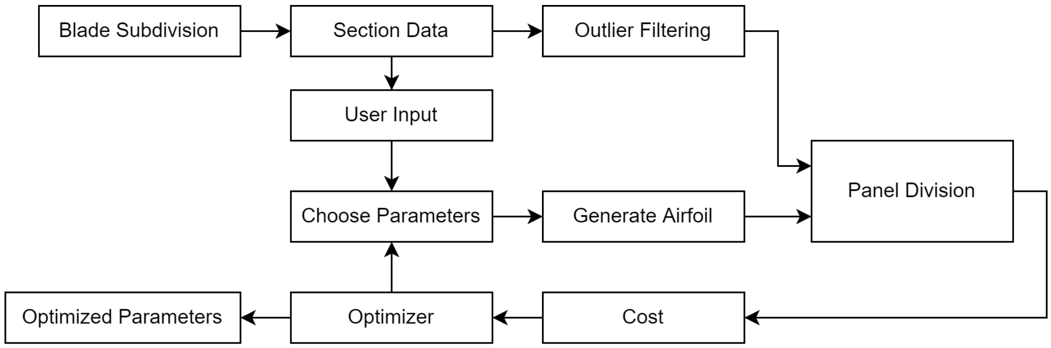

Figure 4.10: Automatic airfoil fit algorithm.

the plane. Increasing the number of points to project allows for more points for fitting the profile, but choosing points that are too far from the section will sample data from an airfoil section that can be significantly different to the airfoil at the the current radius. For the propellers examined in this work, sampling a maximum of 0.25 mm from the plane was found to produce enough points for a reasonable fit while being deemed close enough to accurately represent the chosen 2D section. Once this pseudo 2D data has been assembled, it can then be used to fit a contour.

User Input Seed

As an initial seed for the rest of the optimizer, a section is chosen at approximately the mid-radius portion of the blade. The user then is presented the section data from a narrow slice in this region and selects the approximate leading and trailing edge locations and the a point in the "up" direction of the profile. To better correspond with typical convention of airfoil coordinates, this selection also defines the coordinate system used for fitting the remaining sections. This coordinate system is defined by an origin at the section leading edge, the airfoil trailing edge being at $[1, 0]$ and the Y-axis pointing in the "up" direction of the airfoil. With this conversion, the airfoil fit should be provided a fairly optimal initial guess. A successful fit can then be used as an initial guess for adjacent sections provided the sections are similar enough to the provided initial guess.

Airfoil Fit Cost Function

In order to determine a best-fit airfoil for the provided data, a cost function is needed. For this work, a distance based least squares function is used, but calculating the distance to an arbitrary contour requires some additional processing. As the contour is represented by a finite series of panels, this is done numerically by calculating the distance to the nearest straight line segment that represents the contour. The result is an optimization statement that can be described by Eq. (4.16), where $n_i(x)$ is the normal distance computed by the ith point based on the contour defined by the parameters x. The problem can also have constraints to x should the user choose, though these would be specific to the parameterization chosen.

$$\arg\min_x \sqrt{\sum_{i=1}^{N} (n_i(x))^2} \tag{4.16}$$

Panel Division

In order to calculate the appropriate panel for a given point, it was necessary to determine which panel represented the "closest" option. To do this, we used angular bisecting domains associated with the interface of each panel to divide the domain into regions of interest. A graphic representation of this is shown in Figure 4.11. Here, we search for points that best correspond to panel BC. We find this by first looking at its adjacent panels AB and CD. We find the region on the BC side of the bisector to angle ABC, shown in red, and do the same for angle BCD, shown in green. Points in the overlap region are considered to be in panel BC's region of influence, and their distance from the line segment BC is used to calculate the cost. In high curvature regions, the regions of influence of non-adjacent panels might overlap. In these cases, we examine all the distances to valid panels for a given data point and simply choose the smallest distance to add to the cost.

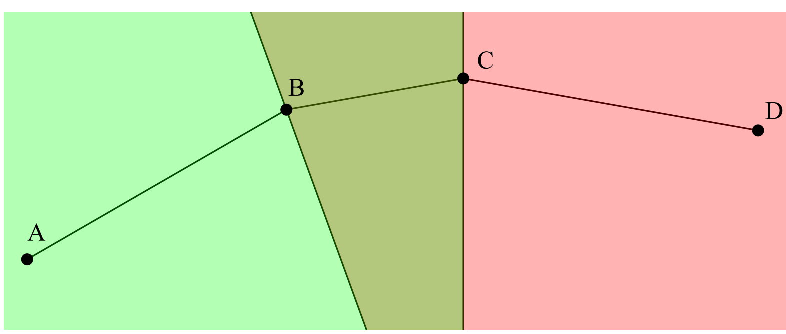

Figure 4.11: Graphical illustration of panel division.

Outlier Filtering

Because of the significant amount of noise at the leading and trailing edge of the blade (even with the color-based filtering), it was desired to remove these points from consideration. One approach was to remove approximately the first 5 % and last 5 % based on chord of the profile data and have the fit carried out on only the mid-section of the data. In cases with substantial amounts of extraneous leading and trailing edge points but good quality midsections, this truncation can improve the fit accuracy.

Chosen Parameters

The airfoil at each propeller section is assumed to be sufficiently described by a NACA 4-digit series airfoil [7] as a wide number of airfoil shapes can be represented through these equations. The equation for describing the thickness of the airfoil is

$$y_t = 5t\left[0.2969\sqrt{x} - 0.1260x - 0.3516x^2 + 0.2843x^3 - 0.1015x^4\right] \tag{4.17}$$

where x is the position from 0 to 1 and t is the maximum thickness. The equation to calculate the mean camber line is

$$y_c = \begin{cases} \frac{m}{p^2}(2px - x^2), & 0 \le x \le p \\ \frac{m}{(1-p)^2}((1-2p) + 2px - x^2), & p \le x \le 1 \end{cases} \tag{4.18}$$

where m is the maximum camber and p is the location of the maximum camber. Lastly, with the adjustment of camber, the ordinates describing the airfoil contour are

$$x_U = x - y_t \sin(\phi),\ x_L = x + y_t \sin(\phi) \tag{4.19}$$

$$y_U = y_c + y_t \cos(\phi),\ y_L = y_c - y_t \cos(\phi) \tag{4.20}$$

where ϕ is defined as

$$\phi = \arctan\left(\frac{dy_c}{dx}\right) \tag{4.21}$$

$$\frac{dy_c}{dx} = \begin{cases} \frac{2m}{p^2}(p - x), & 0 \le x \le p \\ \frac{2m}{(1-p)^2}(p - x), & p \le x \le 1 \end{cases} \tag{4.22}$$

In addition to the parameters describing the airfoil, we also have the parameters used to fit the airfoil to the point cloud. The parameters used are Δx, Δy, θ, ΔL. These control the displacement, angle, and scaling from the base airfoil that goes from 0 to 1 on the x-axis to transform it to a position to match the data. The variables are used in the following transformation to transform the airfoil

$$\begin{bmatrix} x_1 \\ y_1 \end{bmatrix} = \Delta L \left(\begin{bmatrix} \cos(\theta) & -\sin(\theta) \\ \sin(\theta) & \cos(\theta) \end{bmatrix} \begin{bmatrix} x_0 \\ y_0 \end{bmatrix} + \begin{bmatrix} \Delta x \\ \Delta y \end{bmatrix} \right). \tag{4.23}$$

Section Initial Guess and Parameter Bounds

The user provided input for the initial foil section provides a good initial guess for the airfoil position, meaning that the displacement, angle, and scale should all be close to 0,0, and 1, respectively. The initial airfoil guess is a NACA 0012, but the bounds on the parameters are kept wide as the initial airfoil is not known.

An initial guess is still needed however for each of the remaining sections. A logical choice would be the parameters of an adjacent section. Because we assume the propeller blades studied have continuous geometry, the airfoil properties should also change continuously as we move along the radius. Therefore, for small enough subdivisions, we can use the fit from an adjacent section as an initial guess. Applying parameter bounds that are near this guess allows the airfoil to evolve along the blade while keeping it similar to an adjacent section fit. For the analyses done in this work, the bounds relative to the initial guess were .1 chords in each direction for displacement, 3 degrees in each direction for twist angle, and a factor of 20 % in either direction for scale.

Optimizer Test Case

To evaluate the basic functionality of the optimizer, it was run on a pointcloud of artificial data from a known airfoil. The results can be seen in Figure 4.12 and numerical results are tabulated in Tables 4.2 and 4.3. As is shown, the optimizer produces results accurate to within 10 %, even with introduced positional noise of the data, and with the leading and trailing 10 % of the airfoil truncated to simulate elimination of low quality region from the photogrammetry.

Parameter	Thickness (%)	Camber (%)	Cam Loc (%)
True	12	2	40
Calculated	11.97	1.92	42.04
Percent Error	0.23	4.18	-5.1

Table 4.2: Optimizer results on a test case – airfoil properties

Parameter	dX (l/chord)	dY (l/chord)	θ (deg)	Scale
True	0.1	0.15	2	1.1
Calculated	0.0929	0.1496	1.9766	1.1055
Percent Error	7.15	0.24	1.17	-0.5

Table 4.3: Optimizer results on a test case – position and scale

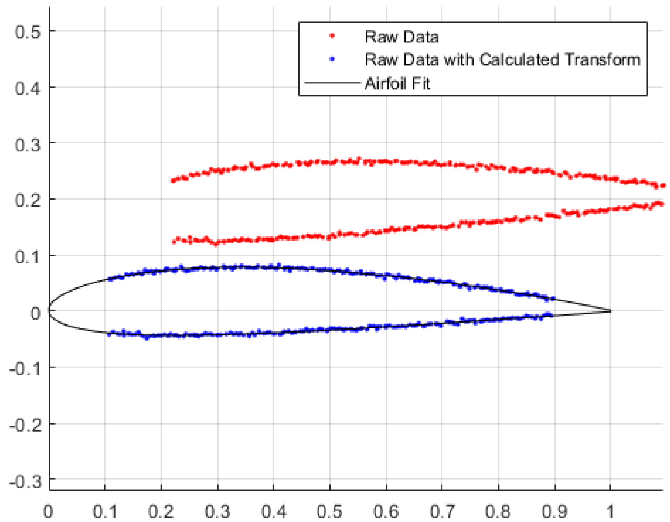

Figure 4.12: Demonstration of fitting algorithm results.

Manual Extraction

Though the automatic airfoil fitting is convenient, it relies on *a priori* knowledge of the airfoil type and clean point cloud data. Depending on the availability of these resources, it may be quicker and easier to extract the blade parameters manually using user input. By having the user select the positions of the leading and trailing edges of sampled radial sections, the twist and chord of the blade can be computed in a matter of minutes. This method is useful for some cases such as the APC 10-inch propeller used in this work. As the manufacturer provided an E63 aifoil as the main airfoil used along its span, the airfoil is already known, and extraction of the twist, chord, and leading edge location are the necessary parameters.

Manual extraction can still be used in conjunction with the automatic airfoil fitting. In this case, the optimizer only needs to find optimum values for the airfoil parameters of thickness, camber, and camber location. These values are difficult to extract by hand otherwise, so the automated portions of the process can still provide some utility.

Fitting the airfoils to the cross sections and overlaying them over the processed point cloud can be seen in Figure 4.13.

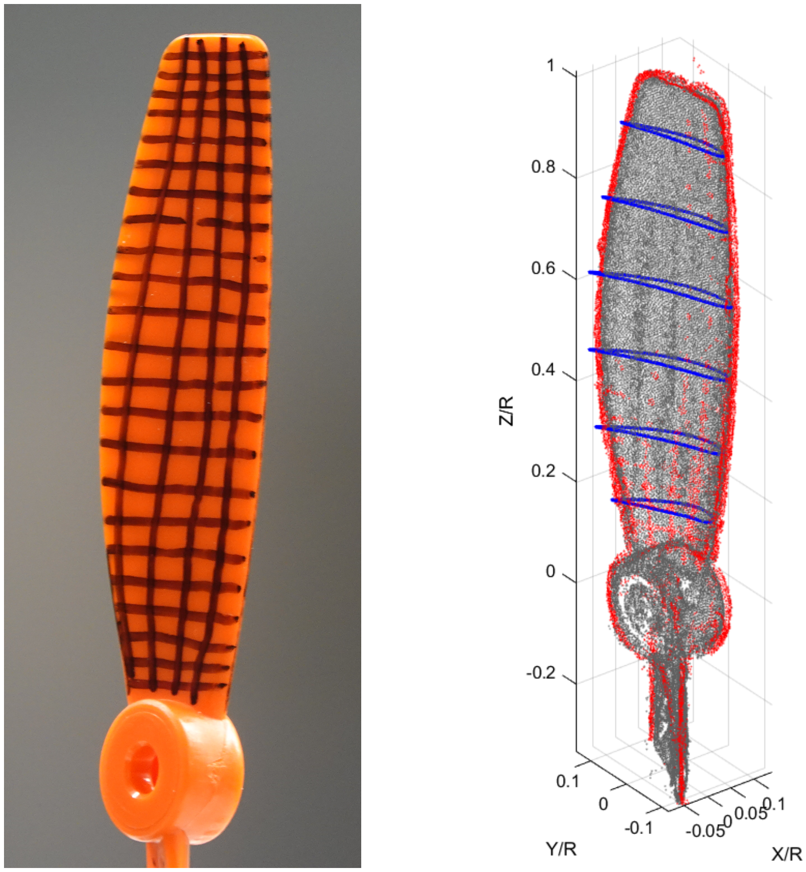

Figure 4.13: Point cloud data with points filtered out in red and fitted airfoils drawn in blue alongside picture of the propeller for reference.

4.5 Photogrammetry Results

Destructive Extraction

To compare the photogrammetry against some form of truth, the propeller was cast in resin and sliced into sections so that the cross sections could be compared. Casting was done by 3D printing a prismatic mold to place the propeller into and pouring an opaque colored epoxy resin in to fill the void. The enclosure had a mount so that the propeller could be bolted at a known angle relative to the walls of the cast, but some inaccuracy in this persisted, as described later. Once the epoxy set, it was removed from the mold and sliced into wafers on a vertical milling machine using a slitting saw. By using the vertical mill's digital encoders, the relative position of the faces of each of the sliced wafers was known to high accuracy (≈ 0.025 mm). Each wafer was then scanned on an Epson V600 scanner at 6400 dpi to digitize each section. The section contours were found using a subpixel edge detection algorithm [37].

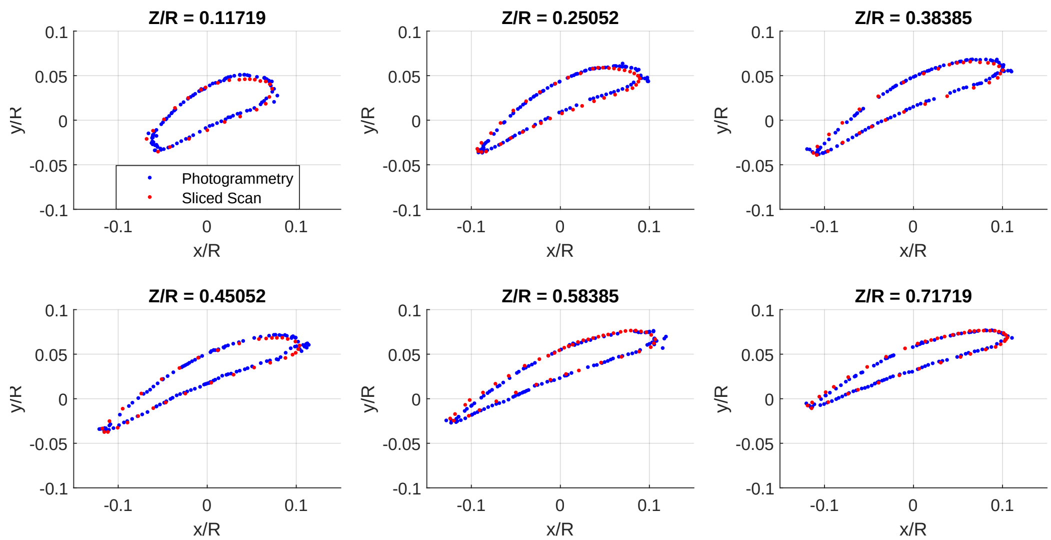

Figure 4.14: Comparison between point cloud and sliced section data on the DAL-PROP 6045.

Figure 4.14 shows that the curves at arbitrary stations produced by photogrammetry show close agreement with the points collected during the destructive extraction.

Photogrammetry Resolution

The algorithm used by COLMAP relies on the presence of "corners" within the image, something a grid provides. Nevertheless, some loss of accuracy can still be seen within regions of one color. For example, as seen in Figure 4.15a, the points in the regions between the black lines appear to have a larger spread than in the regions at the color interfaces.

Note that the physical section seen in Figure 4.15b which is the same station as the points sample for Figure 4.15a does not converge to a point at the trailing edge as one might expect an airfoil, but that the photogrammetry still qualitatively picks up the slightly blunt trailing edge.

Determining a metric for error in the process is difficult because of a lack of a geometric truth for the propellers evaluated. Even the destructive extraction requires optical measurement and still only produces points rather than a contour against which to check accuracy. As a measure of the point cloud accuracy, we compute the root mean square of the normal distance from the airfoil contour that is fit at each section of the point cloud to each of the points used for that section. The results for the 5 propellers scanned in this work are shown in Figures 4.16 and 4.17.

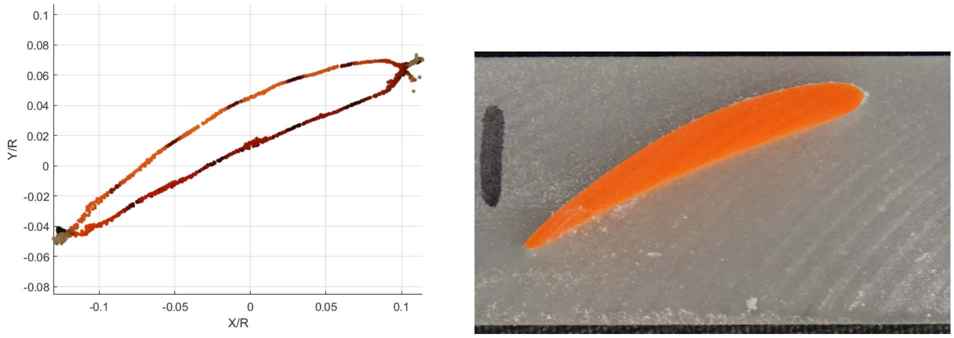

(a) (b)

Figure 4.15: Illustration of accuracy of point cloud versus the physical section.

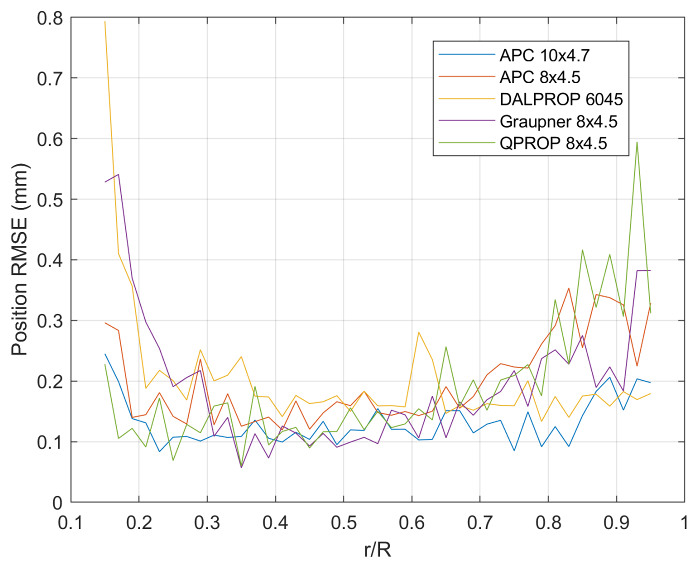

Figure 4.16: RMSE position error relative to fitted airfoil along propeller radius

We see that, relative to the fit airfoil, positional error varies significantly by radial position. Figure 4.16 shows that the estimated error is comparable to the desired level of accuracy of 0.1 mm for much of the blade. At the blade root, the higher error is expected, as the profiles here begin to blend into the propeller hub, and do not correspond well to the NACA 4-digit series. Near the tip, the error is again high as expected. The photogrammetry algorithm has difficulty with edges, leading to a larger number of extraneous points as well as points associated with the background, that are falsely attributed to the blade. The 10 inch APC and the Dalprop propellers have relatively low error in the tip region, likely because their colors (grey and orange, respectively) have high contrast relative to the background and extraneous points are more easily filtered out. The remaining propellers are all black with a

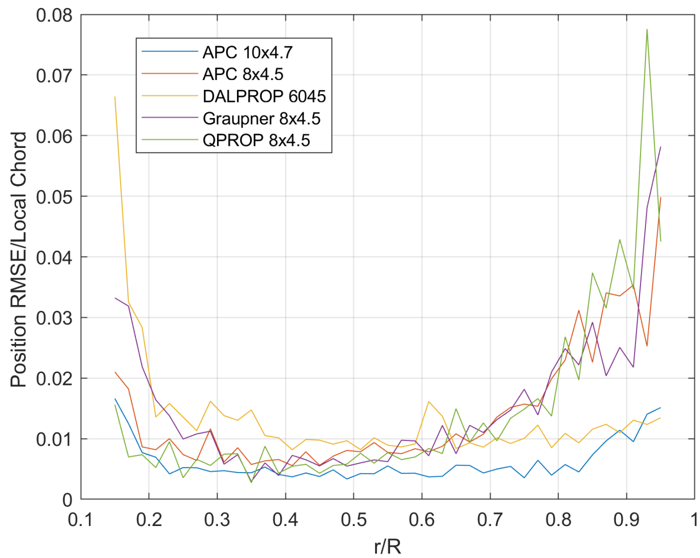

Figure 4.17: RMSE position error relative to fitted airfoil along propeller radius, normalized by local chord

white pattern drawn on, which ended up not being sufficiently high contrast to the background. The fact that the chord tends to decrease near the propeller tip also accentuates the apparent error, visible by comparing the tip regions of Figures 4.16 and 4.17. In regions with good quality, such as in the vicinity of 0.5 r/R, the error for all the propellers is less that 1 %, which is within the goal specified above to be able to differentiate different airfoils within the NACA 4-digit family. This corresponds to a dimensional accuracy of roughly 0.15 mm in most instances on these propellers.

Comparison of Parameters

For the 10-inch APC propeller, we can compare basic propeller metrics between the published values, the destructive extraction, and the photogrammetry. In Figure 4.18, we see that the contours of the published data, the destructive extraction, and the photogrammetry are in close agreement. In fact, the destructive extraction technique appears to have a fixed offset error in the twist angle. This is likely caused by either a consistent error in how the cut sections were positioned in the scanner, or an error in the propeller angle in the casting prior to slicing. The error it highlights the difficulty of correctly aligning the propeller when analyzing its sections, as even a few degrees of misalignment will translate to the extracted specifications. Also plotted on the twist graph is the twist angle computed by the advertised blade pitch, which shows that APC's propeller follows the contour quite closely.

Figure 4.19 shows a similar analysis for the 6-inch propeller, and also demonstrates the accuracy of the automatic fit. While the automatic fit has good agreement with the shape of each curve, it is offset slightly in chord magnitude. The cause of this can be traced to the chosen airfoil type used for fitting. As shown in Figure 4.20, although the airfoil fit matches the upper and lower surfaces of the airfoil on the 6-inch prop well, the truncated section leads to the fit overestimating the chord and, due to the camber, dropping the trailing edge leading to an overestimation of the local twist. If a airfoil with a different parameters that was capable of matching the true shape better were used in the fitting algorithm, the twist and chord would likely be more accurate. As it is known that the leading edge geometry can have a significant effect on the performance of an airfoil, it may be desirable for users in the future to choose a parametric airfoil that is better able to represent the airfoil section of the propeller.

The twist computed using the propeller pitch is plotted as well for comparison. Unlike the APC prop, this propeller seems to use the pitch length as more of a mild suggestion. The fact that this propeller does not use the pitch length as the basis for its twist distribution highlights the importance of extracting the geometry rather than relying on assumptions of the propeller design.

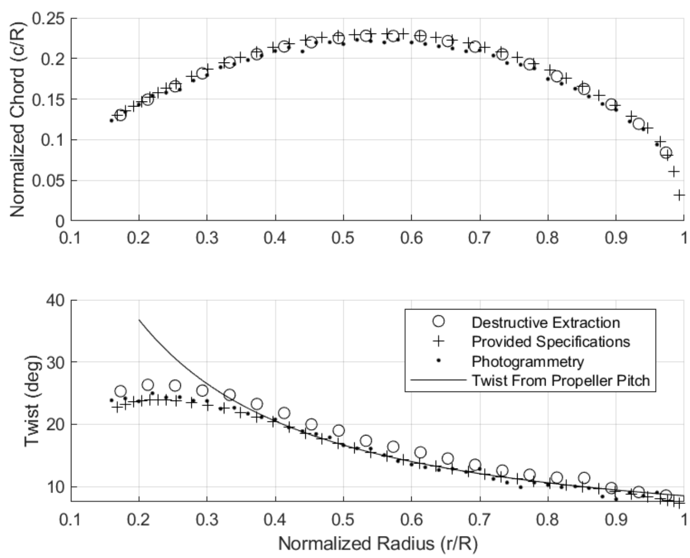

Figure 4.18: Comparison of Twist and Chord extracted using various methods for a 10-inch propeller.

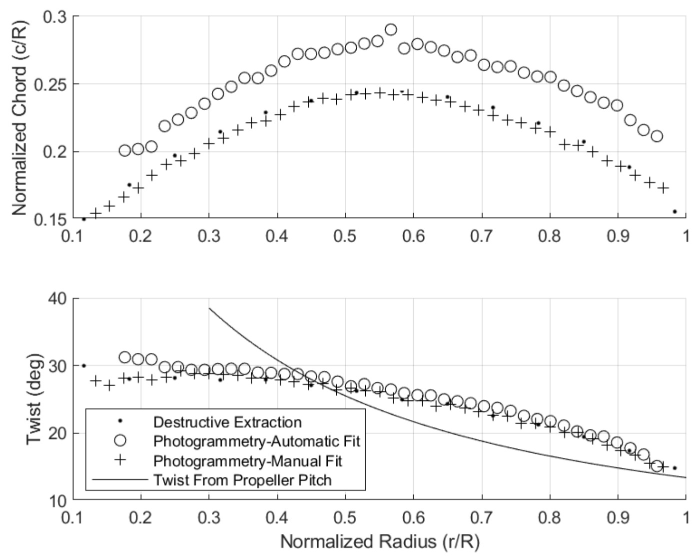

Figure 4.19: Comparison of Twist and Chord extracted using various methods for a 6-inch propeller.

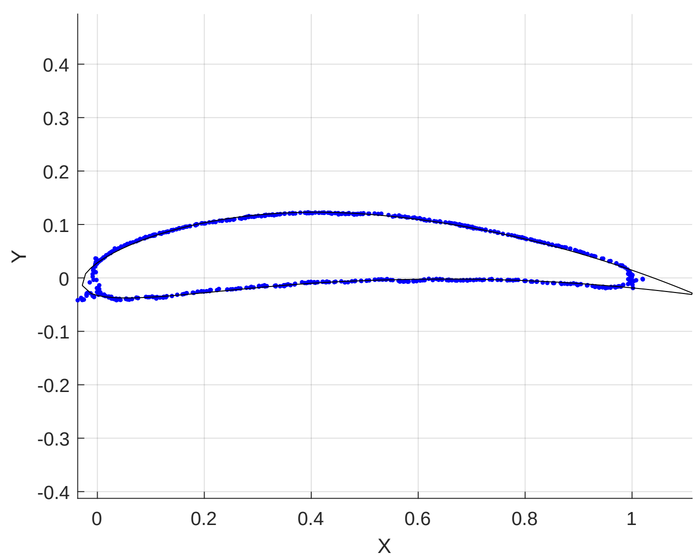

Figure 4.20: Fitted airfoil to section from 6-inch propeller.

Extraction of airfoil camber and thickness is tedious, even with high quality points representing the upper and lower surfaces. This is because the points are unstructured, while computing camber and thickness requires comparing coordinates for points that are at the same station along the chord. Nevertheless, a best attempt at calculating these values is illustrated for the 6 inch propeller in Figure 4.21. As is expected, there is a fair amount of noise in these measurements along the span, and they have similar shapes but some disagreement. The difference in thickness can be explained as before by the fitting producing a longer chord than the true section. A longer chord for the same thickness would produce a lower thickness ratio than truth.

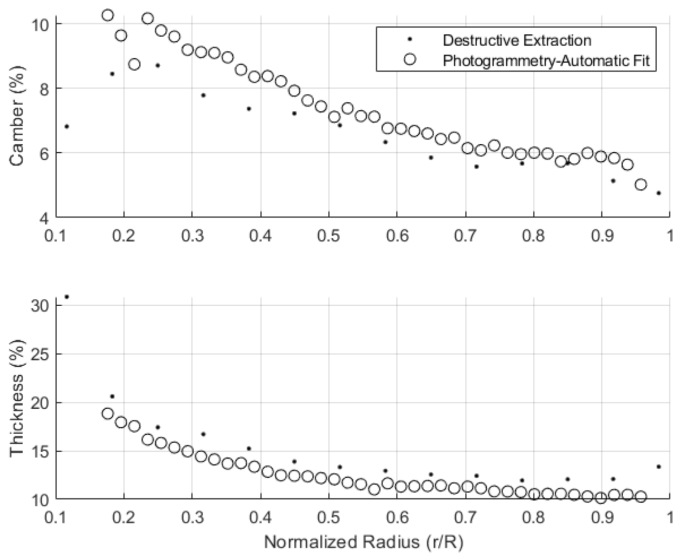

Figure 4.21: Comparison of Camber and Thickness extracted using various methods for a 6-inch propeller.

4.6 Propeller Force Prediction

Experimental Data

Force and torque data were collected for the propellers studied on a commercial off the shelf RCbenchmark 1585 thrust stand [38]. The stand takes real time measurements of thrust, torque, current, and other relevant performance data. The stand also features a scripting mode which allows it to spin the propeller in a sweep of rotational speeds and record the data automatically. Once the data are collected, they can be compared to the experimental data at similar operating conditions.

Simulation Prediction

With the geometry of the propeller known, the propeller can be modeled and simulated for a variety of analyses. To simulate the performance of each of the propellers scanned, we use the software QPROP [39]. QPROP uses a classical blade element and vortex formulation described in its associated theory guide.

One requirement of BET is to have some model of the section lift and drag for sections along the propeller blade. Determining the lift and drag polars for an arbitrary airfoil section is done numerically as there is no guarantee that the fitted section corresponds to one with available data. The airfoil performance is calculated using XFOIL [40], and the subsequent information provided to QPROP. QPROP models the airfoil properties in the following manner

$$c_l(\alpha) = (C_{L_0} + C_{L_a}\alpha)\frac{1}{\sqrt{1 - M^2}} \tag{4.24}$$

where C_{L_0} is the lift coefficient at 0 angle of attack, C_{L_a} is the lift curve slope, and M is the Mach number, which is used for the local Prantdl-Meyer compressibility factor. The bounds of the airfoil model are also specified with the variables $C_{L_{min}}$ and $C_{L_{max}}$ indicating the minimum and maximum lift coefficients. The drag coefficient of the airfoil is modeled as

$$c_d(c_l, Re) = [C_{D_0} + C_{D_2}(c_l - C_L C_{D0})^2][Re/Re_{\text{ref}}]^{Re_{\text{exp}}} \tag{4.25}$$

where

$$C_{D_2} = C_{D_2 u} \text{ if } c_l > C_L C_{D0} \tag{4.26}$$

$$C_{D_2} = C_{D_2 l} \text{ if } c_l < C_L C_{D0}. \tag{4.27}$$

The drag model for the airfoil features a Reynolds number correction. Re_{ref} is the Reynolds number at which the other airfoil properties are referenced, while Re is the section Reynolds number. Re_{exp} is a constant that can be adjusted based on the flow conditions. The program does not feature such an adjustment for the lift curve. Analysis in XFOIL indicates that the C_{L_0} computed for some of the fitted airfoils changes significantly based upon the Reynolds number within the expected range of Reynolds numbers for these propellers. The lack of correction could be a source of error in the analysis. Additionally, the local chord based Reynolds numbers along the blade for most of the propellers in this work are in the range of 1 000s to 150 000, meaning that the Reynolds number is often low enough for the accuracy of XFOIL to be uncertain. To help mitigate the effect of the change in properties with Reynolds number, Reynolds number specific airfoil properties are defined at each station along the blade span for the simulation.

The comparison of experimental results to the predicted performance presented in Figure 4.22 shows good agreement in thrust for the propellers studied. We also examine the agreement between the Thrust and Torque coefficients, defined

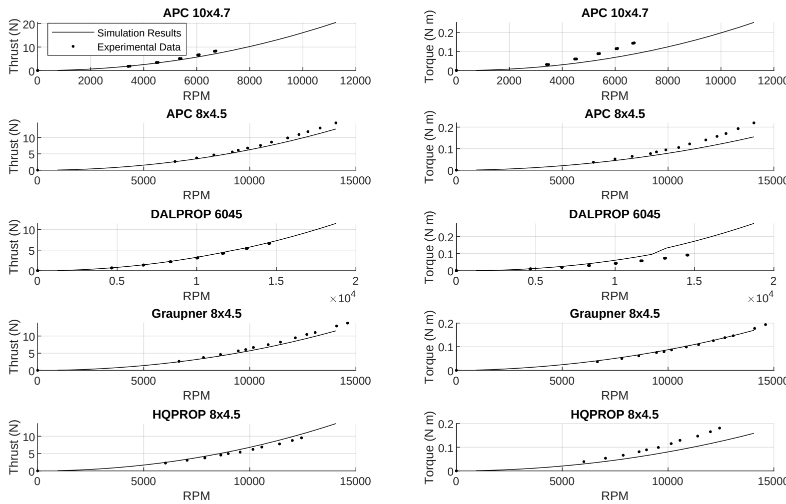

Figure 4.22: Comparison of experimental results of propeller to simulation in QPROP.

as $T = \rho\omega^2 C_T D^4$ and $Q = \rho\omega^2 C_Q D^5$, respectively. Here, ρ is the air density, ω is the rotation speed of the propeller in rad/s, and D is the propeller diameter. Predicted and measured coefficients for each propeller are seen in Figures 4.23a and 4.23b. Predicted thrust coefficients are within 10 % of the measured value for the propellers, however torque predictions feature much greater error. This is likely due to the inherent difficulty of accurately predicting drag at lower Reynolds numbers. In particular, the DALPROP 6045 featured a larger mismatch in torque than the other propellers. One possible reason for this mismatch is that the airfoil section for this propeller has a blunt trailing edge, further increasing the difficulty of accurate drag prediction. The simulation results were found to be highly sensitive to a variety of different parameters. Applying a blade pitch of even a few degrees significantly changed the thrust results. One example of this is found by comparing the HQProp and the APC 8-inch propeller. Though sold by different entities, these propellers happen to be nearly exactly the same in terms of visual inspection. The photogrammetry results confirm this, with the data indicating they possess nearly identical chord, thickness, and camber distribution. The main difference is in the twist distribution, where both propellers have nearly identical contours, but the HQProp has 2 degrees of difference in pitch across the blade. This difference is evident in the experimental thrust data where the APC propeller has a 17 % higher thrust coefficient than the HQProp propeller.

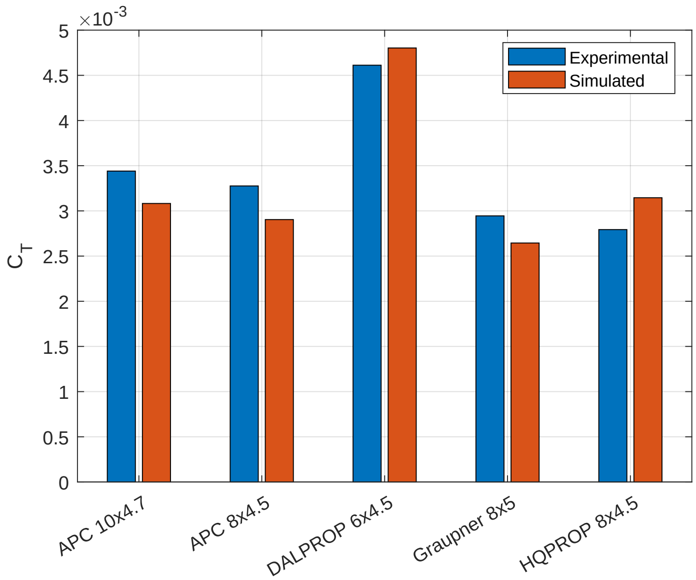

(a) Thrust Coefficient

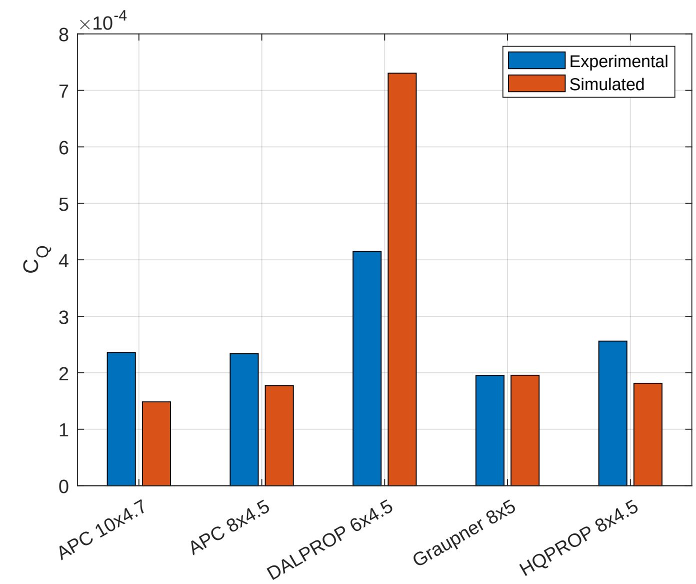

(b) Torque Coefficient

Figure 4.23: Comparison of non-dimensional coefficients from simulation and experiment.

4.7 Conclusion

While many forms of 3D scanning technologies exist, they are often costly or inaccessible to many researchers. This paper has developed a technique that shows that with freely available software, commonly available computing hardware, and today's high-resolution cameras, photogrammetry with accuracy sufficient for BEM can be achieved with little expertise or dedicated equipment. The point clouds produced by photogrammetry are accurate enough to extract the propeller geometric parameters at a resolution comparable to competing 3D scanning methods. The use of the point-to-plane algorithm for automated orientation as well as the airfoil fitting methods allow for rapid extraction of useful propeller parameters rather than just an unstructured mesh or point cloud, thereby facilitating the import of the model into a parametric design software.

Subsequent simulation of the extracted geometry shows good agreement with experimental results in thrust. As accurate geometry is a critical requirement of performing credible simulations, the authors expect that the technique developed will benefit the aerospace research community. The implementation of this work can be found at `https://github.com/ellandetang/PhotoFoil`

References

[1] J Gordon Leishman. "Blade Element Analysis." In: *Principles of Helicopter Aerodynamics*. 2nd ed. Cambridge University Press, 2016. Chap. 3, pp. 115–158. ISBN: 9781107013353.

[2] J. Gordon Leishman. "Momentum Theory Analysis in Hovering Flight." In: *Principles of Helicopter Aerodynamics*. 2nd ed. Cambridge University Press, 2016. Chap. 2.2, pp. 58–64. ISBN: 9781107013353.

[3] Eduardo J. Alvarez and Andrew Ning. "High-Fidelity Modeling of Multirotor Aerodynamic Interactions for Aircraft Design." In: *AIAA Journal* 58.10 (Oct. 2020), pp. 4385–4400. ISSN: 0001-1452. DOI: `10.2514/1.J059178`.

[4] Steven Yoon, Henry C. Lee, and Thomas H. Pulliam. "Computational Analysis of Multi-Rotor Flows." In: *54th AIAA Aerospace Sciences Meeting*. Reston, Virginia: American Institute of Aeronautics and Astronautics, Jan. 2016. ISBN: 978-1-62410-393-3. DOI: `10.2514/6.2016-0812`.

[5] APC. *APC Technical Information - Engineering - Airfoils*. 2021. URL: `https://www.apcprop.com/technical-information/engineering/#airfoil` (visited on 09/08/2021).

[6] J.B. Brandt, R.W. Deters, G.K. Ananda, O.D. Dantsker, and M.S. Selig. *UIUC Propeller Database, Vols 1-3*. 2020.

[7] Ira H. Abbott and A. E. von Doenhoff. *Theory of Wing Sections: Including a Summary of Airfoil Data*. Dover Publications, 1959. ISBN: 9780486605869.

[8] Woodrow W. Chapman, ed. *Handbook for the Metalworking Industries*. 1st. Cincinnati, OH: Gardner Publications, 2002.

[9] Hexagon. *Coordinate Measuring Machine Accuracy on the Shop Floor*. 2022. URL: `https://www.hexagonmi.com/solutions/technical-`

resources/technical-articles/coordinate-measuring-machine-accuracy-on-the-shop-floor (visited on 03/06/2022).

[10] F. Menna and S. Troisi. "Low Cost Reverse Engineering Techniques for 3D Modelling of Propellers." In: *International Archives of the Photogrammetry, Remote Sensing and Spatial Information Sciences - ISPRS Archives* 38.PART 5 (2010), pp. 452–457. ISSN: 16821750.

[11] MSC. *117mm Long CMM Motorized Probe Head*. 2022.

[12] Mohammed Shaheen. "Reverse Engineering Using Laser Scanned And Manufacturing Of A Powered Paraglider Propeller." In: *Journal of Multidisciplinary Engineering Science and Technology (JMEST)* 7.10 (2020), pp. 12810–12815.

[13] Samuel L Prudden. "Rotor Aerodynamic Interaction Effects for Multirotor Unmanned Aircraft Systems in Forward Flight." PhD thesis. RMIT University, 2020.

[14] Francis Gregory Ng and Alvin Chua. "Simulating the Effect of Non-Axial Airflow on the Motion of an Undriven Propeller." In: *International Journal of Advanced Trends in Computer Science and Engineering* 9.1 (2020), pp. 153–159. ISSN: 22783091. DOI: 10.30534/ijatcse/2020/23912020.

[15] Mark Drela. *Propeller Characterization for QPROP*. 2005. URL: http://web.mit.edu/drela/Public/web/qprop/prop_measure.pdf.

[16] Gary Hinze. *Propeller Gauges*. 2016. URL: http://www.endlesslift.com/propeller-gauges/ (visited on 03/07/2022).

[17] Thomas Luhmann. "Close Range Photogrammetry for Industrial Applications." In: *ISPRS Journal of Photogrammetry and Remote Sensing* 65.6 (2010). Publisher: Elsevier B.V., pp. 558–569. ISSN: 09242716. DOI: 10.1016/j.isprsjprs.2010.06.003.

[18] Tianshu Liu, L. N. Cattafesta III, R. H. Radeztsky, and A. W. Burner. "Photogrammetry Applied to Wind-Tunnel Testing." In: *AIAA Journal* 38.6 (June 2000), pp. 964–971. ISSN: 0001-1452. DOI: 10.2514/2.1079.

[19] Alan Jennings and Jonathan Black. "Texture-Based Photogrammetry Accuracy on Curved Surfaces." In: *AIAA Journal* 50.5 (May 2012), pp. 1060–1071. ISSN: 0001-1452. DOI: 10.2514/1.J050956.

[20] Halim Setan and Mohd Sharuddin Ibrahim. "Digital Close Range Photogrammetric System For High Precision Propeller Measurement." In: *Malaysian Science & Technology Congress*. January. 2003.

[21] *PhotoModeler Scanner*. 2022. URL: https://www.photomodeler.com/products/scanner/ (visited on 03/03/2022).

[22] Maarten Vergauwen and Luc Van Gool. "Web-based 3D Reconstruction Service." In: *Machine Vision and Applications* 17.6 (Dec. 2006), pp. 411–426. ISSN: 0932-8092. DOI: `10.1007/s00138-006-0027-1`.

[23] S. Ackermann, F. Menna, A. Scamardella, and S. Troisi. "Digital Photogrammetry For High Precision 3D Measurements In Shipbuilding Field." In: *6th CIRP Int. COnf. on ICME* 1.January (2008), pp. 6–11.

[24] A. Sh. Amini, M. Varshosaz, and M. Saadatseresht. "Deformation Determination of Aircraft Parts by Photogrammetry." In: *International Archives of the Photogrammetry, Remote Sensing and Spatial Information Sciences - ISPRS Archives* 37 (2008), pp. 135–138. ISSN: 16821750.

[25] **Tang, Ellande** and Soon-Jo Chung. "Rapid Extraction of Propeller Geometry Using Photogrammetry." In: *Bulletin of the American Physical Society* 66 (Nov. 2021).

[26] Johannes Lutz Schönberger, Enliang Zheng, Marc Pollefeys, and Jan-Michael Frahm. "Pixelwise View Selection for Unstructured Multi-View Stereo." In: *European Conference on Computer Vision (ECCV)*. 2016.

[27] Johannes Lutz Schönberger and Jan-Michael Frahm. "Structure-from-Motion Revisited." In: *Conference on Computer Vision and Pattern Recognition (CVPR)*. 2016.

[28] Carsten Griwodz, Simone Gasparini, Lilian Calvet, Pierre Gurdjos, Fabien Castan, Benoit Maujean, Gregoire De Lillo, and Yann Lanthony. "AliceVision Meshroom: An Open-Source 3D Reconstruction Pipeline." In: *Proceedings of the 12th ACM Multimedia Systems Conference*. ACM Press, 2021. DOI: `10.1145/3458305.3478443`.

[29] Ewelina Rupnik, Mehdi Daakir, and Marc Pierrot Deseilligny. "MicMac — a Free, Open-Source Solution for Photogrammetry." In: *Open Geospatial Data, Software and Standards* 2.1 (Dec. 2017). Publisher: Open Geospatial Data, Software and Standards ISBN: 4096501700, p. 14. ISSN: 2363-7501. DOI: `10.1186/s40965-017-0027-2`.

[30] Simon Fuhrmann, Fabian Langguth, Nils Moehrle, Michael Waechter, and Michael Goesele. "MVE—An Image-Based Reconstruction Environment." In: *Computers & Graphics* 53 (Dec. 2015). Publisher: Elsevier, pp. 44–53. ISSN: 00978493. DOI: `10.1016/j.cag.2015.09.003`.

[31] Pierre Moulon, Pascal Monasse, Romuald Perrot, and Renaud Marlet. "OpenMVG: Open multiple view geometry." In: *International Workshop on Reproducible Research in Pattern Recognition*. Springer. 2016, pp. 60–74. DOI: `10.1007/978-3-319-56414-2_5`.

[32] Hafizur Rahaman. *Regard3D*. 2022. URL: `http://www.regard3d.org/index.php` (visited on 03/02/2022).

[33] Changchang Wu. *VisualSFM: A Visual Structure from Motion System*. 2011. URL: http://ccwu.me/vsfm/.

[34] Changchang Wu, Sameer Agarwal, Brian Curless, and Steven M Seitz. "Multicore Bundle Adjustment." In: *Computer Vision and Pattern Recognition*. 2011.

[35] Changchang Wu. "Towards Linear-Time Incremental Structure from Motion." In: *2013 International Conference on 3D Vision - 3DV 2013*. IEEE, 2013, pp. 127–134. ISBN: 9780769550671. DOI: 10.1109/3DV.2013.25.

[36] Kl Low. *Linear Least-squares Optimization for Point-to-plane ICP Surface Registration*. Tech. rep. TR04-004. University of North Carolina at Chapel Hill, 2004.

[37] Agustin Trujillo-Pino. *Accurate Subpixel Edge Location*. MATLAB Central File Exchange. 2022. URL: https://www.mathworks.com/matlabcentral/fileexchange/48908-accurate-subpixel-edge-location (visited on 12/23/2022).

[38] *Series 1585 Test Stand Datasheet*. Jan. 2022. URL: https://cdn.rcbenchmark.com/landing_pages/Manuals/Series%201585%20Datasheet.pdf (visited on 10/05/2022).

[39] Mark Drela. *QPROP-Propeller/Windmill Analysis and Design*. 2007.

[40] Mark Drela and Harold Youngren. *XFOIL-Subsonic Airfoil Development Sytem*. 2013.

Chapter 5

DESIGN AND EVALUATION OF A MULTI-COMPONENT FORCE SENSOR

5.1 Introduction

Aerodynamic experiments have historically been a critical component of aerodynamics studies and learning. They remain an important component of the design process for vehicles, albeit complimented by computational studies these days. An important aspect of experiments of this nature is often force sensing, as aerodynamic forces are typically a core performance metric of a design. By the nature of the operation of aircraft, being able to measure all three components of force and all three components of moments of a geometry when subjected to flight conditions is ideal, if not critical.

Force sensing can be achieved through a variety of methods, but one of the most common is through the use of piezoelectric sensors, which are conducive to interfacing with modern computers. Sophisticated arrangements of these sensors can enable one to develop load cells capable of measuring all six components simultaneously. However, such load cells are complex, costly, and can be damaged by accidentally saturating the torque capacity of the load cell. As a result, these style of monolithic sensors are sometimes subobtimal for aerodynamics experiments. Traditionally, force measurements of this nature were conducted with an extensive load balance arrangement, but the complexity of this is a significant disadvantage.

To mitigate the cost and fragility of this type of sensor, an alternative was designed. By designing the sensor to measure forces using single component force sensors, the cost of the system could be significantly reduced. Making a system out of multiple load cells also has several auxiliary advantages. Individual load cells can be replaced if malfunctioning, or swapped with version with higher or lower load ratings in order to change the capacity or sensitivity of the overall load cell. Additionally, the geometric arrangement of the cells could potentially be changed to change the relative sensitivity of the overall sensor in various axes. Once example would be that increasing the distance between the force sensors would increase the maximum amount of torque that the overall sensor could measure.

Previous Work

While the design in this work was developed independently, multicomponent force sensors have been in use for a considerable amount of time. Many wind tunnels have historically had a load balance of some form used to measure aerodynamic forces [1]. These systems were rarely monolithic, and decoupled the forces experienced by a model in the wind tunnel into various components, often with flexural hinges.

This type of design had been done before, albeit in slightly different incarnations. Work by Dwarakanath [2] describes extensively the design and analysis of a similar force-torque sensor. Optimization of the sensor geometry is conducted, and each of the members is built using ring strain gauges. While this work uses ball joints for the interface, the work also comments on using spherical flexture hinges to improve the accuracy for future designs. Another work [3] describes a similar design using ring type sensors in a near-singular configuration along with flexural hinges for the joints. An advantage of the near singular geometry is the ability to increase the relative sensitivity of particular axis relative to others when such forces are expected. For instance, drag in aerodynamic testing is often much smaller than the lift, so commensurate sensitivities in the sensors would be advantageous. The most recent work identified was a bachelor's thesis that described a similar concept [4] for a robotics application. The work uses a similar hexapod arrangement of sensors but with 3D printed ball joints, which appear to be a significant source of error. The work also details a design with ball joint rod ends, but does not demonstrate a physical prototype.

As existing Stewart platform based force sensors appear to be adequate, a version for the author's purpose was constructed. One particular constraint on the design in this work is that the components were limited to low-cost load cells and data acquisition as well as conventional machining and 3D printing.

5.2 Design

Previous Iterations

Prior to the final version of the design, several different concepts were developed of a force sensor capable of measuring all 6 components of forces and moments. The first version of the force sensor attempted to measure the various force components by decoupling the various axes of force. This was achieved by placing each axis of force on a separate stage and attempting to channel undesired forces through the stage using Teflon pads. It was found that this approach did not work for various reasons. In addition to the Teflon-Teflon connection exhibiting more friction than expected, the structure was also found to deflect too much to be in any way practical. The result was that this configuration would not measure even the Z component of force accurately under the conditions of various moments.

The second version sought to resolve some of these issues. Rather than attempting to measure all 6 components of force and torque, it was sought to only measure only the Z force and the X and Y moments. This was done by reducing the assembly to only 3 load cells, and rigidly mounting the top plate to the load cells. While this sensor was able to accurately measure forces in the Z direction, it was required that the forces be applied in the same location every time, and measurement of the moments was poor. The design was improved by installing ball joint rod ends at the interface to the upper plate. The results were successful enough to be used for the preceding Upstream Obstruction test described in Chapter 2. The sensor was able to measure the Z component of force with good accuracy regardless of the application location, but was still insufficient for measuring the X and Y moments accurately.

Stewart Platform Design

The successful iteration of the force sensor for all 6 axes involved a radical re-arrangement of the platform geometry. A Stewart Platform is a parallel manipulator that often sees use in applications requiring positioning with 6 degrees of freedom by controlling the lengths of 6 independent actuators. Conversely, this means we can use this concept to decompose the desired 6 components of force and moments into, ideally, 6 linear and independent components.

Theory

The geometry of the Stewart platform is well known [5]. The core notion of the platform is that 6 degrees of freedom can be achieved by varying the length of six independent linkages. Conversely, because all degrees of motion linked to the linkages, this means that all six components of force can be decomposed into into linear forces along the six linkages. This allows for the possibility of creating a six-axis force sensor using only force sensors designed to measure one component of load. Decomposition of forces in this way has a number of advantages. The choice of linkage geometry changes sensitivity to various forces and moments, allowing for the user to create a sensor with desired relative sensing properties.

Key to the design of the sensor is each linkage acting as a two-force member. A two force member is a body that experiences forces in only two locations. In order to maintain static stability, the line of action of the forces must be the same as the line connecting the two locations. Furthermore, forces must be equal and opposite. This provides a means of ensuring that the forces experienced by the one-component load cell integrated into a linkage will be solely forces aligned with the load cell's direction of measurement, with no off-axis forces or moments introducing error.

Modeling the expected force response of the force stand is relatively simple and can be described using a linear model. For the kth member, consider the coordinates of its endpoints described as vectors in a Cartesian coordinate system, $\vec{a}_k$ and $\vec{b}_k$. We then consider the vector difference of the two, or the direction of the member $\vec{v}_k = \vec{b}_k - \vec{a}_k$. As each member is a two force member by design, the force vector supplied by the member is parallel to this vector. The force of the kth member can thus be described as

$$\vec{F}_k = F_k \hat{\vec{v}}_k, \ \hat{\vec{v}}_k = \frac{\vec{v}_k}{|\vec{v}_k|} \tag{5.1}$$

the sum of the forces from all the members can then be represented in our chosen coordinate system as

$$\vec{F} = \sum_n F_n \hat{\vec{v}}_n. \tag{5.2}$$

For a finite number of members, this can be represented in matrix multiplication form as

$$\vec{F} = \underbrace{\begin{bmatrix} \hat{\vec{v}}_1 & \hat{\vec{v}}_2 & \dots & \hat{\vec{v}}_n \end{bmatrix}}_{V} \begin{bmatrix} F_1 \\ F_2 \\ \vdots \\ F_n \end{bmatrix}. \tag{5.3}$$

Similarly, we can do the same for the moments. Assuming that the endpoints are all on the same portion of the platform, we can represent the moments from the members on the platform using the matrix multiplication representation.

$$\vec{M} = \sum_n b_n \times \vec{F}_n = \sum_n \begin{bmatrix} 0 & -b_{n3} & b_{n2} \\ b_{n3} & 0 & -b_{n1} \\ -b_{n2} & b_{n1} & 0 \end{bmatrix} \hat{\vec{v}}_n F_n \tag{5.4}$$

This can also be represented in a matrix format with respect to the member forces. This means that there is a linear relationship between the member forces and the Cartesian forces and moments on the platform. As cantilever load cells with a Wheatstone Bridge arrangement of strain gauges are being used, the relationship between the measured electrical signal and the measured force is linear. The force experienced by the kth sensor can then be related to its signal output s_k, by a linear coefficient c_k. The need for a constant is removed by taring the sensor and only looking at changes in force and the respective changes in signal.

$$F_k = c_k s_k \tag{5.5}$$

In the case of the Cartesian forces, for example, this changes the equation to

$$\vec{F} = V \begin{bmatrix} c_1 s_1 \\ c_2 s_2 \\ \vdots \\ c_n s_n \end{bmatrix} = C \begin{bmatrix} s_1 \\ s_2 \\ \vdots \\ s_n \end{bmatrix}. \tag{5.6}$$

In reality, the true value of V will differ slightly from the ideal. Given that the coefficients c_k need to be calculated through a calibration procedure regardless, the value of the combined matrix C can be derived through sufficient calibration. The result is that the actual procedure for calibrating the load cell is geometry agnostic. Applying a sufficient variety of forces and moments to produce at minimum a full rank matrix allows for solving for C with a best fit approximation.

While the choice of sensor geometry does not change the linearity of the relationship between the forces experienced by each member and the sensor force and moment outputs, it is possible to make V ill-conditioned for the desired purpose. An arrangement that does not produce a full rank matrix is bad because that indicates that some of the members are not being utilized or not all the forces will be reflected correctly. Similarly, arrangements that are close to a mechanical singularity can cause potential problems in the sensing by substantially increasing the sensitivity to certain forces. This can be used advantageously however if additional sensitivity in a particular direction is desired.

Mechanical Design

Creating a true two force member is hampered by a couple mitigating factors however. In reality, the weight of the linkage assembly means that a more correct model of the linkage is a 3-force member. However, it is expected that because the geometry of the system should not change, the influence of the linkage weight should be small and be calibrated out. The second obstacle to creating a true two-force member is the connections to the assembly. A two-force member ideally has only forces applied at the connection points. This means that ideally any connection needs to be frictionless. There are several methods to create rotational connections that are frictionless or near frictionless. The best option, and one that is used in force balances elsewhere is to use flexural hinges. These hinges have theoretically no moment at their neutral point by allowing rotation through the use of a cantilever beam style spring. Forces associated with small displacements can also be modeled and calibrated out. Difficulty arises when trying to acquire appropriate flexural hinges for the sensor. Hinges with a minimum of 2 degrees of freedom are required, and they need to be set at a specific angle to build the sensor in the correct geometry. Because the desired sensor is an arrangement of 6 linkages, 12 individual hinges would be required, one for each end. The cost of individual hinges or, alternatively, the difficulty involved in manufacturing them meant that it was elected to not utilize them for a low cost sensor. Other low friction options were considered, but were rejected due to cost or complexity. These include options such as air or fluid bearings.

The option that was ultimately chosen was to use ball-joint rod ends. While the presence of stiction in the ball-joint does impact the sensor accuracy, it was decided to be a worthwhile compromise given the cost and form factor of the components. A disadvantage of the ball joints is that, because each member is constrained at two points, each individual sensor is free to rotate. This affects the results because shifting an individual sensor changes the weight distribution slightly and affects the tare value. The overall impact of the design choices are discussed in Section 5.3.

A diagram of the resultant 2-force member used in the final sensor is shown in Figure 5.1. The 1 kg load cell has been converted from a cantilever arrangement to an S-type load cell for axial measurements. This was done with two 3D printed adapters bolted to the load cell with an interface to the ball joint rod end. Because the premise of the sensor relies upon the geometry changing as little as possible while under load, the adapters were printed with several layers of carbon fiber reinforcement to increase their stiffness.

The design of the base and top plates of the sensor were straightforward. In addition to the mounting points for the interface between the ball joint and the plate, the requirements or the plate were that it would not deflect under load to a degree that would affect the geometry of the sensor and thus the readings, and were each made from 0.25" thick aluminum plate. Because 1.5" 8020 extrusion is a common structural material used for experimental setups, each plate was made with a 1.5" pitch hole pattern for 5/16"-18 bolts to be compatible with structures built from the material. A 3D model of the mechanical components of the load cell assembly can be seen in Figure 5.2, as well as the photograph of the physical prototype in Figure 5.3.

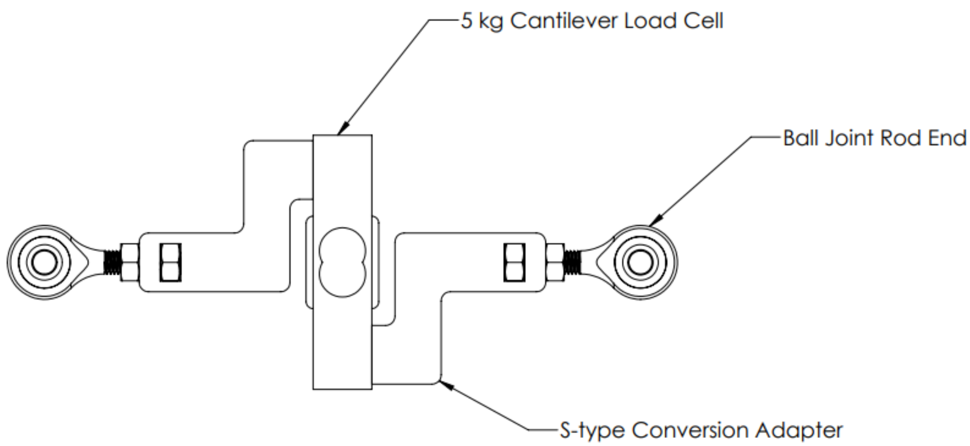

Figure 5.1: Diagram of a single cantilever load cell converted to a 2 force member.

Signal processing

Each of the load cells [6] is a Wheatstone bridge arrangement of strain gauges, outputting a difference in voltage powered by an input excitation voltage along with a ground connection. Each of these four connections is connected to an HX711 24-bit Analog-to-Digital Converter [7], which are in turn coordinated by an Arduino Mega rev 3 [8] development board. The board then samples the data from each sensor and writes the output alongside a timestamp to a serial connection, where it is parsed and written into storage by Matlab. Conversion to forces is done in post processing using the calibration settings identified in Section 5.3.

5.3 Calibration

Calibration is a critical portion of the sensor use process. The process is straightforward in concept. The user applies known forces to the sensor, then measures the subsequent outputs. As is shown in section 5.2, the response of the sensors to loads applied to the force sensor are theoretically linear. By applying various loads, one can then apply a linear regression to the output signals and derive the calibration matrix. Provided that neither the geometry of the sensor nor the signal response of each sensing component does not change significantly, this means that the calibration matrix should be applicable for any loading provided a reasonable tare point is selected.

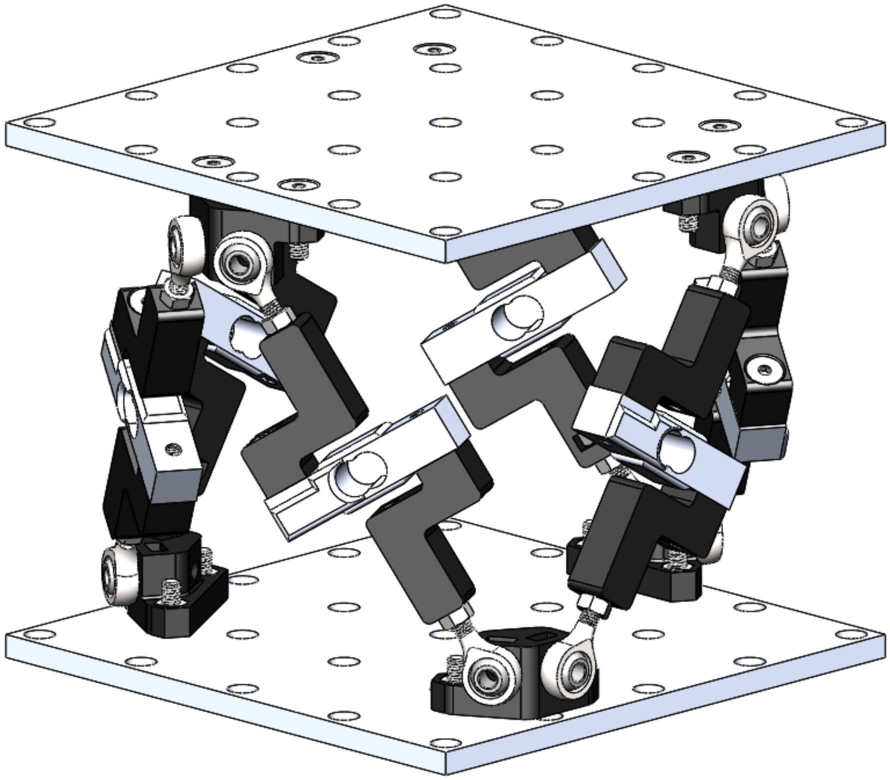

Figure 5.2: 3D Model of the Load Cell Assembly Prototype.

Producing a useful calibration matrix requires calibration force inputs that form a full rank matrix. In other words, 6 linearly independent forces need to be applied to the sensor. To achieve this, standard weights are are applied to the sensor and known locations, applying known forces and moments to the sensor. Applying a force in the Z direction as well as moments in the X and Y directions is simple in the sensor's typical orientation. However, applying X and Y forces and a Z moment with only weights requires either a pulley to change the force direction or mounting the sensor in a different orientation. Calibration in this work elected to change the orientation of the sensor to apply different forces. While the sensor in a different orientation is now measuring the weight of the it's own components, it is still possible to gather calibration information as the change in signals to changes in applied load is what is desired.

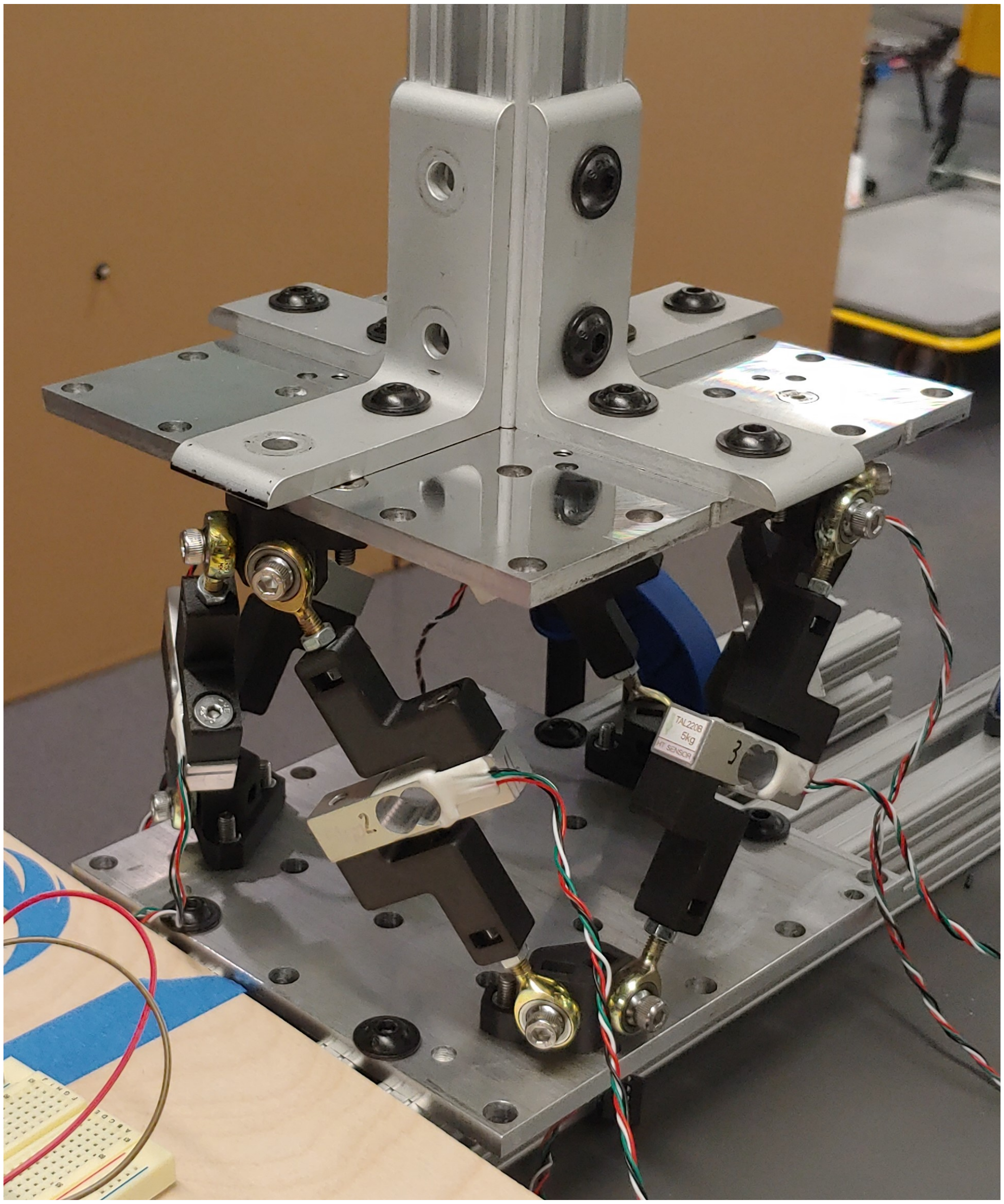

Figure 5.3: Physical Model of the Load Cell Assembly Prototype.

Accuracy Evaluation

To quantify the effectiveness of the sensor, a series of tests to quantify the sensor's accuracy were conducted. As the force sensor is fundamentally an analog device, it is expected that the sensor readings will be potentially influenced by the ambient temperature, electrical conditions, and some degree of baseline noise. In addition, there are inaccuracies expected that are inherent to the design. Small changes in geometry can lead to the true signal to output function changing from the calibration conditions. Additionally, while the individual sensors were designed to be two force

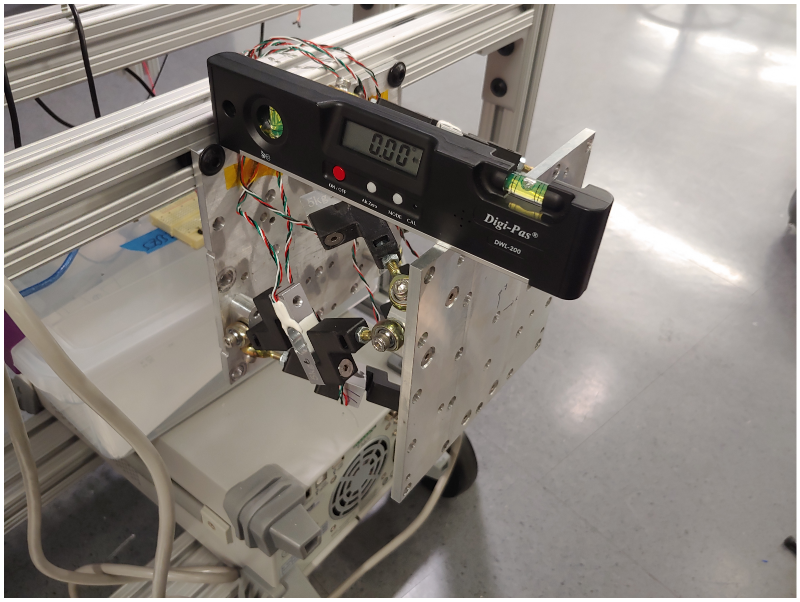

Figure 5.4: Y Axis Calibration configuration.

members by using ball joint rod ends, the ball joints do still have some inherent friction which can limit the accuracy by transferring unwanted forces to the sensors.

Quantifying the sensor accuracy essentially consisted of taking a series of the measurements for the same applied load and observing how the output changes. To evaluate the accuracy the force sensor, three separate sessions were conducted. Each session consisted of loading 4 different calibration weights to the same spot. In each session this was repeated 30 times. Each of the sessions targeted a different axis, so that all six axes of the force sensor could be evaluated.

The first session had the sensor mounted upright to apply a force in the Z axis and moments in the X and Y axes. The second session mounted the sensor sideways similar to when it was being calibrated and applied a force along the Y axis and moment about the Z axis. The third configuration was similar to the second, but oriented to apply a force along the X axis instead. The samples of each session were collected over the course of several days, in order to better capture potential sensor drift.

The metric used to evaluate the error is a normalized form of the Root Mean Square Percentage Error (RMSPE) of the data, that is

$$RMSPE = \sqrt{\frac{\sum_{i=1}^{N}(\frac{y_{i,\text{meas}}}{y_{i,\text{exp}}} - 1)^2}{N}} \cdot 100 \tag{5.7}$$

where $y_{i,\text{meas}}$ is the ith measurement, $y_{i,\text{exp}}$ is the ith expected expected value, and

N is the number of data points. The normalization by the expected value of each measurement is done to compare the accuracy of individual measurements against each other.

5.4 Results

Evaluation of the accuracy resulted in the following metrics. As can be seen in Fig. 5.5, 5.6, and 5.7, the Root Mean Square Percentage Error of the measurements along the studied axes is in the single digit percents, typically below 3% for F_z, M_x, and M_y, and below 5% for F_x, F_y, and M_z.

The error varied significantly over time as more samples were collected. Some instances had significantly higher error than others. The likely cause of this was that one of the members of the force sensor was at the extreme of its travel on the ball joint rod ends and was contacting its mounts. This in turn caused the load cell to be loaded improperly and return a bad reading. Examining the signals in Figures 5.8, 5.9, and 5.10, we can see how significantly the raw signal from the sensors changes over time. These figures show a collection of the tare signals for each sample collected. The signals also reflect some change to the individual load cells as the sensor is shifted and moved in between samples. Very large jumps in the signal reflect either a sample collected a large amount of time from the previous sample, several days in this case, or an adjustment of an individual load cell. Fortunately, the previous error metrics indicate that, while the tare point of the sensor changes over time, the linearity and calibration of the sensor does not seem to change significantly.

We can also examine how the measured values compare to the applied loads for each of the 4 loadings across all the different samples. The measurement shown with the applied loads for each case can be seen in Figures 5.11,5.12, and 5.13. The analogous errors for each case are shown in Figures 5.14, 5.15, and 5.16.

In addition to the loaded components for each test case, we can also examine the unloaded axes during each test to evaluate their adherence to the expected value of 0. Figures 5.17, 5.18, and 5.19 show the Root Mean Square error of each session for the other components of the axes in their respective units. Likewise, Figures 5.20, 5.21, and 5.22 show the compiled errors for the unloaded axes for each case.

The data show that the unloaded axes have relatively good error characteristics. The force axes have errors that are typically less than .1 N or about 10 grams of force for applied calibration loads of up to 500 g.

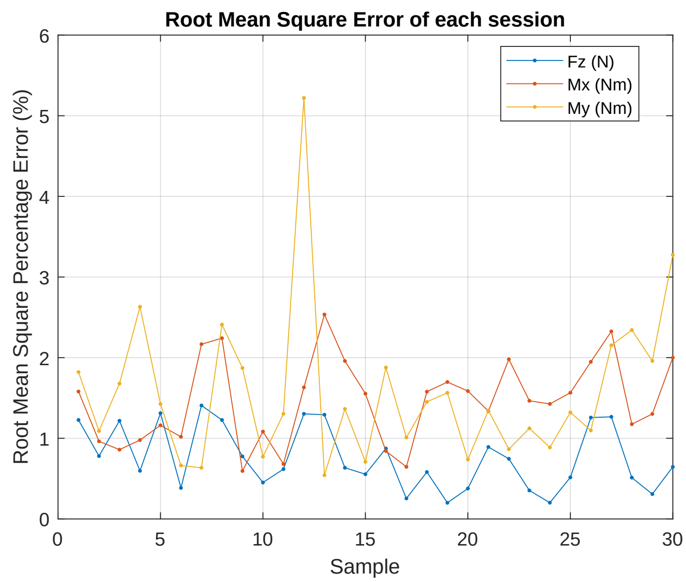

Figure 5.5: Accuracy evaluation of F_z, M_x, and M_y with the sensor in the vertical position.

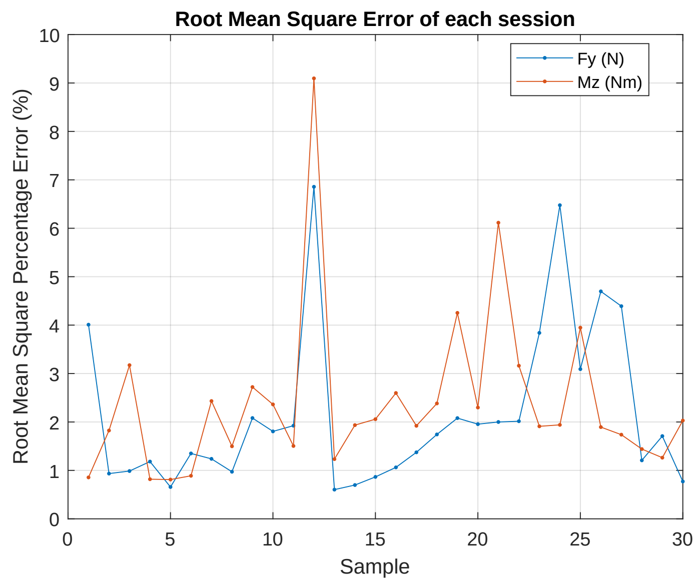

Figure 5.6: Accuracy evaluation of F_y and M_z with the sensor in a horizontal position.

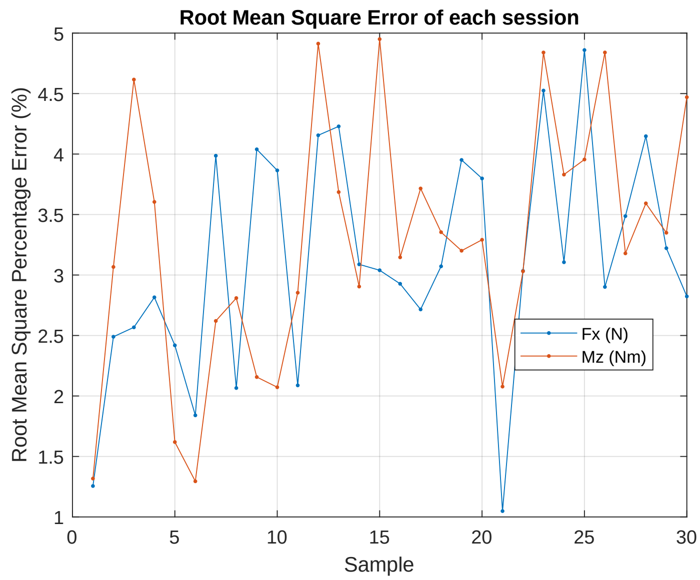

Figure 5.7: Accuracy evaluation of F_x and M_z with the sensor in a horizontal position.

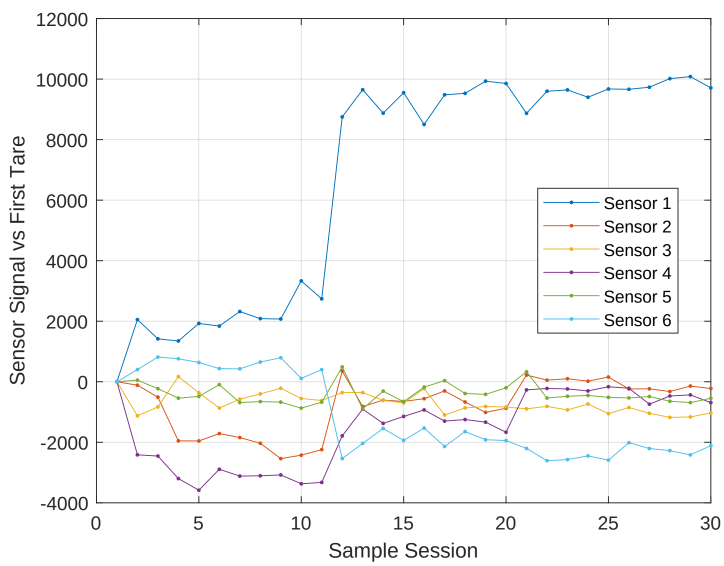

Figure 5.8: Tare signals during evaluation of F_z, M_x, and M_y with the sensor in the vertical position.

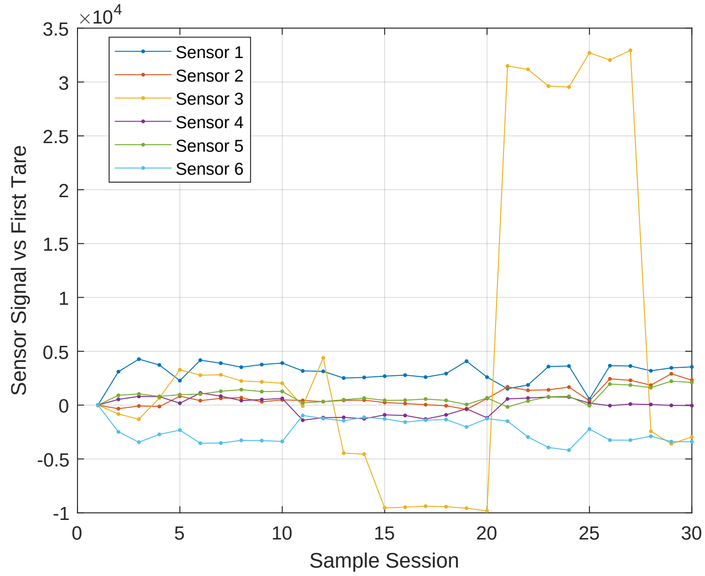

Figure 5.9: Tare signals during evaluation of F_y and M_z with the sensor in a horizontal position.

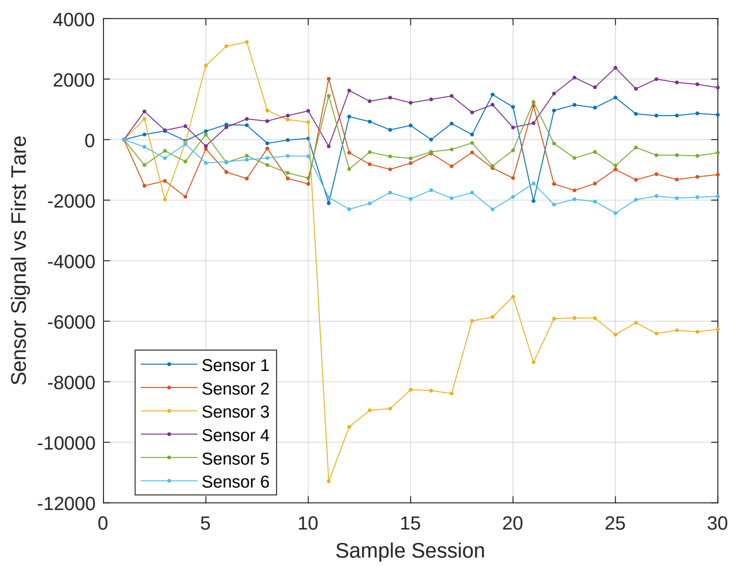

Figure 5.10: Tare signals during evaluation of F_x and M_z with the sensor in a horizontal position.

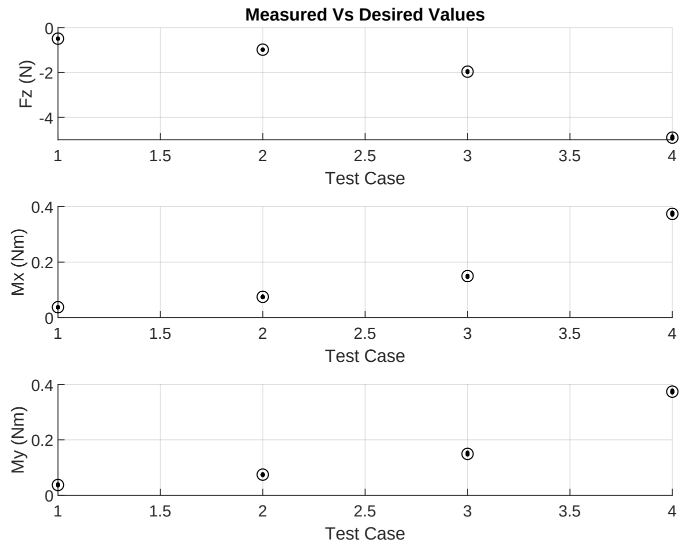

Figure 5.11: Expected and measured values during F_z, M_x, and M_y evaluation.

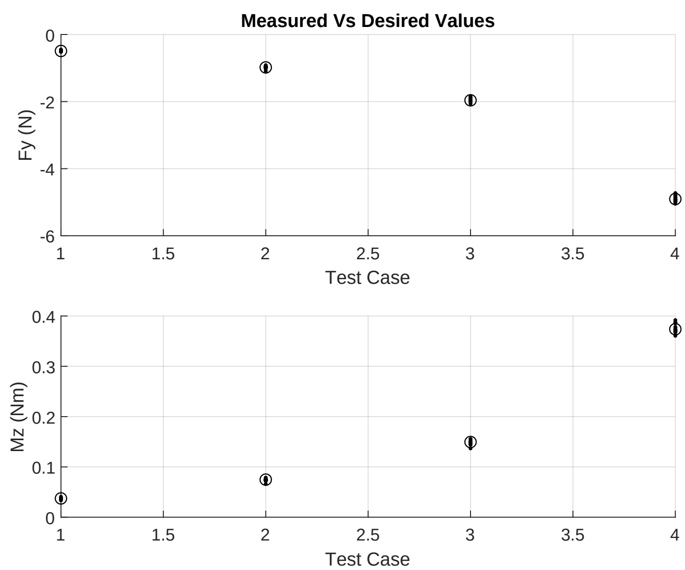

Figure 5.12: Expected and measured values during F_y and M_z evaluation.

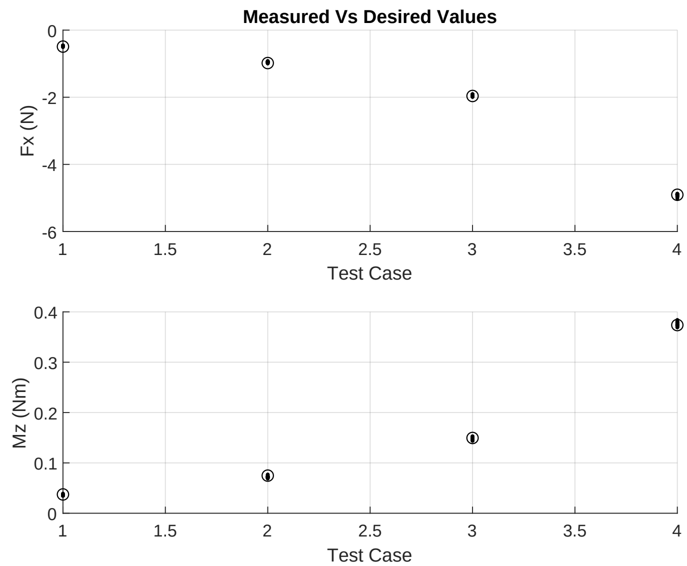

Figure 5.13: Expected and measured values during F_x and M_z evaluation.

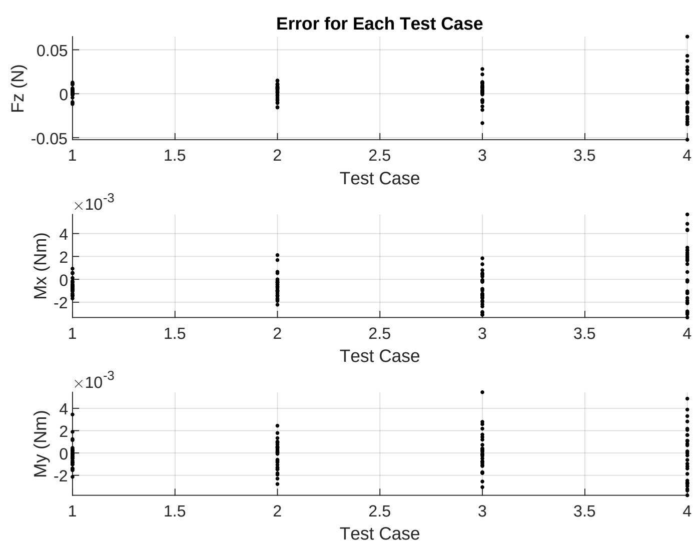

Figure 5.14: Error during F_z, M_x, and M_y evaluation.

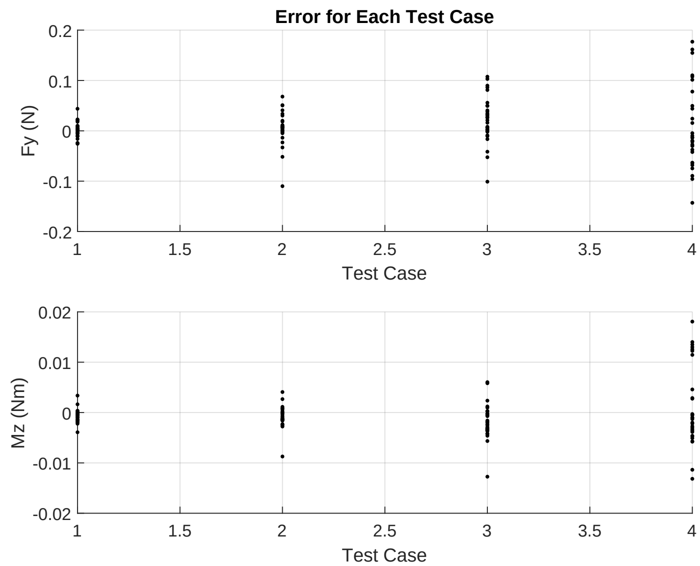

Figure 5.15: Error during F_y and M_z evaluation.

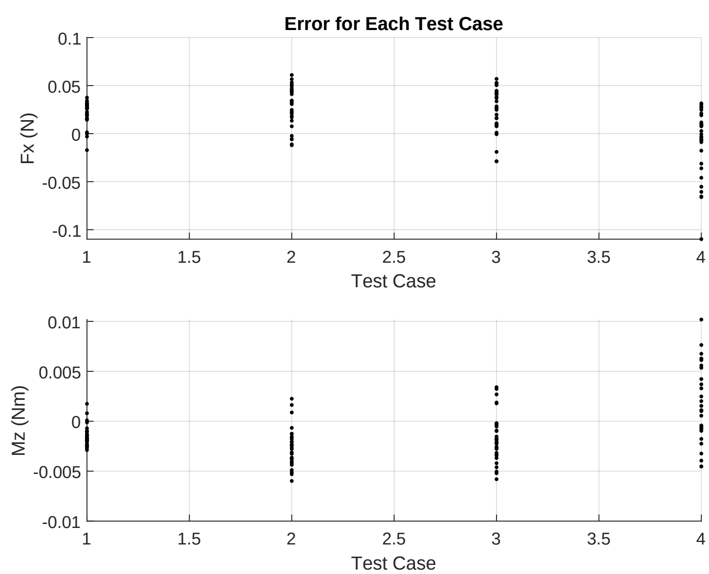

Figure 5.16: Error during F_x and M_z evaluation.

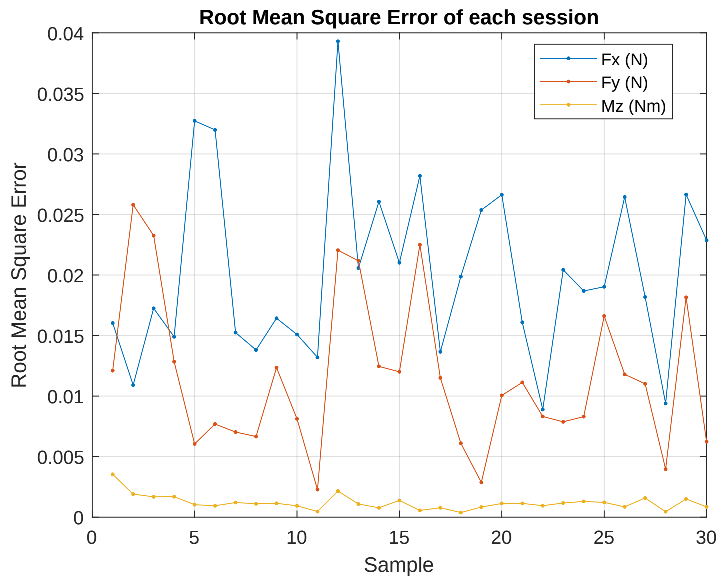

Figure 5.17: RMSE error of unloaded axes during F_z, M_x, and M_y evaluation.

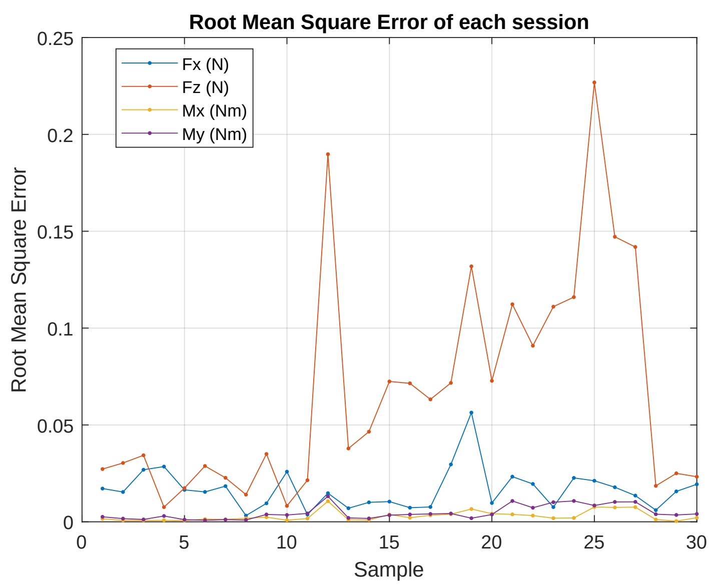

Figure 5.18: RMSE error of unloaded axes during F_y and M_z evaluation.

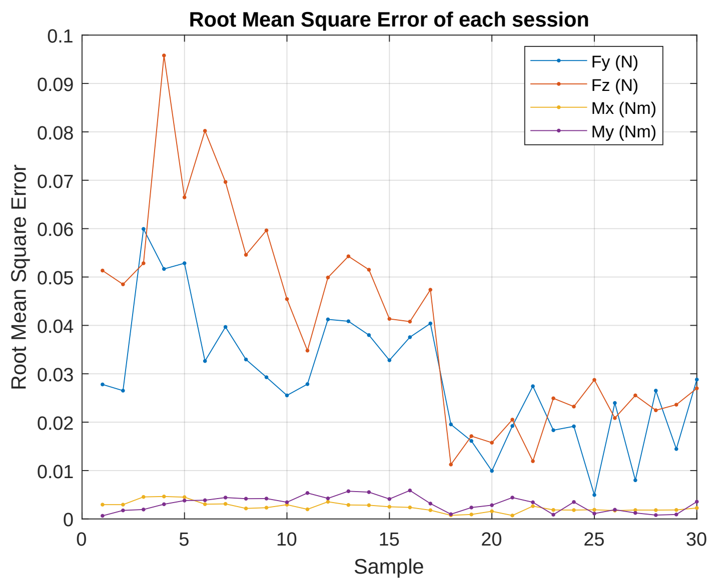

Figure 5.19: RMSE error of unloaded axes during F_x and M_z evaluation.

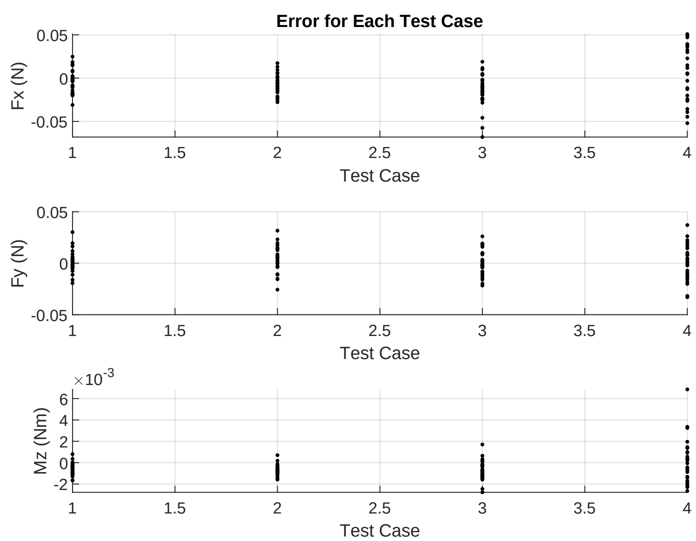

Figure 5.20: Error of unloaded axes during F_z, M_x, and M_y evaluation.

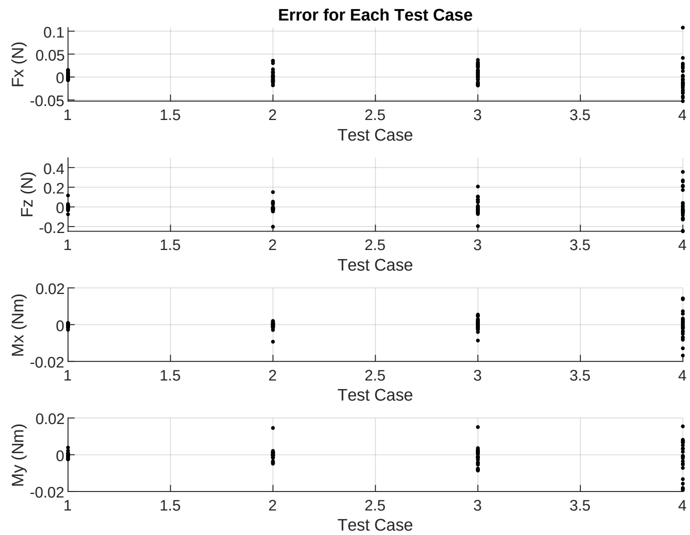

Figure 5.21: Error of unloaded axes during F_y and M_z evaluation.

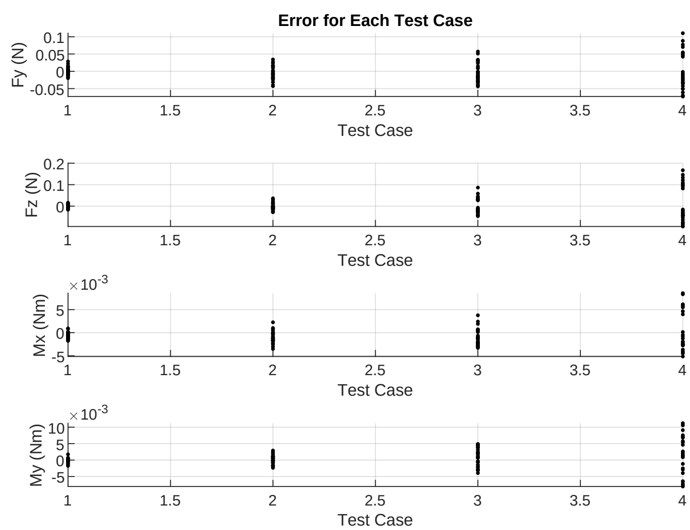

Figure 5.22: Error of unloaded axes during F_x and M_z evaluation.

5.5 Future Work

The sensor described serves its purpose as a low cost, moderate accuracy force sensor in six dimensions. However there are potential improvements to be made. The ball joints used to connect each member to the sensor assembly are a convenient, low-cost option. However, the three degrees of freedom afforded by their design proved to be a detriment with regard to measurement repeatability, as each member was allowed to move about its axis. A low resistance joint with only two degrees of rotation might for more convenient operation. While the cost of traditional flextural hinges that would be more appropriate for this form of sensor would undermine the accessibility of the design, there are potential alternatives. 3D printing technology has become quite convenient in recent years, and the production of custom flexural hinges by this method might sidestep the typically prohibitively costly manufacturing process while improving the accuracy. As the sensor design relies on minimal deflection or changes to the geometry however, care must be taken to manufacture hinges with sufficient stiffness.

Another drawback of the platform design is the form factor. For comparable maximum measurement limits, the sensor is much larger than analogous monolithic sensors. The main reason for this was the choice of force measurement components, which were cantilever load cells that were converted for axial measurements. Load cells with a different form factor could reduce the size of the overall sensor, though changes in the sensor geometry would alter its relative sensitivity to various forces and moments.

Further investigations into the sensor robustness and accuracy would also be worthwhile. The theory indicates that there is a direct linear map from the forces experienced by each member to the Cartesian forces. While this work performed the calibration for the entire sensor simultaneously, it would be worth exploring whether the majority of the calibration could be retained if a member is replaced. Because the force transformation should be the same provided that the replacement member is of sufficiently similar geometry, it may be possible to only need to scale one row of the calibration matrix to account for the new hardware.

5.6 Conclusion

This work presents a design for a sensor capable of measuring all six Cartesian components of force and moment simultaneously. In contrast to other commercially available sensors, this design uses multiple low-cost sensors in a Stewart platform arrangement to decouple forces and make measurements. The remainder of the force sensor is composed of parts made using typical manufacturing processes such as on a vertical mill. In addition to the cost advantages of using multiple low-cost sensors rather than a monolithic sensor, the geometry of the design can be more easily changed to adjust the overall force or moment sensitivity as desired. The sensor is also more robust to overloading as individual measurement components can be replaced rather than the entire sensor needing to be repaired.

Calibration of the sensor is relatively quick and straightforward. As the sensor outputs raw analog signals, no specialized data acquisition hardware is required, and the linear nature of the sensor and its constituent components mean that only a simple linear matrix is needed to map the signals to the output forces. An evaluation of the sensor accuracy shows that the sensor has a root mean square percentage error that is generally below 3% in the Z force and X and Y moment axes, and below 5% in the X and Y force and Z moment axes. While this metric might be poor by the standards of commercial off the shelf sensors for a similar purpose, the cost of this sensor is several times cheaper and is manufacturable with the equipment available at most engineering universities. The sensor is sufficient for projects where one might wish to examine steady state trends but high precision is not required.

References

[1] Jewel B. Barlow, William H. Rae, and Alan Pope. *Low-Speed Wind Tunnel Testing*. 3rd ed. Wiley-Interscience, Dec. 1999. ISBN: 978-0-471-55774-6.

[2] T. A. Dwarakanath, Bhaskar Dasgupta, and T. S. Mruthyunjaya. "Design and Development of a Stewart Platform Based Force-Torque Sensor." In: *Mechatronics* 11.7 (2001), pp. 793–809. ISSN: 09574158. DOI: 10.1016/S0957-4158(00)00048-9.

[3] R. Ranganath, P. S. Nair, T. S. Mruthyunjaya, and A. Ghosal. "A Force–Torque Sensor Based on a Stewart Platform in a Near-Singular Configuration." en. In: *Mechanism and Machine Theory* 39.9 (Sept. 2004), pp. 971–998. ISSN: 0094-114X. DOI: 10.1016/j.mechmachtheory.2004.04.005.

[4] Maria Rosa Ruiz. *Design and Analysis of a Stewart-Platform-Based Six-Axis Load Cell*. 2017.

[5] D. Stewart. "A Platform with Six Degrees of Freedom." en. In: *Proceedings of the Institution of Mechanical Engineers* 180.1 (June 1965), pp. 371–386. ISSN: 0020-3483, 2058-1203. DOI: 10.1243/PIME_PROC_1965_180_029_02.

[6] *Load Cell - 5kg, Straight Bar (TAL220B) - SEN-14729 - SparkFun Electronics*. 2022. URL: https://www.sparkfun.com/products/14729 (visited on 10/29/2022).

[7] *SparkFun Load Cell Amplifier - HX711 - SEN-13879 - SparkFun Electronics*. 2022. URL: https://www.sparkfun.com/products/13879 (visited on 10/29/2022).

[8] *Arduino Mega 2560 Rev3*. en. 2022. URL: https://store-usa.arduino.cc/products/arduino-mega-2560-rev3 (visited on 10/29/2022).

Chapter 6

INTERACTION BETWEEN A PROPELLER AND A LIFTING SURFACE IN TRANSITIONAL FLIGHT

6.1 Introduction

Air Taxis are one of the most common potential eVTOL platforms. A variety of organizations are pursuing the concept as a commercial venture [1]. In contrast to helicopters, the historically dominant vehicle for this mission profile, these vehicles also aim to mitigate their power consumption in forward flight by adding lifting surfaces and flying as fixed wing vehicles. The result of this configuration though is a complex aerodynamic interaction between the the various components on the craft. In particular, the rotors used for hover interact with the wings, both in hover and during the transition to forward flight. Depending on the configuration, the presence of lifting surfaces can have a significant effect on the performance of propellers in hover [2]. It has also been demonstrated that propellers used for hover generate a significant amount of drag on their own in forward flight [3, 4]. Needless to say, the presence of hardware used for hovering has a significant impact on the forward flight performance and vice versa. A better understanding of these interactions could be important in design of future VTOL craft, as well as improving efficiency and safety of existing craft.

In contrast to helicopters, the historically dominant vehicle for this mission profile, these vehicles also aim to mitigate their power consumption in forward flight by adding lifting surfaces and flying as fixed wing vehicles. The result of this configuration though is a complex aerodynamic interaction between the the various components on the craft. In particular, the rotors used for hover interact with the wings, both in hover and during the transition to forward flight. Depending on the configuration, the presence of lifting surfaces can have a significant effect on the performance of propellers in hover [2]. It has also been demonstrated that propellers used for hover generate a significant amount of drag on their own in forward flight [3, 4]. Needless to say, the presence of hardware used for hovering has a significant impact on the forward flight performance and vice versa. A better understanding of these interactions could be important in design of future VTOL craft, as well as improving efficiency and safety of existing craft.

Propellers in a tractor configuration are relatively well studied with regards to their effects on a wing [5, 6]. Examining interactions with rotors in a hover orientation is less understood, particularly in forward flight. Analytical treatments rely on a large number of assumptions [7].

Many programs exist that are theoretically capable of simulating the effects described above. At one extreme are fully volumetrically discretized CFD codes such as ANSYS FLUENT. While these methods can theoretically compute accurate results for any type of problem, present limits on computing power render them too time consuming for much design work. Mid-fidelity techniques like the Vortex Particle Method [8], or the Free Vortex Wake Method [9] hold potential as effective design tools. These techniques are integrated into design softwares such as Rotorcraft Comprehensive Analysis System (RCAS), Comprehensive Analytical Model of Rotorcraft Aerodynamics and Dynamics (CAMRAD), or Comprehensive Hierarchical Aeromechanics Rotorcraft Model (CHARM). Given the increasing importance of simulation tools in the engineering design process today, sets of validation experimental data are important to improve trust in the fidelity of tools. These codes are often validated against historical sets of data [10].

To produce a set of data adequate for reference as design guidelines and for comparison with software, a rapidly adjustable test setup is required, akin to the NASA multirotor test bed [11]. This work seeks to examine the effect of various geometric arrangements at different flight conditions, so it is preferable to have large amounts of data in terms of different geometries. A test assembly to achieve these goals has been designed and is described in subsequent sections.

This work will be laid out as follows. Section 6.2 will describe the experimental setup and hardware design. Section 6.3 will describe the independent characterization of the wing, while Section 6.4 will describe the independent characterization of the propeller. To then examine the interaction in detail, Section 6.5 will first examine the case with the rotor upstream or leading the wing, while Section 6.6 will examine the case with the rotor downstream or trailing the wing.

6.2 Experimental Setup

To study the interaction outlined above and collect a large amount of spatial experimental data for the development of a model, a test assembly was constructed. The design consists of force sensors on a propeller and a rectangular finite wing, a 2D computer controlled traverse to change the position of the propeller relative to the wing, and a Fan Wall array to simulate forward flight. Each of these elements are summarized in the following sections, and a diagram, sans Fan Wall, is shown in Figure 6.1.

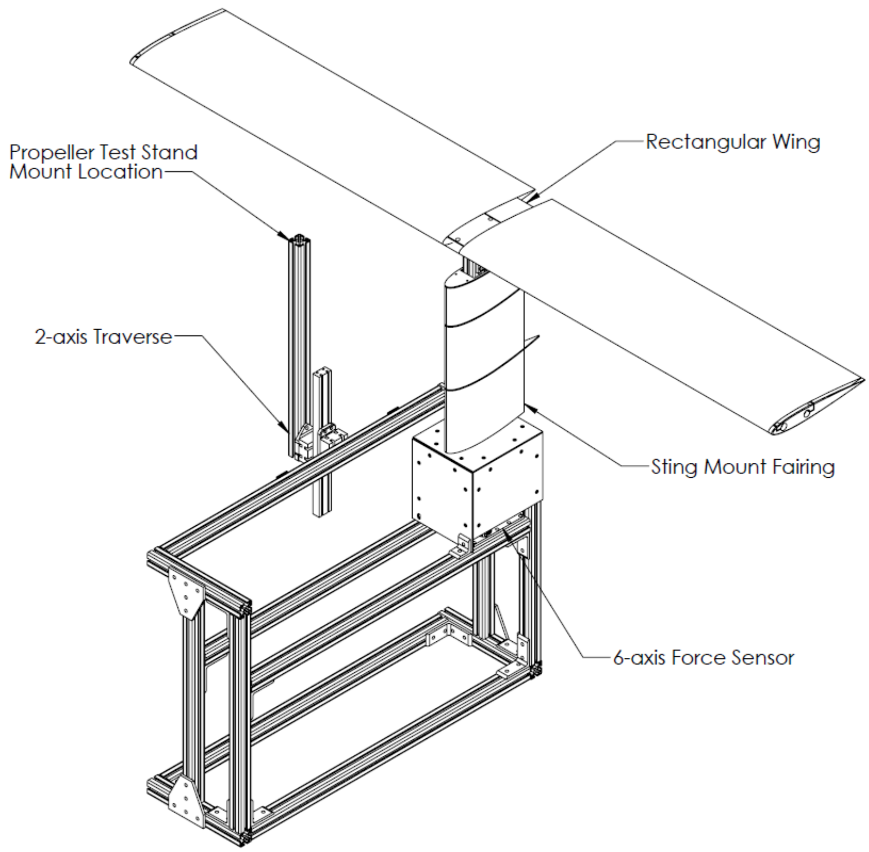

Figure 6.1: Diagram of the combined assembly for aerodynamic testing.

CAST Fan Array Wind Tunnel

The Center for Autonomous Systems and Technologies (CAST) is the site where much of the physical testing will take place. One of the tools in CAST is the Real World Wind Tunnel, a square array of 1296 fan pairs used to make an open air wind tunnel for use in the space. The wind tunnel has a profile of roughly a 3 meter square, and is capable of going up to speeds of up to 12.8 m/s. Additionally, the fans of the wind tunnel are capable of individual control, allowing for more complex spatially and time varying wind profiles to be created. The tunnel will be used to study the effects of early transition flight on the geometric configuration. Because the fan portion of the fan array is raised above the ground of the test facility it is stored in, the testing frame onto with the components are attached is raised to place the wing and propeller into the airflow.

Figure 6.2: Combined Test Assembly Installed in the CAST Flight Arena.

Figure 6.3: Assembly shown with Fan Array in View.

Finite Rectangular Wing

In order to study the effects of the interaction with a lifting surface as found on a vehicle, a canonical finite wing was constructed for use in the experiments. The wing is composed of a straight extrusion of a NACA 0012 airfoil with a chord of 12 inches and therefore no taper or wingtip devices. The chord of 12 inches was selected to be equivalent to the propeller diameter used for the experiments. The size was also chosen because drone scale propellers are often sold in sizes of whole

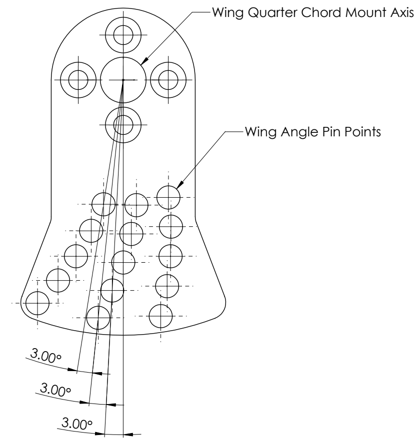

Figure 6.4: Drawing of fixture plate used to set wing angle of attack.

inches, so chord/diameter ratios would be represented numerically in a neat fashion. The NACA 0012 is one of the most commonly studied airfoils found in research, and data for it at many Reynolds numbers is readily available. Data for finite rectangular wings made with this airfoil are also readily available [12, 13, 14, 15, 16]. The intention is to conduct experiments with a wing that is directly comparable to data in the literature.

The profile was cut from Foamular Insulation foam on a CNC hot wire cutter to produce an accurate profile, and was then wrapped in Black Econokote to produce a smooth surface finish. For structure, a pair of aluminum rods run along the span at $1/8$th of a chord ahead and behind the airfoil quarter chord. With the mounting hardpoint in the center and hardware at the tips to retain the structure, the total span of the wing is approximately 83 inches. The wing center has a component to attach to a section of 1.5" 8020 extrusion as well as adjust the angle of attack in discrete, three degree increments up to a pitch angle of 21 degrees in either direction. A drawing for the component for setting the angle of attack is shown in Figure 6.4. In order to isolate the force on the wing, the extrusion that the wing is mounted on is aerodynamically isolated by a streamlined fairing that covers, but does not contact, the beam that connects the wing to the force sensor. The shroud ideally influences the airflow as little as possible.

Airfoil Section	Chord (m)	Span (m)	Area (m^2)	Aspect Ratio
NACA 0012	0.3048	2.1082	0.6426	6.9167

Table 6.1: Finite Wing characteristics in SI units.

Aerodynamic Fairing

As the wing is connected to the force sensor using a sting mount, it is important to attempt to remove the aerodynamic influence of the sting. As a blunt object, the sting is expected to have several times the drag of a streamlined shape such as the wing. Unaddressed, this may overshadow the drag data read by the sensor. In order to aerodynamically isolate the sting mount, a fairing was designed to enclose the sting such that it should observe only still air and therefore not contribute to the force readings as the aerodynamic conditions change.

The first version of the fairing was assembled by bolting 3D printed panels end on end with bulkheads in between to add structure, as shown in Figure 6.5. As the sting used in this study was a piece of 1.5" wide 8020 extrusion, it was sought to enclose this with an appropriate airfoil to shield it. A NACA 0018 with a 12" chord was chosen, and was positioned such that the sting was places at the 30% chord line of the airfoil, the location of maximum thickness. Ultimately, it was found that this design lacked sufficient rigidity for effective testing. The flexibility of the fairing meant that the it would oscillate with greater and greater frequency and he freestream speed increased. This limited the maximum freestream speed of testing, as sufficiently large oscillations would result in the fairing contacting the sting and influencing the force measurements.

To remedy this issue, the fairing was redesigned with 2 3/4" aluminum rods as the core structure seen in Figure 6.6. The introduction of rigid elements substantially improves the vibration characteristics of the fairing. Additionally, the fairing panels that form the airfoil are now attached to the structural elements rather than each other, allowing them to be assembled more simply. The redesigned fairing surrounds, but does not contact the wing mount as shown in Figure 6.7 The fairing was also attached to the frame with components to protect the force sensor from aerodynamic interference. This is seen in Figure 6.8. The force sensor described in Chapter 5 is enclosed in the fairing structure to isolate it from the flow.

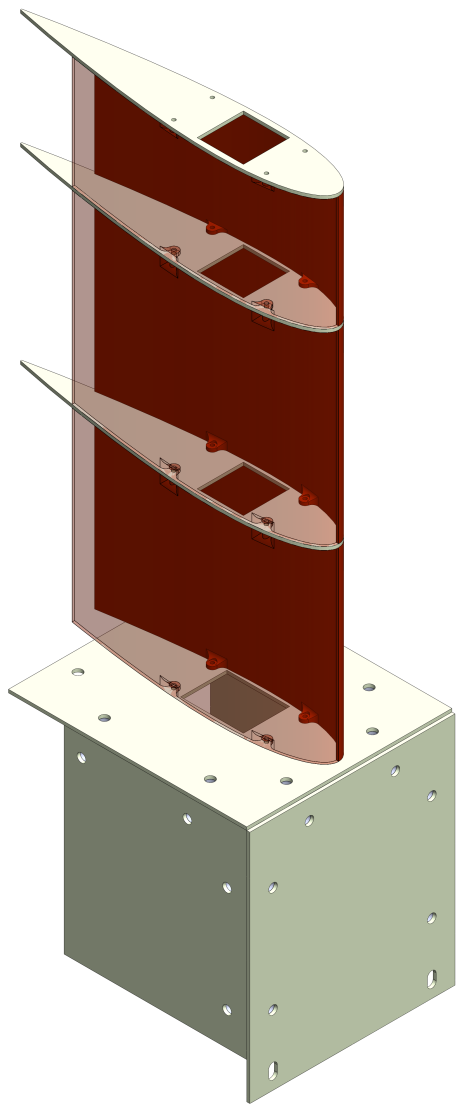

Figure 6.5: First version of sting fairing, built using stacked sections.

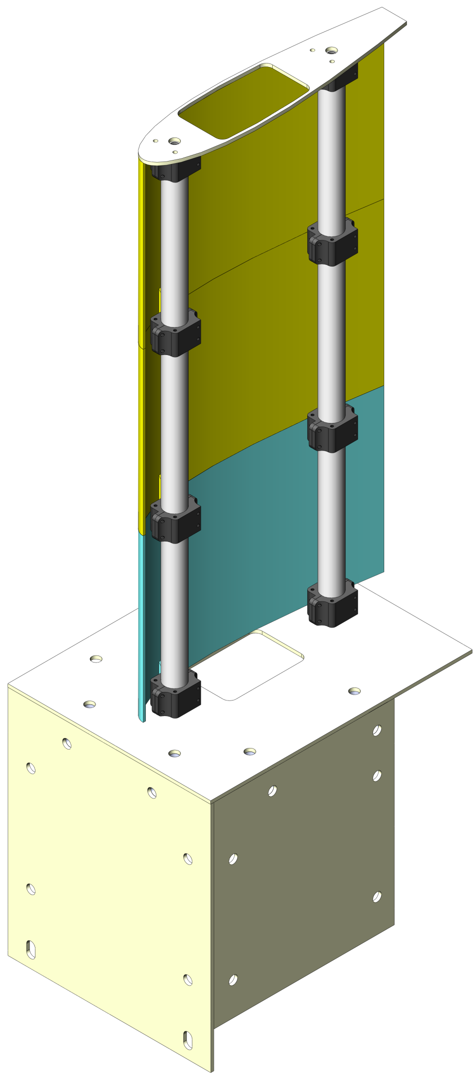

Figure 6.6: Second version of sting fairing. Panels are attached to hardpoints mounted to the structural aluminum elements.

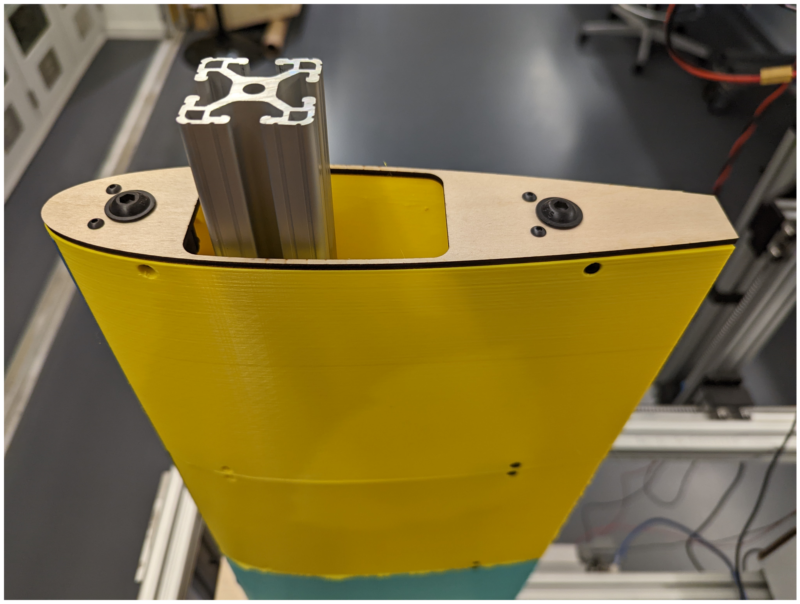

Figure 6.7: Installation of sting fairing around the wing mounting member.

Propeller Test Stand

The propeller was mounted on an RCbenchmark 1585 test stand [17]. The test stand has the capacity to measure force, torque, rotation speed, electrical current and voltage, and other parameters relevant to electric motor performance. Although the main configuration of interest is one where the propeller is in a hover configuration, there is nothing preventing the propeller from being mounted at various angles of attack relative to the airflow or in a thruster configuration. As the thrust stand is mounted directly to the motor and propeller, its attachment to the rest of the test frame does not need to be shielded for force measurement unless one is concerned about the wake of the structures interfering with other components of the assembly. Due to hardware limitations, the propeller test stand was kept exposed.

With the load cells on the stand, it is also possible to measure aerodynamic drag as described in Chapter 3. The load cells present on the stand for torque can also be used to measure linear force. By performing the appropriate calibration and sampling the load cell measurements directly through the RCbenchmark software, it's possible to measure the propeller thrust and the propeller drag, or more specifically, the force component perpendicular to thrust, simultaneously.

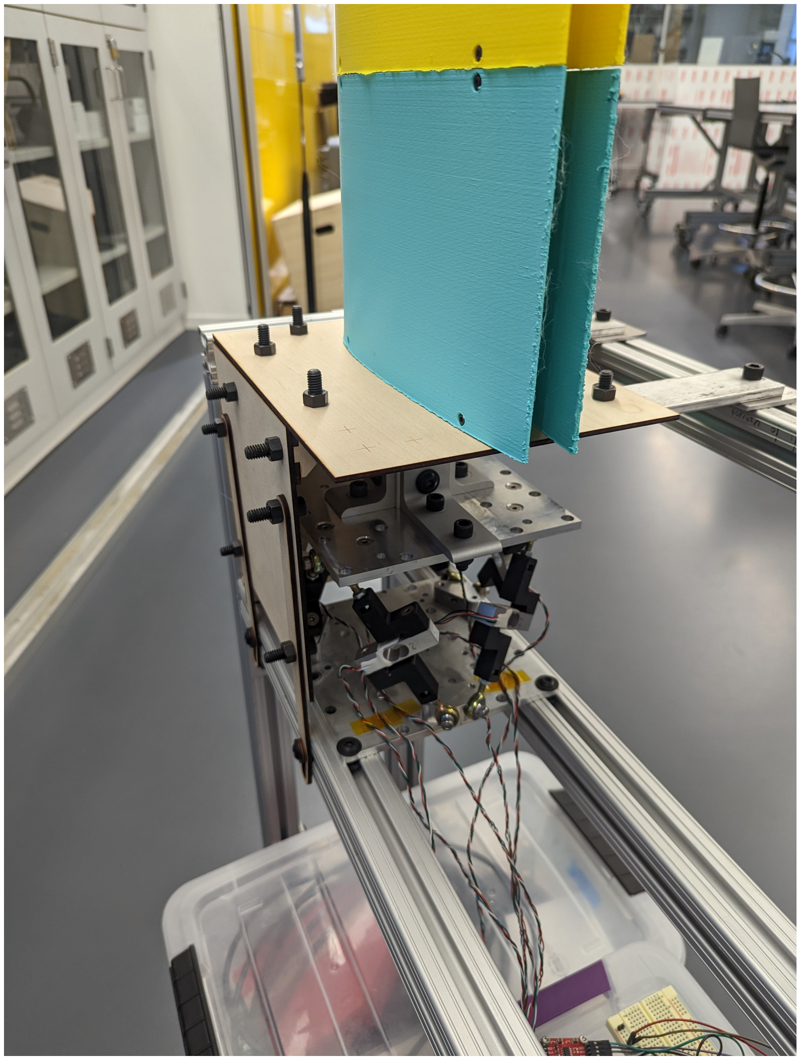

Figure 6.8: Force sensor installation in assembly.

2-axis Traverse

In order to quickly and precisely reconfigure the relative geometry of the propeller, a 2-axis CNC traverse was constructed. The axes were composed of two 300 mm Ballscrew linear actuators using NEMA17 Stepper Motors and fitted with end stops for reproducible position homing. The screws have a pitch of 5 mm. The linear actuators are controlled with Tic T825 Multi-Interface Stepper Motor Controllers, which feature a provided GUI for either position and velocity control. The motor controllers interface with a provided interface software to control position. The software provides options for arbitrary degrees of microstepping as well. For this work, the stepping was set to $1/8$ steps, which, combined with the stepper motors' 1.8° step increments, allowed for a minimum theoretical position resolution of 0.003125 mm or 0.000123 inches.

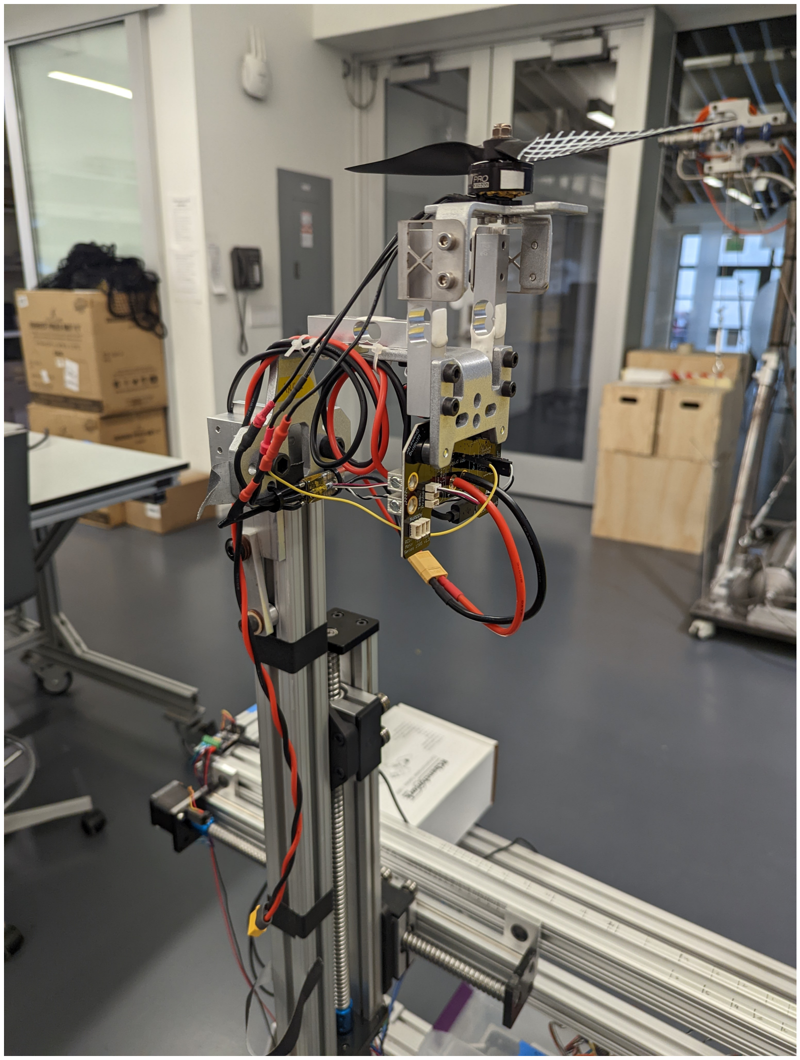

Figure 6.9: Propeller test stand installed on 2-axis traverse.

6.3 Wing Characterization

To establish a quantitative baseline, the wing was characterized using the 6 component force sensor in front of the CAST fan array wind tunnel. The wing's angle of attack was varied from -21 degrees to 21 degrees in 3 degree increments. At each angle of attack, the flow speed was varied in 10 percent increments of 6.44 m/s. The various air speeds and angles of attack are then fitted to standard non-dimensional coefficients, and compiled for reference in Figure 6.14

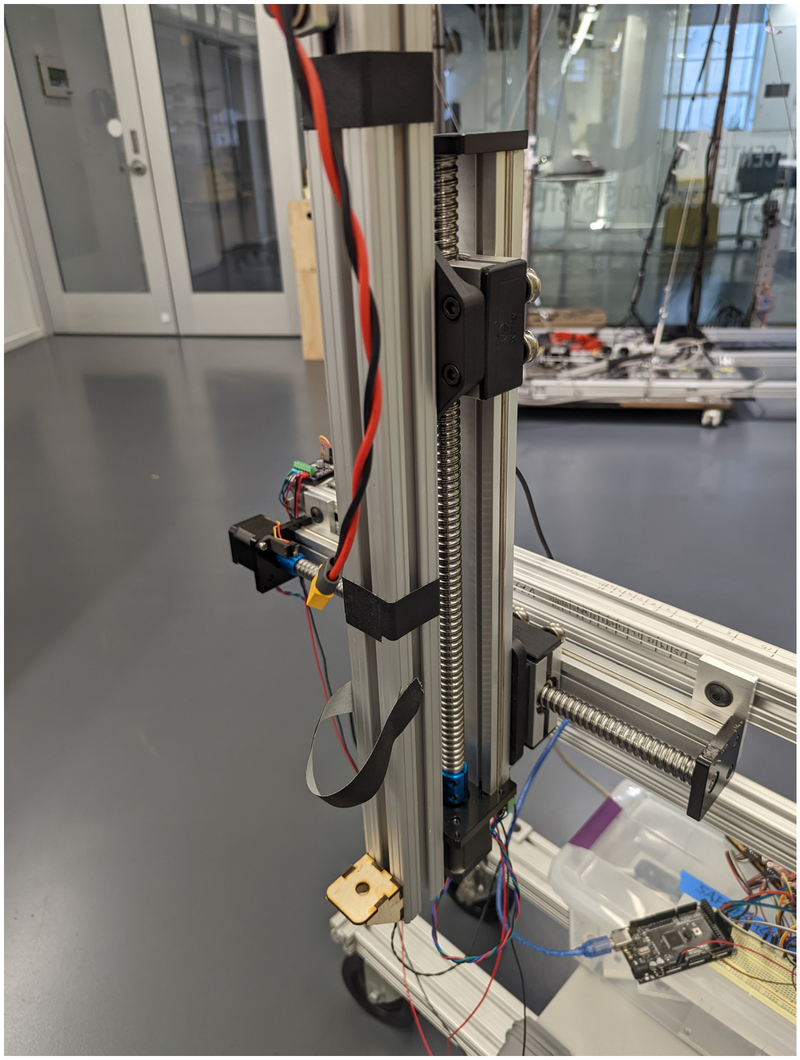

Figure 6.10: Two-axis traverse built from linear actuators.

The Lift and Drag on the wing are non-dimensionalized using the Lift and Drag coefficients C_L and C_D, respectively [18].

$$C_L = \frac{L}{\frac{1}{2}\rho V_\infty^2 A} \tag{6.1}$$

$$C_D = \frac{D}{\frac{1}{2}\rho V_\infty^2 A} \tag{6.2}$$

L and D are the Lift and Drag forces, respectively, ρ is the air density, V_∞ is the freestream velocity, and A is the planview area of the wing, 996 in^2 or 0.6426 m^2. The lift and drag values of wing are shown in Figures 6.11 and 6.12. The data were collected for various freestream velocities at each fixed angle of attack, but the data for the same Reynolds number are drawn together to illustrate the effect of the change in Reynolds number on the results. The Reynolds number for the wing is computed using the freestream velocity and the wing chord of 12 inches. The wing data were collected using the force sensor described in Chapter 5, which has an evaluated accuracy of 3% in the lift direction and 5% in the drag direction. Error bars representing the range of these accuracy values are drawn in the subsequent plots.

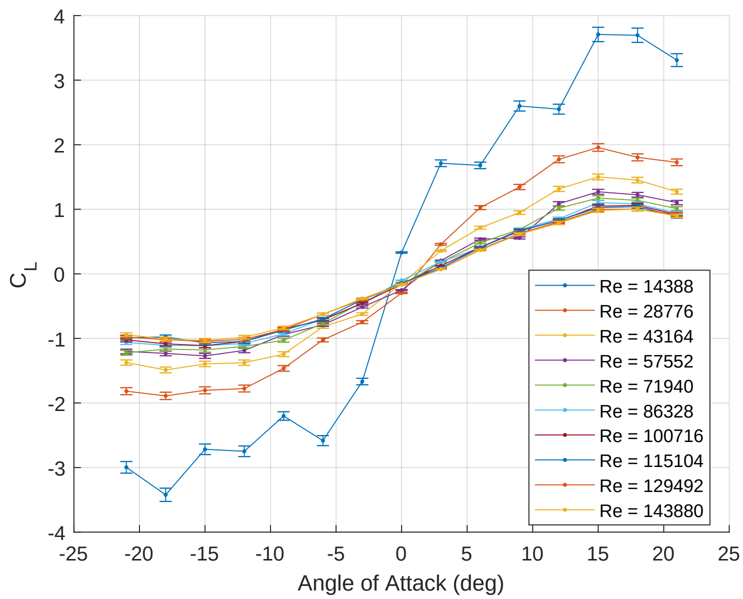

Figure 6.11: Lift Coefficients computed from force data.

There is an observed convergence of the data as the Reynolds number increases, highlighting low Reynolds number effects. However, there is are several sources of error. At low throttles, the measurement and prediction of the freestream velocity from the fan array is more difficult. Errors in velocity for small values would be more visible in the lift and drag coefficients as the velocity is in the denominator. Furthermore, it is observed that the behaviour of the wing is slightly asymmetric. Although the wing was manufactured with the best processes available, there are still errors present. The most obvious consequence of this is that the angle of attack at which the wing exhibits 0 lift is slightly positive. This is visible in Figure 6.14, which shows the fitted lift and drag coefficients with 95% confidence intervals for the wing across the studied Reynold numbers.

In addition, knowing the pitching moment of the wing is often desirable. Because the wing studied in this work was mounted on top of a sting, the measured forces and moments had to be transformed to be represented in a more conventional fashion.

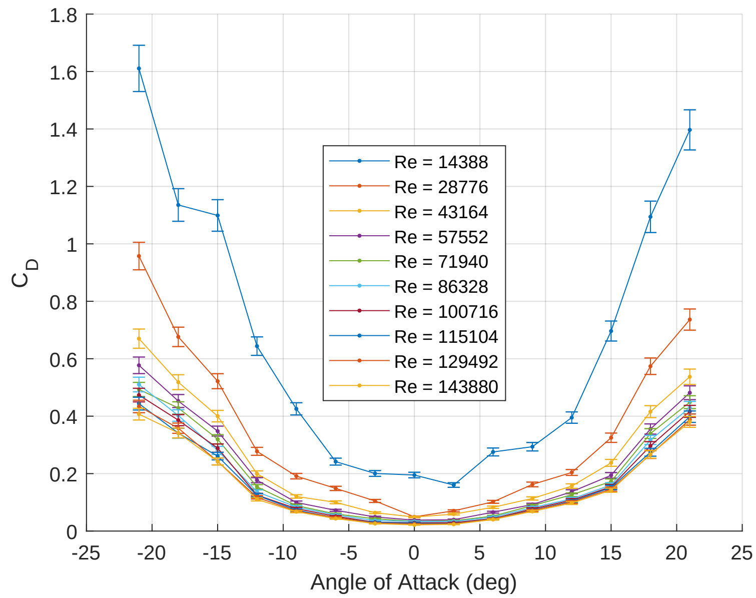

Figure 6.12: Drag Coefficients computed from force data.

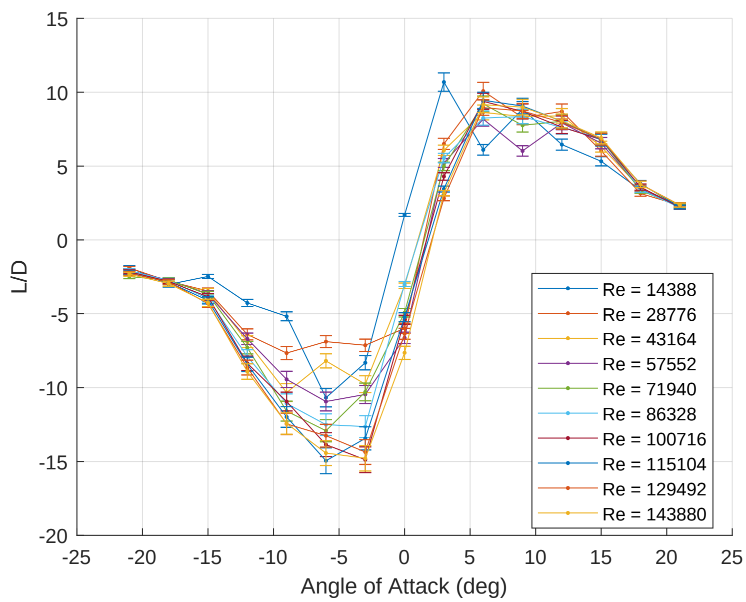

Figure 6.13: Lift to drag ratio at each data point.

The wing was mounted at its quarter chord a fixed distance directly above the the force sensor's origin. Computing the pitching moment was a matter of using the known distance to the mount location to subtract the moment associated with the drag force. Like the lift and drag forces, the moment is represented by a non-dimensional coefficient.

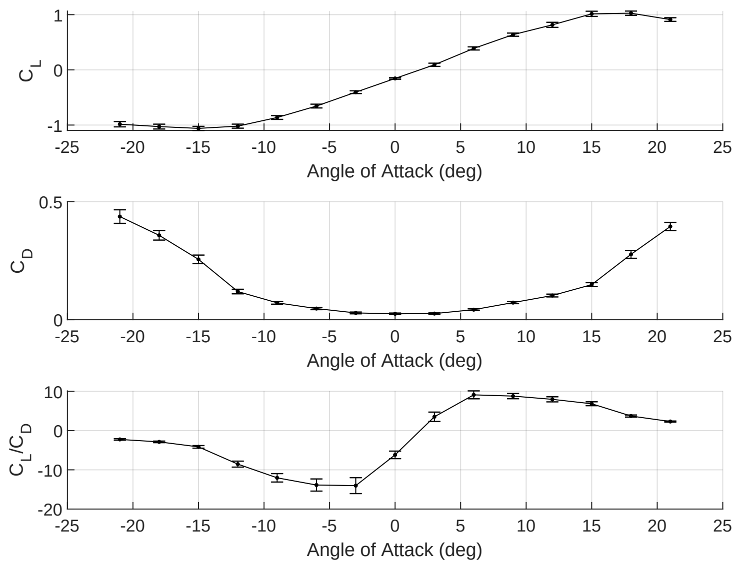

Figure 6.14: Lift and drag coefficients from data fits with 95% confidence intervals.

$$C_M = \frac{M}{\frac{1}{2}\rho V_\infty^2 A c} \tag{6.3}$$

The variable c is the chord length of the wing, 12 inches. The results of this are shown in Figure 6.15. While the data do have a linear trend within the low angle of attack region of the wing, the data are substantially more scattered than the analogous lift and drag data. Possible explanations for this are that the moment was small enough that the inherent sensor noise was affecting measured results, or that the noise introduced by the larger signal associated with the drag was substantially affecting the results.

The wing generally exhibits the expected behavior of a finite wing. For most of the angles of attack studied, the lift curve of the wing is quite linear. At the limits of the angles of attack studied the drag appears to continue increasing while the lift remains level or begins decreasing, suggesting the onset of stall.

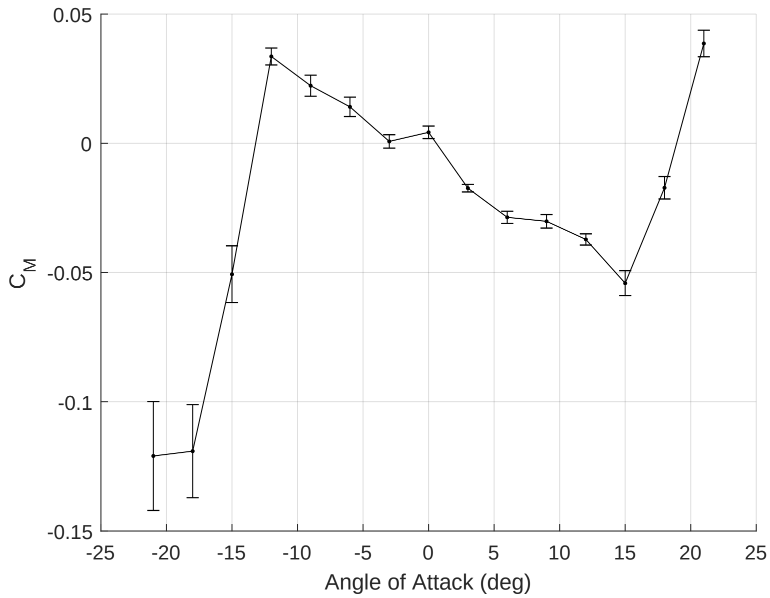

Figure 6.15: Moment coefficients computed from force data with 95% confidence intervals.

6.4 Propeller Characterization

The motor and propeller used in these experiments was a T-motor U3 with a T-motor 12×4 inch propeller. To establish a baseline, the propeller was run at various speeds in hover and in forward flight conditions. At each of these conditions, thrust, torque, and drag were collected. To minimize the effect of the test stand on the results, the propeller was mounted to the motor with the resulting downwash projecting away from the test stand. For the tests, the propeller was kept at 0 angle-of-attack, meaning the rotation axis was perpendicular to the freestream velocity. This was done to represent the canonical case of a VTOL vehicle transitioning to forward flight where it is assumed that some forward propulsion is providing the thrust while the vehicle remains level.

Propeller Coefficients

The propeller was characterized using the following common non-dimensionalizations.

$$T = \rho\omega^2 C_T D^4 \tag{6.4}$$

$$Q = \rho\omega^2 C_Q D^5 \tag{6.5}$$

where T is the Thrust, Q is the Torque, D is the propeller diameter, and ω is the propeller angular speed in radians per second. One metric of propeller performance is the Figure of Merit, defined as

$$M = \frac{P_{\text{ideal}}}{P_{\text{measured}}}. \tag{6.6}$$

Expressed using the non-dimensionalizations of force and torque, and using the ideal induced power from Disk Actuator theory described in Appendix C, the figure of merit in hover can be equivalently represented as

$$M = \sqrt{\frac{2}{\pi}} \frac{C_T^{3/2}}{C_Q}. \tag{6.7}$$

In forward flight, the estimated induced velocity based on Glauert momentum theory can be used.

$$T = 2\rho A_{disk} V_i \sqrt{V_\infty^2 + 2V_\infty V_i \sin\alpha + V_i^2} \tag{6.8}$$

where A_{disk} is the disk area, α is the propeller angle of attack, and V_i is the induced velocity across the disc. V_i has an analytic solution for $\alpha = 0$, but the expression can be solved numerically with little effort otherwise. The ideal power in forward flight is then

$$P_{\text{ideal}} = T(V_\infty \sin\alpha + V_i). \tag{6.9}$$

The data shown in Figures 6.16 and 6.17 seem to show good agreement with these equations, even at forward velocities and with the wing present. The fitted coefficients for all the sample data, not just that with no obstruction or forward velocity, are $C_T = 0.00204$ and $C_Q = 1.0003 \times 10^{-4}$.

The data show that there is relatively small variability in the propeller performance in forward flight. The data in Figures 6.16 and 6.17 also have the presence of the wing and a freestream velocity and show relatively minor changes in the thrust and torque output. Figures 6.18, 6.19, and 6.20 show the thrust, torque, and figure of merit values computed from the experimental data for the propeller in isolation from Chapter 3. The data show that the non-dimensional coefficients vary with the advance ratio, and the individual rotation speed. The variability with rotation speed is a known effect that is observable in static testing. The most likely explanation is a change in Reynolds number on the propeller blade as the rotation speed changes. Interestingly, the thrust and torque curves are not necessarily continuous, being divided by the freestream velocity. Also note that the figure of merit decreases substantially in Figure 6.20, as the ideal power expression is expected to decrease substantially in forward flight but the measured power for a given thrust is relatively constant.

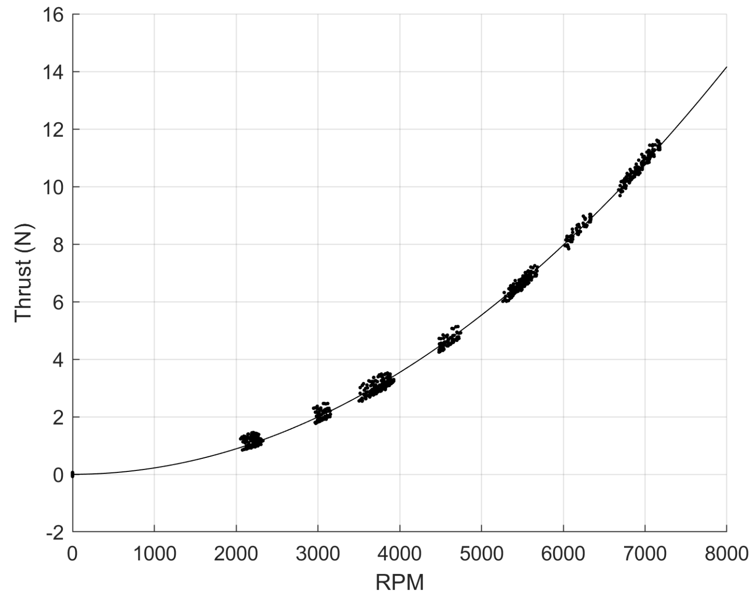

Figure 6.16: Experimental thrust measurements.

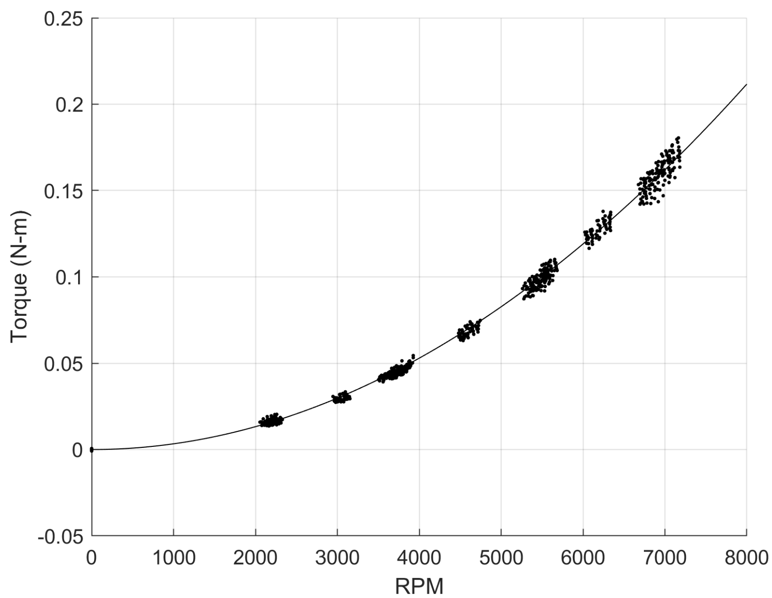

Figure 6.17: Experimental torque measurements.

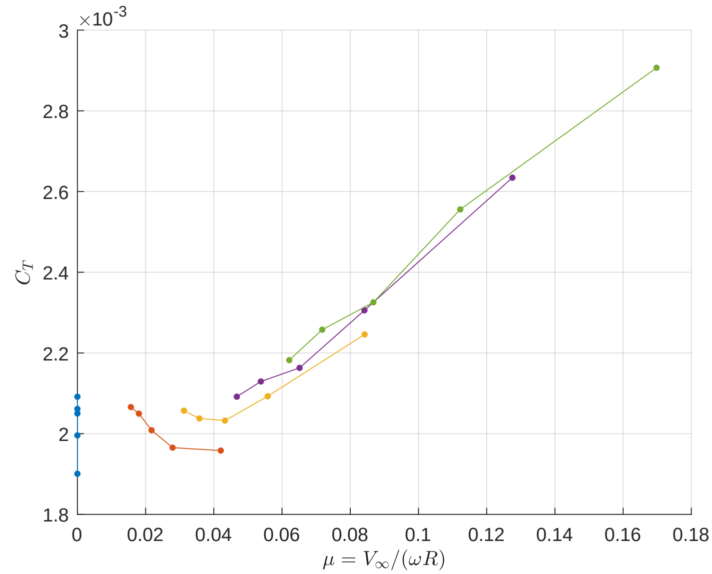

Figure 6.18: Change in thrust coefficient with advance ratio. Curves are at constant velocity.

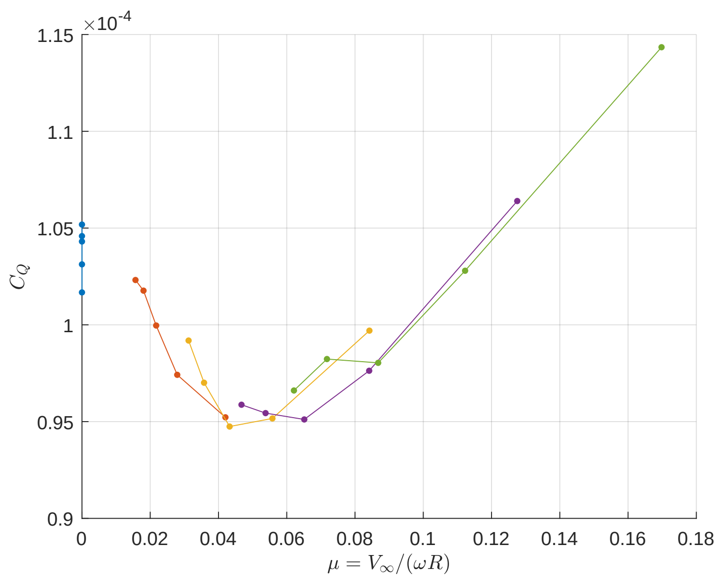

Figure 6.19: Change in torque coefficient with advance ratio. Curves are at constant velocity.

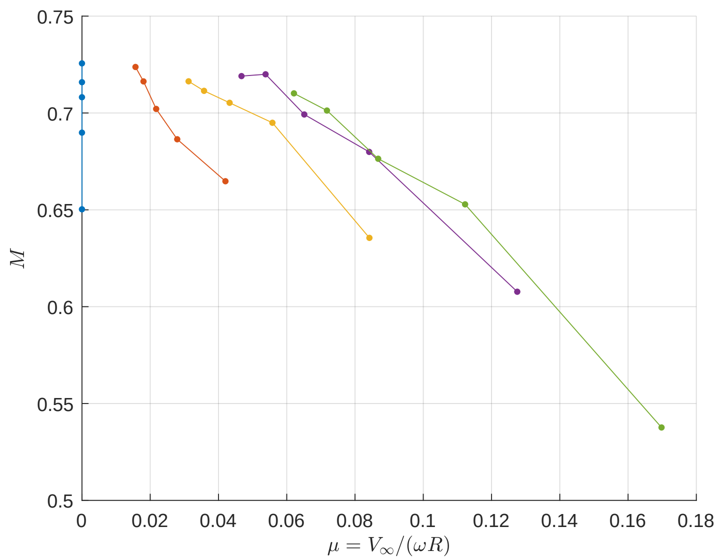

Figure 6.20: Change in figure of merit with advance ratio. Curves are at constant velocity.

Propeller Downwash

One salient attribute in identifying whether the propeller wake will interact with another body is the direction of the downwash. To quantify the downwash, smoke was emitted into the propeller intake and was recorded passing into the propeller wake. It was found that the most convenient way to trace the smoke trail was to take a time average of the frames of the recording and trace the result to measure the angle of the downwash relative to the freestream.

Figure 6.21: Long exposure image with approximate angle traced in green.

The effective downwash angle can also be predicted from Glauert's momentum analysis in forward flight [19]. The result of the theory produced by balancing mass, momentum, and energy is seen in Eq. (6.8). The downwash angle is then calculated by assuming that the resulting flow velocity from the propeller is a vector sum of the freestream velocity and the rotor downwash velocity. From the same theory, the rotor far wake speed is $w = 2V_i$. As the propeller is held at $\alpha = 0$, the expected downwash angle is calculated using the ratio of the velocities.

$$\theta_{\text{downwash}} = \arctan(w/V_\infty) \tag{6.10}$$

For each datapoint collected, we can then plot the ratio of the induced velocity computed from the measured thrust and rotation speed versus the measured downwash angle from the recording. We can compare this plot to the simple expected geometric result. As shown in Figure 6.22, there is a clear discrepancy in the true vs expected values. In contrast, if we instead use the velocity ratio of induced velocity at the disk, we have much better agreement, though there is still a discrepancy at higher velocity ratios.

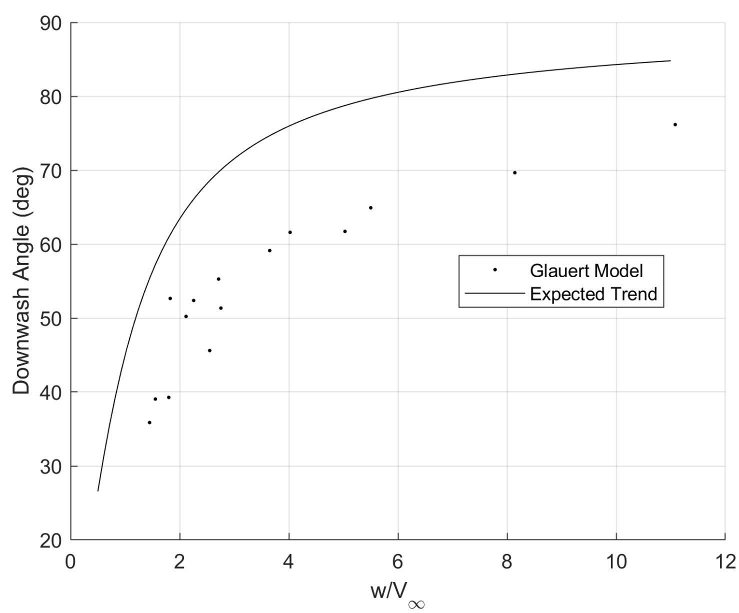

Figure 6.22: Downwash angle calculated from estimated far wake velocity.

One potential problem with this formulation is that the predicted angle has a dependence on thrust. However, Thrust is a measured quantity in the experimental setup, not an input. An alternative option is to instead use a parameter that can be directly controlled while running experiments. We instead examine the observed downwash angle relative to the advance ratio $J = \frac{V_\infty}{\omega r}$, where r is the propeller radius. Plotting the data in this manner is shown in Figure 6.24. We use a power fit to predict the downwash angle for the range of advance ratios studied and find $\theta = -3.4872 * J^{.1231} + 3.3493$ where θ is in radians.

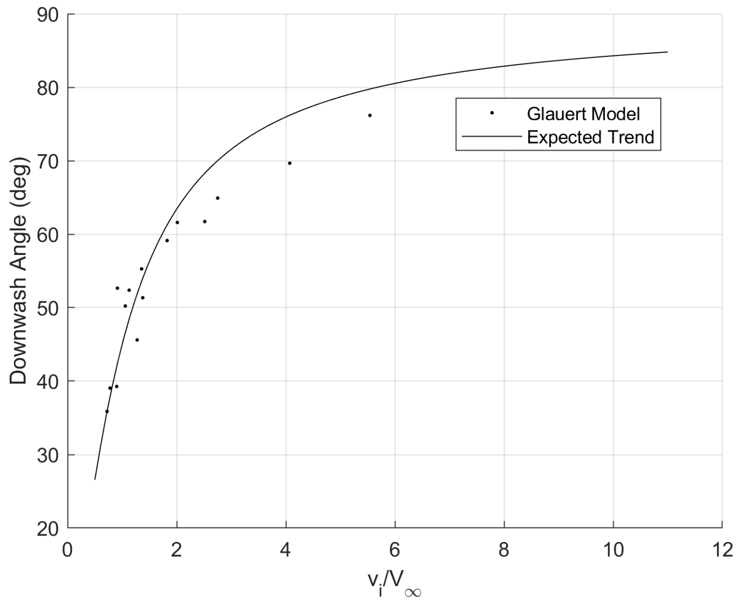

Figure 6.23: Downwash angle calculated from estimated disk induced velocity.

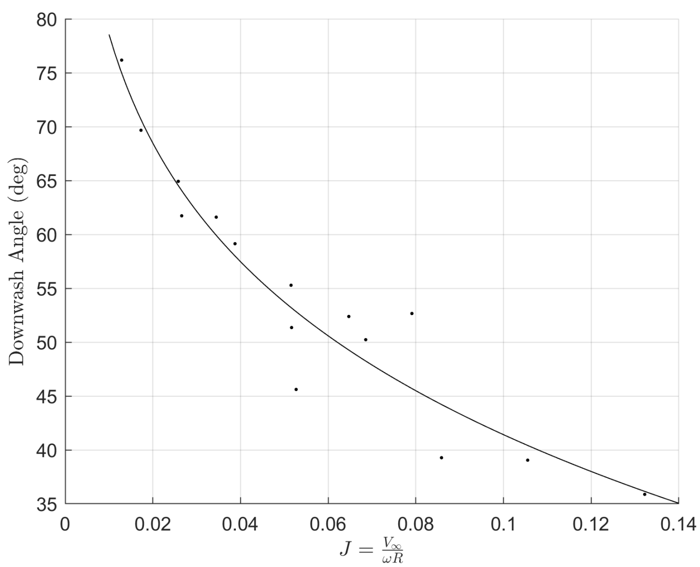

Figure 6.24: Downwash angle versus advance ratio.

6.5 Leading Propeller-Wing Interactions

The aerodynamic interactions between a propeller and a wing are complex and can be very sensitive to a number of variables such as the freestream velocity, the rotational speed of the propeller, and the relative position of the two, among others. Because of the large number of variables, the search space to fully define the interaction is intractable. To mitigate this, we restrict the test conditions to examine limited

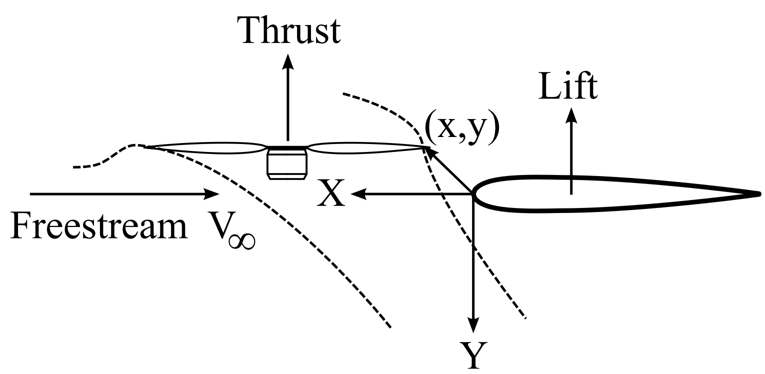

Figure 6.25: Diagram and coordinate system for propeller wing-interactions with the propeller leading the wing.

examples of the effect. Only one propeller was used in the experiments shown with $\frac{d}{c} = 1$. The propeller was also mounted at a fixed angle such that its rotation axis was perpendicular to the freestream direction. The propeller was only tested at one station along the wing span, inboard to try and avoid saturating the moment sensing on the wing's force sensor. The wing was held at only a single angle of attack, -6 degrees. In addition to orienting the lift downward as desired, this was the angle of attack with the highest magnitude lift-to-drag coefficient. The speed of the propeller was varied in the range of 2000 to 5000 RPM while the freestream velocity was kept in the range from 0 to 6.4 m/s.

The coordinate system used for the propeller is also shown in Figure 6.25. The origin is determined by aligning the trailing edge of the propeller disk to the leading edge of the wing. Furthermore, to avoid the interaction of the downwash of either the propeller or the wing with portions of the test stand, the Lift and Thrust are oriented downwards so that their wakes propagate into the cleaner airflow above.

The propeller was moved to a number of positions within the range of both linear actuators. The propeller was spun to a discrete range of rotational speeds at a range of freestream speeds while force data was collected for both the propeller and the wing.

Propeller Performance

The propeller performance observed with the propeller leading the wing can be seen in Figures 6.26, 6.27, and 6.28. The contours are the same general shape as seen for the data for the propeller in isolation, although the larger amount of data shows additional scatter. The amount of scatter in the data is visibly larger at larger advance ratios. The increased scatter in this case is likely due to the fact that larger advance ratios generally mean smaller rotations speeds. The smaller rotations speeds correlate with smaller propeller forces. The smaller forces can mean larger relative error, compounded with the smaller rotational velocities in the denominators of the expressions for the coefficients, leading to a larger scatter.

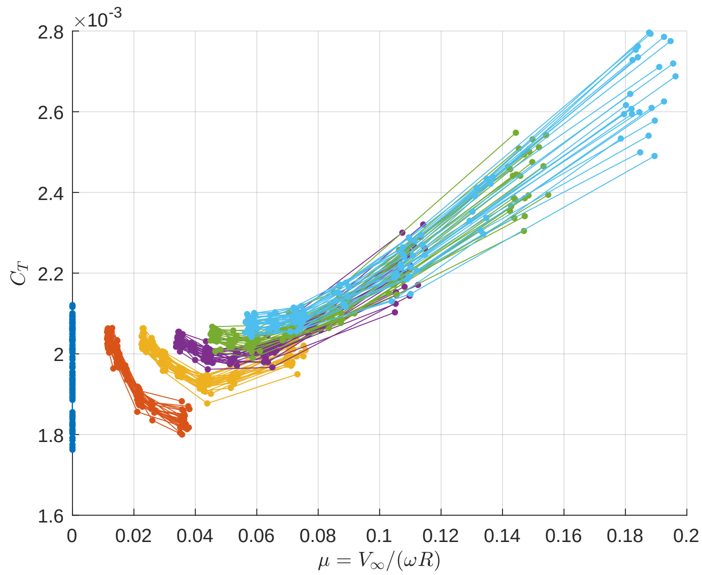

Figure 6.26: Change in thrust coefficient with advance ratio. Curves are at constant velocity.

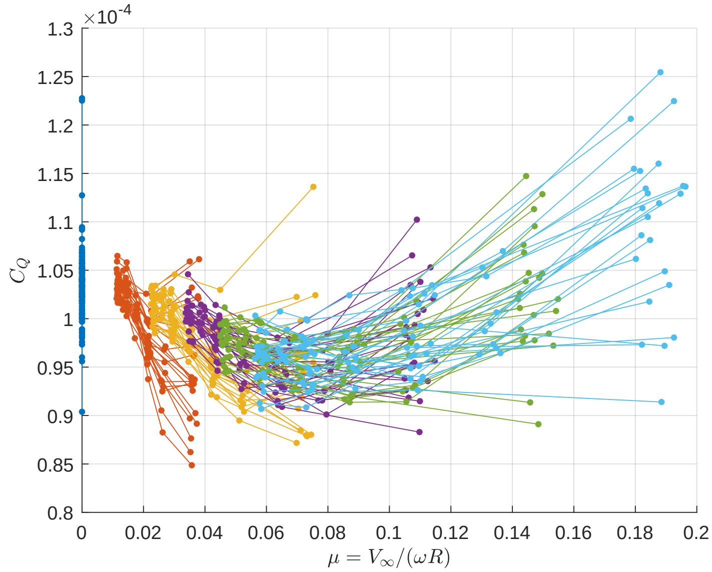

Figure 6.27: Change in torque coefficient with advance ratio. Curves are at constant velocity.

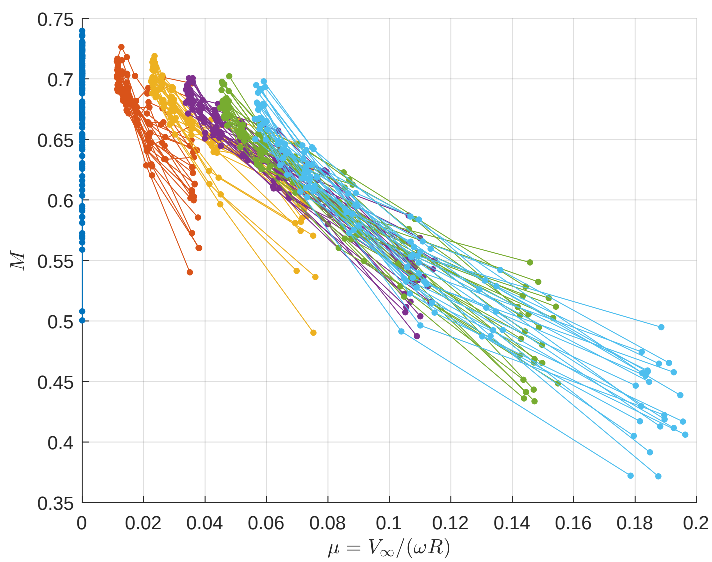

Figure 6.28: Change in figure of merit with advance ratio. Curves are at constant velocity.

Change in Aerodynamic Forces

One significant and notable effect was the change in measured lift coefficient on the wing seen in Figures 6.29 and 6.30. Error bars for the data were omitted for clarity, but the analysis in Chapter 5 indicates that the accuracy of the sensor measurements is within 3%. The change in lift coefficient is measured as

$$\Delta C_L = \frac{L_0 - L}{\frac{1}{2}\rho V_{\infty}.^2 A} \tag{6.11}$$

where L_0 is the lift with no propeller rotation at the same conditions. The change in drag coefficient is defined the same way. In these figures, we see how the lift coefficient of the wing changes with respect to the propeller advance ratio $\mu = \frac{V_\infty}{\omega R}$ where ω is the angular velocity of the propeller and R is the propeller radius. The data presented between the two plots is the same, but the X and Y positions of the propeller are indicated by the colors in each plot, respectively. From the plots, we see that in cases with high advance ratios, where the propeller rotational speed is at a minimum in the tests, the change in lift coefficient is small as one would expect. However, the effect is substantially more pronounced at lower advance ratios. Despite the propeller diameter used in this test being less than 15% of the span of the wing, the resulting effect can be equivalent to the complete loss of lift on the wing or a complete reversal in the lift direction. The degree of this effect appears to be somewhat dependent on the propeller position, but only for lower advance ratios.

The plot highlighting the Y position in Figure 6.30 appears to illustrate that larger Y positions lead to a larger loss of lift. This is as expected, because it allows for more instances where the rotor downwash can intersect the wing surface. The relation with the X position is much less clear and requires more scrutiny. Each X position appears to be able to produce a range of effects. These trends are similar for the drag seen in Figure 6.31, which increases by up to 0.25 points of drag in certain cases.

Initially, it was hypothesised that the effect could be predicted by projecting the propeller disk along the estimated downwash angle. However, it was found that the reduction of lift was still significant regardless of position for certain advance ratios. For example, Figure 6.29 shows that the experiments run between an advance ratio of 0.05 to 0.1 generally result in between a 0.2 to 0.5 point decrease in lift coefficient, regardless of the propeller X position. As the previous experiments found the downwash angle to be loosely correlated to advance ratio, we would expect that a change in the X position for a constant advance ratio would result in a significant jump in the lift on the wing. Instead, even at positions where we expect the wake to completely miss the wing, we still see a similar drop in lift. This suggests that a simple wake model describing the interaction between the lifting propeller and the wing is insufficient. Ultimately, while a general trend with respect to the rotor Y position was observed, a definite correlation with one of the measured configuration properties and the change in lift was not found for the leading edge rotor.

While a precise relation was not found to describe the effect, the overall implications of the experimental data are clear: a lifting surface will suffer significant performance degradation if it interacts with the wake of a propeller. Placement of the propeller above the main lifting surface of a craft could result in interactions that would disable the wing's ability to produce lift while trying to accelerate, or make it significantly more difficult to reach a fixed wing cruise. A further implication is that care must be taken to avoid interactions between the lifting rotor and other aerodynamic surfaces. For example, placement of the elevator of a craft where it could interact with the wake of a propeller could result in a loss of pitch authority using that surface.

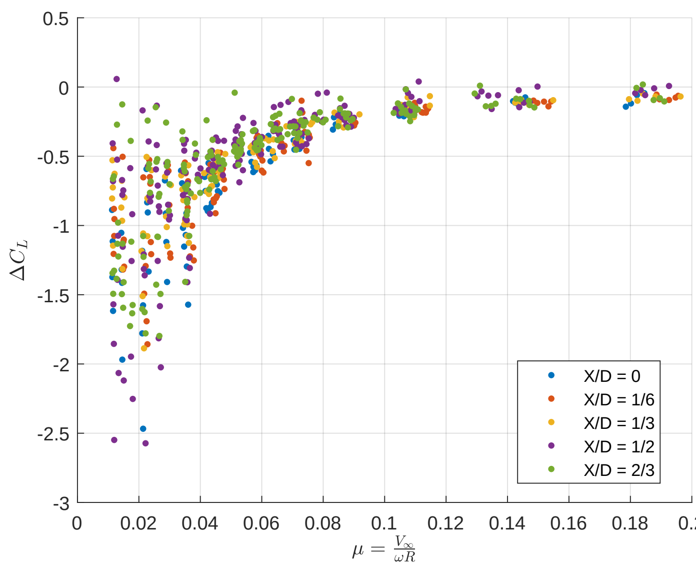

Figure 6.29: Change in wing lift coefficient versus advance ratio, propeller X position highlighted.

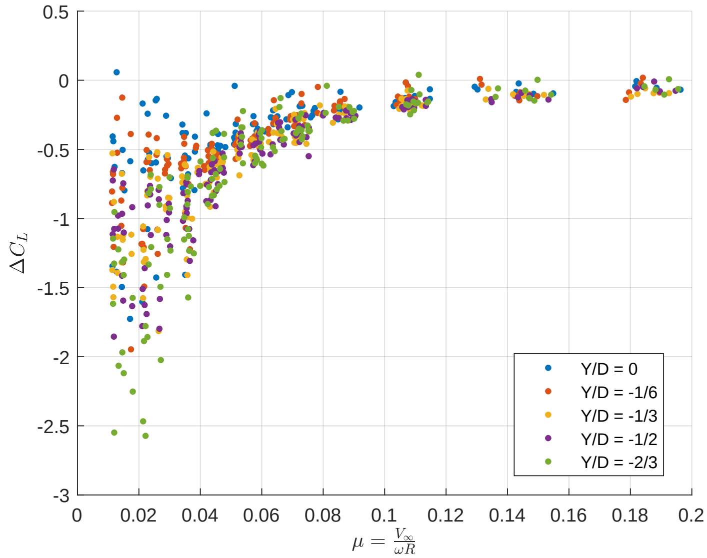

Figure 6.30: Change in wing lift coefficient versus advance ratio, propeller Y position highlighted.

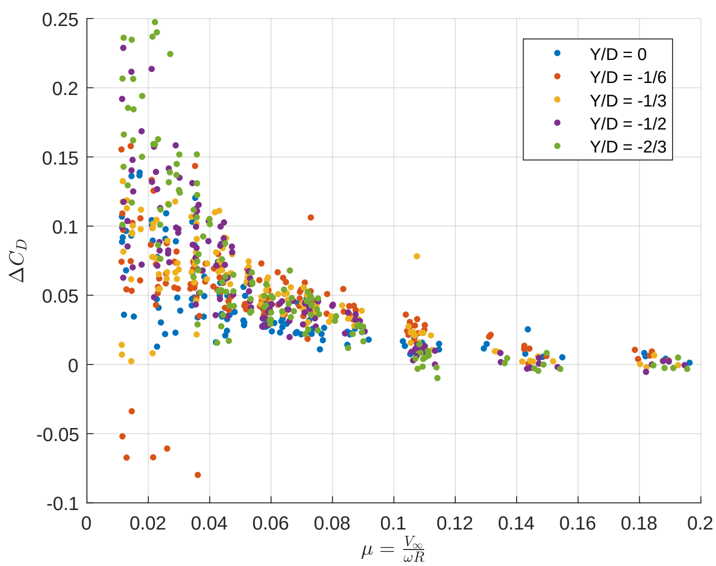

Figure 6.31: Change in wing drag coefficient versus advance ratio, propeller Y position highlighted.

Change in Roll Moment

As a natural consequence of the lift on a portion of the wing decreasing, the previously symmetrical wing develops a substantial roll moment. Figure 6.32 shows how the roll moment, non-dimensionalized in the same manner as the pitching moment above, changes with advance ratio. Again, there is a visible trend within the data, but also a large scattering based on the specific conditions. The change in roll in this case actually opposes the roll induced by the propeller itself, suggesting that the roll authority of a vehicle might be reduced in forward flight.

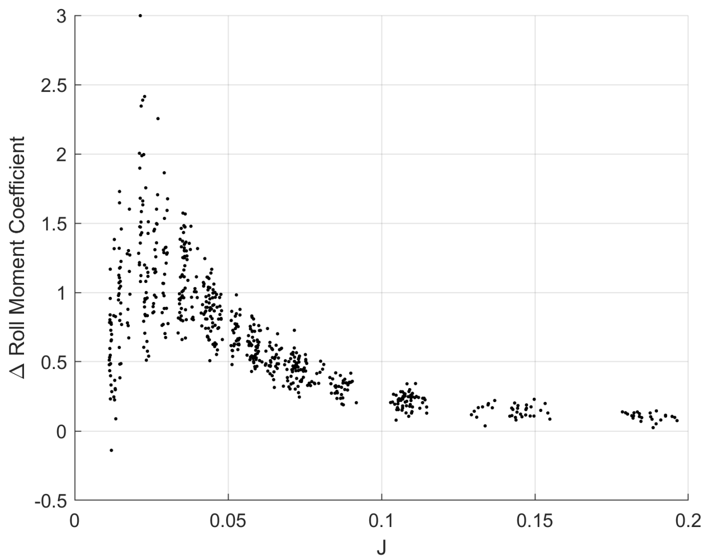

Figure 6.32: Change in wing roll moment coefficient versus advance ratio.

Tuft Testing

Once the initial experimental results were analyzed, tuft testing was conducted to gain insight into the flow quality of the effect. A cotton tuft was attached to the end of a slender rod. By recording video of the tuft at the end of the rod as it is moved in the region around the propeller then tracing the tuft at different points in time, the flowfield can be visualized in a rudimentary fashion. The flowfield for the propeller viewed from the side at two different rotation speeds can be seen in Figures 6.33 and 6.34, with the propeller downwash oriented upwards. The natural inclination of the tuft in freestream is slightly downwards due to the force of gravity. The higher rotation speed leads to a clear change in the flow field, with the wake propagating further and having a larger effect on the surrounding flow. One effect visible downstream of the propeller is that the flow appears to be affected even substantially outside of an expected streamtube region. Flow vectors downstream of the rotor also appear to be inclined slightly in the downstream direction, apparently entrained by the rotor wake.

The effect of the rotor on the flow from a different perspective can be seen in Figure 6.35. In this image, the rotor downwash direction is upwards. As the camera is positioned at an angle, the freestream vector lines converge to a vanishing point. Examination of the vectors near to the rotor shows a wake extending into the vector field well behind the rotor and causing flow to deviate from the freestream direction. The dynamic motion of the tuft, visible in the video, shows that there are apparently two vortices shed from the propeller with opposite rotation directions.

Qualitatively, the tuft investigation shows that the presence of the rotor has a significant effect on the surrounding flow in forward flight. Though the propeller creates a streamtube that projects downward and downstream, the flow has difficulty returning to the freestream direction immediately downstream of the streamtube. The streamtube appears to behave somewhat like a bluff body in the flow, creating a low velocity region immediately behind it and affecting the flow outside of its immediate vicinity.

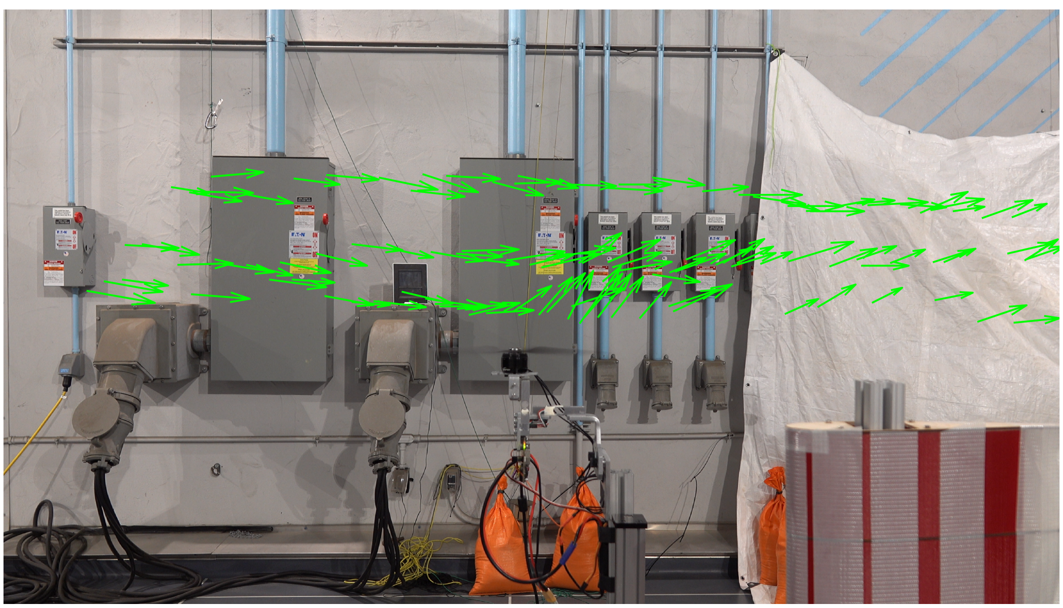

Figure 6.33: Tuft vectors for 3000 RPM at 5.15 m/s seen from the side.

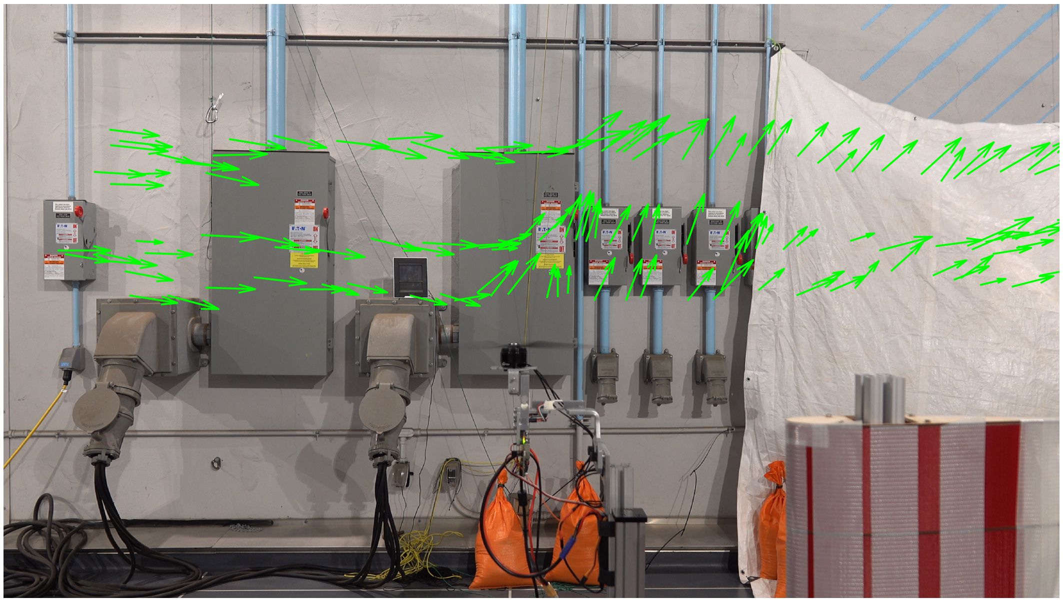

Figure 6.34: Tuft vectors for 6000 RPM at 5.15 m/s seen from the side.

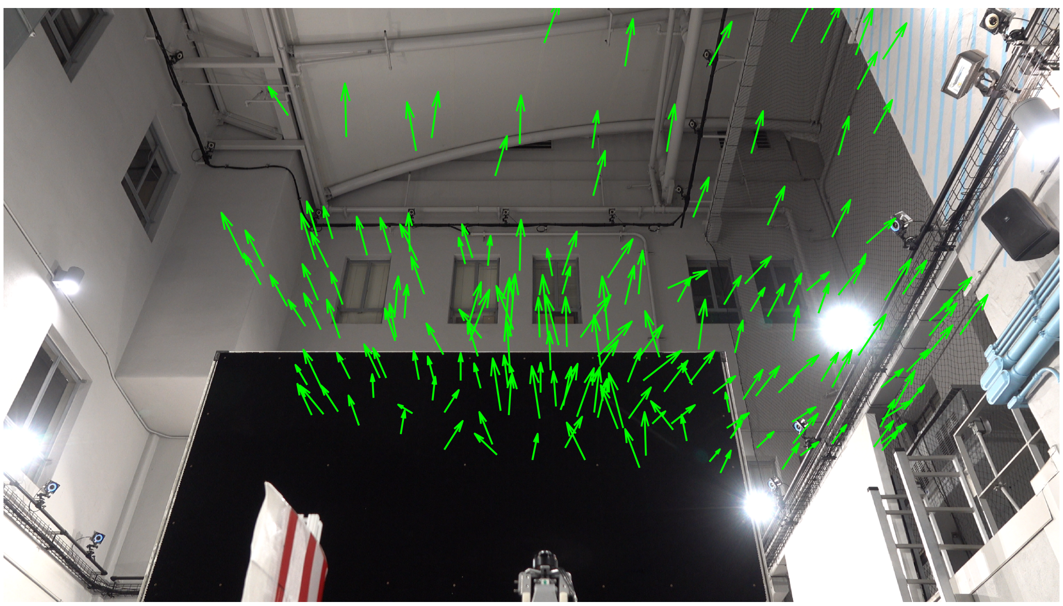

Figure 6.35: Tuft vectors for 3000 RPM at 5.15 m/s seen from below.

Tuft testing was also done to examine the flowfield in the vicinity of the propeller and wing system. A view of the suction side of the wing can be seen in Figures 6.36 and 6.37. Figure 6.36 shows the flow vectors without the propeller influence, which appear to smoothly pass over the wing surface. In contrast, the flow vectors seen in Figure 6.37 show that the leading edge vectors are diverted towards the pressure side of the wing by the rotor airflow. Similarly, the pressure side of the wing can be seen in Figures 6.38 and 6.39. In Figure 6.38, the flow vectors travel smoothly over the pressure side of the wing, with a set of the vectors at the leading edge heading towards the suction side of the wing instead. The presence of the propeller forces the vectors at this location downwards instead, and also appears to make the flow on the pressure side less steady.

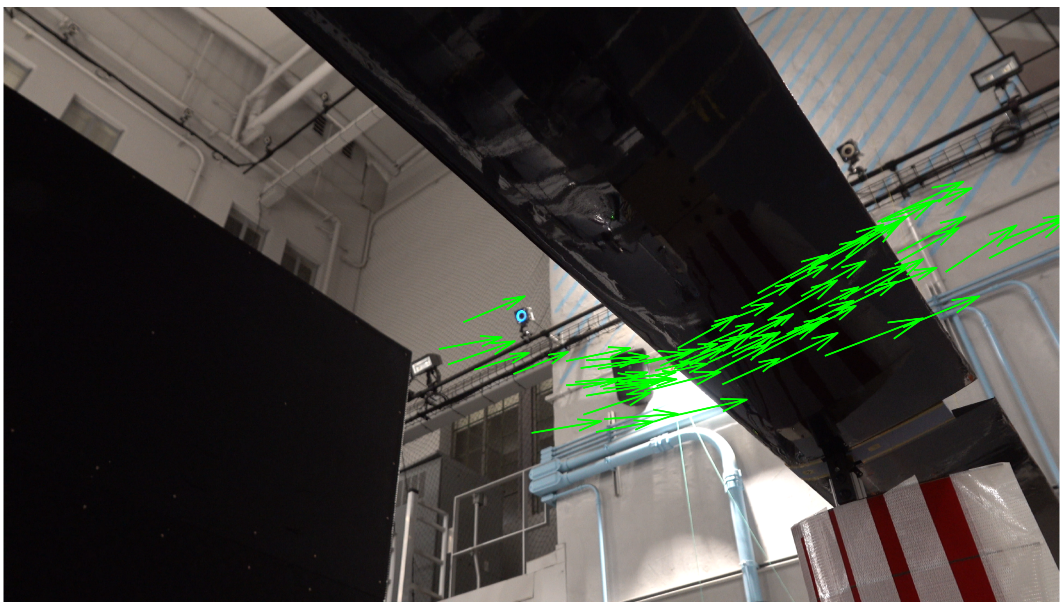

Figure 6.36: Tuft vectors for wing suction side at 5.15 m/s.

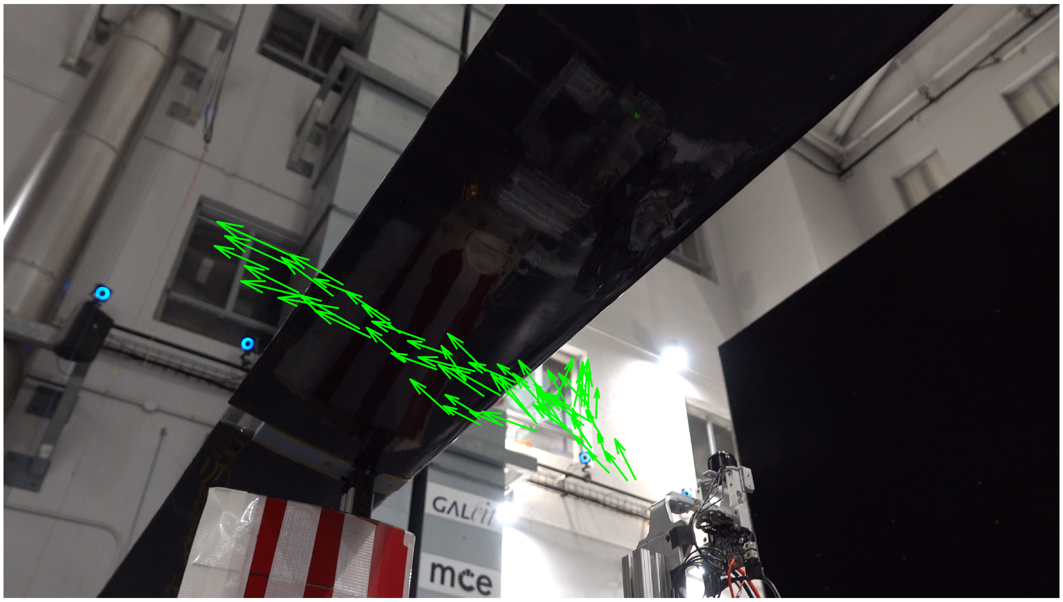

Figure 6.37: Tuft vectors for wing suction side at 3000 rpm and 5.15 m/s.

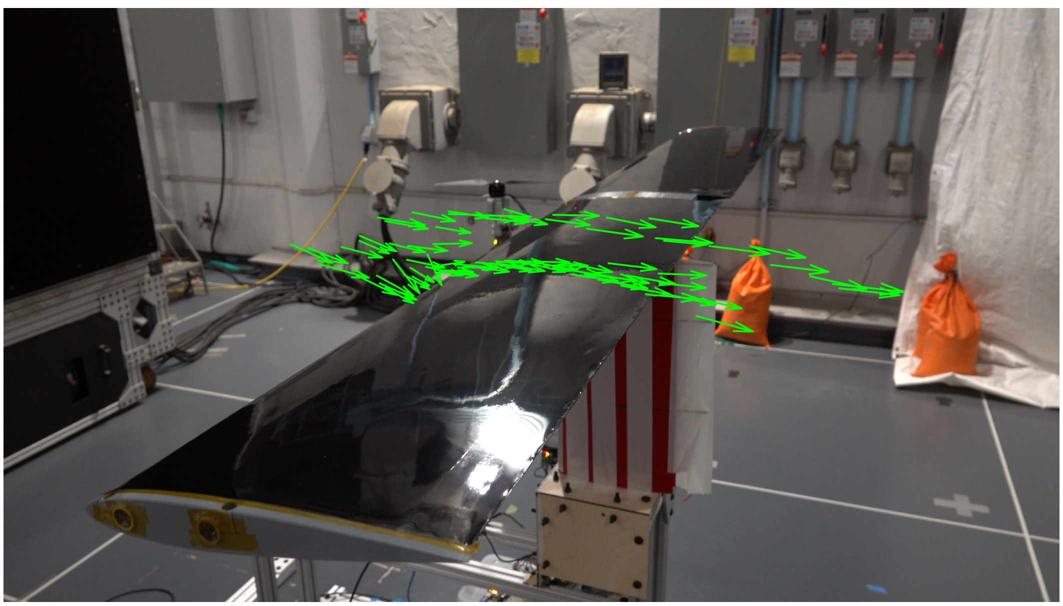

Figure 6.38: Tuft vectors for wing pressure side at 5.15 m/s.

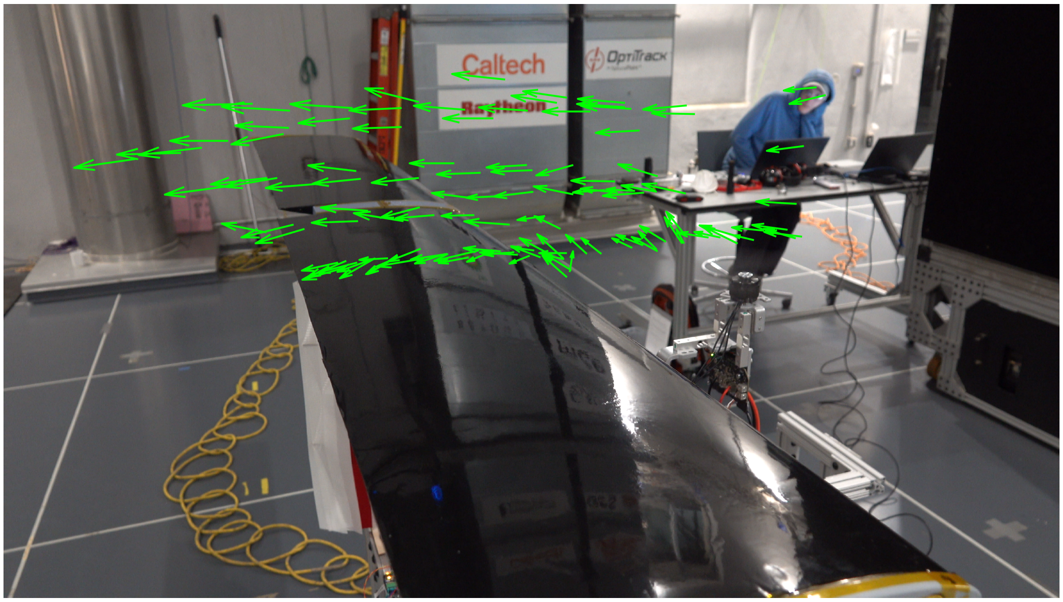

Figure 6.39: Tuft vectors for wing pressure side at 3000 rpm and 5.15 m/s.

Actuator Disk CFD

To complement the tuft experiments, basic computational Fluid Dynamics (CFD) simulations were run in ANSYS Fluent [20]. The simulations consisted of an actuator disk in edgewise flow with a constant disk loading of 36 Pa across the surface with a 4 m/s freestream velocity. While an adaptive refinement scheme was used, a true grid sensitivity study was considered unneeded, as the license allowed limit of 500,000 elements in the simulation was quickly reached. The presented graphics are thus the result of simulations run at the maximum available resolution.

Figure 6.40 shows the streamlines computed. In addition to the streamlines from the freestream which are slightly perturbed by the presence of the actuator disk, streamlines passing in close proximity to or through the actuator disk exhibit an effect akin to the shed vortex wake off a wing, coiling in a helical structure as they propogate at an angle downstream. Figures 6.41 and 6.42 show select vector plots of the flow around the actuator disk. The view along the plane of symmetry shows the rotor wake directly connected to the actuator disk as a high velocity region, but also an entrained region downstream of this which adds a slight downward velocity component to the flow. The horizontal section in Figure 6.42 also shows the rotor wake, not as a cohesive cylinder, but as a oblate shape with attached vortical structures. This view also highlights how the rotor wake has a significant impact on the surrounding flow, adjusting the flow direction at least a diameter to either side of the rotor and creating a low velocity region downstream.

The CFD results support the observations in the previous sections. The idealized rotor disk appears to exhibit a wake rollup phenomenon similar to a wing. Simultaneously, the effects of the rotor wake are not limited to the hypothetical streamtube passing through the rotor disk. The presence of a rotor causes significant changes in the airflow over many rotor diameters downstream. The entrained flow region behind disk wake is also consistent with the exhibited effect of the measured lift changing even when the propeller was placed as far forward as possible during experiments.

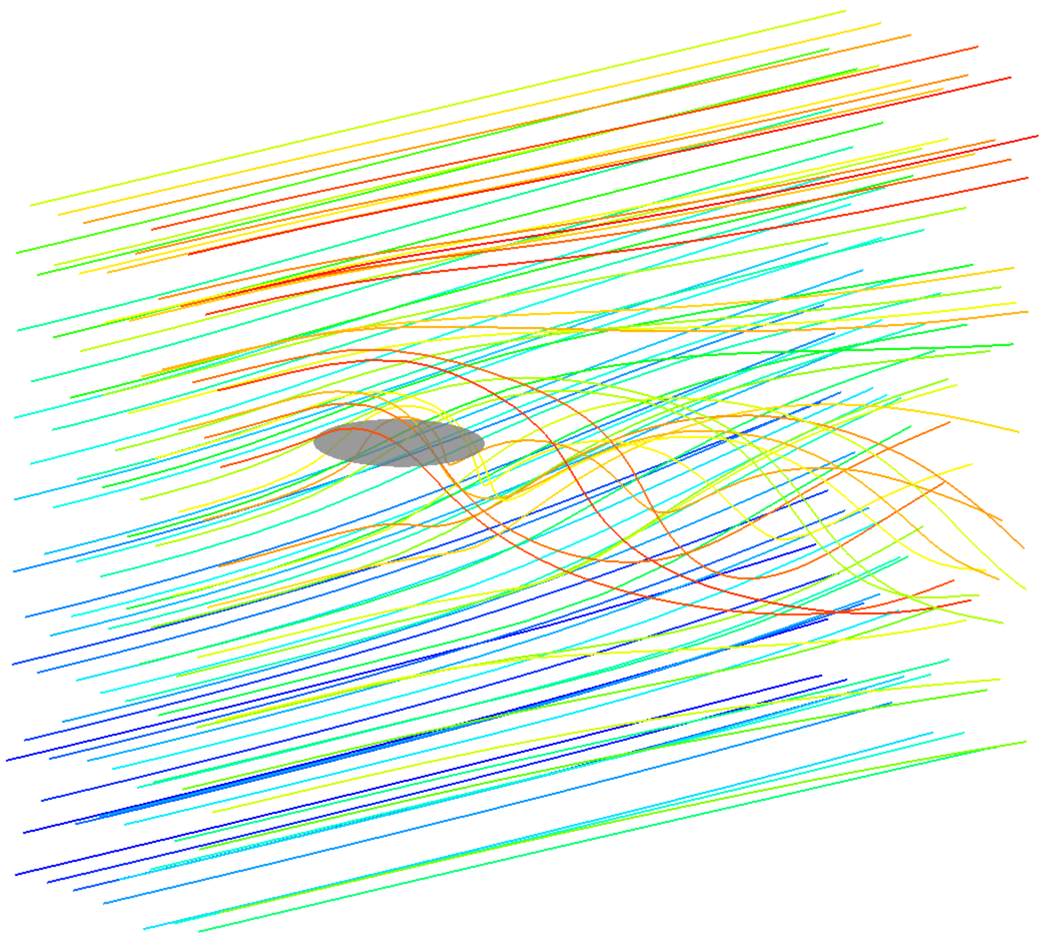

Figure 6.40: Streamlines depicting the flow in the half domain of an actuator disk in freestream flight.

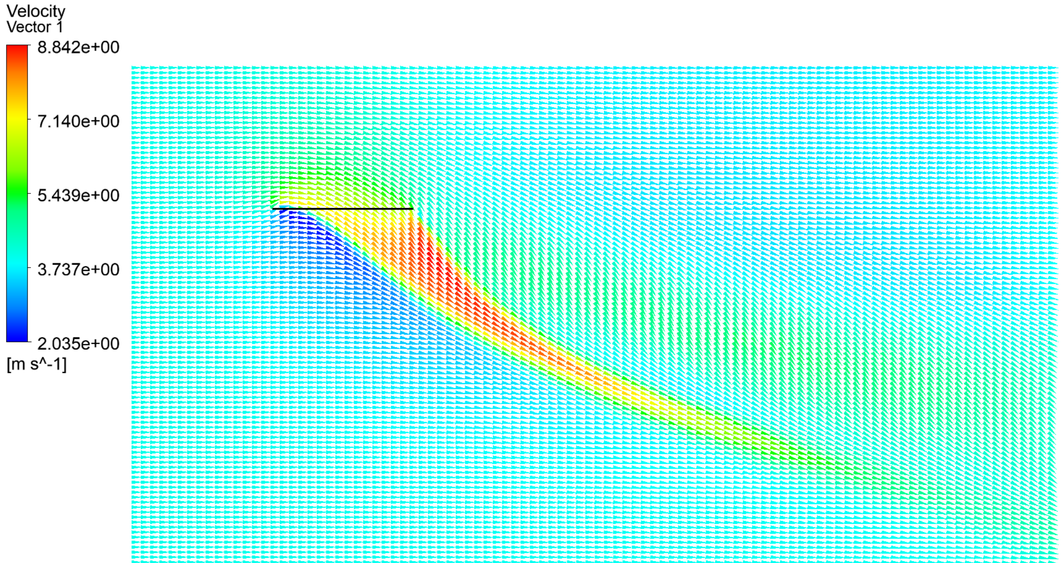

Figure 6.41: Velocity vectors in the plane of symmetry.

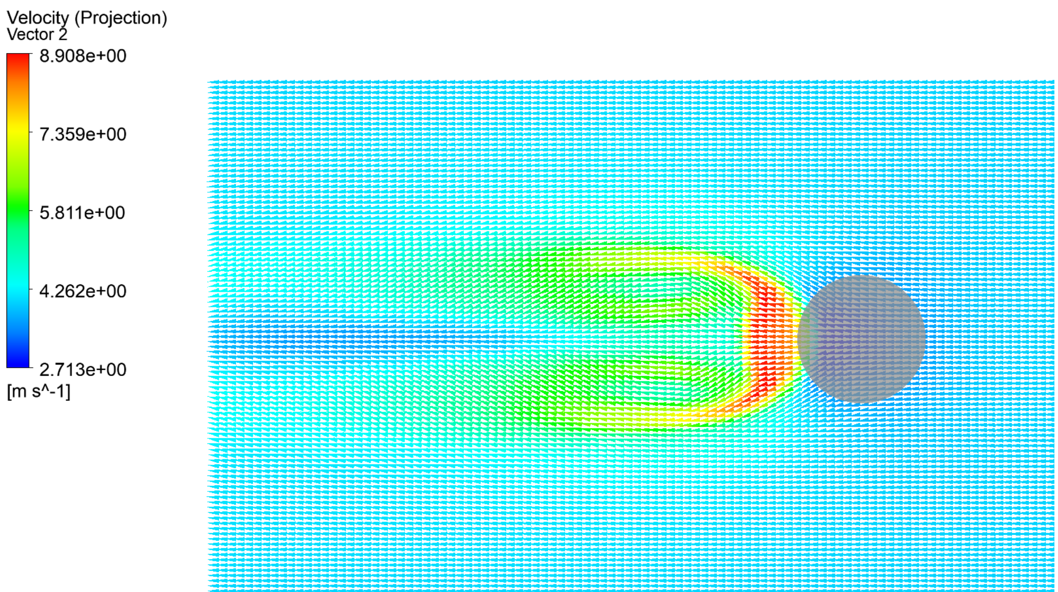

Figure 6.42: Velocity vectors in a plane sampled 1 radius below the actuator disk.

6.6 Trailing Propeller-Wing Interactions

To compliment the above work, the effect of propeller aligned to the trailing edge of the wing was also studied. In contrast to the prior case, the effect of the propeller on the wing is expected to be small in most cases, as the wake of the propeller should be primarily downstream of the wing. However, a propeller still has an effect upon the flow upstream of itself, so the effect is still quantified.

To study the effect, the testing frame is reconfigured. As the testing frame is built of structural extrusion, rearranging the individual testing components around consists of loosening retention bolts and translating the components. To maximize the geometric search area of the propeller aft of the wing, the wing assembly was translated as far forwards as possible on the test assembly. As before, the position of the propeller is moved to different locations relative to the wing and the propeller rotation speed and freestream velocity from the wind tunnel are stepped at each of these locations while the force is measured.

The new arrangement and associated coordinate system are shown in Figure 6.43. The coordinate system is aligned to the trailing edge of the wing and the propeller is once again studied in a level configuration.

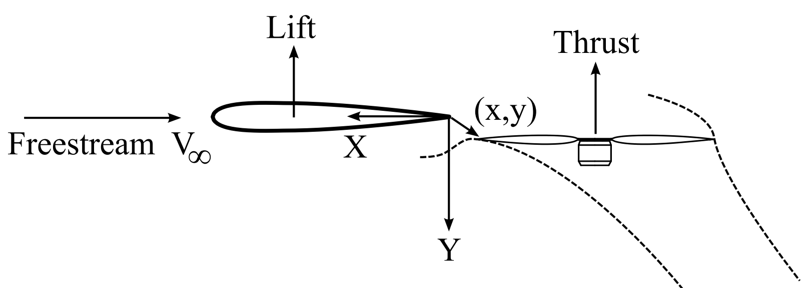

Figure 6.43: Diagram and coordinate system for propeller wing-interactions with the propeller trailing the wing.

Change in Propeller Performance

Examination of the forces experienced by the trailing propeller shows some changes to the performance relative to the leading or isolated rotor cases. Positioning the rotor at the trailing edge appears to decrease the thrust coefficient at high advance ratios relative to the other cases, as well as introducing some more variability in the torque curves. The figure of merit is also lower than for the isolated or leading cases.

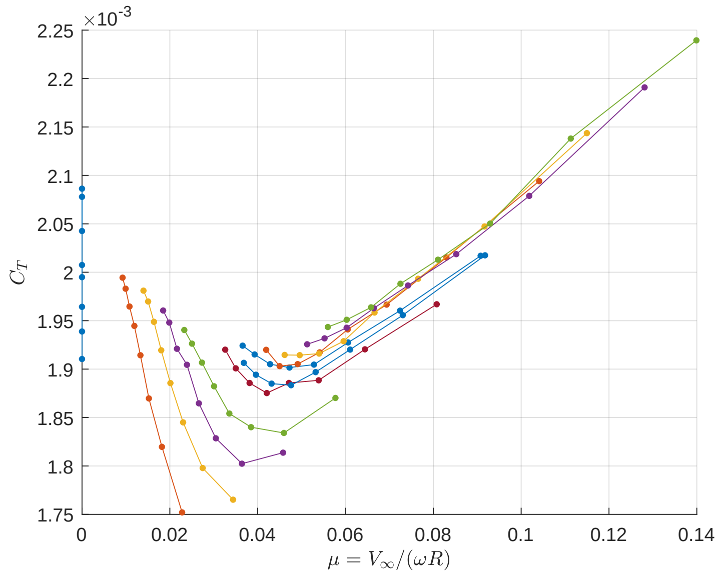

Figure 6.44: Change in thrust coefficient with advance ratio. Curves are at constant velocity.

One possible reason for the decrease in thrust and torque measurements is the occlusion of the propeller by the wing upstream of it. High advance ratios refer to situations where the propeller rotation speed is low relative to the freestream velocity. The result is that the measured forces may be less the result of the propeller rotation and more associated with the propeller acting as a body producing lift and drag. As a result, one effect could be the decrease of the thrust and drag coefficients at high advance ratios.

Effect on Wing Lift

As with the leading edge placement of the propeller, a significant change in the total lift force on the wing was observed. However, this arrangement appears to increase the lift seen by the wing rather than decrease it. The data shown in Figure 6.47 shows how the lift coefficient changes for various propeller placements with $Y = 0$. The lift coefficient increases substantially at low advance ratios, likely in part because the flow velocity is small at these values and forces on the wing will have an outsized effect when represented through the lift coefficient which has V_∞in the denominator. A similar effect is visible for the drag coefficient in Figure 6.48, which increases substantially as the advance ratio decreases. While the increase of both the lift and the drag mean that the benefit gained by the interaction is not free, it does indicate that the effect can behave akin to a high lift device on a wing such as a flap. Increasing the lift on the wing, even at the expense of additional drag, reduces the

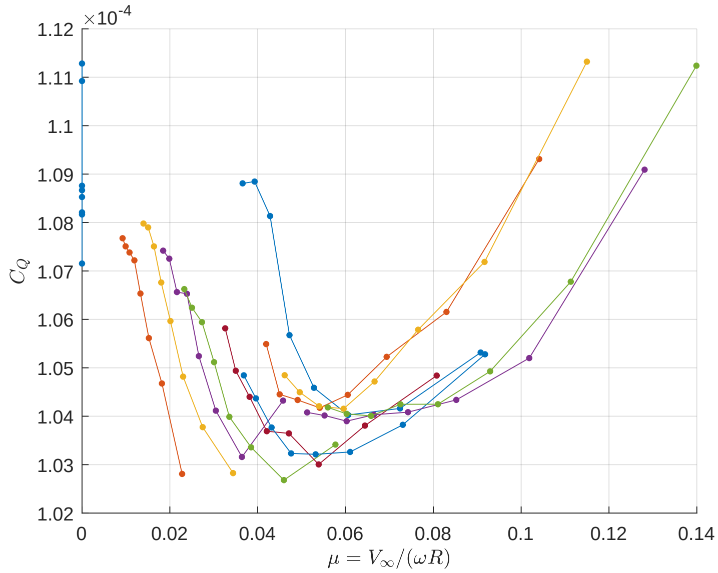

Figure 6.45: Change in torque coefficient with advance ratio. Curves are at constant velocity.

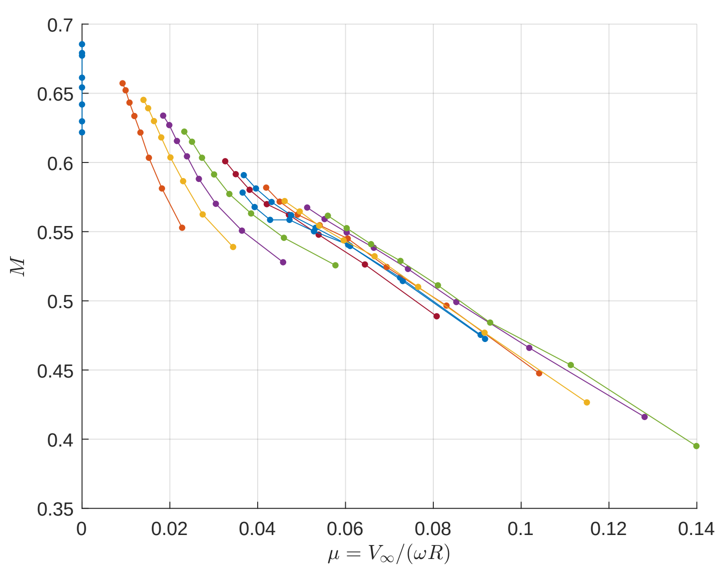

Figure 6.46: Change in figure of merit with advance ratio. Curves are at constant velocity.

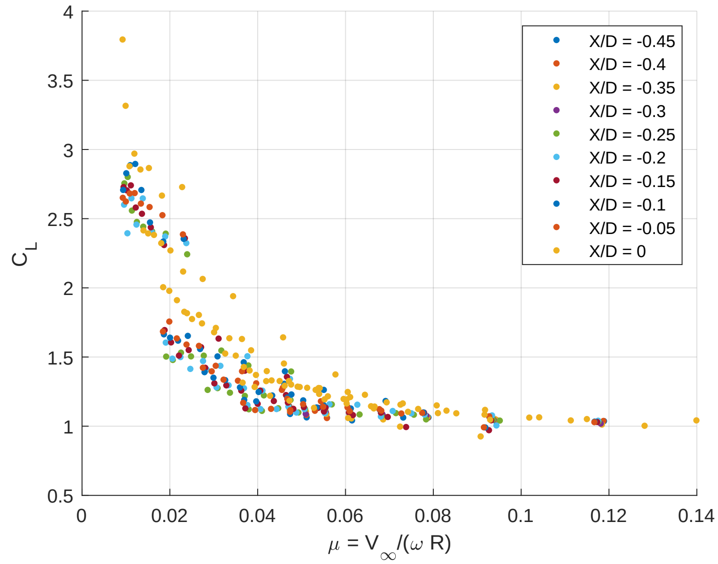

Figure 6.47: Measured wing lift coefficient as a function of propeller advance ratio.

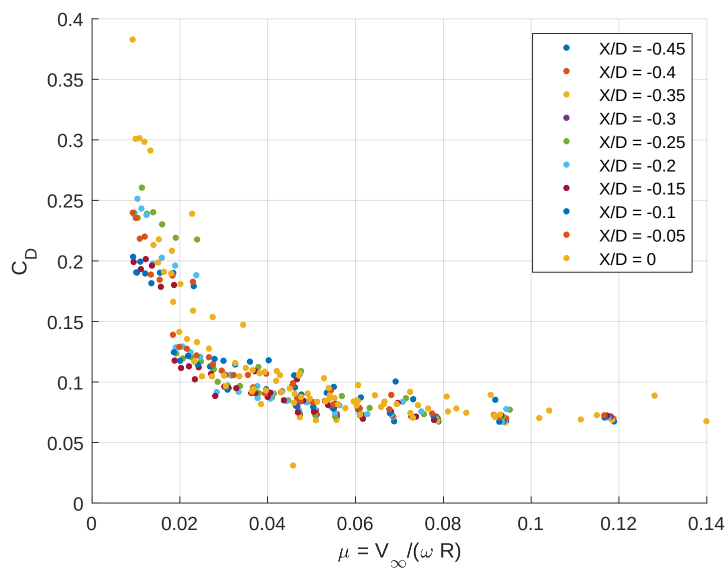

Figure 6.48: Measured wing drag coefficient as a function of propeller advance ratio.

amount of thrust that the lifting rotors need to produce. As the power consumption of the rotors to produce lift is relatively high compared to that required in fixed wing, this could have a significant effect on the overall power consumption.

While the general trend of an increase in lift is visible for the propeller in multiple positions, it is visible that the effect reduced somewhat as the propeller moves further away from the wing. To help quantify this as well as provide an empirical model for the effect, the data are fit to an equation of the form

$$C_L = C_a e^{C_b \mu} + C_c \tag{6.12}$$

with an analogous equation for drag. The exponential form of the equation as opposed to a power form allows for the value of μ to go to 0 without creating a singularity, and allows for the coefficient to trend towards a value as the advance ratio increases. This should represent the case where the wing experiences forces with no influence from the propeller, and should be equivalent to the lift coefficient of the wing measured during characterization. As the fit results are expected to produce an expression exhibiting exponential decay, that is $C_b < 0$, the value of C_c produced by a fit would be the An example of implementing this fit for the lift data at a single position can be seen in Figure 6.49 and for the drag in Figure 6.50. As can be seen visually, the exponential fit matches the experimental data well. Repeating the fit for the various positions studied, the fit coefficients for the lift curves can be seen in Figure 6.51 and for the drag curves in Figure 6.52. Error bars show 95th percentile confidence intervals. What the data show is that there is not a clear trend in the fitted coefficients with respect to the propeller position. There is still a change in the coefficients once the distance of the propeller edge from the trailing edge exceeds one-quarter diameter. After this point, the error bars for the data become significantly larger, and the C_a coefficients are near zero.

Lift-to-Drag

One aspect of the interaction between the trailing edge propeller and the finite wing is that both the lift and drag of the wing are observed to increase. Based on the fits applied to model the force interaction, an expected lift-to-drag ratio for the wing can be computed. The curve for the propeller positioned at the wing trailing edge can be seen in Figure 6.53. At higher advance ratios, the ratios approaches the expected lift over drag ratio for the wing at this angle of attack, while at very low advance ratios the performance degrades. The model does predict a slight increase in the lift to drag for the wing at a low advance ratio. This implies that it is possible to extract some amount of performance benefit from the interaction between the two. The narrow and relatively small range of advantageous advance ratios however means that craft would need to be carefully designed to take advantage of this effect.

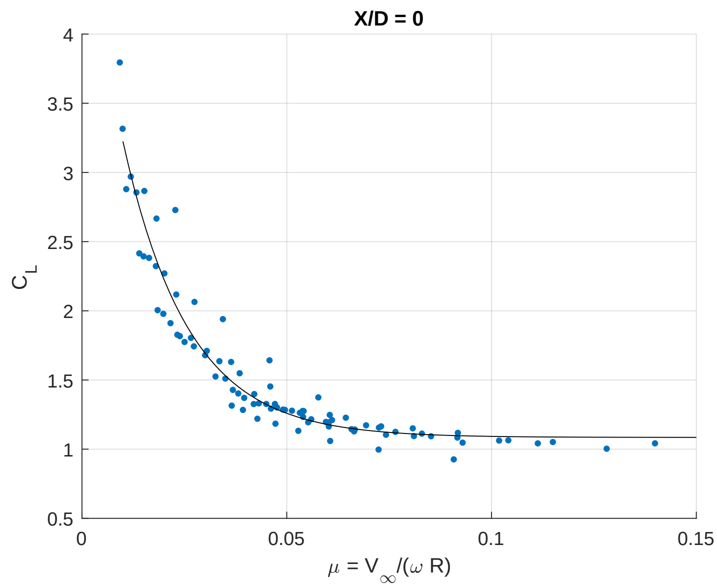

Figure 6.49: Example of empirical fit of lift coefficient data.

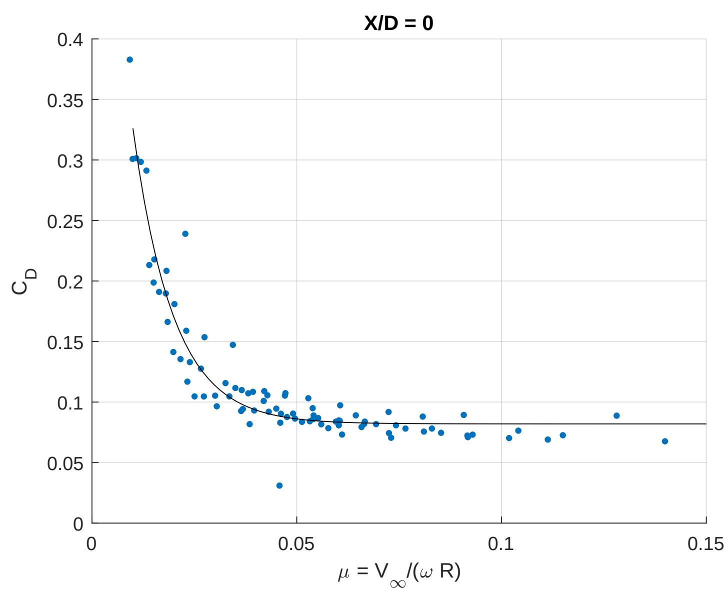

Figure 6.50: Example of empirical fit of drag coefficient data.

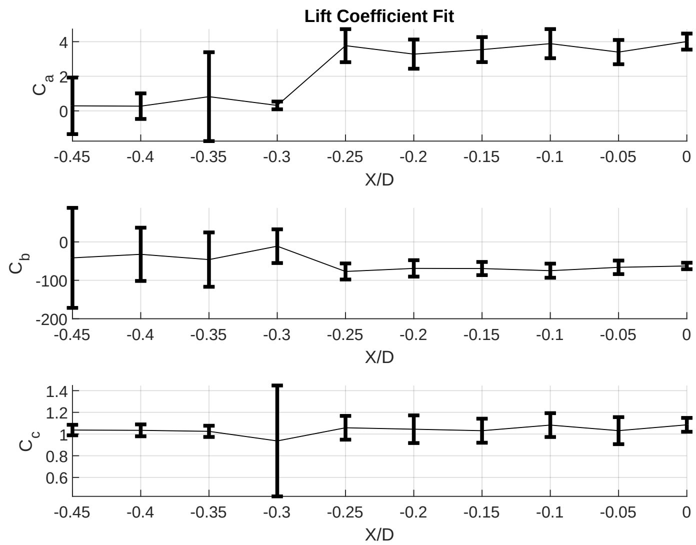

Figure 6.51: Lift fit coefficients for propeller as a function of X position.

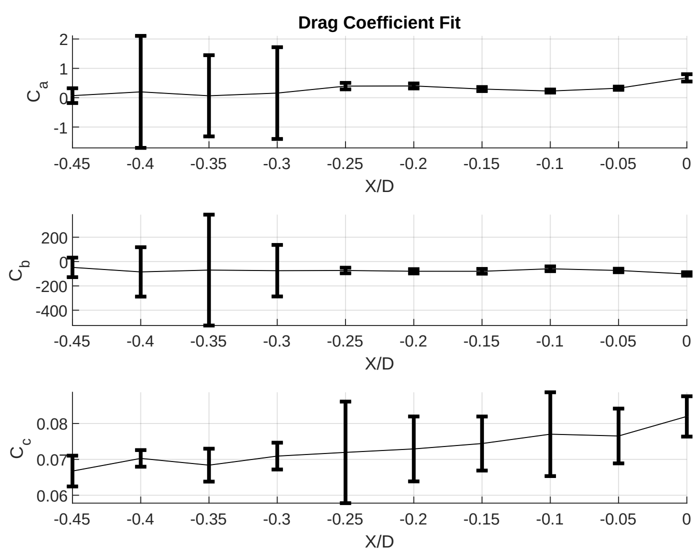

Figure 6.52: Drag fit coefficients for propeller as a function of X position.

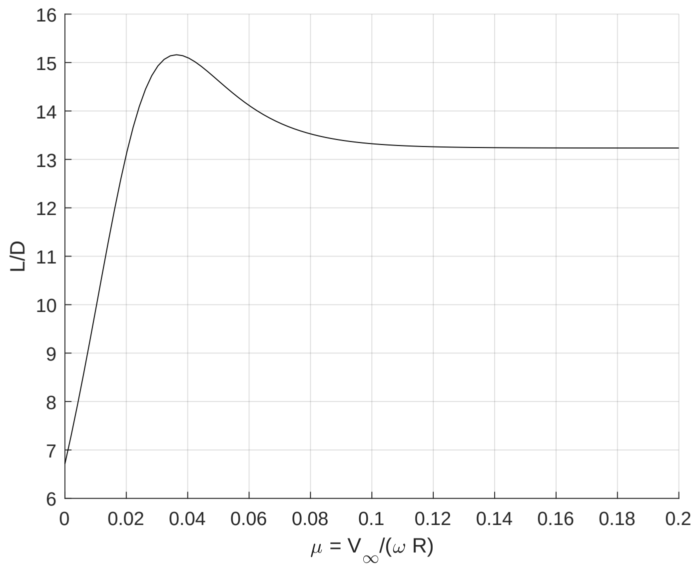

Figure 6.53: Empirically fit lift-to-drag ratio for a trailing edge propeller.

6.7 Simulation in DUST

The experimental results are briefly corroborated with simulation in DUST [21]. A simulation for the isolated wing is first compared to the fitted experimental coefficients in Figure 6.54. The wing was only simulated for half the angle of attack range as the problem is symmetrical. What is seen is that the simulation predicts the lift curve slope reasonably well, albeit without the asymmetry in the physical wing. The drag is substantially underpredicted, which is a problem established in Chapter 3 with respect to DUST. The onset of stall is not observed in the range of simulated angles of attack. The pitching moment appears to be the correct order of magnitude.

Simulations were then run for cases analogous to the experiments with the wing at six degrees angle-of-attack and propellers aligned with the wing trailing edge. Analogous plots to the experimental data for lift and drag are provided in Figures 6.55 and 6.56. There is a similar trend to the experimental data of a convergence to a particular coefficient value as the advance ratio increases, alongside a slight increase in lift and drag as the advance ratio decreases, although substantially less than was seen in experiments. However, the prediction fails as the advance ratio trends towards 0, with the simulated lift and drag coefficients plunging into the large negatives.

The negative values for lift and drag coefficients at low advance ratios simply reflect the larger influence that the propeller flow has upon the wing forces at particularly low freestream velocities V_∞. Examining the lift as a function of the freestream

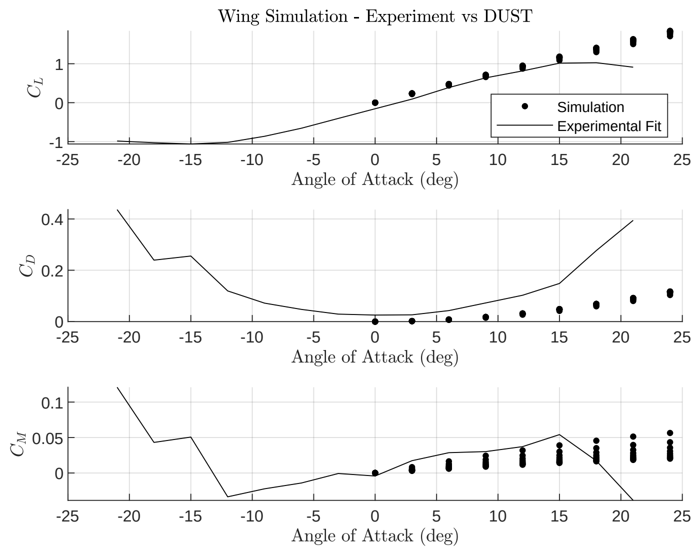

Figure 6.54: Lift, drag, and pitching moment comparison between experiments and simulation in DUST for the rectangular wing.

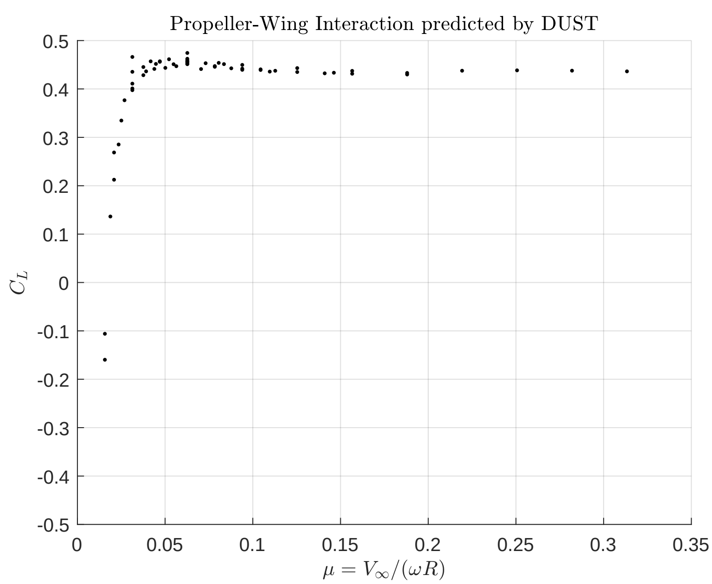

Figure 6.55: Change in lift coefficient predicted by DUST for trailing rotor arrangement.

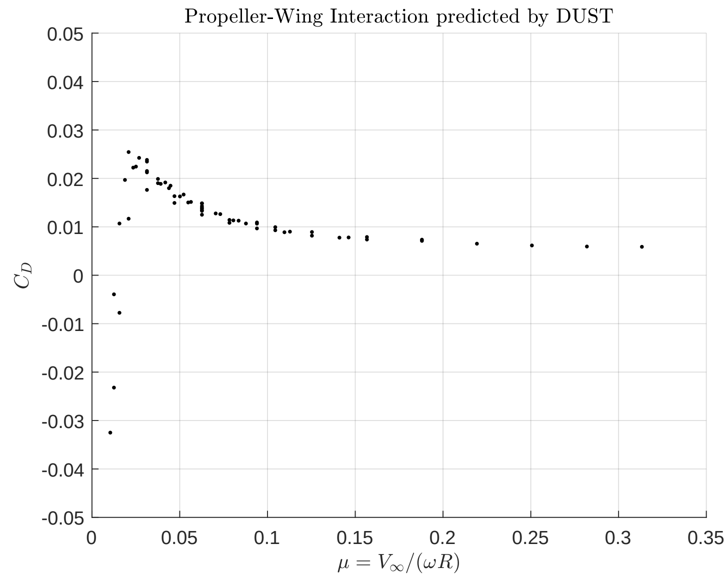

Figure 6.56: Change in drag coefficient predicted by DUST for trailing rotor arrangement.

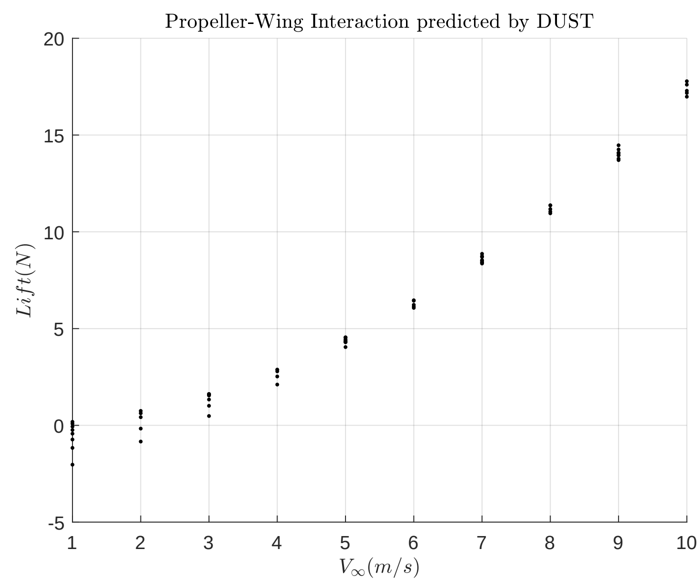

Figure 6.57: Wing lift predicted by DUST at various forward flight speeds and propeller rotation speeds.

velocity in this set of simulations in Figure 6.57, it can be seen that the variability in lift at low velocities s small compared to the overall lift predicted for the wing in the trailing configuration. Nevertheless, the qualitative and quantitative differences between the experimental and simulation data for the trailing propeller highlights the potential deficiencies of a mid-fidelity tool such as DUST for this problem.

6.8 Future Work

Due to the diversity of possible configurations and the size of the search space, only a relatively limited set of configurations were studied. The interaction was also only studied with a single propeller, a T-Motor 12×4. Future work could greatly expand on the results seen here by repeating experiments with different propellers to study different chord-diameter ratios. From the work described in Chapter 2, studies with other propellers may even reveal a way to describe the interaction based on the disk loading of the propeller, abstracting the blades away in favor of representing it by its influence on the flow.

An additional limitation of the particular hardware setup meant that the propeller was located at only one location in the spanwise direction. Lifting line theory generally predicts that a rectangular wing with no twist will have a non-uniform self-induced downwash along its span. If the flow induced by the propeller modifies the local angle of attack, it would be expected that the degree of this effect will differ based on where along the span the propeller is placed. Comparing the change in lift as a function of location along the span could reveal additional performance improvements or provide additional data to confirm or improve models.

While the experimental hardware was the best that was available to the author, substantial improvements could be made to increase the fidelity of the experiment results. Many of the structural components of the test-stand were exposed to the airflow, introducing the likelihood of aerodynamic interactions. For instance, the propeller test assembly was completely unshielded because the development of an assembly to streamline the components while being able to translate alongside the propeller was deemed impractical. The propeller test stand itself also featured a great number of exposed components. While the convenience of the off-the-shelf hardware and its associated software was deemed to be worth the uncertainty, it would be ideal to use a sensor setup with lower form factor to avoid the introduced error. The 2-axis traverse used was also commercial off-the-shelf. Installation and implementation was convenient as a result, but the hardware was lacking in certain respects. While the backlash in the system along its movement axis was minimal, the carriage's stability in motion along other axes was poor. In the test arrangement used in this work, the thrust of the propeller was in the same direction as the weight of the carriage assembly, eliminating backlash in the system motion. However, if the thrust were reversed, the play in the system could be a significant problem in the positional consistency as well as the system safety. The existing hardware provides a wealth of opportunities to further study as it is, but data quality could be improved with an upgraded assembly.

6.9 Conclusion

As eVTOL aircraft become more and more common, an understanding of the aerodynamic interaction between lifting propellers and wings is increasingly important. Although the search space of aerodynamic interactions is large, this work describes a practical test assembly to examine this effect by computerizing the relative position of the propeller and wing alongside integrated force sensors. Through steady state testing, the experiments here highlight the varying effects that result from this interaction in the low speed conditions as the vehicle transitions from hover to forward flight.

The presence and operation of a propeller positioned ahead of a wing has a significant effect on its measured performance. At lower advance ratios, the propeller can have the effect of completely negating the lift generation of the wing and introducing a number of unintended moments into the system. These results indicate that suboptimal placement of the propeller on the vehicle can result in lifting surfaces not only being hampered, but even a hindrance at low speeds. The interaction between the propeller wake and a lifting surface also means that care should be taken to avoid interactions between craft propeller wakes and control or stability surfaces such as elevators.

The interaction between a propeller and a wing with the propeller at the trailing edge however has potential advantages. While the propeller generates thrust in forward flight, the measured lift coefficient of the wing was observed to increase, alongside its drag. This effect was observed to decrease as the distance between the propeller and the wing increased. An empirical fit was applied to the data which suggests that the interaction allows for an improvement in the wing's lift-to-drag ratio for a narrow range of advance ratios.

References

[1] Alessandro Bacchini and Enrico Cestino. "Electric VTOL Configurations Comparison." In: *Aerospace* 6.3 (Feb. 2019), p. 26. DOI: `10.3390/aerospace6030026`.

[2] **Ellande Tang** and Soon-Jo Chung. "Experimental Model of Effects of Large Upstream Obstructions on Drone Scale Propellers." In: *AIAA Scitech 2021 Forum* (Jan. 2021). DOI: `10.2514/6.2021-1648`.

[3] Xichen Shi, Patrick Spieler, **Tang, Ellande**, Elena-Sorina Lupu, Phillip Tokumaru, and Soon-Jo Chung. "Adaptive Nonlinear Control of Fixed-Wing VTOL with Airflow Vector Sensing." In: *ICRA* (Mar. 2020). arXiv: 2003.07558. DOI: 10.1109/ICRA40945.2020.9197344.

[4] Rajan Gill and Raffaello D'Andrea. "Propeller Thrust and Drag in Forward Flight." In: *2017 IEEE Conference on Control Technology and Applications (CCTA)*. ISSN: 0307904X. Mauna Lani Resort, HI, USA: IEEE, Aug. 2017, pp. 73–79. ISBN: 978-1-5090-2182-6. DOI: 10.1109/CCTA.2017.8062443.

[5] Leo Veldhuis. *Propeller Wing Aerodynamic Interference*. Delft, 2005.

[6] Abdullah S. Aljabri. *The Prediction of Propeller/Wing Interaction Effects*. 1982.

[7] Michael R. Derby and Larry A. Young. *Rotor/Wing Interactions in Hover*. Tech. rep. TM-2002-211392. NASA, 2002.

[8] Eduardo J. Alvarez and Andrew Ning. "High-Fidelity Modeling of Multirotor Aerodynamic Interactions for Aircraft Design." In: *AIAA Journal* 58.10 (Oct. 2020), pp. 4385–4400. ISSN: 0001-1452. DOI: 10.2514/1.J059178.

[9] J. Gordon Leishman, Mahendra J. Bhagwat, and Ashish Bagai. "Free-Vortex Filament Methods for the Analysis of Helicopter Rotor Wakes." In: *Journal of Aircraft* 39.5 (Sept. 2002), pp. 759–775. ISSN: 0021-8669. DOI: 10.2514/2.3022.

[10] Alex Zanotti, Alberto Savino, Michele Palazzi, Matteo Tugnoli, and Vincenzo Muscarello. "Assessment of a Mid-Fidelity Numerical Approach for the Investigation of Tiltrotor Aerodynamics." en. In: *Applied Sciences* 11.8 (Apr. 2021), p. 3385. ISSN: 2076-3417. DOI: 10.3390/app11083385.

[11] Carl Russell and Sarah Conley. "The Multirotor Test Bed -– A New NASA Test Capability for Advanced VTOL Rotorcraft Configurations." In: *Vertical Flight Society's 76th Annual Forum and Technology Display* (2020).

[12] E. V. Laitone. "Wind Tunnel Tests of Wings at Reynolds Numbers Below 70 000." en. In: *Experiments in Fluids* 23.5 (Nov. 1997), pp. 405–409. ISSN: 0723-4864, 1432-1114. DOI: 10.1007/s003480050128.

[13] Seok Ho Lee and Yong Oun Han. "Experimental Investigation of High-Angle-of-Attack Aerodynamics of Low-Aspect-Ratio Rectangular Wings Configured with NACA0012 Airfoil Section." en. In: *International Journal of Aeronautical and Space Sciences* 21.2 (June 2020), pp. 303–314. ISSN: 2093-274X, 2093-2480. DOI: 10.1007/s42405-019-00215-z.

[14] Byung Ho Park and Yong Oun Han. "Steady Aerodynamic Characteristics of Two-Dimensional NACA0012 Airfoil for One Revolution Angle of Attack." en. In: *International Journal of Aeronautical and Space Sciences* 19.2 (June 2018), pp. 291–304. ISSN: 2093-274X, 2093-2480. DOI: 10.1007/s42405-018-0010-x.

[15] Chris C. Critzos, Harry H. Heyson, and Robert W. Boswinkle. *Aerodynamic Characteristics of NACA 0012 Airfoil Section at Angles of Attack from 0 Degrees to 180 Degrees*. Tech. rep. NACA-TN-3361. Jan. 1955.

[16] Ravindra A Shirsath and Rinku Mukherjee. "Experimental and Computational Investigations of Aerodynamic Characteristics of a Finite Rectangular Wing-in-Ground Effect." en. In: *Proceedings of the Institution of Mechanical Engineers, Part G: Journal of Aerospace Engineering* (Sept. 2022), p. 095441002211147. ISSN: 0954-4100, 2041-3025. DOI: 10.1177/09544100221114700.

[17] *Series 1585 Test Stand Datasheet*. Jan. 2022. URL: https://cdn.rcbenchmark.com/landing_pages/Manuals/Series%201585%20Datasheet.pdf (visited on 10/05/2022).

[18] Ira H. Abbott and A. E. von Doenhoff. *Theory of Wing Sections: Including a Summary of Airfoil Data*. Dover Publications, 1959. ISBN: 9780486605869.

[19] J. Gordon Leishman. *Principles of Helicopter Aerodynamics*. 2nd ed. Cambridge aerospace series 18. Cambridge: Cambridge University Press, 2006. ISBN: 978-1-107-01335-3.

[20] *Ansys® Academic Research Fluent, Release 22.1*. 2022.

[21] Matteo Tugnoli, Davide Montagnani, Monica Syal, Giovanni Droandi, and Alex Zanotti. "Mid-Fidelity Approach to Aerodynamic Simulations of Unconventional VTOL Aircraft Configurations." en. In: *Aerospace Science and Technology* 115 (Aug. 2021), p. 106804. ISSN: 1270-9638. DOI: 10.1016/j.ast.2021.106804.

Chapter 7

INTEGRATION OF FINDINGS INTO AN EVTOL PERFORMANCE MODEL

7.1 Introduction

The previous chapters have considered and studied numerous effects associated with the flight and operation of an eVTOL aircraft. While each chapter studying their respective subject reported their own findings, the ultimate objective of this work is to consider topics that will have an impact on knowledge of eVTOL aerodynamics and to develop design guidelines for future craft. To this end, the findings of the previous chapters are implemented onto models for 3 aircraft that have been worked on by the author. The primary topic of investigation in implementing these models will be to look at the change in predicted energy consumption of the craft with and without the models.

Evaluating the performance of an aircraft from first principles is an typical first step in vehicle design and is done by many authors [1, 2, 3, 4]. The work here will leverage existing models for fixed wing aircraft, as well as models for propellers in forward and axial flight.

While work has been found that seeks to account for the drag of propellers on eVTOL designs, they examine the static drag associated with the propellers, rather than the additional drag associated with the propeller's rotation [5, 6]. As the drag of a static propeller can be accounted for like many other components in a typical vehicle drag buildup, this work seeks to examine the change in performance associated with generating thrust.

Existing work found that involves transitional flight for eVTOL aircraft typically concerns other configurations such as tailsitters or tiltwings, which feature a conceptually much simpler blown wing. Many of these are primarily focused on the controls formulation with little consideration for complex aerodynamic effects [7, 8, 9], model the craft in a simplistic manner as only an airfoil [10], acknowledge blown wing effects but not more complicated effects [11, 12, 13], or perhaps use a panel method to account for dynamic performance, but still not implement more complex interactions [14].

7.2 eVTOL Operation

For eVTOL vehicles, the phases of flight can be abstracted to 6 distinct modes.

- **Ascent** The vehicle raises elevation to clear surrounding obstacles, and gain enough altitude for safe transition. The vehicle can also seek to reach the desired cruise elevation ahead of time. Theory pertaining to rotorcraft in axial ascent can be used here.

- **Transition** The vehicle begins accelerating to try and reach cruise speed. During this phase, the rotors are making up for any deficit in lift from the wing while the vehicle picks up speed.

- **Cruise** In this phase, the vehicle operates like a traditional fixed wing aircraft, and the appropriate theory can be applied. Additional maneuvers such as climbing, maximum endurance flight, or avoidance of terrain and other obstacles can happen in this period, with the appropriate energy calculations.

- **Back Transition** In order to begin the landing approach, the craft needs to decelerate. This maneuver can take many forms, but is theoretically straightforward. This mode of flight has been found to be very dangerous in field experiments done by the author however, as described in Section 7.2

- **Descent** From a hover condition, the vehicle reduces altitude until landing. Ideally this step could be mixed with the deceleration phase of operation, but in practice trying to reduce altitude as in a landing maneuver while attempting to back-transition into hover is a risky maneuver that leaves little margin for error and has been avoided in vehicle operations.

- **Hover** It may be desired to hover for some period of time for some mission objective. This phase of flight is the easiest to predict from static testing given the similarities.

The general procedure developed for computing the range of the vehicle is to first compute the energy required for Ascent, Transition, Back-Transition, and Descent. Once these are calculated, the remaining energy can be allocated to either hover or cruise as appropriate for the mission, and the range, loiter time, or other desired performance metrics can be calculated.

Energy Consumption in Transition Flight

As the vehicle dynamics in hover and forward flight are generally known. The region of flight that the work in the previous chapters benefit the most is the transition from hover to fixed wing forward flight. This is because this is the region where the propellers will be operating in forward flight and the wings will be generating lift. There some choices to be made for the specific strategy for transition. As lifting rotors are generally mounted with their thrust axes pointing upwards or nearly upwards relative to the vehicle, increasing the angle of attack to try and increase the wing lift at low speeds will tilt the lifting rotors backwards, functionally increasing the drag. The optimal strategy is dependent on the choice of cost function, whether that is minimum energy consumed during transition or something else.

Dangers of Back-Transition

Attempts to decelerate from level flight or near cruise flight speeds has resulted in several vehicle crashes. While difficult to determine the exact cause, the most likely reasons identified by the author were either the entrance of the craft into a vortex ring state or a loss of control authority. The vortex ring state is a dangerous mode of operation where the propellers begin ingesting their own wake, leading to a loss of lift. There is a potential for this to happen in back-transition as the rotors are potentially flying into their own wake as the vehicle decelerates. The other possibility that is supported by the vehicle logs in question is that the vehicle enters an unstable control mode during back-transition. The control output was observed to reach a maximum while trying to decelerate, followed by the vehicle alternating between pitch and roll oscillations that resulted in rapid loss of altitude. A contributing factor to this is that a disadvantage of electric vehicles is that Li-po batteries are able do deliver less maximum power once they have been drained. The reduction in maximum control authority at this point in the flight is likely a contributor to the control saturation.

Other Energy Considerations

The powers computed are based upon the experimental data from the propellers, and are representative of the mechanical power required to turn them. However, there is an additional efficiency loss associated with the conversion of stored electrical energy into mechanical work. As the thrust stand is able to measure the voltage and current simultaneously with the mechanical torque and rotation speed, it is possible to quantify this efficiency. While the efficiency can vary significantly by the combination of battery voltage, electronic speed controller, motor, and propeller, experiments generally found that this efficiency was on the order of 70% provided poor combinations were avoided.

Pulling data from the T-Motor website [15], which publishes measurements for each of their motors, the overall efficiency is evident. Data collected for the motors being sold in 2019 can be seen in Figures 7.1 and 7.2. While T-Motor does not provide mechanical power or torque data, it does provide electrical power data. Plotting the electrical power loading against the disk loading in Figure 7.1 shows that the data fit the ideal curve with good agreement with an efficiency correction. While the propeller performance varies considerably, the maximum efficiency across all the different motors and propellers follow the same contour as that predicted by disk actuator theory described in Appendix C. Comparison of the ideal to measured electrical power in Figure 7.2 shows the effective figure of merit of the data set. There is a large spread, with poor combinations being as low as 30%, and good combinations being as high as 70%.

An additional factor limiting the energy reservoir of the aircraft is the health of the batteries. While there are a number of considerations affecting battery health in the short and long term, a basic one is that it is very harmful to the battery to be completely drained. As a result, a typical rule of thumb in the drone community is to leave 20% reserve, meaning only 80% of the battery's nominal capacity is available for use.

7.3 Vehicle Model

To evaluate the impact of modeling the additional forces and interactions on the performance of an eVTOL vehicle, the findings of the previous chapters are applied to models of existing vehicles. The three vehicles used are ones that the author has contributed to and are either complete or in development. Each of the aircraft had some combination of lifting surfaces, lifter propellers, and thruster propellers. The vehicles have known configurations, hardware specifications, and either experimentally measured or simulation derived aerodynamic properties. To describe the vehicles in forward motion, models for fixed-wing characteristics are described and combined with propeller models for forward flight.

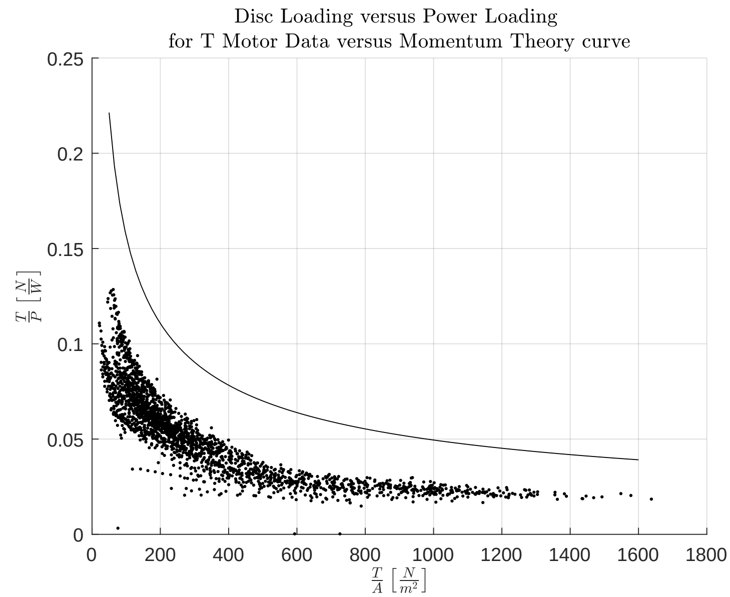

Figure 7.1: Disk loading versus power loading for T-Motor data.

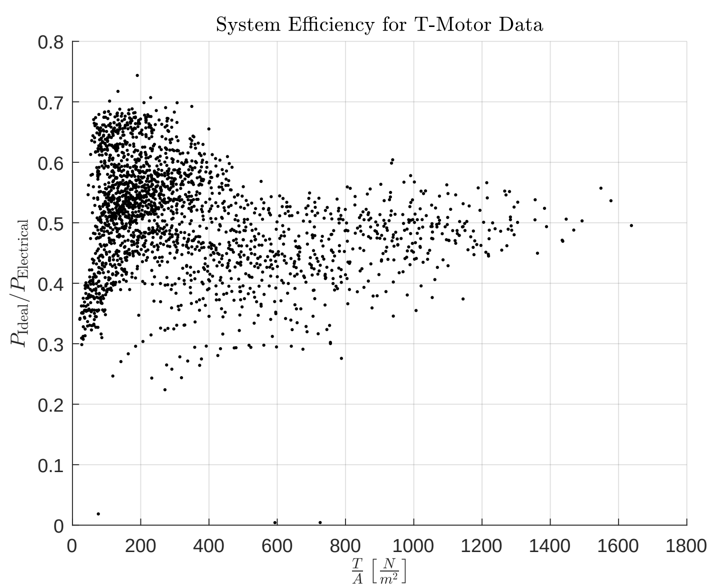

Figure 7.2: Ideal power versus electrical power loading for T-Motor data.

Vehicles

Properties of the vehicles used are summarized in Table 7.1. The AV VTOL is an experimental controls platform designed to test novel transition flight algorithms [16]. It features foam construction as well as 4 wingtip mounted propellers for vertical lift. The aircraft was designed to fly in the CAST fan array wind tunnel for transition experiments, and static wind tunnel data for it were collected. The vehicle can be seen in Figure 7.3. The Autonomous Flying Ambulance Version 3 (AFA V3) was a prototype vehicle intended to be a 1/5th scale model of the full scale flying ambulance [17]. Aerodynamic data were collected during the design process. The design was composed of a plywood structure with a formed balsa skin. The physical vehicle was lost during flight testing during a transition attempt. The vehicle immediately prior to said flight test can be seen in Figure 7.4. The Autonomous Flying Ambulance Version 4 (AFA V4) is a version currently in development [18]. The design has been developed from the ground up for the same mission. The prototype airframe is seen in Figure 7.5. Design details are provided from the design specifications and simulations of the craft.

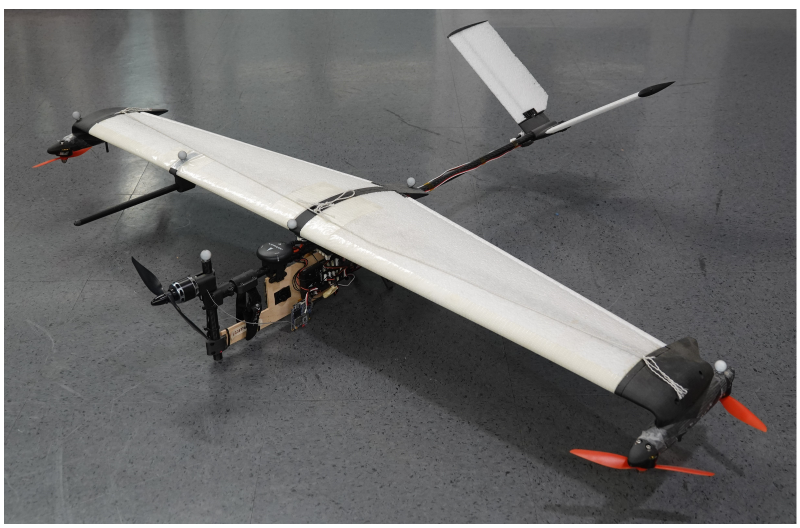

Figure 7.3: AV VTOL.

Figure 7.4: AFA Version 3.

Figure 7.5: AFA Version 4.

Vehicle	AV VTOL	AFA V3	AFA V4
Reference Area (m^2)	0.223	.566	.744
Battery	6S 1300mAh	6S 6000mAh ×2	6S 9000 mAh ×2
Dry Mass (kg)	1.45	7.1	7.8
Total Mass (kg)	1.55	8.5	10
Lifting Propeller	King-Kong 6x4	Various, 8-inch	T-Motor 14×4.8
Thrusting Propeller	APC 7×4	Various, 8-inch	APC 15×8

Table 7.1: Comparison of various properties for the selected vehicles.

A basic model will be used to model the aerodynamic forces on each each aircraft. The expressions for the lift and drag forces, respectively, are

$$F_L = \frac{1}{2}\rho V_\infty^2 C_L S \tag{7.1}$$

$$F_D = \frac{1}{2}\rho V_\infty^2 C_D S \tag{7.2}$$

where L is the lift force, D is the drag force, ρ is the air density, V_∞ is the freestream velocity, and S is the chosen aerodynamic area, generally the planform wing area. The associated non-dimensional coefficients C_L and C_D are modeled as

$$C_L(\alpha) = C_{L\alpha}\alpha + C_{L0} \tag{7.3}$$

$$C_D(\alpha) = C_{D0} + C_{DL}C_L(\alpha)^2 \tag{7.4}$$

where $C_{L\alpha}$, C_{L0}, C_{D0}, and C_{DL} are empirically derived constants, and α is the vehicle angle of attack in radians. For the AV VTOL, it was found that the above model poorly represents the curve of the experimental drag data. As a result, the drag coefficient may also be modeled as

$$C_D(\alpha) = C_{D0} + C_{D\alpha}\alpha + C_{\alpha 2}\alpha^2. \tag{7.5}$$

Aerodynamic parameters for each vehicle can be found in Tables 7.2, 7.3, and 7.4.

Additionally, the standard method for modeling propeller thrust and torque respectively are

$$T = \rho\omega^2 D^4 C_T \tag{7.6}$$

$$Q = \rho\omega^2 D^5 C_Q \tag{7.7}$$

where ω is the propeller rotation speed, and D is the propeller diameter, and C_T and C_Q are nondimensional coefficients for Thrust and Torque respectively. The torque can be used to calculate the mechanical power directly as

$$P = \omega Q = \rho\omega^2 D^5 C_Q \tag{7.8}$$

C_{L0}	$C_{L\alpha}$	C_{D0}	$C_{D\alpha}$	$C_{\alpha 2}$
0.3707	3.2566	0.1543	0.178	1.619

Table 7.2: Aerodynamic coefficients for the AV VTOL

C_{L0}	$C_{L\alpha}$	C_{D0}	C_{DL}
0.3605	2.0344	0.0709	0.2042

Table 7.3: Aerodynamic coefficients for the AFA V3

C_{L0}	$C_{L\alpha}$	C_{D0}	C_{DL}
0.6	5.1	0.0216	0.0384

Table 7.4: Aerodynamic coefficients for the AFA V4

Change in Vehicle Hover Power with Upstream Obstruction

The only vehicle with propellers that are obstructed of the studies ones is the AV VTOL. Being mounted at the propeller wing tips, the rotors are separated from the wing by a spacing of roughly 1/3 the lifting propeller diameter. The findings of Chapter 2 were generally that the interaction between a propeller and a large upstream obstruction could be described using the equation

$$\frac{F_{\text{wall}}}{T} = f\left(\frac{d}{D}\right) \tag{7.9}$$

where $f\left(\frac{d}{D}\right)$ represents the curve produced by the analytic expression from the chapter that describes the effect regardless of propeller diameter or pitch. The effect of the upstream obstruction is to reduce the effective thrust produced. Thus, if an original thrust of T_D is desired, this can be related to the actual thrust required to be produced by the propeller T_A as

$$T_D = F_{\text{wall}}\sigma + T_A = T_A(f\left(\frac{d}{D}\right)\sigma + 1). \tag{7.10}$$

The value σ represents a modification of the wall force to account for its non-infinite extent. The findings of from Chapter 2 showed that the torque coefficient C_Q did not change substantially with the presence of the obstruction. As a result the actual mechanical power P_A required by the propeller can be related to the power required by an unobstructed propeller producing the desired thrust P_D by

$$\frac{P_A}{P_D} = \frac{\omega_A^3}{\omega_D^3}. \tag{7.11}$$

We can relate the expected rotational speeds by

$$\frac{T_D}{T_A} = \frac{C_T\omega_D^2}{C_{T_A}\omega_A^2} \tag{7.12}$$

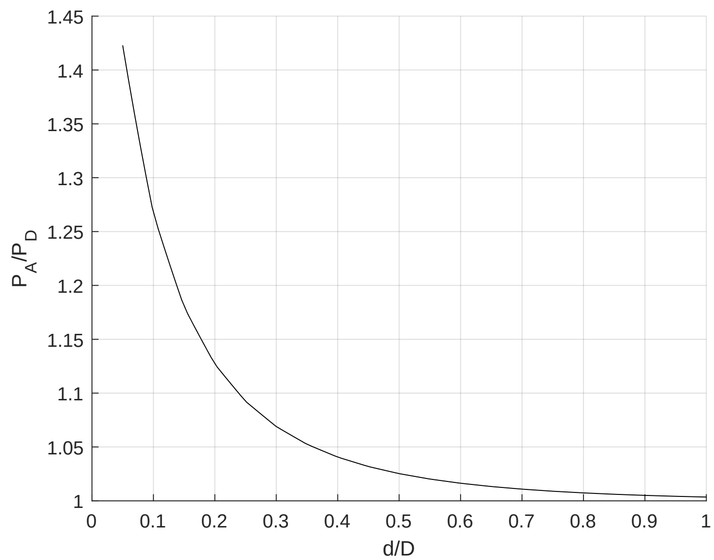

Figure 7.6: Modified hover power ratio with upstream obstruction.

where C_{T_A} is the thrust coefficient of the obstructed propeller. The mechanical power can then be related to the thrust coefficients by

$$\frac{P_A}{P_D} = \left(\frac{1}{f\left(\frac{d}{D}\right)\sigma + 1} \frac{C_T}{C_{T_A}} \right). \tag{7.13}$$

If the value of σ is assumed to be 1/4, as roughly a quarter of the propeller area is obstructed on the vehicle, and it is assumed that $C_T = C_{T_A}$, the change in efficiency is shown in Figure. 7.6. The plot shows a 5% increase in the power required to hover because of the obstruction. This is a relatively small amount in its own, but because hover has a much higher power consumption relative to the other phases of flight it can represent a significant portion of the craft's energy reserves. Given this, it may be worth the extra mass to place the propeller further from the wing in order to reduce this interaction. A trade study could be done to properly weight the change in rotor power from the obstruction against the change in rotor power from increased weight.

Propeller Power in Axial Flight

As data for the propellers on the vehicles studied in axial flight was not available, a model was used to estimate the power consumption. The model applies momentum theory and assumes that the power required to overcome the profile drag of the blades does not change with forward speed.

From Johnson, Chapter 3 [4], the power coefficient associated with the propeller itself is

$$C_P = C_{P_i} + C_{P_0} \tag{7.14}$$

where C_{P_i} is the ideal induced power associated with producing thrust, while C_{P_0} is the profile drag power, which is the power associated with overcoming the drag of the blades. It is noted by Johnson that the effective induced power typically exceeds the ideal induced power from Disk Actuator theory by approximately 10 to 20%. In effect.

$$C_{P_i} = \kappa C_{P_{\text{ideal}}},\ \kappa \approx 1.15 \tag{7.15}$$

The profile drag power coefficient in turn can be approximated for axial flight as

$$C_{P_0} = \frac{\sigma c_{d_0}}{8} \tag{7.16}$$

where σ is the rotor solidity, the ratio of the blade planform area to the rotor disk area, and c_{d_0} is a constant that has its origins in helicopter blade element theory, but here will be an empirically derived parameter. Note that the definition in Johnson of the power coefficient is slightly different than the convention used here. In Johnson, the power coefficient is defined as

$$C_P\ (\text{Johnson}) = \frac{P}{\rho A(\omega R)^3} \tag{7.17}$$

where $A = \pi R^2$ is the rotor disk area and R is the rotor radius. Because this work uses the diameter D for non-dimensionalization, power coefficients will differ by a factor of $\pi/32$. One way to identify the profile power parameter is to take the measured mechanical power input in static tests and subtract the ideal induced power based off the disk loading. The remainder will then be the power associated with the profile power, and a value for σc_{d_0} can be assigned.

The ideal power required for a constant thrust can be derived using expressions from Disk Actuator theory described in Appendix C. The ideal power in axial flight, also called the climb condition, is computed as

$$P_{\text{ideal}} = T(V_\infty + V_i) \tag{7.18}$$

where T is the thrust, V_∞ is the freestream or forward velocity, while V_i is the velocity induced by the disk. The expression derived in forward flight that relates the thrust to the induced velocity at the disk is

$$T = \rho A(V_\infty + V_i)2V_i. \tag{7.19}$$

Substituting the expression for the induced velocity in static (hover) conditions $V_{i_h}^2 = \frac{T}{2\rho A}$ changes the expression to

$$V_{i_h}^2 = (V_\infty + V_i)V_i. \tag{7.20}$$

From here two relations can be derived. The first is that the ratio of static to forward flight induced velocity is equivalent to the ratio of forward flight induced power to static induced power for the same thrust

$$\frac{V_{i_h}}{V_i} = \frac{V_\infty + V_i}{V_{i_h}} = \frac{T(V_\infty + V_i)}{TV_{i_h}} = \frac{P_i}{P_{i_h}} \tag{7.21}$$

where P_{i_h} is the induced power in static conditions. The second is an application of the quadratic formula along with the assumption of a positive value of V_i to compute the induced velocity

$$V_i = \frac{-V_\infty}{2} + \sqrt{\frac{V_\infty^2}{4} + V_{i_h}^2}. \tag{7.22}$$

With an expression for the induced velocity, it is then possible to calculate the induced power for a given thrust and combine this with the profile power expression to compute the expected required rotor power. Combining Eqs 7.22 and 7.18 and applying the correction from Eq. (7.15), the expression for the induced power for a given thrust in static conditions is

$$P_i = \kappa T\left(\frac{V_\infty}{2} + \sqrt{\frac{V_\infty^2}{4} + V_{i_h}^2}\right). \tag{7.23}$$

Conversely, as a propeller does not have constant performance as the axial velocity increases, the change in thrust with a constant power input may be desired. McCormick [3] provides an expression derived from disk actuator theory for the thrust in axial forward flight assuming that the profile power requirement of the propeller is constant and that the mechanical power delivered to the propeller does not change with forward flight speed

$$\frac{T_h^{3/2}}{\sqrt{2\rho A}} = \frac{T}{2}\left[V_\infty + \left(V_\infty^2 + \frac{2T}{\rho A}\right)^{1/2}\right] \tag{7.24}$$

where T_h is the thrust available in static (hover) conditions. As the freestream velocity increases, the thrust produced for a constant power input decreases. Note the similarity to Eq. (7.23). While it is possible to find an analytic expression for the thrust T as a function of the static thrust, the expression

$$T = \frac{\sqrt[3]{\sqrt{3}\sqrt{8\sqrt{2}A^3\rho^3V^3\left(\frac{T_0^3}{A\rho}\right)^{3/2} + 27T_0^6} + 9T_0^3}}{\sqrt[3]{2}3^{2/3}} - \frac{2^{5/6}A\rho V\sqrt{\frac{T_0^3}{A\rho}}}{\sqrt[3]{3}\sqrt[3]{\sqrt{3}\sqrt{8\sqrt{2}A^3\rho^3V^3\left(\frac{T_0^3}{A\rho}\right)^{3/2} + 27T_0^6} + 9T_0^3}} \tag{7.25}$$

is quite complicated and it is less tedious to simply solve the relation numerically. A numerical solution can be found easily using the Newton–Raphson method which iteratively finds the root of an expression $f(x)$ by computing the next iteration of the root as

$$x_{n+1} = x_n - \frac{f(x_n)}{f'(x_n)}. \tag{7.26}$$

With the preceding expressions, it is possible to estimate a propeller's power consumption for a given thrust and the expected thrust for a constant power based on the propeller's static performance. As the craft's angle of attack is expected to be small, the thrusters are treated as being in axial flow while computing power or thrust in the modeling of each aircraft.

Experimental data was not collected for all the propellers used in the above models. Subsequent energy analysis uses the stated diameter of the propeller alongside values for the thrust and torque coefficients that were considered typical based on the static tests of other propellers. The values used were $C_T = 0.003$ and $C_Q = 0.00015$.

Propeller Power in Forward Flight

Momentum theory can be used to estimate the induced power in forward (or edgewise) flight. The core theory remains unchanged, namely that the ideal power is equal to the product of the thrust and the flow through the disk.

$$P_{\text{ideal}} = T(V_\infty \sin(\alpha) + V_i) \tag{7.27}$$

The $\sin(\alpha)$ portion accounting for the portion of the freestream in the axial direction of the rotor disk. From Glauert momentum theory [2] described in Eq. (6.8), the induced velocity in forward flight can be related to the thrust by

$$T = 2\rho A V_i\sqrt{V_\infty^2 + 2V_\infty V_i \sin\alpha + V_i^2}. \tag{7.28}$$

For the case of $\alpha = 0$ this can be solved analytically, but otherwise is easier to solve numerically using Newton's method as before.

In forward flight, an expression for the profile power from Johnson, Chapter 5 is approximated as

$$C_{P_0} = \frac{\sigma c_{d_0}}{8}(1 + 4.6\mu^2) \tag{7.29}$$

where $\mu = V_\infty \cos(\alpha)/(\omega R)$ is the rotor advance ratio using the inflow angle of attack α. This approximation is stated to be accurate to within 3% for $\mu \leq 0.3$ and within 5% for $\mu \leq 0.5$.

By combining the ideal induced power and profile as before for axial flight, the mechanical power for a rotor in forward flight can be estimated. As the lifting rotor thrust will be assumed to match the lift deficiency, an expression for the change in rotor thrust with a constant power input will not be used.

Implementation of the Rotor Drag Model

The rotor drag model is the model implemented from Chapter 3, represented in Eq. (3.10). The equation used to model the propeller drag is

$$\frac{H}{\rho V_\infty^2 D^2} = C_H \left(\frac{\omega D/2}{V_\infty}\right)^{C_n} \left(\left(\frac{\pi}{2}\right)^2 - \alpha^2\right)(\alpha - C_a) \tag{7.30}$$

where H is the rotor drag, ω is the rotational speed of the propeller in rad/s, and C_H,C_n, and C_a are experimentally derived coefficients. The previous propeller models described in Sections 7.3 and 7.3 estimate the power consumption based on an assumed propeller thrust, however, the rotor rotation speed is relevant for the drag calculation in forward flight. To reconcile this, the estimated rotor rotation speed is computed as

$$\omega = \sqrt{\frac{T}{\rho D^4 C_T}}. \tag{7.31}$$

although the thrust coefficient has been observed to change in forward flight, the thrust coefficient is assumed constant for this analysis. The reason for this is twofold. One is that a representative model of how the thrust coefficient changes with the advance ratio was not developed in this work. The second is that experiments indicated that the thrust coefficient would differ by a maximum of 10% relative to static in the range of expected advance ratios, and outside this range the actual forces produced by the propeller would be small compared to the remainder of the vehicle. Thus using the static thrust coefficient was considered an appropriate approximation.

One additional simplification was considered for the the rotor drag. While this component of the force is defined as perpendicular to the thrust, this means that the components in the lift and drag directions are dependent on the vehicle angle of attack. While this is not a problem for computing the vehicle drag, incorporating the contribution of the rotor drag into the consideration of the calculation of the rotor thrust leads to a difficult to solve equation. However, as the rotor drag is often an order of magnitude less than the rotor thrust, and the contribution in the lift direction is based on multiplication with a $\sin\alpha$, it was decided to disregard the rotor drag contribution in the lift direction in the context of the subsequent power and energy calculations.

Rotor drag data was not collected for the propellers used on the AFA V3 and AFA V4. For the AFA V3, one of the propellers of 8-inch diameter was used as this was the diameter used on the actual craft. For the AFA V4, as the propellers used are 14-inch propellers from T-Motor, the properties of the T-Motor 12 inch were applied with a 14-inch diameter as a replacement.

Implementation of Propeller-Wing Model

The data of Chapter 6 demonstrated that there is a measurable change in the lift and drag properties of a finite wing in the vicinity of a propeller. The work presented is a significant simplification of the cases expected in actual eVTOL aircraft, featuring only a canonical finite wing and a single propeller. In contrast, eVTOL aircraft are expected to have wings designed for their particular application as well as multiple lifting propellers. Nevertheless, in an effort to represent this effect to some degree, the implementation of a form of the model is considered. As the placement of the rotor leading the wing was not found to confer any significant benefit in the configurations studies, it will be assumed that the leading rotors are positioned in such a way as to minimize this interaction. As it was possible to produce a beneficial interaction from the trailing rotor placement, this effect will be considered. The model used to describe the effect of the trailing rotor was shown in Eq. (6.12). For implementation in the model, a few assumptions are made.

Because independent aerodynamic data for the wings and the rest of the craft are not available, the modification to the lift and drag coefficient is applied to the aerodynamic parameters to the whole craft. Furthermore, because experiments were not done to observe the effect of multiple propellers, it will be assumed that the effect observed with a single propeller is transferable to the entire craft. Lastly, it is assumed that the interaction acts as a coefficient modifier to the lift coefficient, trending towards non-interaction lift coefficient of the wing as the advance ratio increases. As data at nonzero angles of attack were not collected, it is also assumed that this modifier is independent of the angle of attack. The model implemented in this work produces the modified lift coefficient

$$C_{L2} = C_L(\alpha)\left(\frac{C_a}{C_c}e^{C_b\mu} + 1\right) = C_L(\alpha) f_{pw_L}(\mu) \tag{7.32}$$

where $C_L(\alpha)$ is the aircraft's original lift coefficient as a function of angle of attack, and C_a, C_b, and C_c are fitted coefficients found in Chapter 6. An analogous expression $f_{pw_D}(\mu)$ is used for the Drag coefficient. The model adjusts the total vehicle lift and drag based on the experimental data, approaching the nominal values as the advance ratio increases.

Energy Required for Steady State Hybrid Flight

To model the flight a number of simplifying assumptions are made.

- Required lifting thrust is equally distributed among all available lifting rotors.
- Rotor rotation speed changes instantaneously to meet the required conditions.
- Rotor Drag is additive and equivalent for each rotor to the freestream measurements.
- For acceleration, Thrusters are operating at maximum throttle. The disproportionate impact of the lifting rotors on the power consumption motivates transition to fixed wing flight as quickly as possible.
- The lifting rotors are all installed with thrust axes aligned with the vehicle up direction.
- Thrust and torque coefficients for the lifting rotors are treated as constant for the transitional flight regime.
- The vehicle angle of attack is constant during acceleration to represent a simplistic transition control law.

To balance the force of gravity in forward flight, the required lifting thrust per rotor is computed as

$$T = \frac{mg - F_L f_{pw_L}(\mu) - F_T \sin(\alpha)}{\cos(\alpha)} \frac{1}{N_{\text{Lifters}}} \tag{7.33}$$

where T is thrust force produced by each rotor, m is the vehicle mass, g is the acceleration due to gravity, and N_{Lifters} is the number lifting rotors on the vehicle. F_T is the thruster force and is computed to match the total drag. The lifter thrust can be used to compute the lifter angular velocity ω. The overall drag is computed by taking the sum of the vehicle drag modified by the propeller-wing interaction, rotor drag, and contribution from the lifters at nonzero angles of attack. The effective drag of the craft is then

$$D_{\text{Total}} = (F_D(V_\infty, \alpha) f_{pw_D}(\mu) + N_{\text{Lifters}} H(V_\infty, \omega, \alpha) \cos(\alpha) + T \sin(\alpha))/\cos(\alpha) \tag{7.34}$$

To compute the steady state power draw, the thruster force F_T is matched to the drag, and the power computed based on the axial and forward flight models described. As the propellers are the main consumers of mechanical power in the system, the total system power is generally

$$P_{\text{Total}} = P_{\text{Thruster}} + P_{\text{Lifter}} N_{\text{Lifters}}. \tag{7.35}$$

Energy Required for Acceleration to Fixed Wing Cruise

For modeling acceleration, the previous lift and drag models are used, but the aircraft's thrusters are assumed to be operating at max throttle in order to accelerate as quickly as possible. This is motivated by the fact that hovering is extremely energy intensive relative to fixed wing flight, and energy minimization typically occurs by minimizing the time spent transitioning as a result. To compute the total mechanical energy required for acceleration, a basic dynamics model is constructed to estimate the vehicle's velocity over time.

$$a = (F_T \cos(\alpha) - D_{\text{Total}})/m \tag{7.36}$$

Because the thruster force and the vehicle drag have a velocity dependence, the acceleration equation is a differential equation that will be solved numerically using Matlab's *ode45* function.

The instantaneous power consumption is computed using the steady state power consumption values from the previous section, with the exception that the power associated with the thruster on the vehicle is a fixed value. The value of the thruster power is computed by first establishing a static thrust. As the vehicle is operating at maximum throttle, the whatever propeller is being used is expected to be operating at its maximum rotations speed in static conditions. A good rule of thumb for determining this is to use the rotor tip speed. The author has identified a tip speed of $V_{\text{tip}} = 150\, m/s$ to be a safe upper limit to prevent a rapid unplanned rotor disassembly for rotors of this size. The rotation speed is then

$$\omega = \frac{V_{\text{tip}}}{R}. \tag{7.37}$$

The static thrust is then computed using the C_T value for the propeller, and the static mechanical power consumption is computed as

$$P_{\text{Thruster}} = \omega Q \tag{7.38}$$

where Q is computed using the C_Q value for the propeller. The total energy is then computed as

$$E_{\text{Acceleration}} = \int_{t=0}^{t_f} P_{\text{Total}}(\tau) d\tau \tag{7.39}$$

where t_f is the time at which the vehicle reaches the desired cruise speed as determined by the numerical integration to compute the vehicle velocity.

7.4 Results

Analyses conducted are a comparison on three metrics of performance for the vehicle. The first is the effective vehicle drag as a function of forward flight speed. The model assumes steady state conditions and computes the appropriate lifter thrust appropriately. The next is the steady state power consumption. This is again done assuming a constant forward flight speed, and represents the required mechanical power should the vehicle wish to fly at low speed in a hybrid mode. The last study examines the energy required to accelerate from hover to cruise in fixed wing forward flight to look at the cumulative effect of the additional modeling in transition. For each of these studies, the vehicle was examined with each variation of implemented models to determine how significant the addition of model is in the context of the vehicle's power consumption.

Vehicle Drag

In addition to affecting the power consumption, the effective vehicle drag is directly related to the length of time required to transition. Figures 7.7, 7.8, and 7.9 show the effective vehicle drag for each of the vehicles as a function of the vehicle's forward

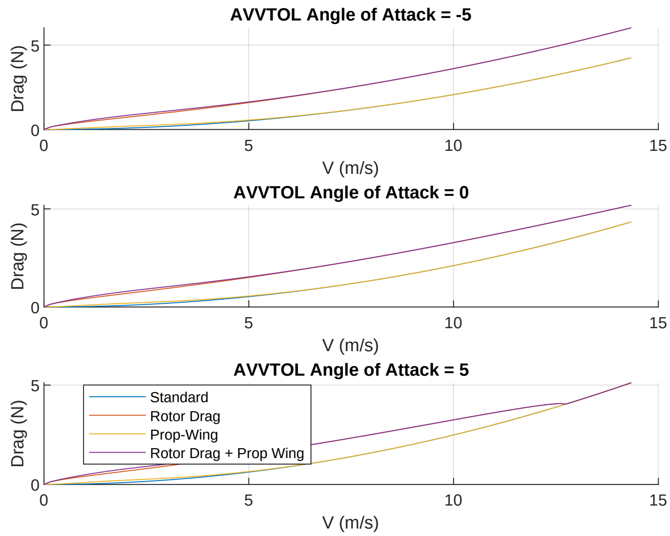

Figure 7.7: Effective vehicle drag for the AV VTOL at various forward speeds.

flight speed. Each figure shows the curve for the respective vehicle at three different angles of attack. The results show that the rotor drag has a significant effect upon the total effective drag of the vehicle, more than doubling it in some cases. For some cases shown the model with rotor drag returns back to the basic model. These are cases where the vehicle achieves full wing-borne lift and the lifting rotors are no longer needed.

In contrast, the prop wing interaction model has a relatively minimal impact on the rotor drag. Although a slight difference is visible at low speeds where the advance ratio is also low, the effect is generally negligible. Interestingly, the increased drag may have been a contributor in the loss of the physical AFA V3 prototype. During field testing, the craft failed to reach fixed wing cruise speeds in a transition attempt, and entered an unstable back-transition that led to a loss of the vehicle.

Steady State Power Consumption

The results of the analysis on the steady state power consumption are similar to those of the effective vehicle drag, as shown in Figures 7.10, 7.11, and 7.12. As the primary consumer of power in such a vehicle are the rotors used for hover, the effect of the rotor drag on the overall power consumption for the surveyed cases is relatively small across all vehicles. The effect of the propeller-wing interactions are even less noticeable.

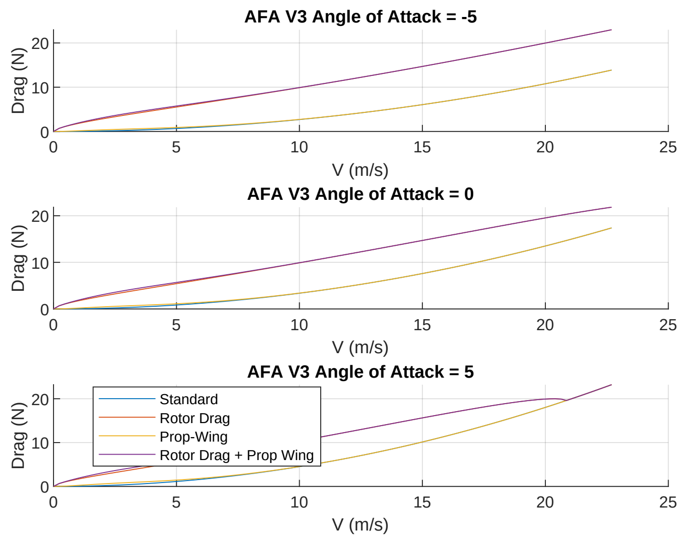

Figure 7.8: Effective vehicle drag for the AFA V3 at various forward speeds.

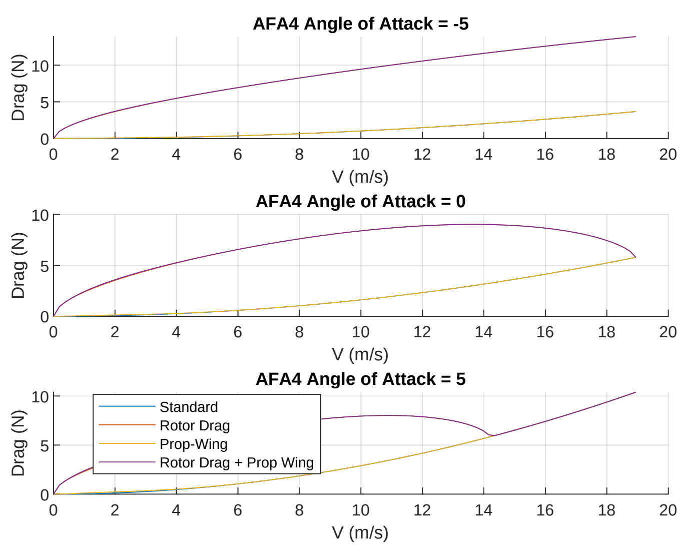

Figure 7.9: Effective vehicle drag for the AFA V4 at various forward speeds.

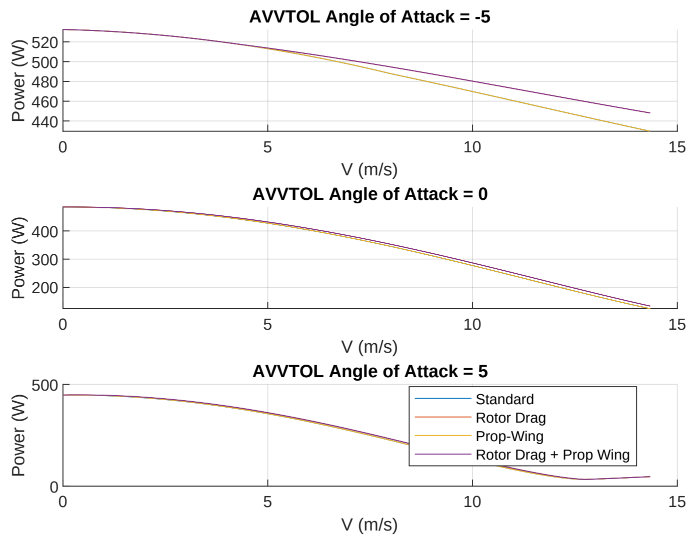

Figure 7.10: Steady State Power Consumption for the AV VTOL at various forward speeds.

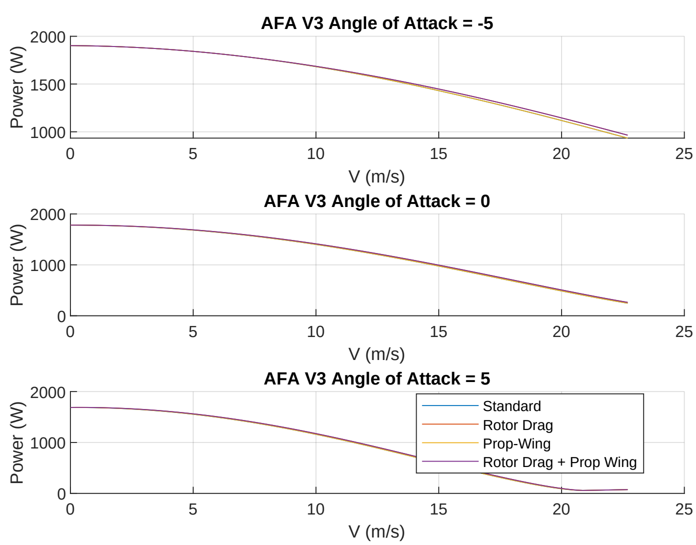

Figure 7.11: Steady State Power Consumption for the AFA V3 at various forward speeds.

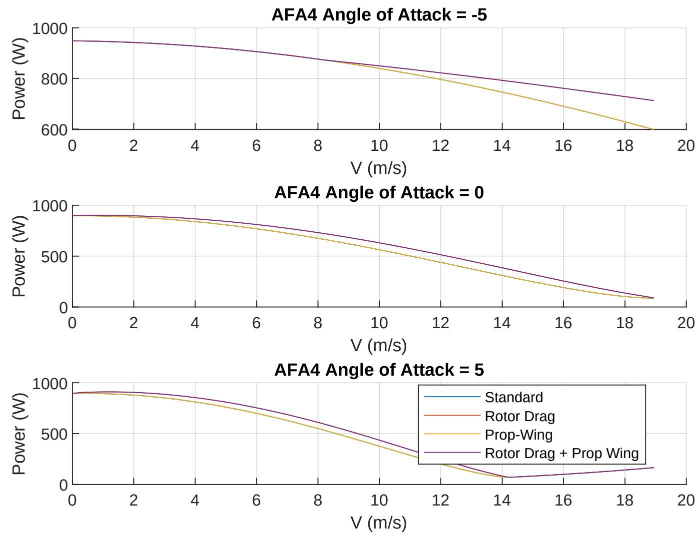

Figure 7.12: Steady State Power Consumption for the AFA V4 at various forward speeds.

Acceleration Energy

The simulated energy required for acceleration is seen in Figures 7.13, 7.14, and 7.15. Although the change in steady state power consumption is relatively minor, the total energy consumed by the systems during acceleration increases substantially with the implementation of the rotor drag model, on the order of 10 to 40%. As the steady state plots show, the power consumption change directly associated with the addition of the rotor drag and propeller-wing models is relatively small. However, the addition of the rotor drag slows the vehicle acceleration, requiring more time to reach the desired cruise speed. The result is that more energy is required to keep the vehicle aloft with the lifting rotors, increasing the overall energy consumption.

As the results show, the effect of the propeller-wing interactions as modeled on the chosen metrics is relatively small. To portray the change in energy in a more meaningful manner, the percentage increase in acceleration energy relative to the base model for each vehicle due to the addition of the rotor drag and propeller-wing interaction models is shown in Figures 7.16, 7.17, and 7.18. The rotor drag is shown to have a significantly larger effect upon the acceleration energy than the propeller-wing interaction.

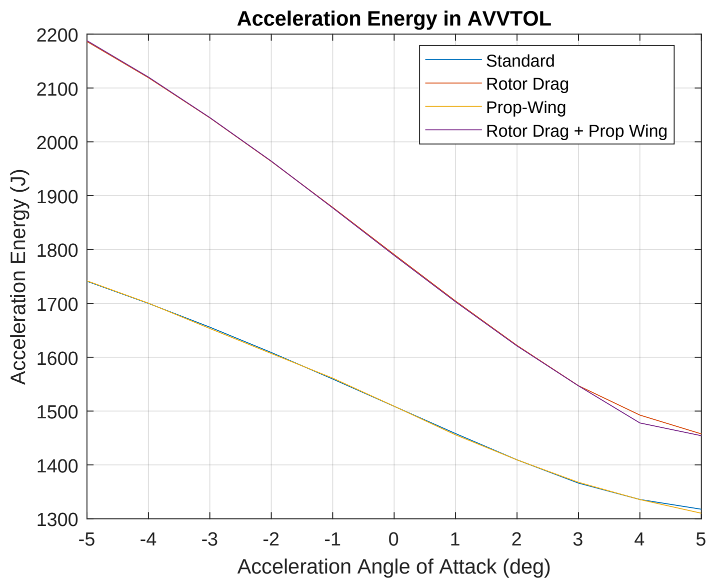

Figure 7.13: Total acceleration energy for the AV VTOL at various angles of attack.

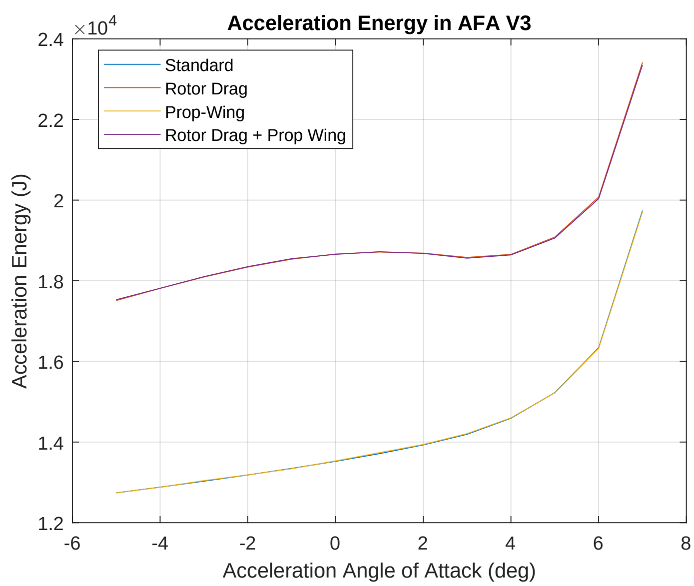

Figure 7.14: Total acceleration energy for the AFA V3 at various angles of attack.

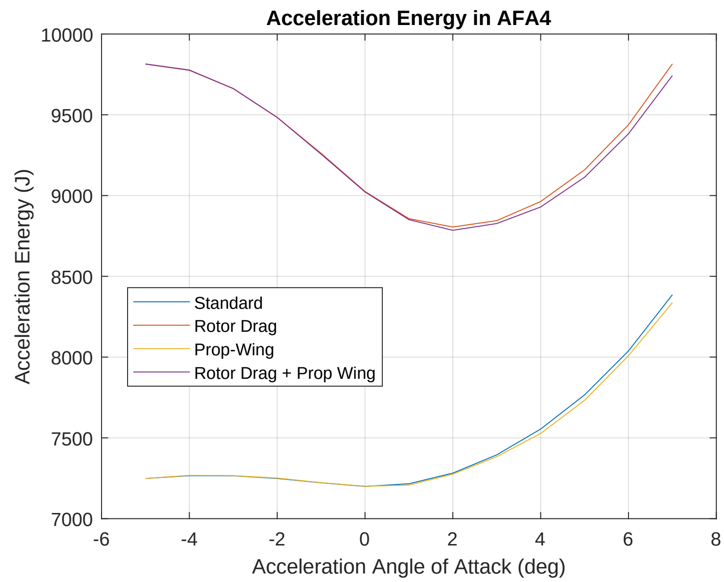

Figure 7.15: Total acceleration energy for the AFA V4 at various angles of attack.

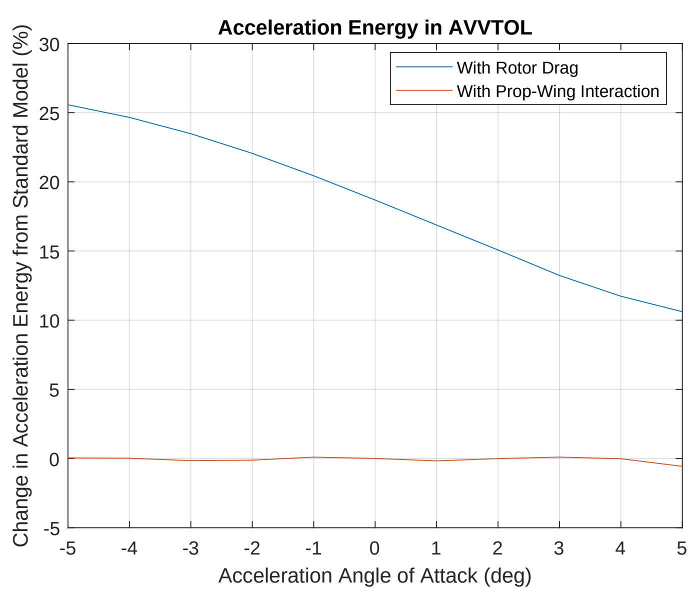

Figure 7.16: Percentage change in acceleration energy for the AV VTOL at various angles of attack.

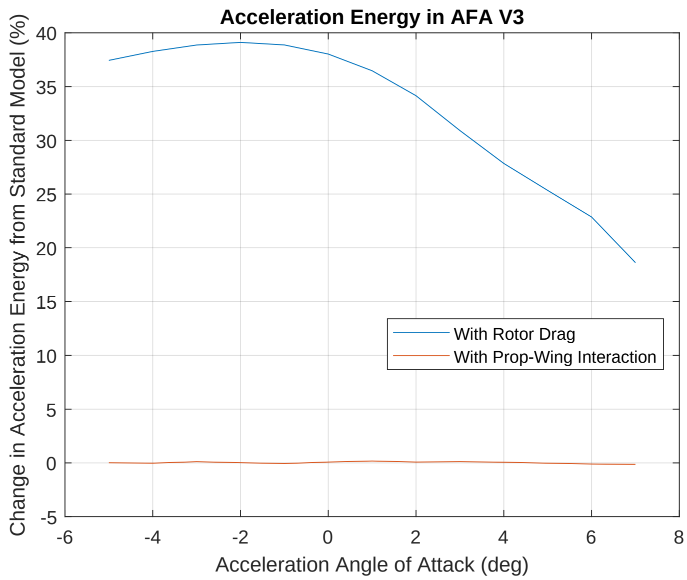

Figure 7.17: Percentage change in acceleration energy for the AFA V3 at various angles of attack.

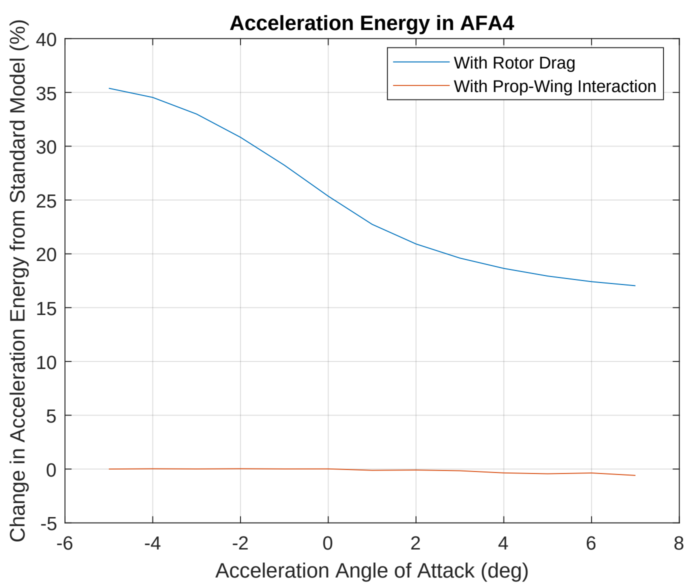

Figure 7.18: Percentage change in acceleration energy for the AFA V4 at various angles of attack.

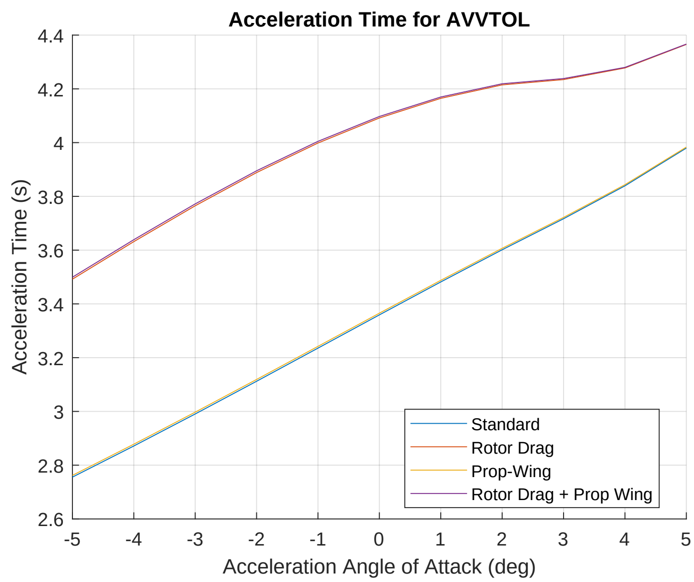

Figure 7.19: Time taken to accelerate for the AV VTOL at various angles of attack.

Acceleration Performance

Failure to model aerodynamic effects can significantly impact the transition process for a craft. The implementation of the rotor drag increases the acceleration time for all the vehicles visible in Figures 7.19, 7.20, and 7.21. Although the increase is only on the order of seconds, this generally represents a 30% increase in the required optimal transition time. This change transfers to the acceleration distance as well, seen in Figures 7.22, 7.23, and 7.24. The increase in predicted transition distance can be several dozen meters for the heavier vehicles.

As with the energy, the percentage change on the acceleration time can be seen in Figures 7.25, 7.26, and 7.27 and the percentage change in acceleration distance can be seen in Figures 7.28, 7.29, and 7.30.

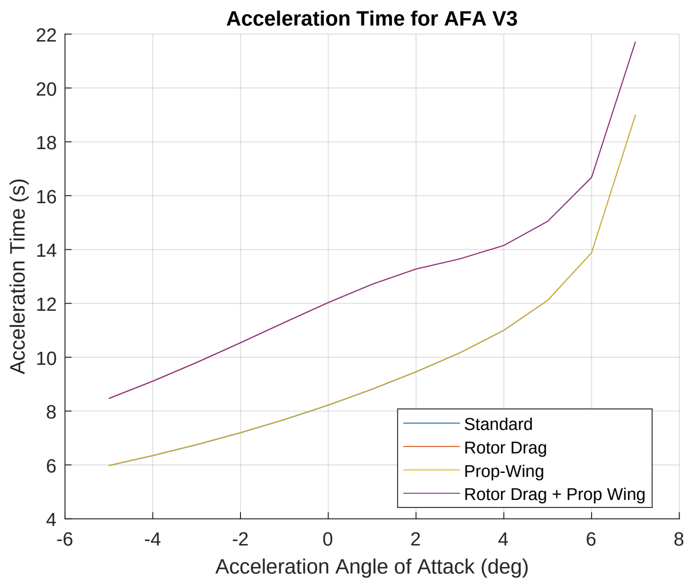

Figure 7.20: Time taken to accelerate for the AFA V3 at various angles of attack.

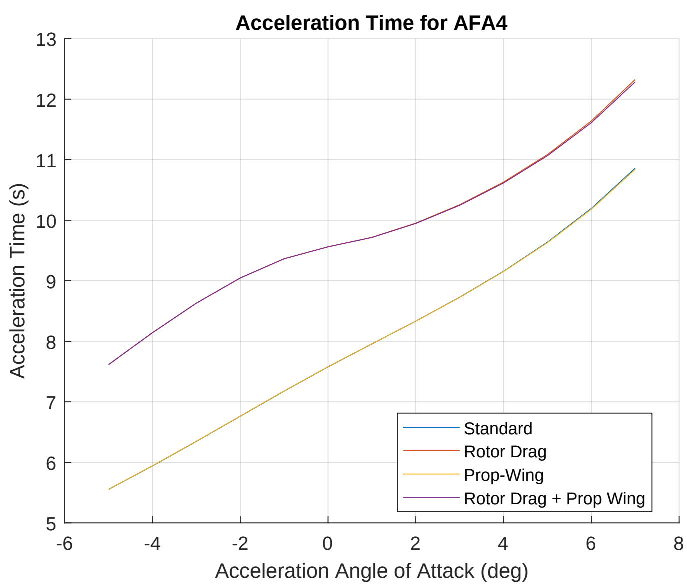

Figure 7.21: Time taken to accelerate for the AFA V4 at various angles of attack.

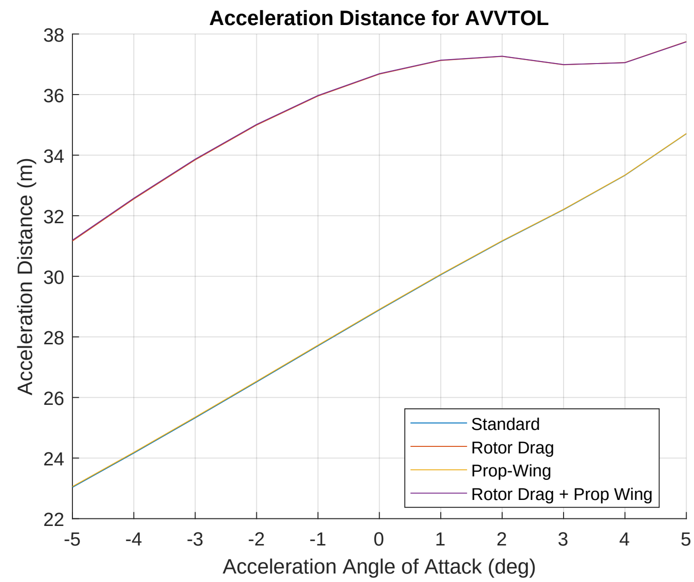

Figure 7.22: Distance taken to accelerate for the AV VTOL at various angles of attack.

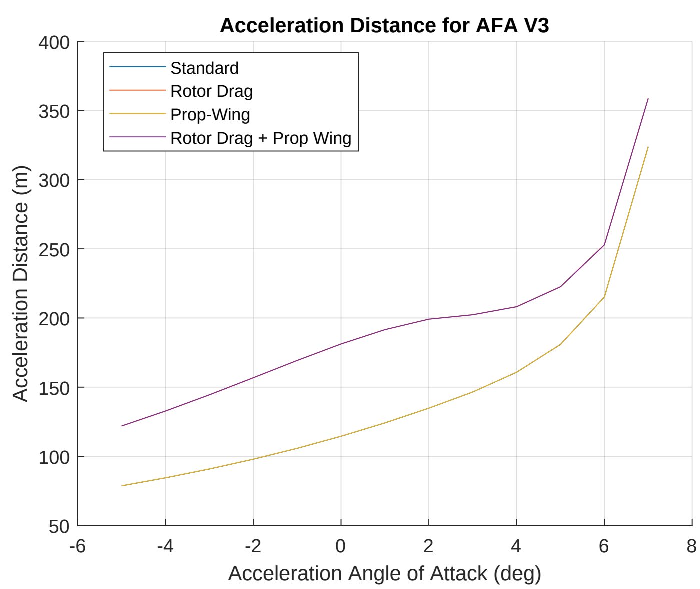

Figure 7.23: Distance taken to accelerate for the AFA V3 at various angles of attack.

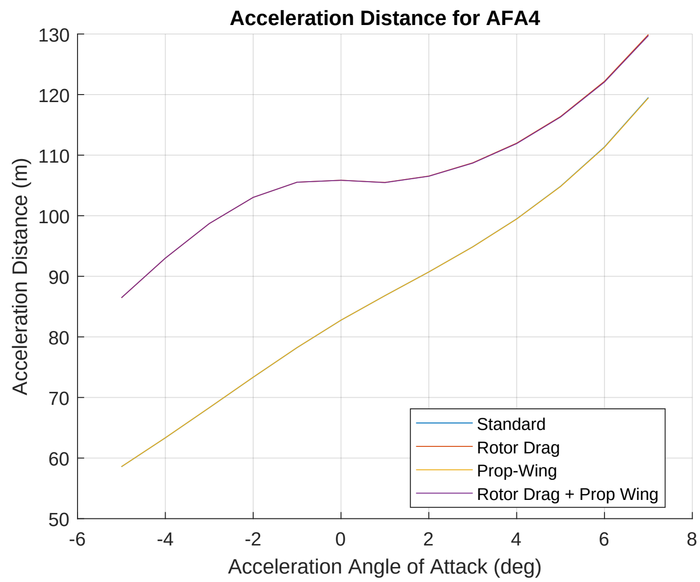

Figure 7.24: Distance taken to accelerate for the AFA V4 at various angles of attack.

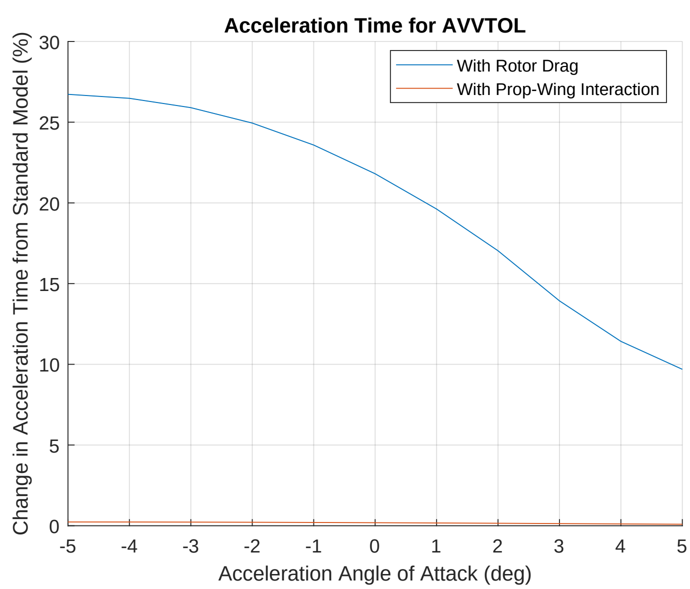

Figure 7.25: Percentage change in time taken to accelerate for the AV VTOL at various angles of attack.

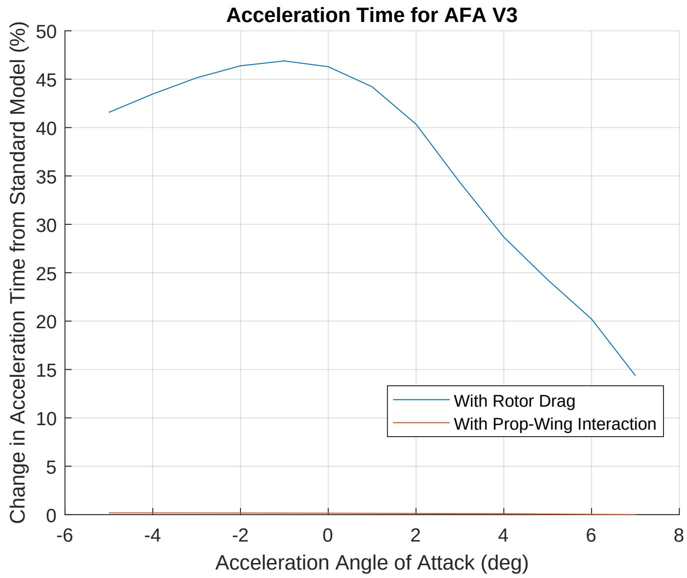

Figure 7.26: Percentage change in time taken to accelerate for the AFA V3 at various angles of attack.

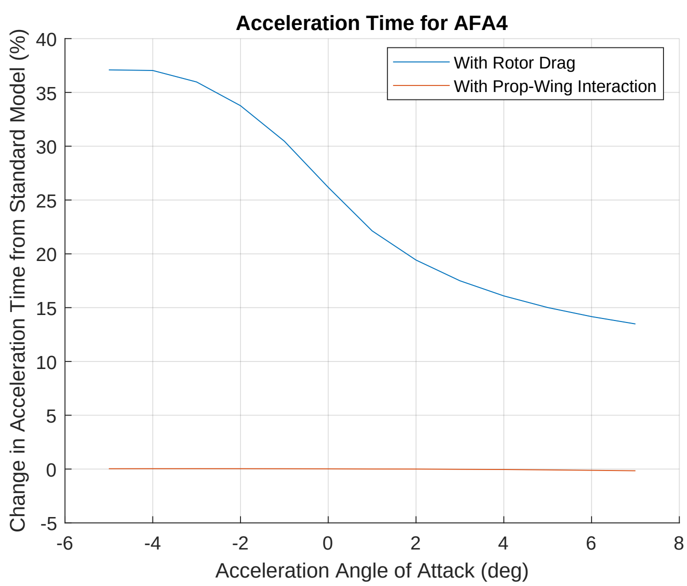

Figure 7.27: Percentage change in time taken to accelerate for the AFA V4 at various angles of attack.

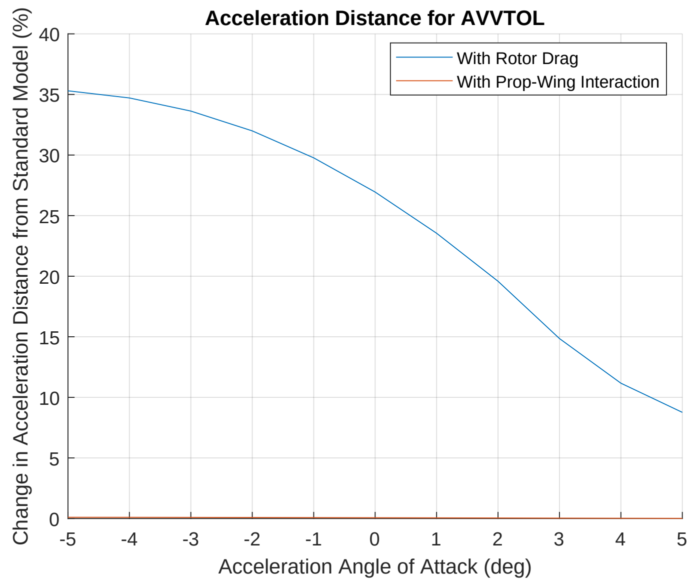

Figure 7.28: Percentage change in distance taken to accelerate for the AV VTOL at various angles of attack.

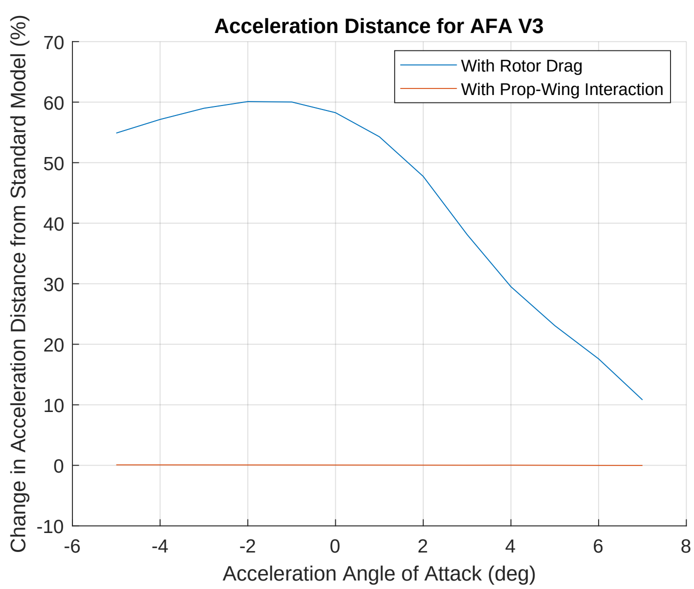

Figure 7.29: Percentage change in distance taken to accelerate for the AFA V3 at various angles of attack.

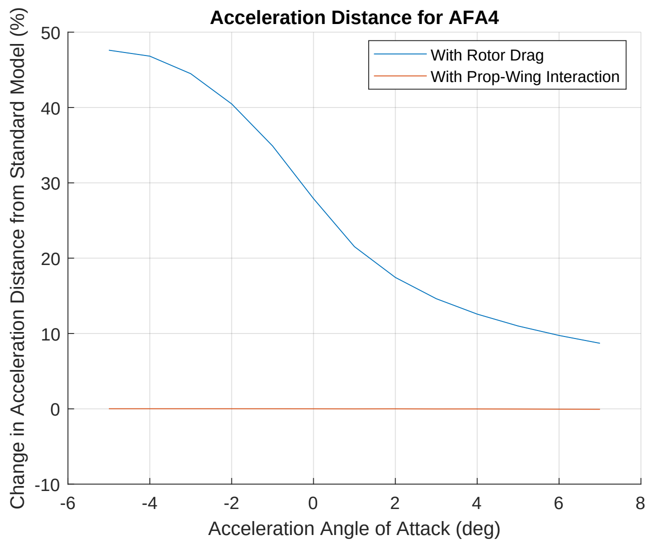

Figure 7.30: Percentage change in distance taken to accelerate for the AFA V4 at various angles of attack.

7.5 Future Work

While the simplistic model used here does show a notable change in performance of the studied craft, it is possible to integrate the findings in ways that are more general and would potentially enhance prediction of energy consumption for this class of vehicles or improve dynamics models. For instance, integrating the rotor drag, prop-wing interaction, or upstream obstruction results into a dynamics model for a craft would provide a more complete model for the development of control law.

The representation of the various craft here was a simplistic rendering of the vehicles aerodynamics, but particularly so with the calculation of the lifter thrust. Although equally distributed thrust among all lifting rotors is an ideal scenario from an energy perspective, there is no guarantee that this would be the case. In a real aircraft, the thrust provided by the lifters might be changing dynamically as they are used to maintain the attitude of the aircraft in concert with the control surfaces of the vehicle. Rather than the fixed angle of attack during acceleration, the vehicle might also be continuously changing its attitude as it accelerates to achieve the best efficiency while accelerating.

An ideal, though more computationally expensive version of this work would be to incorporate the models into a simulation with full vehicle dynamics with realistic control algorithms. This more accurate representation of the craft could then be used to model the energy consumption in a manner that takes control and path planning into account in the estimation.

7.6 Conclusion

The integration of the various models in this work has a significant impact on the performance of the aircraft as predicted by the assembled models. The presence of the upstream obstruction on one craft can modify the already substantial hover power consumption on such a craft to negative effect. The craft studied likely consumed an additional 5% power in hover as a result of the interaction. Neglecting the rotor drag also disregards a significant source of vehicle drag and power consumption. In some portions of flight, the additional drag from the lifting rotors can double the overall vehicle drag. While this does not directly affect the power consumption tremendously, the increased drag can make it substantially more difficult to transition to fixed wing flight. Thrusters might be underpowered if this is not accounted for, and the longer time to transition means that more energy is consumed while accelerating and the craft requires more space to reach cruise. The energy consumption in acceleration with the rotor drag model can be 30 to 50% higher than without. Neglecting this portion of the modeling can lead to severely underestimating the energy consumption of this phase of flight.

In contrast to the other two effects, the interaction between the propellers and wings in forward flight is relatively minor, provided the strongly adverse interaction observed in Chapter 6 is avoided. The region where positive or negative interactions are observed is quickly exited while accelerating. Even so, the effect is minimal in studies of the craft in steady state conditions.

References

[1] John D. Anderson. *Introduction to Flight*. 3rd ed. McGraw-Hill series in aeronautical and aerospace engineering. New York: McGraw-Hill, 1989. ISBN: 978-0-07-001641-5.

[2] J. Gordon Leishman. *Principles of Helicopter Aerodynamics*. 2nd ed. Cambridge aerospace series 18. Cambridge: Cambridge University Press, 2006. ISBN: 978-1-107-01335-3.

[3] Barnes W. McCormick. *Aerodynamics of V/STOL Flight*. Academic Pr, 1967. ISBN: 0124823505.

[4] Wayne Johnson. *Helicopter Theory*. Revised. Dover Publications, Dec. 1994. ISBN: 0-486-68230-7.

[5] Alessandro Bacchini, Enrico Cestino, Benjamin Van Magill, and Dries Verstraete. "Impact of Lift Propeller Drag on the Performance of eVTOL Lift+Cruise Aircraft." en. In: *Aerospace Science and Technology* 109 (Feb. 2021), p. 106429. ISSN: 12709638. DOI: 10.1016/j.ast.2020.106429.

[6] Philipp Stahl, Christian Rössler, and Mirko Hornung. "Benefit Analysis and System Design Considerations for Drag Reduction of Inactive Hover Rotors on Electric Fixed-Wing VTOL Vehicles." en. In: *2018 Aviation Technology, Integration, and Operations Conference*. Atlanta, Georgia: American Institute of Aeronautics and Astronautics, June 2018. ISBN: 978-1-62410-556-2. DOI: 10.2514/6.2018-4150.

[7] Yih Tang Yeo and Hugh H. Liu. "Transition Control of a Tilt-Rotor VTOL UAV." en. In: *2018 AIAA Guidance, Navigation, and Control Conference*. Kissimmee, Florida: American Institute of Aeronautics and Astronautics, Jan. 2018. ISBN: 978-1-62410-526-5. DOI: 10.2514/6.2018-1848.

[8] Rudrapatna V. Ramnath. "Transition Dynamics of VTOL aircraft." en. In: *AIAA Journal* 8.7 (July 1970), pp. 1214–1221. ISSN: 0001-1452, 1533-385X. DOI: 10.2514/3.5875.

[9] Gerardo Flores and R. Lozano. "Transition Flight Control of the Quad-Tilting Rotor Convertible MAV." In: *2013 International Conference on Unmanned Aircraft Systems (ICUAS)*. Atlanta, GA, USA: IEEE, May 2013, pp. 789–794. DOI: 10.1109/ICUAS.2013.6564761.

[10] Boyang Li, Jingxuan Sun, Weifeng Zhou, Chih-Yung Wen, Kin Huat Low, and Chih-Keng Chen. "Transition Optimization for a VTOL Tail-Sitter UAV." en. In: *IEEE/ASME Transactions on Mechatronics* 25.5 (Oct. 2020), pp. 2534–2545. ISSN: 1083-4435, 1941-014X. DOI: 10.1109/TMECH.2020.2983255.

[11] Sebastian Verling, Thomas Stastny, Gregory Battig, Kostas Alexis, and Roland Siegwart. "Model-based Transition Optimization for a VTOL Tailsitter." In: *2017 IEEE International Conference on Robotics and Automation (ICRA)*. Singapore, Singapore: IEEE, May 2017, pp. 3939–3944. ISBN: 978-1-5090-4633-1. DOI: 10.1109/ICRA.2017.7989454.

[12] Koji Muraoka, Noriaki Okada, Daisuke Kubo, and Masayuki Sato. "Transition Flight of Quad Tilt Wing VTOL UAV." en. In: *28th International Congress of the Aeronautical Sciences*. Brisbane, Australia: ICAS, 2012, p. 10.

[13] B. Yuksek, A. Vuruskan, U. Ozdemir, M. A. Yukselen, and G. Inalhan. "Transition Flight Modeling of a Fixed-Wing VTOL UAV." en. In: *Journal of Intelligent & Robotic Systems* 84.1-4 (Dec. 2016), pp. 83–105. ISSN: 0921-0296, 1573-0409. DOI: 10.1007/s10846-015-0325-9.

[14] Yunus Govdeli, Sheikh Moheed Bin Muzaffar, Raunak Raj, Basman Elhadidi, and Erdal Kayacan. "Unsteady Aerodynamic Modeling and Control of Pusher and Tilt-Rotor Quadplane Configurations." en. In: *Aerospace Science and Technology* 94 (Nov. 2019), p. 105421. ISSN: 12709638. DOI: 10.1016/j.ast.2019.105421.

[15] *T-MOTOR The Safer Propulsion System*. URL: https://uav-en.tmotor.com/ (visited on 11/16/2022).

[16] Xichen Shi, Patrick Spieler, **Tang, Ellande**, Elena-Sorina Lupu, Phillip Tokumaru, and Soon-Jo Chung. “Adaptive Nonlinear Control of Fixed-Wing VTOL with Airflow Vector Sensing.” In: *ICRA* (Mar. 2020). arXiv: 2003.07558. DOI: 10.1109/ICRA40945.2020.9197344.

[17] Xichen Shi, Kyunam Kim, Salar Rahili, and Soon Jo Chung. “Nonlinear Control of Autonomous Flying Cars with Wings and Distributed Electric Propulsion.” In: *Proceedings of the IEEE Conference on Decision and Control* 2018-December.Cdc (2019), pp. 5326–5333. ISSN: 07431546. DOI: 10.1109/CDC.2018.8619578.

[18] **Tang, Ellande**, Patrick Spieler, Matthew Anderson, and Soon-Jo Chung. “Design of the Next-Generation Autonomous Flying Ambulance.” In: *AIAA Scitech 2021 Forum*. Reston, Virginia, Jan. 2021, pp. 1–14. ISBN: 978-1-62410-609-5. DOI: 10.2514/6.2021-1514.

Chapter 8

CONCLUSION

Each chapter of this work examines a different facet of the operation of an eVTOL vehicle, or a tool to enable study. Chapters 4 and 5 describe such tools. Chapter 4 details a technique for the extraction of the geometry of propellers. Using freely available software, commonly available computing hardware, and modern cameras, photogrammetry with accuracy sufficient for accurate simulation can be achieved with little expertise or dedicated equipment. The use of the point-to-plane algorithm for automated orientation as well as the airfoil fitting methods allow for rapid extraction of useful propeller parameters rather than just an unstructured mesh or point cloud, thereby facilitating the import of the model into a parametric design software. Chapter 5 meanwhile shows the design of a sensor capable of measuring all six Cartesian components of force and moment simultaneously. The sensor successfully uses multiple low-cost sensors in a Stewart platform arrangement to decouple forces and make measurements. The geometry of the design can be changed to adjust the overall force or moment sensitivity as desired. The sensor is also more robust to overloading as individual measurement components can be replaced rather than the entire sensor needing to be repaired. An evaluation of the sensor accuracy shows that the sensor has a root mean square percentage error that is generally below 3% in the Z force and X and Y moment axes, and below 5% in the X and Y force and Z moment axes.

With these tools developed, analysis on different phases of operation were done. Chapter 2 is relevant to hover, seeking to examine how bodies such as a wing or fuselage might interact with a propeller by studying the canonical case of a propeller with a large obstruction in its upstream. It was found that upstream obstructions have a significant effect on the thrust performance of the propeller. On their own, the thrust of some propellers nearly doubled. The data for multiple different propellers can be collapsed to a similar curve if the net force of the propeller and upstream obstruction arrangement is considered. In this case, the total force drops to zero as the two are brought closer together, but nearly disappears once the separation exceeds half a propeller diameter. The pressure measurements taken at the surface to study the effect were corroborated with CFD simulations in ANSYS Fluent and good agreement between the two is shown with ANSYS's Transition-SST turbulence model. Subsequent simulations also help demonstrate that the results found are scalable to different rotor diameters and pressure jumps. The simulations provide insight into the separated flow region near the axis of the propeller and finds that the Thwaites method for separation prediction is a satisfactory predictor for the separation location. To find a physical basis for the solution, an analytic model based on the Morillo flowfield was implemented. Though there are qualitative discrepancies between the Morillo model and the simulation, results for the two agree well with the application of a simple correction. The model can provide a framework for improving future simulations, panel-codes, or low order models for future aircraft development.

Chapter 3 then examines the performance of an isolated rotor in forward flight. The particular force that was identified was the Rotor Drag, the component of force produced that is perpendicular to the rotor thrust. Using experimental data collected from a set of propellers, a novel model is derived. It is found that the model fits well with the data and that there are trends amongst the derived coefficients. The power parameter as well as the angle of attack parameter are both fairly similar across the various propellers. The majority of the propellers featured power and angle parameters that had values near 1.3 and -3, respectively, making these useful rough estimates for modeling this effect on other propellers. Comparing the data with Vortex Particle Method simulations showed good agreement with thrust and torque, but poor agreement for the rotor drag. While the cause is not conclusively known, the lack of certain viscous effects may be the reason. Nevertheless, a rough correction of multiplying the rotor drag by two is a basic method to compensate for the error.

Chapter 6 continues the study by examining a rotor in forward flight, but now including the presence of a wing. A propeller positioned ahead of a wing has a significant effect on its measured performance. At lower advance ratios, the propeller can have the effect of completely negating the lift generation of the wing and introducing a number of unintended moments into the system. This interaction was shown to occur at the full range of positions considered for the propeller, even where it was initially not expected there would be interference. The interaction between the propeller wake and a lifting surface also means that care should be taken to avoid interactions between craft propeller wakes and control or stability surfaces such as elevators. The interaction between a propeller and a wing with the propeller at the trailing edge however has potential advantages. While the propeller generates thrust in forward flight, the measured lift coefficient of the wing was observed to increase, alongside its drag. This effect was observed to decrease as the distance between the propeller and the wing increased. An empirical fit was applied to the data which suggests that the interaction allows for an improvement in the wing's lift-to-drag ratio for a narrow range of advance ratios.

Having examined some characteristic of propeller-wing interactions in each phase of flight, Chapter 7 seeks to evaluate how much the findings affect the performance of an eVTOL aircraft. Energy analysis of the craft in hover as well as in transitional forward flight show significant changes to predicted energy consumption as a result of the inclusion of the findings in this work. The presence of the upstream obstruction on one craft can modify the already substantial hover power consumption on such a craft to negative effect. The craft studied likely consumed an additional 5% power in hover as a result of the interaction. Neglecting the rotor drag also disregards a significant source of vehicle drag and power consumption. In some portions of flight, the additional drag from the lifting rotors can double the overall vehicle drag. The increased drag can make it more difficult to transition to fixed wing flight, consuming 30 to 50% more in acceleration with the rotor drag model than without. However, the interaction between the propellers and wings in forward flight are relatively minor, provided the strongly adverse interactions observed in Chapter 6 are avoided. The region where positive or negative interactions are observed is quickly exited while accelerating. While a purpose build craft might be able to take advantage of the effect, the effect as modeled is minimal in studies of the craft in steady state conditions.

8.1 Future Work

The work here addresses certain gaps in knowledge associated with the flight of eVTOL aircraft, but there remain avenues for further exploration

- Better identification of the cause of the discrepancy between simulation and experiment results, particularly for the rotor drag in forward flight and propeller wing interactions would be ideal. Given the importance of simulation in modern engineering, improving simulation accuracy would be a worthwhile endeavor.

- The experimental setups in this work were not able to study the chosen effects with multiple propellers. However, most eVTOL craft feature multiple propellers operating simultaneously. Studying the interaction between multiple propellers would be more physically representative of eVTOL craft. Example topics are studying how the non-dimensionalization changes for the upstream obstruction curves with two propellers in close proximity, or better understanding how the rotor drag is affected by the propeller being near the wake of another propeller.

- In a similar vein, studying the interaction between multiple propellers and their interactions with a finite wing would be more representative of an actual eVTOL aircraft. In addition to being more representative of an eVTOL craft, it would be interesting to see how the observed effects change with multiple propellers and whether they are additive or show a completely new interaction.

- The implementation of the findings on a basic model was informative, but integration into a full dynamics model could be additionally useful. In addition to providing a better estimate for the power consumption, the integration into a dynamics model would help inform trade studies in the design phase of a craft by allowing for changes in the design to occur based upon the relative merits associated with these effects.

Appendix A

ELLIPSOIDAL COORDINATE SYSTEM

A key component of the modeling a rotor disk is the use of an elliptical coordinate system, defined using the coordinates $(\nu, \eta, \overline{\psi})$. We express the Cartesian coordinates (x, y, z) in terms of the elliptical coordinates with the following equations

$$x = -\sqrt{1-\nu^2}\sqrt{1+\eta^2}\cos\left(\overline{\psi}\right) \tag{A.1}$$

$$y = \sqrt{1-\nu^2}\sqrt{1+\eta^2}\sin\left(\overline{\psi}\right) \tag{A.2}$$

$$z = -\nu\eta. \tag{A.3}$$

To ensure that there is no overlap in the mapped 3-dimensional space, we also restrict the range of the elliptical variables to the following

$$-1 \leq \nu \leq 1 \tag{A.4}$$

$$0 \leq \eta \leq \infty \tag{A.5}$$

$$0 \leq \overline{\psi} \leq 2\pi. \tag{A.6}$$

The elliptical coordinates can also be expressed in terms of the Cartesian coordinates using the following equations

$$\nu = \frac{-sign(z)}{\sqrt{2}}\sqrt{1-\overline{S}+\sqrt{(\overline{S}-1)^2+4z^2}} \tag{A.7}$$

$$\eta = \frac{1}{\sqrt{2}}\sqrt{\overline{S}-1+\sqrt{(\overline{S}-1)^2+4z^2}} \tag{A.8}$$

$$\overline{\psi} = \arctan\left(\frac{-y}{x}\right) \tag{A.9}$$

$$\overline{S} = x^2+y^2+z^2. \tag{A.10}$$

Contours of the ellipsoidal coordinate drawn in Cartesian space can be seen in Figure. A.1.

The derivative of function $f(\nu, \eta, \overline{\psi})$ can be expressed in cartesian coordinates using

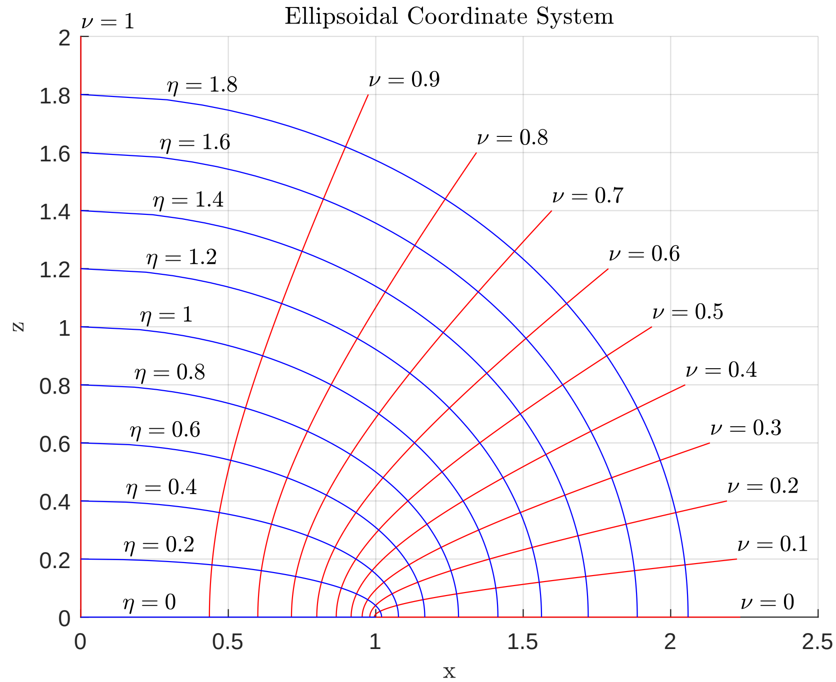

Figure A.1: Ellipsoidal coordinate system at $\overline{\psi} = 0$.

the following equations, derived by the application of the chain rule

$$\frac{\partial f}{\partial x} = \frac{\sqrt{(1+\eta^2)(1-\nu^2)}}{\nu^2+\eta^2}\left(\nu\frac{\partial f}{\partial \nu} - \eta\frac{\partial f}{\partial \eta}\right)\cos\left(\overline{\psi}\right) + \frac{1}{\sqrt{(1+\eta^2)(1-\nu^2)}}\frac{\partial f}{\partial \overline{\psi}}\sin\left(\overline{\psi}\right) \tag{A.11}$$

$$\frac{\partial f}{\partial y} = -\frac{\sqrt{(1+\eta^2)(1-\nu^2)}}{\nu^2+\eta^2}\left(\nu\frac{\partial f}{\partial \nu} - \eta\frac{\partial f}{\partial \eta}\right)\sin\left(\overline{\psi}\right) + \frac{1}{\sqrt{(1+\eta^2)(1-\nu^2)}}\frac{\partial f}{\partial \overline{\psi}}\cos\left(\overline{\psi}\right) \tag{A.12}$$

$$\frac{\partial f}{\partial z} = -\frac{1}{\nu^2+\eta^2}\left(\eta(1-\nu^2)\frac{\partial f}{\partial \nu} + \nu(1+\eta^2)\frac{\partial f}{\partial \eta}\right). \tag{A.13}$$

In the elliptical coordinate system, the disk surface is represented by the region $\eta = 0$. This represents a circle of radius 1 in the x-y plane at $z = 0$. On this surface, a radial coordinate can be represented by $\overline{r} = \sqrt{1-\nu^2}$. While this means that $\pm\nu$ represent the same radial location on the disk, the sign of the z coordinate means that they refer to different faces on disk.

Appendix B

LEGENDRE FUNCTIONS

Critical to the development of a potential flow solution is the Laplace's equation

$$\nabla^2\Phi = 0. \tag{B.1}$$

In an ellipsoidal coordinate system $(\nu, \eta, \overline{\psi})$, the equation takes the form

$$\frac{\partial}{\partial \nu}\left[(1-\nu^2)\frac{\partial \Phi}{\partial \nu}\right] + \frac{\partial}{\partial \eta}\left[(1+\eta^2)\frac{\partial \Phi}{\partial \eta}\right] + \frac{\partial}{\partial \overline{\psi}}\left[\frac{(\nu^2+\eta^2)}{(1-\nu^2)(1+\eta^2)}\frac{\partial \Phi}{\partial \overline{\psi}}\right] = 0. \tag{B.2}$$

A solution to this differential equation can be found using separation of variables by assuming that Φ has the form

$$\Phi(\nu, \eta, \overline{\psi}) = \Phi_1(\nu)\Phi_2(\eta)\Phi_3(\overline{\psi}). \tag{B.3}$$

The differential equation can then be separated into

$$\frac{d}{d\nu}\left[(1-\nu^2)\frac{d\Phi_1}{d\nu}\right] + \left[-\frac{m^2}{1-\nu^2} + n(n+1)\right]\Phi_1 = 0 \tag{B.4}$$

$$\frac{d}{d\eta}\left[(1+\eta^2)\frac{d\Phi_2}{d\eta}\right] + \left[\frac{m^2}{1+\eta^2} - n(n+1)\right]\Phi_2 = 0 \tag{B.5}$$

$$\frac{d^2\Phi_3}{d\overline{\psi}^2} + m^2\Phi_3 = 0. \tag{B.6}$$

It is then found that Legendre Polynomials of the First Kind $P_n^m(\nu)$ are solutions to Eq. (B.4) and Legendre Functions of the Second Kind $Q_n^m(i\eta)$ are solutions to Eq. (B.5).

The Legendre functions of the first kind utilize the following normalization

$$\overline{P}_n^m(\nu) = (-1)^m \frac{P_n^m(\nu)}{\rho_n^m} \tag{B.7}$$

$$(\rho_n^m)^2 = \int_0^1 (P_n^m(\nu))^2 d\nu = \frac{1}{2n+1}\frac{(n+m)!}{(n-m)!}. \tag{B.8}$$

This normalization confers the advantages of the integral over the disk domain being equal to one. The Laplace functions of the second kind utilize the following normalization

$$\overline{Q}_n^m(i\eta) = \frac{Q_n^m(i\eta)}{Q_n^m(i0)}. \tag{B.9}$$

This normalization confers the advantage of making all the Legendre functions of the second kind have a value of 1 on the actuator disk.

For $-1 < z < 1$

$$P_n^m(z) \triangleq (-1)^m (1-z^2)^{m/2} \frac{d^m P_n(z)}{dz^m} \tag{B.10}$$

$$Q_n^m(z) \triangleq (-1)^m (1-z^2)^{m/2} \frac{d^m Q_n(z)}{dz^m}, \text{replace } \log\frac{z+1}{z-1} \text{ with } \log\frac{1+z}{1-z}. \tag{B.11}$$

For z outside $(-1, +1)$

$$P_n^m(z) \triangleq (z^2-1)^{m/2} \frac{d^m P_n(z)}{dz^m} \tag{B.12}$$

$$Q_n^m(z) \triangleq (z^2-1)^{m/2} \frac{d^m Q_n(z)}{dz^m}. \tag{B.13}$$

Legendre Function of the First Kind

Examples of the Legendre Functions of the first kind are computed as

$$\begin{aligned} P_0(z) &= 1 \\ P_1(z) &= x \\ P_2(z) &= \frac{1}{2}(2x^2-1). \end{aligned}$$

Examples of the normalized versions are

$$\begin{aligned} \overline{P}_0(z) &= 1 \\ \overline{P}_1(z) &= \sqrt{3}x \\ \overline{P}_2(z) &= \frac{\sqrt{5}}{2}(2x^2-1). \end{aligned}$$

Recurrence Relations

$$\overline{P}_{n+1}^m(\nu) = \sqrt{\frac{(2n+3)(2n+1)}{(n+1)^2-m^2}} \left[\nu \overline{P}_n^m(\nu) - \sqrt{\frac{n^2-m^2}{4n^2-1}} \overline{P}_{n-1}^m(\nu)\right] \tag{B.14}$$

$$\overline{P}_n^{m+1}(\nu) = \frac{1}{\sqrt{1-\nu^2}} \left[\sqrt{\frac{(2n+1)(n+m)}{(2n-1)(n+m+1)}} \overline{P}_{n-1}^m(\nu) - \frac{n-m}{\sqrt{(n+m+1)(n-m)}} \nu \overline{P}_n^m(\nu)\right] \tag{B.15}$$

Differentiation Relation

$$(1-\nu^2)\frac{d\overline{P}_n^m(\nu)}{d\nu} = \sqrt{\frac{(2n+1)(N^2-m^2}{(2n-1)}} \overline{P}_{n-1}^m(\nu) - n\nu \overline{P}_n^m(\nu) \tag{B.16}$$

Legendre Function of the Second Kind

Normally, the Legendre Functions of the Second Kind are represented with a complex input z such as in the following equations

$$\begin{aligned}
Q_0(z) &= \frac{1}{2}\log\frac{z+1}{z-1}\\
Q_1(z) &= \frac{z}{2}\log\frac{z+1}{z-1} - 1\\
Q_2(z) &= \frac{1}{4}(3z^2 - 1\log\frac{z+1}{z-1} - \frac{3}{2}z
\end{aligned}$$

where log is the complex natural logarithm. In this application, the input to the function is the complex value $z = i\eta$. For convenience in notation and for the subsequent implementation, the representation of the equations is modified. We can use the relation

$$\arctan(x) = \frac{1}{2}i\log(1-ix) - \frac{1}{2}i\log(1+ix) = \frac{1}{2}i\frac{1-ix}{1+ix} \tag{B.17}$$

with a change of variable

$$\arctan\left(\frac{1}{x}\right) = \frac{1}{2}i\log\frac{1-i/x}{1+i/x} = \frac{1}{2}i\log\frac{ix+1}{ix-1} \tag{B.18}$$

therefore

$$\log\frac{i\eta+1}{i\eta-1} = -2i\arctan\left(\frac{1}{\eta}\right). \tag{B.19}$$

The singularity introduced by the $1/\eta$ portion can lead to computation difficulties. Fortunately, for the domain in question, namely $\eta \geq 0$, $\arctan\left(\frac{1}{\eta}\right) = \frac{\pi}{2} - \arctan(\eta)$. The Legendre functions of the second kind can then be represented as the following

$$\begin{aligned}
Q_0(i\eta) &= -i\left(\frac{\pi}{2} - \arctan(\eta)\right)\\
Q_1(i\eta) &= \eta\left(\frac{\pi}{2} - \arctan(\eta)\right) - 1\\
Q_2(i\eta) &= \frac{i}{2}(3\eta^2+1)\left(\frac{\pi}{2} - \arctan(\eta)\right) - \frac{3}{2}i\eta.
\end{aligned}$$

With normalization, the functions become

$$\begin{aligned}
\overline{Q}_0(i\eta) &= \frac{2}{\pi}\left(\frac{\pi}{2} - \arctan(\eta)\right)\\
\overline{Q}_1(i\eta) &= -\eta\left(\frac{\pi}{2} - \arctan(\eta)\right) + 1\\
\overline{Q}_2(i\eta) &= \frac{2}{\pi}(3\eta^2+1)\left(\frac{\pi}{2} - \arctan(\eta)\right) - \frac{6}{\pi}\eta.
\end{aligned}$$

Recurrence Relation

Propagation of the function to higher orders is found using the recurrence relations

$$\overline{Q}_{n+1}^{m}(i\eta) = \overline{Q}_{n-1}^{m}(i\eta) - \eta(2n+1)K_n^m\overline{Q}_n^m(i\eta) \tag{B.20}$$

$$\overline{Q}_n^{m+1}(i\eta) = \frac{1}{\sqrt{1+\eta^2}}\left[\overline{Q}_{n-1}^{m}(i\eta) - \eta(n-m)K_n^m\overline{Q}_n^m(i\eta)\right] \tag{B.21}$$

where

$$K_n^m = \left(\frac{\pi}{2}\right)^{(-1)^{n+m}} H_n^m \tag{B.22}$$

$$H_n^m = \frac{(n+m-1)!!(n-m-1)!!}{(n+m)!!(n-m)!!} \tag{B.23}$$

$$\begin{aligned} (n)!! &= (n)(n-2)(n-4)\dots(2), \text{ for n even} \\ (n)!! &= (n)(n-2)(n-4)\dots(1), \text{ for n odd} \\ (0)!! = 1,\ (-1)!! &= 1,\ (-2)!! = \infty,\ (-3)!! = -1. \end{aligned} \tag{B.24}$$

Differentiation Relation

$$(1+\eta^2)\frac{d\overline{Q}_n^m(i\eta)}{d\eta} = -\left[\frac{1}{K_n^m}\overline{Q}_{n+1}^{m}(i\eta) + \eta(n+1)\overline{Q}_n^m(i\eta)\right] \tag{B.25}$$

Numerical Instabilities in Normalized Legendre Functions of the Second kind

It was observed that higher order instances of the Legendre Functions of the Second Kind become numerically unstable at higher values of η, visible in Fig. B.1, and that the value at which the instability first presents itself decreases as the order n increases. It was found that this was the result of floating point precision errors that arise as the polynomial powers making up the functions increase with n.

As large value inputs to the Functions are necessary for calculations of the upstream, a solution was devised. It was found that, as the input η became large, that the function value would approach the following equation

$$\overline{Q}_n(i\eta) \approx c\left(\frac{\pi}{2} - \arctan(\eta)\right)\eta^{n+1}. \tag{B.26}$$

It was observed that the Legendre Functions would typically decrease towards 0 before the numerical instabilities became apparent. Therefore, arbitrary cutoffs were calculated as a switchover from the normal function computation to the approximation. In this work these cutoffs were chosen to be when $\overline{Q}_n \leq 10^{-7}$. The value of η could then be used to compute c such that the function remains continuous.

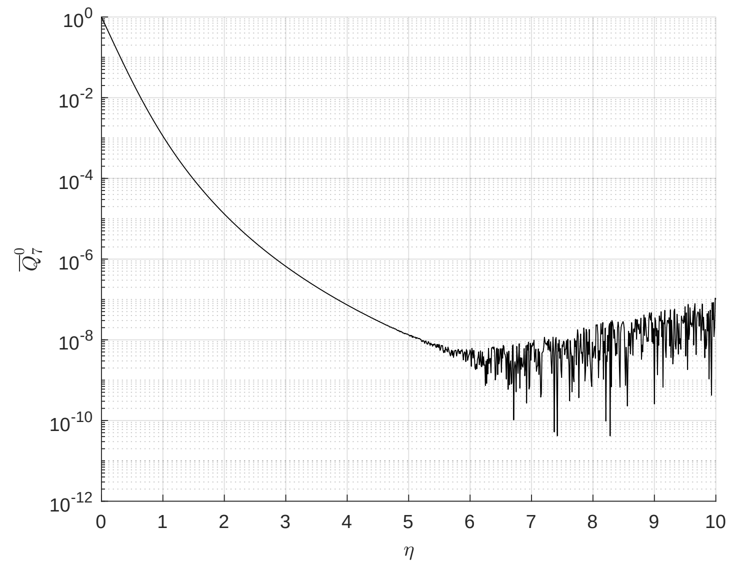

Figure B.1: Numerical Instability in the Normalized Legendre Function of the Second Kind.

Appendix C

DISC ACTUATOR THEORY

The propeller is the spinny bit that hurts if you touch it.

Matt Anderson

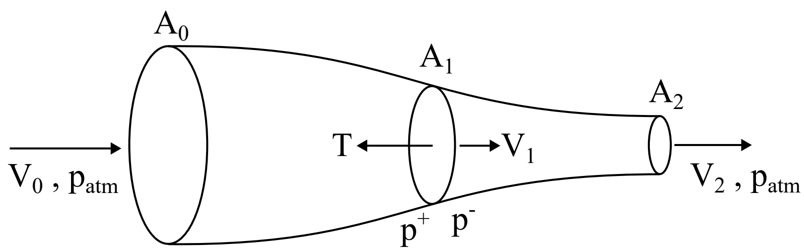

Figure C.1: Streamtubes and stations in Disk Actuator Theory.

Disk Actuator theory or Momentum theory is one of the most basic means of abstracting and analyzing a propeller.

First consider the quasi 1-D streamtube of flow the passes through the area of the propeller disk. In this streamtube 3 stations are considered: the far upstream, the actuator disk, and the far downstream, indexed 0, 1, and 2, respectively. An incompressible fluid is assumed. Being a streamtube, there can be no flow across its surface. A uniform velocity and pressure at each cross section of the streamtube are also assumed. Therefore, from mass conservation it is found that

$$\dot{m} = \rho A_0 V_0 = \rho A_1 V_1 = \rho A_2 V_2. \tag{C.1}$$

The disk is assumed to produce thrust by creating a pressure difference in the pressure immediately upstream, p^+, and downstream, p^- of the disk. It is also assumed that the far upstream and the far downstream are at atmospheric pressure. From Bernoulli's theorem, the pressures far upstream and downstream of the disk are related to the disk pressures on their respective sides to produce

$$\frac{1}{2}\rho V_1^2 + p^+ = \frac{1}{2}\rho V_0^2 \tag{C.2}$$

$$\frac{1}{2}\rho V_1^2 + p^- = \frac{1}{2}\rho V_2^2. \tag{C.3}$$

Subtracting one from the other, the pressure jump across the disk is calculated, which is related to the thrust by

$$p^{-} - p^{+} = \Delta p = \frac{T}{A_1}. \tag{C.4}$$

The above equation can be re-written as

$$T = A_1 \frac{1}{2} \rho \left(V_2^2 - V_0^2 \right). \tag{C.5}$$

Next, momentum conservation in the system is used. From the Reynolds Transport Theorem, the Flux of the fluid momentum through the boundaries plus any forces on the fluid should be equal to 0. As a streamtube, there is no flux through the streamtube sides, and the pressures at the upstream and downstream boundaries is equal to atmospheric by assumption. The force on the fluid is equal to the negative of the Thrust, therefore the momentum equation can be expressed as

$$\dot{m}(V_2 - V_0) = T \tag{C.6}$$

By substituting this into the previous equation, it is found that

$$2V_1 = V_2 + V_0 \tag{C.7}$$

which relates the flow at the disk to the upstream and downstream flows. The thrust can then be expressed as

$$T = 2\rho A_1 V_1 (V_1 - V_0). \tag{C.8}$$

The velocity added at the disk relative to the freestream is called the induced velocity $V_i = V_1 - V_0$. Representing the thrust with this value yields

$$T = 2\rho A_1 (V_0 + V_i) V_i. \tag{C.9}$$

With the relations between the velocities known, the wake contraction of the downstream flow can be calculated.

$$\frac{A_2}{A_1} = \frac{V_1}{V_2} = \frac{V_1}{2V_1 - V_0} = \frac{V_i + V_0}{2V_i + V_0} \tag{C.10}$$

The ideal power, that is the kinetic energy associated with producing the thrust, can be computed using a control volume analysis of the energy and is equivalent to multiplying the Thrust by the flow velocity passing through the propeller disk.

$$P_{\text{ideal}} = TV_1 = T(V_0 + V_i) \tag{C.11}$$

Several useful relations can also be calculated for the specific case of hover, when $V_0 = 0$. In this case, the velocity at the disk is equal to

$$V_1 = V_i = \sqrt{\frac{T}{2\rho A_1}} \tag{C.12}$$

and the wake area A_w relative to the propeller disk area A is equal to

$$\frac{A_2}{A_1} = \frac{A_w}{A} = \frac{1}{2}. \tag{C.13}$$

Additionally, the ideal or induced power is equal to

$$P_i = T\sqrt{\frac{T}{2\rho A_1}} = \sqrt{\frac{T^3}{2\rho A_1}}. \tag{C.14}$$